University of Aveiro Department of Physics,
2000

José Manuel Henriques Castanheira

Climatic Variability of the Atmospheric Circulation at the Global Scale

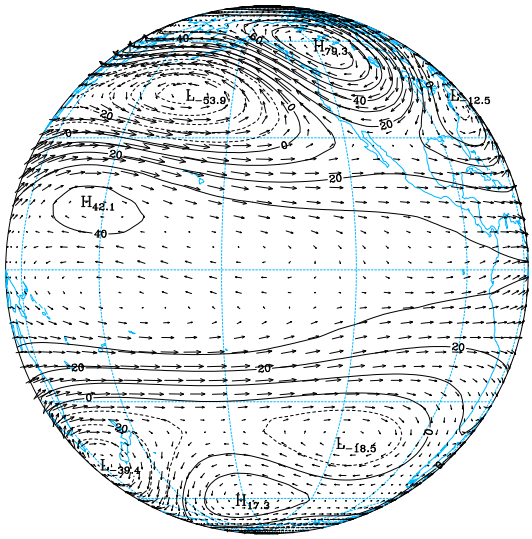

University of Aveiro Department of Physics
2000

José Manuel Henriques Castanheira

Climatic Variability of the Atmospheric Circulation at the Global Scale

Dissertation presented to the University of Aveiro for the fulfillment of the requirements for the Degree of Doctor in Physics, realized under the scientific supervision of the Professor Carlos DaCamara of the University of Lisbon and Professor Alfredo Rocha of the University of Aveiro.

o júri

presidente

Doutor Manuel Carlos Serrano Pinto
professor catedrático da Universidade de Aveiro

Doutor Alfredo Moreira Caseiro Rocha
professor auxiliar da Universidade de Aveiro

Doutor Carlos do Carmo de Portugal e Castro da Camara
professor auxiliar da Faculdade de Ciências da Universidade de Lisboa

Doutor Hans Friedrich Graf
senior scientist of the Max-Planck Institute for Meteorology - Hamburgo, Alemanha

Doutora Jean Patricia Palutikof
reader of the Climatic Research Unit - University of East Anglia - Inglaterra

Doutor João Alexandre Medina Corte Real
professor associado da Faculdade de Ciências da Universidade de Lisboa

Acknowledgements I want to express my deep gratitude to my advisors, Professor Carlos DaCamara and Professor Alfredo Rocha, for their constant encouragement, their advice and guidance throughout the course of this work.

I want also to thank Professor Ian Simmonds of the University of Melbourne who made available the Melbourne University Atmospheric General Circulation Model.

This work is dedicated to my children, João Francisco and José Pedro, and my wife Lurdes whose understanding and moral support are essential for this endeavor.

Abstract

A study on Climatic Variability of the Atmospheric Global Circulation for the months of December, January and February is presented, based on a simultaneous analysis of the geopotential and horizontal motion fields, by means of an expansion on a base of normal modes of the linearized primitive equations.

In a first part (Chapter 3), an analysis is presented of the Climatic Variability simulated by a set of ten parallel and independent integrations of the Melbourne University AGCM (version VII.1). All simulations were forced by the same observed SST and Sea Ice fields for the period of January 1979 to December 1988. In order to reduce the dimensionality of the simulated data set, the geopotential and horizontal wind fields were expanded on the normal modes of the model's reference atmosphere, allowing a dynamically consistent filtering of both wind and mass fields. By means of an analysis of variance, performed over the normal mode expansion coefficients, circulation variability was then partitioned into its internal and SST-forced components.

Modes of variability of the Global Circulation were identified by means of a Complex Principal Component Analysis (CPCA) that was also performed on the normal mode expansion coefficients. The forced variability patterns were obtained performing the CPCA on averaged values of the 10 simulations, that were computed for each month of each year (ensemble means). On the other hand, the internal (free) patterns of variability were obtained performing the CPCA on the deviations of monthly individual simulations from respective ensemble averages (that were used to compute the forced patterns). Based on described method, teleconnection patterns of Pacific/North America (PNA) and North Atlantic Oscillation (NAO) appear as free variability patterns of the Global Circulation. In the case of the forced variability, two conspicuous patterns were revealed, one for the barotropic and the other for the fourth baroclinic component, both related with the global effect due to the SST anomalies associated with the El Niño/Southern Oscillation 'cycle'.

In a second part (Chapter 4), a study is presented of the variability of the Global Circulation based on National Centers for Environmental Prediction (NCEP) reanalysis data, respecting to the period from January 1973 to December 1996. The geopotencial and horizontal wind fields were, in this case, expanded on the normal modes of the re-analysis reference atmosphere. Variability patterns of the re-analyzed atmosphere were then calculated by means of a CPCA performed on the expansion coefficients and using previous results from simulations as a guideline. Obtained results for the re-analysis allowed to validate those obtained from the simulations, as they also revealed global variability patterns associated with PNA and NAO patterns. Circulation patterns associated with the SST anomalies in the tropical Pacific were also obtained that revealed to be in close agreement with those respecting to the forced simulated circulation.

Finally, given the greater vertical resolution of the re-analyzed atmosphere, it was also possible to investigate the variability of the low stratospheric circulation, as well as its connection to the tropospheric circulation. It was found that the largest variability mode of the low stratospheric global circulation describes the intensity fluctuations of the cyclonic polar vortex in northern winter, being significantly correlated with the projections of the tropospheric circulation anomalies onto a characteristic pattern of the NAO . The second mode of variability of the stratospheric circulation allowed to establish a connection between the phase of equatorial QBO and the phase of a pattern of extratropical stratospheric circulation anomalies, dominated by a contribution due to zonal wavenumber $s = 1$.

Performed study conclusively demonstrates that projecting the atmospheric circulation onto a base of normal modes is not only an appropriate method, but lays the grounds for studying Climatic Variability of the Global Circulation. Usefulness of such a method resides on the fact that computed statistics are based on the very primitive variables of global circulation, therefore not simply relying on information provided by a 'proxy' variable of circulation, such as the 500 hPa geopotential field.

Resumo

Apresenta-se um estudo da Variabilidade Climática da Circulação Atmosférica Global para os meses de Dezembro, Janeiro e Fevereiro, baseado numa análise simultânea dos campos do geopotencial e do movimento horizontal, através de uma expansão daquele campos numa base de modos normais das equações primitivas linearizadas.

Numa primeira parte (Capítulo 3), procedeu-se à análise da Variabilidade Climática simulada por um conjunto de 10 integrações paralelas e independentes da versão VII.1 do AGCM da Universidade de Melbourne, todas forçadas pelos mesmos campos observados das SSTs e da cobertura de gelos oceânicos, durante o período de Janeiro de 1979 a Dezembro de 1988. A fim de se reduzir a dimensionalidade dos dados de base, os campos do vento horizontal e do geopotencial foram expandidos nos modos normais da atmosfera de referência do modelo, permitindo realizar uma filtragem consistente dos campos de massa e do movimento da atmosfera. Através de uma análise de variância realizada sobre os coeficientes da expansão nos modos normais, a variabilidade da circulação foi decomposta nas suas componentes livre e forçada.

Os modos de variabilidade da Circulação Global foram identificados através de uma análise em componentes principais complexas (CPCA), também realizada sobre os coeficientes da expansão nos modos normais. Os padrões de variabilidade forçada foram obtidos realizando a CPCA sobre os valores médios das 10 simulações para cada mês de cada ano, sendo os padrões de variabilidade livre identificados realizando a CPCA sobre os desvios dos valores simulados para cada mês em relação aos respectivos valores médios das 10 simulações. Com este método de análise, os padrões de teleconexão do Pacífico/América do Norte (PNA) e da Oscilação do Atlântico Norte (NAO) surgiram como padrões de variabilidade livre da Circulação Global. No caso da variabilidade forçada, realçam-se dois padrões, um para a componente barotrópica e outro para a quarta componente baroclínica, ambos relacionados com o efeito global devido às anomalias das SSTs associadas ao "ciclo" El Niño/Oscilação Austral.

Numa segunda parte (Capítulo 4), procedeu-se ao estudo da variabilidade da Circulação Global representada pelas reanálises do National Centers for Environmental Prediction (NCEP), referentes ao período de Janeiro de 1973 a Dezembro de 1996. Os campos do geopotencial e do vento horizontal foram agora expandidos na base de modos normais da atmosfera de referência das reanálises. Igualmente através de uma CPCA realizada sobre os coeficientes da expansão e tomando os resultados das simulações como referência, calcularam-se os padrões de variabilidade da atmosfera reanalisada. Os resultados obtidos com as reanálises permitiram validar os das simulações, revelando igualmente padrões de variabilidade global associados à PNA e à NAO. Identificaram-se também padrões semelhantes aos do forçamento simulado, associados com as anomalias das SSTs no Pacífico tropical.

Por fim, dada a maior resolução vertical da atmosfera reanalisada, foi ainda possível investigar a variabilidade da circulação da baixa estratosfera, bem como a sua conexão com a circulação troposférica. O modo de maior variabilidade da circulação global da baixa estratosfera descreve as flutuações de intensidade do vortex polar, durante o Inverno do Hemisfério Norte, e apresenta correlação significativa com as projecções das anomalias da circulação troposférica sobre um padrão característico da NAO. O segundo modo de variabilidade da circulação estratosférica estabelece uma associação entre a fase da QBO equatorial e a fase de um padrão de anomalias da circulação estratosférica extratopical, dominado pela contribuição do número de onda zonal $s = 1$.

O estudo efectuado demonstra, de forma conclusiva, que a expansão da circulação atmosférica numa base de modos normais constitui um método, não só adequado, mas sobretudo útil para o estudo da variabilidade global da circulação, residindo essa utilidade no facto de as estatísticas da circulação poderem, assim, ser estabelecidas com base nas variáveis primitivas da circulação global e não apenas em informação proveniente de uma variável 'proxy' da circulação, tal como, por exemplo, o campo do geopotencial aos 500 hPa.

Contents

List of Figures

List of Tables

Chapter 1

Introduction

The atmosphere, being a forced dissipative nonlinear dynamical system, is an example of a chaotic system in the sense that two initial states, differing by small amounts of their variables, evolve in such a way that the differences grow exponentially. In fact, at the end of a finite time interval, the relation between those two states do not differ from the statistical relation between any other two belonging to the same climatic state. This behaviour of the atmosphere imposes a theoretical temporal limit to the deterministic predictability of its instantaneous states, which has been established to be about 3 weeks [e.g., Lorenz, 1982; Chen, 1989]. In practice, due to unavoidable errors in and incompleteness of observations of the initial conditions as well as the imperfections of the models, useful predictions of the daily sequence of the weather states don't go beyond one or two weeks [e.g., Chen, 1989; Shukla, 1998].

In this context it is important to note that the temporal limit mentioned above refers only to the system's memory of the initial state conditions, i.e., the predictability of the day-to-day sequence of weather is an initial condition sensitive problem.

In the case of seasonal forecasting the problem is different. In fact, as pointed out by Palmer and Anderson [1994], even though the seasonal forecasts may yet constitute a problem of initial conditions, through the establishment of the slow evolution of the lower boundaries, particularly that of sea surface temperatures (SSTs), the forecast of the mean state of the atmosphere is essentially a problem of boundary conditions. These determine the statistics of the different atmospheric circulation regimes. To forecast the statistics of these regimes, for the seasonal scale and for longer scales, using atmospheric general circulation models (AGCM) requires making an ensemble of integrations, all subject to the same forcing fields, in particular, all forced by the

same prescribed fields of sea surface temperature (SST) and sea ice cover. Such an ensemble will allow to obtain, at least theoretically, an estimate of the probabilities of occurrence of specific circulation regimes, during the forecasted period.

Analysis of ensembles of simulation, performed with AGCM [e.g., Stern and Miyakoda, 1995; Rowell, 1998; Shukla, 1998], as well as observational studies [e.g., Horel and Wallace, 1981; Ropelewski and Halpert, 1989] allow to conclude that the statistics of circulation and precipitation patterns of the tropical atmosphere are strongly determined by the underlying SST.

In the case of the extratropical circulation, where the largest fraction of circulation variability is associated with the non-linearity and internal instability of the atmospheric system, observational studies [e.g., Horel and Wallace, 1981; Karoly, 1989] and results of numerical simulations [e.g., Graham *et al.*, 1994; Lau and Nath, 1996] also show that, at least during the extreme episodes of the ENSO (El Niño/Southern Oscillation) cycle, the statistics of the extratropical circulation patterns, mainly those of winter mean circulation over the Pacific and North America, are influenced, in a considerable way, by the SST anomalies of the tropical Pacific.

The extent to which the apparent high potential predictability of the tropical atmosphere and the small, but yet considerable over certain regions, potential predictability of the extratropical atmosphere can be realized in routine forecasting will depend on the accuracy of the atmospheric models and on the ability to predict the SST itself. Recently remarkable progress were made on the understanding, modeling and forecasting of SST anomalies of tropical Pacific [Ji *et al.*, 1996, and articles here in]. On the other hand, the AGCMs are successful on the simulation of seasonal mean response to El Niño-like SST anomalies exhibiting global circulation patterns resembling those observed [e.g., Kumar *et al.*, 1996]. These progresses make it possible for the United States National Weather Service (US NWS) to perform routine seasonal dynamic forecast (3-monthly means) for a set of 13 consecutive periods. For example, on December 17th 1998, forecasts of the seasonal means were issued for the following 13 periods: January to March (JFM (99)), February to April (FMA (99)), March to May (MAM (99)),....,JFM (2000). These forecasts are issued, with an operational nature, by the Climate Prediction Center (CPC), and are freely available on Internet (http://www.cpc.ncep.noaa.gov).

The US NWS uses three different method to perform seasonal forecasts, two of them based on statistical models and the other based on the integration of general

circulation models of the ocean and of the atmosphere (dynamic forecasts) [Carson, 1998]. Dynamic forecasts are performed in a two-tiered process. On the first step, the procedure consists of the production of a forecast of global SSTs, using a version of the NCEP (National Centers for Environmental Prediction) coupled ocean-atmosphere GCM. In the following step, the predicted SSTs are used as prescribed boundary conditions to generate an ensemble of integrations of a version of the NCEP atmospheric GCM [Carson, 1998; Smith and Livezey, 1999]. At the present, 18 integrations with different initializations are done to produce a forecast.

Seasonal forecasts for the European region appear to be more difficult. Part of the difficulties result from the great internal variability of the atmosphere and the apparent small ENSO influence on this region [Fraedrich, 1994; Davies *et al.*, 1997; Rowell, 1998]. European research on seasonal forecast recently received a strong impulse through the PROVOST (PRediction Of climate Variations On Seasonal to inter-annual Timescales) program. It involves the cooperation of eleven European institutions, and one of it's main goals is "to quantify the potential predictability of seasonal mean atmospheric variability, over Europe and other key areas worldwide (where, for example, there may be European interests), based on ensemble of atmospheric model integrations, with prescribed observed SST" [Carson, 1998].

Results obtained recently with ensemble integrations of two versions of the Hadley Center AGCM are encouraging for the possibility of making winter (DJF) and spring (MAM) seasonal forecasts over the North Atlantic and European regions [Davies *et al.*, 1997; Rodwell *et al.*, 1999]. This potential atmospheric predictability its mainly due to the prescription of the North and Tropical Atlantic SST anomalies.

The social-economic value of seasonal forecasts has been demonstrated for some tropical regions. In Peru, for example, agricultural planning takes in consideration the likelihood of a cold or warm phase of El Niño as a basis for government decisions as whether to plant dry crops such as cotton, or others, like rice, that are more water responsive. A substantial increase in agricultural yields have resulted from such guidance [Palmer and Anderson, 1994].

In the United States, studies of the ENSO influence on the agricultural yields and price of certain products has also demonstrated the potential economic value of seasonal forecasting [Hansen *et al.*, 1998, 1999; Phillips *et al.*, 1999].

The social-economic value of seasonal forecasting extends to other sectors beyond agricultural management such as, for example, the energy production [Davies *et al.*,

1997; Carson, 1998]. Regarding this matter, it is important to mention that all models of management/decision should integrate the seasonal forecasts in a probabilistic way. In fact, seasonal forecasts are formulated in terms of probability distributions of mean values of meteorological variables such as temperature and precipitation, for the forecasted period. It should be noted that in many cases, especially in extratropical regions such as Europe, the difference between predicted probabilities distribution and the climatological ones may be small [Palmer and Anderson, 1994].

In the above paragraphs the AGCM ensemble integration method was presented mentioning their practical value for forecasting at seasonal and longer time scales. Another aspect, closely related to that of forecasting, is the use of the ensemble simulation method to uncover systematic errors in the AGCMs [Kumar *et al.*, 1996; Smith and Livezey, 1999]. This error identification can lead to future improvements of the models themselves. In a purely scientific viewpoint the ensemble of simulations constitute a valuable experimental method, impossible to use in the real atmosphere, for the characterization of the atmospheric variability modes as well as the identification their causes [Harzallah and Sadourny, 1995; Renshaw *et al.*, 1998]. In the work presented here, this last perspective, that is also a fundamental approach for the development of forecasting ability at seasonal and longer times scales, was followed.

This work can be divided in two parts. In a first part (Chapter 3), an analysis is presented of the Climatic Variability simulated by a set of ten parallel and independent integrations of the Melbourne University AGCM (version VII.1). All simulations were forced by the same observed SST and Sea Ice fields for the period of January 1979 to December 1988. The variability of the global atmospheric circulation was decomposed in its internal and forced components, and the patterns of circulation variability were calculated. The time series (PCs) associated with forced circulation patterns were then correlated with the time series of SST anomalies in order to obtain forcing SST patterns.

In a second part (chapter 4), it is presented a study on the variability of global circulation based on the NECP re-analysis data, for the period of the January 1973 to December 1996. The results from simulations are used here as guidelines and, at the same time, are validated against 'observations'. Because of the greater resolution of the lower stratosphere of NCEP re-analysis, it was also possible to study variability modes not investigated in the simulations. Hence, in this part of the work, it is also analyzed the variability of stratospheric circulation as well as its connection with the

tropospheric circulation during Northern Hemisphere winter.

The simulated and observed variabilities of the geopotential and wind components were analyzed by means of an expansion of those fields onto the normal modes of the reference atmospheres of the model and of the re-analysis, respectively [Kasahara and Puri, 1981; Tanaka, 1994]. Using this method, the variabilities of the geopotential and wind components are simultaneously analyzed, giving a measure of the variability of the atmospheric circulation in terms of the variability of the total energy (kinetic energy + available potential energy).

The major component of interannual variability of the tropical atmosphere is associated with the ENSO phenomenon. Even though the centre of action of this phenomenon is located in the tropical Pacific, its influence on the extratropical circulation extends to, at least, half of the globe [Horel and Wallace, 1981; Karoly, 1989]. On the other hand, one might expect that the spatial organization of the low frequency internal variability, such as the interannual one, has a global scale character of its own. With these premises in mind, the expansion of the geopotential and horizontal wind fields in a 3-dimensional normal modes basis (a basis of functions defined for the whole atmosphere) appeared to be an adequate approach for the study of those types of variability.

Another important aspect in the study of the variability of atmospheric global circulation is the need to use a basis of functions that allows to, as much as possible, minimize the number of variables (degrees of freedom) that must be retained for analysis. A basis of normal mode vector functions, constituted by solutions of the linearized primitive equations, retains important characteristics of the atmosphere dynamics. So, if on one hand the expansion in a normal modes basis may allow for a significant reduction of the variables number, on the other hand it provides a dynamically consistent method for the filtering of the mass and horizontal motion fields of the atmosphere, allowing to distinguish between inertio-gravity and planetary waves, as well as between barotropic and baroclinic components.

Chapter 2

Theoretical Framework

2.1 Climatic system

The Climatic System, constituted by the Atmosphere, Hydrosphere, Cryosphere, Lithosphere and Biosphere, is extremely complex due to the nonlinear interactions of its components, as well as the nonlinearity of the processes occurring inside each one. Even though it is a closed system, where numerous irreversible processes occur, the Climatic System does not evolve to a maximum entropy state, maintaining highly organized processes, from the global regimes of wind and ocean currents to the complex processes related to life, due to the high quality (i.e., low entropy) of the incoming solar radiation and its systematic variation with latitude [Peixoto and Oort, 1992].

The distribution of solar radiation at the top of the atmosphere presents fluctuations from the daily scale, related to earth's rotation, or the seasonal scale, related to translational motion and the tilt of the rotational axis, through fluctuations with periods of about 11-years, due to variations of solar activity, to fluctuations in time scales of ten to hundred thousand years, related to variations of the orbital parameters. The effects of fluctuations in the distribution of solar radiation are visible in the actual behaviour of the climatic system, for example, in the observed daily and seasonal cycles of the surface temperatures. On longer time scales, those effects can be observed on the fluctuations of the stratospheric temperature associated with the 11-year sunspot cycle [van Loon and Labitzke, 1993]. With respect to time scales of thousands of years, results of empirical nature provide strong evidence of consistent phase relationships between the precisely known changes of Earth's orbital parameters and the North Hemisphere glacial-interglacial cycles as well as the cycles of enhanced or weakened

monsoons in middle and tropical latitudes, during the Pleistocene [Kutzbach, 1992].

The causes of the above mentioned variations are referred as external factors of the climatic system, since they force its evolution but are not influenced by the climatic variables themselves.

The behavior of each climatic subsystem is governed by its internal dynamics, with characteristic space-time scales spectra, and by the dynamics of its boundaries, often involving very complex feedback mechanisms among the various subsystems. Because of the nonlinearity of its internal dynamics and its interactions, the climatic subsystems present high variability without any external forcing variations. This *internal (free)* variability occurs in a very long, possibly unlimited, spectrum of time scales. An example of internal variability is given by the fluctuations of weather patterns in middle and high latitudes, governed by dynamically unstable synoptic systems and presenting a chaotic component on their time averages [Madden, 1976]. Another example, in the scale of several centuries, may be found in the general deglaciation of the past 18,000 years. Between 11.000 and 10.000 years before the present date, the general warming trend was interrupted by a very significant return to cold conditions that persisted for a few centuries, and was then followed by an equally abrupt warming. A weakened or even absent thermohaline circulation on the Atlantic Ocean, due to a strong increase of fresh water discharge from St. Lawrence's river, is pointed as a possible cause of the return to cold conditions [Bengtsson, 1992].

The climate has continuously been changing, it has a past and it will certainly have a future. For the study of climate variations, the concept of climatic state should be precisely defined and a less restrictive notion of external forcing should be presented.

2.2 Climatic state

A complete definition of climatic state should be formulated in terms of a statistical description of the variables that characterize each one of the subsystems that constitute the global climatic system, assuming fixed external forcing conditions. Such a description should not only include means values but also the variances about the mean, the covariance between variables possibly separated in space and time, probabilities of extreme events, and so on [Leith, 1978]. The more restricted definition of climatic state of a given subsystem (*e.g.*, the Atmosphere) involves the statistical description of its variables, as well as the specification of the mean conditions of the

other components of the global climatic system, and other external forcings that may condition the set or sets of possible statistics.

Analytical procedures for determining the climatic state or states of a given subsystem from its governing equations and the prescribed boundary conditions would include the derivation and solution of a new set of equations whose dependent variables are statistics, as well as the calculation of statistics from the analytical solutions of the original equations. However, the extreme nonlinearity of the equations renders this procedure unfeasible, being the statistics empirically calculated, based on observed or simulated data sets [Lorenz, 1970].

The establishment of statistical properties of a given climatic state, from observed or simulated data, requires an averaging method. The most common method, and the only feasible one until recently, is to compute averages over a time interval T. If the Atmosphere is the considered internal system, then the climatic state is defined based on the statistics of atmospheric variables, evaluated for the time interval T, together with the mean conditions of the Oceans, Cryosphere, Continents, and other external forcings. In that case, the averaging time interval must, at least, exceed the average life span of the synoptic weather systems in the atmosphere, otherwise the climatic state fluctuations would be indistinguishable from the meteorological fluctuations themselves. One can then define climatic states for a month, a season, a year, a decade, and so on. The respective statistics are estimated from a sample of N time intervals T, for example, N January months or N northern winter seasons.

It is a well-known result of sampling theory that, defining the climatic state as the averaged weather over a finite time interval T, then each climatic state variable has a standard deviation $\sigma_n^2 = \sigma^2/n$, where σ^2 is the standard deviation of the weather state variables, and n is the number of independent weather states on the time interval T [Leith, 1973]. The climatic state fluctuations, resulting from weather states fluctuations, occur even with fixed boundary conditions, and form what is named free variability, internal variability or, also, climatic noise.

Like the climatic state realizations, that is, the month or seasonal averages, the climatic mean, estimated from a sample of N months or seasons, also has an associated uncertainty. The way to reduce it would be to increase the number N of realizations, and the true climatic mean will be calculated in the limit when N tends to infinite. However, this procedure, besides not being feasible, would lead to the theoretical impossibility of considering climate as changing with time, i.e., it would not be suitable

to the problem of climatic changes. A finite value of N must be chosen as a solution of compromise. In the case of the atmosphere, the traditional 30 year period, determined by the World Meteorological Organization, is still a useful reference for the value of N [Peixoto and Oort, 1992].

Another theoretical question, related to the climatic state definition and of great practical importance for the numeric simulations of climatic changes, is to know if the Climatic System is transitive or intransitive. If the system's dynamics, after a transient period when it looses the memory of the initial conditions, leads to an unique and stable set of statistics compatible with a fixed set of boundary conditions, then the system is transitive. On the other hand, if the system dynamics lead to two or more stable statistics sets, depending on the initial conditions and compatible with the same set of boundary conditions, then the system is intransitive. If the system is transitive, the statistics, calculated over a long enough time interval, are unique, and the numerically simulated equilibrium states (e.g., global mean temperature for a double concentration of CO_2) are also unique.

The atmosphere, unless it is drastically simplified, is probably not intransitive [Lorenz, 1990; Bengtsson, 1992]. On the other hand, some modeling results suggest an intransitive behaviour of the thermohaline circulation in the Atlantic Ocean [Bengtsson, 1992]. However, there is not enough information at the present to know whether the global climatic system is transitive or intransitive. The climatic system may yet be almost intransitive. In this case the system will be characterized by a set of statistics for a long, but finite, period of time, followed by a more or less abrupt change to another set of statistics for an equally long time, without any variations on the external forcings. According to Lorenz [1970], almost intransivity becomes plausible if the considered system includes, besides the Atmosphere, other components of the climatic system, even if such an inclusion is restricted to the SSTs only. However, this possibility would raise serious difficulties, when the results of long term simulation are analyzed. Thus, for practical purposes it is assumed that the climatic system, after a transient period when it looses its memory of the initial conditions, will tend to an unique equilibrium state, which is still a debated assumption [Schneider, 1992].

2.2.1 A dynamical concept of climatic state

The concept of climatic state, based on statistics over an infinite time, is, as mentioned before, incompatible with a dynamic notion of the Climate. The conventional compromise, defining the climatic state with a finite number of realizations (e.g. 30 years) is still useful. However, it is not suitable for the mathematical formulation of a climate dynamics that continuously responds to slow changing external forcings. In order to facilitate the presentation of a dynamic concept of climatic state, a less stringent notion of external forcing must be presented.

One of the factors that make climatic forecasts difficult and complex is the multiplicity of feedback mechanisms among the different components of the climatic system. The Atmosphere is governed by its internal nonlinear dynamics that is forced by the slower evolutions of the Oceans and the Cryosphere, which are sensitive to atmospheric state themselves. On the other hand, the Ocean forces and responds to even slower variations of the Cryosphere and the Lithosphere. In this way, when defining a given subsystem, the external character of its boundaries is only conceptual, since the other components of the global climatic system respond physically to the state of the considered subsystem. Thus, a judicious separation between what should be part of the system and what should belong to its environment is then needed.

Depending on the problem under study, a separation based on the time scales of the different processes may be adequate. For example, in weather forecasting the Atmosphere is the sole component of the internal system, with the SSTs, sea ice covering, and snow considered as fixed external conditions. On the other hand, for seasonal forecasting the internal system should also include the coupled dynamics of those components, specially the SSTs [Palmer and Anderson, 1994], in order to forecast their fluctuations. For longer time scales, like the ones implicit on the study of climatic changes related to the rise of greenhouse gas concentration, the internal system should encompass, besides the Atmosphere, the complete Ocean and Cryosphere dynamics, processes in Continental surfaces and the Biosphere [Peixoto and Oort, 1992].

Another way to define the internal system consists in prescribing the time evolution (predicted or observed) of the slower components, (e.g., the SSTs), which determine the statistics of the components with short response times like the Atmosphere [Palmer and Anderson, 1994]. Another example, where the internal system encompasses the Atmosphere, Ocean, Cryosphere and Biosphere, is given by the climatic change simu-

lations forced with scenarios of growth rates of greenhouse gas concentrations from the IPCC (Intergovernmental Panel on Climate Change).

The nonlinearity of the equations and the uncertainties of the initial state make it impossible to forecast the weather states for periods beyond one or two weeks. However if surface conditions, especially SSTs, are previously forecasted for a period of several months, for example a season, the influence of those conditions on the weather regimes statistics can be evaluated from an ensemble of numeric integrations of the atmospheric circulation [Palmer and Anderson, 1994]. This procedure applies directly the concept of ensemble used for a definition of climatic state suitable to the study of Climate Dynamics.

The climatic state is then defined by the statistics calculated, for a given period T, over a conceptual and infinite set of identical Atmospheres, each one evolving independently, but all subject to the same boundary conditions. The real Atmosphere is the observed realization of the mental and infinite set of copies. In the case of the global Climatic System, the climatic state is then defined by the distribution of probabilities of the values of the climatic variables of a period T, in a conceptual and infinite set of Earth's, each one evolving independently, and all subject to the same radiative forcing. This concept presents several analogies to the kinetic theory of gases: the weather state fluctuations correspond to the individual movements of molecules, while the macroscopic thermodynamic properties, like pressure and temperature, correspond to the mean values of climatic variables calculated over all members of the ensemble [Leith, 1978; Schneider, 1992].

The description of the time evolution of the climatic states of a given subsystem, using an ensemble of independent numeric integrations with prescribed (observed or forecasted) boundary conditions, is a statistical description were the subsystem looses the memory of its initial internal conditions. However, there is a memory of the initial conditions through the prescribed evolution of the boundaries.

The prescription of the boundaries excludes the possible feedback mechanisms between the internal and the external systems. This makes the success of these types of studies depend of the errors in the boundary prescription as well as on the models themselves, particularly on their parameterizations. Although the responses of the external systems to changes in the internal system are excluded, the results of those responses can be anticipated, as long as the errors in boundary prescription are unimportant and the model is realistic enough [Harzallah and Sadourny, 1995].

2.3 Climatic signal and noise

The introduction of the concepts of climatic signal and climatic noise is facilitated by the definition of climatic state in terms of the statistics evaluated over an ensemble. The climatic signal is associated with the differences between the parameters of the distributions of probabilities that characterize two climatic states. A climatic state change occurs if some of the parameters (e.g., the mean or the standard deviation) of those distributions are different. It should be noted that it is not necessary a variation of the ensemble means for a climatic change to happen; it may result, for example, from a change on the probabilities of extreme events.

The climatic noise is associated with the differences between two distinct realizations of the same climatic state. For example, the differences between the mean temperatures of two July months, of the same year, but of two distinct conceptual copies (simulations) of the atmosphere, are due to climatic noise. The same is true for the differences between two July months of different years, if the forcing is the same in both years.

The detection of a climatic signal in the observed atmosphere involves the estimation of the random components (noise) of the variability of the monthly or seasonal means based on daily data, and the comparison with the observed interannual variability for the same means [Madden, 1976; Trenberth, 1985]. The use of this method is particularly difficult in the extratropical regions, where the Atmosphere possesses a high internal variability that may obscure completely the answer to oceanic forcing.

Another method for the study of oceanic forcing, widely used in the 80's and early 90's, compares the interannual variance of monthly or seasonal means in two AGCM simulations . A control simulation is forced by climatological SSTs, and the other one, an anomaly type simulation, is forced by SST fields, which include global or regional, idealized or observed interannual variability [Pitcher *et al.*, 1988; Kawamura *et al.*, 1995]. The interpretation of the results of such kind of experiments is based on two premises of debatable validity [Harzallah and Sadourny, 1995; Rowell, 1998]: i) the forcing due to an anomaly is independent of other possible anomalies that may exist in the global SST field and were replaced by climatological values, ii) the internal variability is the same on the anomaly simulation and the control simulation, where the SST gradients were smoothed.

A third method to investigate the external forcing of atmospheric circulation results

from the use of the theoretical concept of atmospheric ensemble first proposed by Leith [1978]. The method consists in performing an ensemble of parallel and independent simulation, all forced by identical external forcings. This method, much used since the second half of the 90's, and closely related to the increase of the power of scientific calculation, allows to isolate the climatic signal, even in regions were the atmosphere possesses high internal variability, as long as a large enough number of simulations are done. This is the method used in this work, so in the next section, statistical models of analysis of variances, which produce unbiased estimates of the internal and forced variabilities, will be presented.

2.3.1 Internal and forced variability decomposition

Consider a set of M independent simulations of the atmospheric circulation for a period of N years. All the simulations are forced by the same SST and sea ice cover fields, differing only in the initial atmospheric states, which are supposed to be a random sample of initial states.

The value y_{mn} of a climatic variable Y (e.g. monthly mean pressure at given point), at the year n ($n = 1, ..., N$), obtained in the m^{th} simulation ($m = 1, ..., M$), may be decomposed as the sum of two independent components:

$$y_{mn} = \beta_n + \varepsilon_{mn} \tag{2.1}$$

where β_n is the ensemble mean that depends only on the external forcing, and ε_{nm} represents the random fluctuations due to internal variability. The distribution of probabilities of the values ε_{nm}, for each year n, is characteristic of climatic state, and may also change from year to year due to oceanic forcing. In sum, it can be considered that the M simulations form a set of N ensembles, each one with M independent members.

Climatic signal in the ensemble means

Considering that the N ensembles are also independent among themselves, and that all have identical variances, σ^2, then the quantities y_{mn} can be interpreted as random variables on the following model:

$$\Omega_1 \begin{cases} y_{mn} = \beta_n + \varepsilon_{mn} & (m = 1, ..., M;\ n = 1, ..., N) \\ E\left[\varepsilon_{mn}\right] = 0 \\ E\left[\varepsilon_{mn}\varepsilon_{m'n'}\right] = \delta_{mm'}\delta_{nn'}\sigma^2 \end{cases}$$

where $E[\ ]$ represents the mathematical expectation operator, and $\delta_{nn'}$ is 0 or 1, according as $n \neq n'$ or $n = n'$, respectively.

This model is different from the "one-way layout fixed-effect model" discussed by Scheffé [1959, sec. 3.1] only in the fact that it does not require that the fluctuations ε_{mn} have a normal distribution. However, the normality condition is not necessary to deduct the expressions of the variances presented by Scheffé [1959, tabela 3.1.1], as it can be demonstrated using rule 2 he presented on its section 2.6.

Unbiased estimates of the β_n constants and of the internal variance $\sigma^2_{INT} = \sigma^2$ are given by

$$\hat{\beta}_n = \frac{1}{M}\sum_{m=1}^{M} y_{mn} \tag{2.2}$$

$$\hat{\sigma}^2_{INT} = \frac{1}{N}\sum_{n=1}^{N}\frac{1}{M-1}\sum_{m=1}^{M}\left(y_{mn} - \hat{\beta}_n\right)^2. \tag{2.3}$$

The variance due to oceanic forcing *(forced variance)* is defined by the following expression

$$\sigma^2_{SST} = \frac{1}{N-1}\sum_{n=1}^{N}(\beta_n - \beta)^2, \tag{2.4}$$

where $\beta = \sum_{n=1}^{N}\beta_n/N$ is the average of the constants β_n. According to the table of analysis of variance presented by Scheffé [1959, table 3.1.], an unbiased estimate of the forced variance, σ^2_{SST}, is given by the following expression

$$\hat{\sigma}^2_{SST} = \frac{1}{N-1}\sum_{n=1}^{N}(\hat{\beta}_n - \hat{\beta})^2 - \frac{\hat{\sigma}^2_{INT}}{M}, \tag{2.5}$$

with $\hat{\beta}$ an unbiased estimate β given by

$$\hat{\beta} = \frac{1}{N}\sum_{n=1}^{N}\hat{\beta}_n = \frac{1}{MN}\sum_{n=1}^{N}\sum_{m=1}^{M} y_{mn}. \tag{2.6}$$

Finally, the total variance is defined by

$$\sigma^2_{TOT} = \sigma^2_{INT} + \sigma^2_{SST}. \tag{2.7}$$

Climatic signal in the means and variances of the ensembles

In the model Ω_1, all N ensembles have identical internal variances, σ^2. Consider now a model Ω_2 where, besides the climatic signal in the means of the ensembles, there is also a climatic signal in the variances of the ensembles, i.e., the internal variances, σ_n^2, change from year to year,

$$\Omega_2 \begin{cases} y_{mn} = \beta_n + \varepsilon_{mn} & (m = 1, ..., M;\ n = 1, ..., N) \\ E\left[\varepsilon_{mn}\right] = 0 \\ E\left[\varepsilon_{mn}\varepsilon_{m'n'}\right] = \delta_{mm'}\delta_{nn'}\sigma_n^2 \end{cases}$$

Defining a mean internal variance as

$$\sigma^2 = \frac{1}{N}\sum_{n=1}^{N}\sigma_n^2, \tag{2.8}$$

the following change of variables can be performed

$$\tilde{y}_{mn} = \frac{\sigma}{\sigma_n}y_{mn} = w_n y_{mn} \tag{2.9}$$

to obtain a new model $\tilde{\Omega}_2$, which is similar to the model Ω_1,

$$\tilde{\Omega}_2 \begin{cases} \tilde{y}_{mn} = \tilde{\beta}_n + \tilde{\varepsilon}_{nm} & (m = 1, ..., M;\ n = 1, ..., N) \\ E\left[\tilde{\varepsilon}_{mn}\right] = 0 \\ E\left[\tilde{\varepsilon}_{mn}\tilde{\varepsilon}_{m'n'}\right] = \delta_{mm'}\delta_{nn'}\sigma^2 \end{cases}$$

where

$$\tilde{\beta}_n = \frac{\sigma}{\sigma_n}\beta_n = w_n\beta_n \qquad \text{e} \qquad \tilde{\varepsilon}_{mn} = \frac{\sigma}{\sigma_n}\varepsilon_{mn} = w_n\varepsilon_{mn}. \tag{2.10}$$

The use of expressions like 2.3 and 2.5 to estimate the internal and forced variances of $\tilde{y}_{mn}$ would have implicit the hypothesis that the absence of climatic signal would correspond to

$$\tilde{\beta}_1 = \tilde{\beta}_2 = \tilde{\beta}_3 = ... = \tilde{\beta}_n. \tag{2.11}$$

The expressions of the variances must be modified so that the absence of climatic signal in the ensemble means corresponds to the hypothesis

$$\omega: \ \ \beta_1 = \beta_2 = \beta_3 = ... = \beta_n = \beta, \tag{2.12}$$

To obtain the new unbiased estimates of the internal and forced variances, adequate to the situation described by the model Ω_2, the method presented in section 3.1 of Scheffé [1959] was followed.

Consider, then, the model $\tilde{\Omega}_2$ with the constants $w_n\beta_n$ explicitly written instead of $\tilde{\beta}_n(= w_n\beta_n)$. Unbiased estimates of the constants β_n are given by the values $\hat{\beta}_n$ that minimize the following sum of squared deviation

$$S_{\tilde{\Omega}_2} = \sum_{n=1}^{N}\sum_{m=1}^{M}\left(\tilde{y}_{mn} - w_n\hat{\beta}_n\right)^2 = \sum_{n=1}^{N} w_n^2 \sum_{m=1}^{M}\left(y_{mn} - \hat{\beta}_n\right)^2. \tag{2.13}$$

Calculating the partial derivatives with respect to $\hat{\beta}_n$ and equating them to 0, one obtains

$$\hat{\beta}_n = \frac{1}{M}\sum_{m=1}^{M} y_{mn}. \tag{2.14}$$

Under the hypothesis 2.12 of absence of climatic signal in the ensembles means, the sum of squares, which must be minimized in order to obtain an unbiased estimate of β, is given by

$$S_{\omega} = \sum_{n=1}^{N}\sum_{m=1}^{M}\left(\tilde{y}_{mn} - w_n\hat{\beta}\right)^2 = \sum_{n=1}^{N} w_n^2 \sum_{m=1}^{M}\left(y_{mn} - \hat{\beta}\right)^2. \tag{2.15}$$

Again, calculating the derivative with respect to $\hat{\beta}$ and equating to 0, one obtains

$$\hat{\beta} = \frac{\sum_{n=1}^{N} w_n^2\hat{\beta}_n}{\sum_{n=1}^{N} w_n^2}. \tag{2.16}$$

Expanding the squares of the differences in (2.13), (2.15) e (2.17), it is easy to show that

$$S_{\omega} - S_{\tilde{\Omega}_2} = \sum_{n=1}^{N} w_n^2 \sum_{m=1}^{M}\left(\hat{\beta}_n - \hat{\beta}\right)^2. \tag{2.17}$$

Using the rule 2 of the section 2.6 of Scheffé, one obtains

$$E\left[\frac{S_{\omega} - S_{\tilde{\Omega}_2}}{N-1}\right] = \sigma^2 + \frac{1}{N-1}\sum_{n=1}^{N} w_n^2 \sum_{m=1}^{M}\left(E\left[\hat{\beta}_n\right] - E\left[\hat{\beta}\right]\right)^2, \tag{2.18}$$

where

$$E\left[\hat{\beta}_n\right] = \beta_n \qquad \text{e} \qquad E\left[\hat{\beta}\right] = \frac{\sum_{n=1}^{N} w_n^2\beta_n}{\sum_{n=1}^{N} w_n^2} = \beta. \tag{2.19}$$

Now, if the variance due to the oceanic forcing is defined by the expression

$$\sigma_{SST}^2 = \frac{1}{N-1}\sum_{n=1}^{N} w_n^2(\beta_n - \beta)^2, \tag{2.20}$$

then, an its unbiased estimate is given by

$$\hat{\sigma}^2_{SST} = \frac{1}{N-1}\sum_{n=1}^{N} w_n^2(\hat{\beta}_n - \hat{\beta})^2 - \frac{1}{M}\frac{1}{N}\sum_{n=1}^{N} w_n^2 \frac{1}{M-1}\sum_{m=1}^{M}\left(y_{mn} - \hat{\beta}_n\right)^2. \qquad (2.21)$$

Since $\sigma = \sum_{n=1}^{N}\sigma_n/N$ and

$$\hat{\sigma}^2_n = \frac{1}{M-1}\sum_{m=1}^{M}\left(y_{mn} - \hat{\beta}_n\right)^2 \qquad (2.22)$$

is an unbiased estimate of the internal variance of the n^{th} ensemble, then another unbiased estimate of σ^2_{SST} will be given by

$$\hat{\sigma}^2_{SST} = \frac{1}{N-1}\sum_{n=1}^{N} w_n^2(\hat{\beta}_n - \hat{\beta})^2 - \frac{1}{M}\frac{1}{N}\sum_{n=1}^{N} \frac{1}{M-1}\sum_{m=1}^{M}\left(y_{mn} - \hat{\beta}_n\right)^2. \qquad (2.23)$$

The use of the expression 2.21 to calculate an estimate of forced variance of the ensemble means requires the knowledge of the ratios of internal variances, σ_n^2, of the ensembles, i.e., to determine the climatic signal on the ensemble means, the climatic signal on the internal variances should be previously known. For this reason, the expression 2.21 is of difficult use. The difficulties are not completely solved, if the estimate of mean internal variance, σ^2, in the second term on the right-hand side of equation 2.21, is replaced by the average of the estimates of the internal variances of the N ensembles, as it can be verified by equation 2.23.

Case where the ensembles are not independent

In the models discussed above, it was considered that n designated the year simulated. Consider now that n represents winter months (DJF), so that, instead of N ensembles, there will be $3N$ ensembles.

By the construction of the set of simulations, its known that

$$E\left[\varepsilon_{mn}\varepsilon_{m'n'}\right] = 0 \qquad \text{if } m \neq m'. \qquad (2.24)$$

If y_{mn} and $y_{mn'}$ represent monthly mean values of two winter months, of the same simulation, but of different years, it is very unlikely that $E\left[\varepsilon_{mn}\varepsilon_{mn'}\right] \neq 0$ [Lorenz, 1990]. If, on the contrary, n and n' represent two different months, but of the same winter, then $E\left[\varepsilon_{mn}\varepsilon_{mn'}\right]$ may be different from zero. Let's see then, how the estimates of the internal and forced variances are affected by the correlation between ensembles.

Consider again the model Ω_1, and a variable $y_{\cdot n}$ defined by

$$y_{\cdot n} = \frac{1}{M} \sum_{m=1}^{M} y_{mn}. \tag{2.25}$$

This variable verifies the following model

$$\Omega_3 \begin{cases} y_{\cdot n} = \beta_n + \varepsilon_{\cdot n} & (n = 1, ..., 3N) \\ E\left[\varepsilon_{\cdot n}\right] = 0 \\ E\left[\varepsilon_{\cdot n}\varepsilon_{\cdot n'}\right] = \delta_{nn'}\dfrac{\sigma^2}{M} \end{cases}$$

where, according to the central limit theorem, if M is large enough, the free fluctuations $\varepsilon_{\cdot n}$ have an approximately normal distribution.

Let $y_{\cdot\cdot}$ denote the average of $y_{\cdot n}$, its 'variance' is calculated by

$$\frac{1}{3N-1} \sum_{n=1}^{3N} \left(y_{\cdot n} - y_{\cdot\cdot}\right)^2 = \frac{1}{3N-1} \sum_{n=1}^{3N} \left[(\beta_n - \beta) + (\varepsilon_{\cdot n} - \varepsilon_{\cdot\cdot})\right]^2. \tag{2.26}$$

where $\beta = \sum_{n=1}^{3N} \beta_n / 3N$. Expanding the square of the sum of in the right-hand side of equation 2.26 and using the mathematical expectation operator, one obtains

$$\begin{aligned} E\left[\frac{1}{3N-1} \sum_{n=1}^{3N} \left(y_{\cdot n} - y_{\cdot\cdot}\right)^2\right] &= \frac{1}{3N-1} \sum_{n=1}^{3N} \left(\beta_n - \beta\right)^2 \\ &\quad + E\left[\frac{1}{3N-1} \sum_{n=1}^{3N} \left(\varepsilon_{\cdot n} - \varepsilon_{\cdot\cdot}\right)^2\right]. \end{aligned} \tag{2.27}$$

Finally, as the expression in the $E[\ ]$ operator on the right-hand side of equation 2.27 is an unbiased estimate of the variance of $\varepsilon_{\cdot n}$, that equation can be rewritten in the following form

$$\frac{1}{3N-1} \sum_{n=1}^{3N} \left(\beta_n - \beta\right)^2 = E\left[\frac{1}{3N-1} \sum_{n=1}^{3N} \left(y_{\cdot n} - y_{\cdot\cdot}\right)^2\right] - \frac{\sigma^2}{M}. \tag{2.28}$$

Consider, now, that the ensembles n and $n+1$ are not independent, i.e.,

$$E\left[\varepsilon_{mn}\varepsilon_{m(n+1)}\right] = \rho\sigma^2, \tag{2.29}$$

where ρ is the correlation coefficient, and that all the remaining pairs of ensembles are independent, i.e.,

$$E\left[\varepsilon_{mn}\varepsilon_{mn'}\right] = 0 \qquad \text{if} \qquad |n - n'| > 1. \tag{2.30}$$

In these conditions, because the ensemble members are independent, the variable $\varepsilon_{\cdot n}$ has still the variance σ^2/M, but the covariance is now given by

$$E\left[\varepsilon_{\cdot n}\varepsilon_{\cdot n'}\right] = \begin{cases} \rho\dfrac{\sigma^2}{M} & \text{if} \quad |n-n'| = 1 \\ \\ 0 & \text{if} \quad |n-n'| > 1 \end{cases} \tag{2.31}$$

This is a result that can be easily obtained, replacing $\varepsilon_{\cdot n}$ by $\sum_{m=1}^{M}\varepsilon_{mn}/M$, using the linearity of the operator $E[\ ]$ and the equalities (2.24), (2.29) and (2.30). Similarly, expanding the square of the difference in the second term of the right-hand side of (2.27), and using the result (2.31), one obtains (see Scheffé [1959, pag. 338])

$$\frac{1}{3N-1}\sum_{n=1}^{3N}\left(\beta_n-\beta\right)^2 = E\left[\frac{1}{3N-1}\sum_{n=1}^{3N}\left(y_{\cdot n}-y_{\cdot\cdot}\right)^2\right] - \frac{\sigma^2}{M}\left(1-\frac{2\rho}{3N}\right). \tag{2.32}$$

It can be concluded, then, that in case the ensembles are not independent, the internal variance is correctly estimated by 2.3, however, if $\rho > 0$, the forced variance is slightly underestimated by (2.5).

2.4 Atmospheric normal modes

An hydrostatic and adiabatic atmosphere can freely oscillate around a reference state at rest. The vertical and horizontal structures of each mode of oscillation can be separated, the horizontal structure being identical to that of a free oscillation mode of an incompressible, homogeneous, hydrostatic and inviscid fluid over a rotating sphere.

The normal modes (3-dimensional structures of the free oscillations) constitutes a basis, with physical significance, to expand the mass and horizontal motion fields of the atmosphere. This fact constitutes a fundamental propriety for the work here presented.

This section describes the theory of the normal modes in the approximation of a shallow-atmosphere, i.e., in the 'traditional' approximation of an atmosphere with a vertical dimension much smaller than the horizontal one, and considering the gravity acceleration, g, and the radius, r, constant and equal to their mean values at the earth's surface.

2.4.1 Linearized primitive equations

Under the approximation of a shallow-atmosphere and using the coordinates (λ, θ, p) with λ the longitude, θ the latitude and p the pressure, the horizontal momentum, continuity, hydrostatic and thermodynamic energy equations may be written in the following form

$$\frac{\partial u}{\partial t} - 2\Omega v \sin\theta + \frac{1}{a\cos\theta}\frac{\partial \phi}{\partial \lambda} = -\mathbf{V}\cdot\nabla u - \omega\frac{\partial u}{\partial p} + \frac{\tan\theta}{a}uv + F_u \tag{2.33}$$

$$\frac{\partial v}{\partial t} + 2\Omega u \sin\theta + \frac{1}{a}\frac{\partial \phi}{\partial \theta} = -\mathbf{V}\cdot\nabla v - \omega\frac{\partial v}{\partial p} - \frac{\tan\theta}{a}u^2 + F_v \tag{2.34}$$

$$\nabla\cdot\mathbf{V} + \frac{\partial \omega}{\partial p} = 0 \tag{2.35}$$

$$\frac{\partial \phi}{\partial p} = -\frac{RT}{p} \tag{2.36}$$

$$\frac{\partial T}{\partial t} - \frac{pS_0}{R}\omega = -\mathbf{V}\cdot\nabla T - \omega\frac{\partial T}{\partial p} + \frac{Q}{C_p} \tag{2.37}$$

where S_0 is the static stability parameter of the reference state defined as

$$S_0 = \frac{R}{p}\left(\frac{kT_0}{p} - \frac{\mathrm{d}T_0}{\mathrm{d}p}\right). \tag{2.38}$$

The remaining symbols definitions are:

$\mathbf{V}$	horizontal wind velocity
u, v	zonal and meridional components of the wind
ω	vertical-p velocity ($= \mathrm{d}p/\mathrm{d}t$)
T	deviation of temperature from the reference state temperature $T_0(p)$
ϕ	deviation of geopotential from the reference state gepotential $\phi_0(p)$
R	specific gas constant of dry air
C_p	specific heat at constant pressure
k	$= R/C_p$
$a,\ \Omega$	radius and angular speed of earth's rotation
F_u, F_v	zonal and meridional components of frictional force
Q	diabatic heating rate

In the the derivation of the thermodynamic equation 2.37 the term $\omega RT/pC_p$ has been neglected assuming that $T_0 >> T$. Multiplying (2.37) by $R/(pS_0)$, then calculating the derivatives with respect to p, and finally using on the resulting equation

the relations (2.35) and (2.36), the thermodynamic energy equation takes the form

$$\frac{\partial}{\partial t}\frac{\partial}{\partial p}\left(\frac{1}{S_0}\frac{\partial \phi}{\partial p}\right) - \nabla \cdot \mathbf{V} = \frac{\partial}{\partial p}\left[\frac{R}{pS_0}\left(\mathbf{V}\cdot\nabla T + \omega\frac{\partial T}{\partial p}\right)\right] - \frac{\partial}{\partial p}\left(\frac{kQ}{pS_0}\right). \tag{2.39}$$

The right-hand sides of equations 2.33, 2.34 and 2.39 contain the nonlinear terms, frictional forces and the diabatic heat sources. Considering an inviscid and adiabatic atmosphere, and linearizing those equations about a reference state at rest with a mean static stability parameter S_0, one obtains the following system of three equations on the dependent variables u, v and ϕ:

$$\frac{\partial u}{\partial t} - 2\Omega v \sin\theta + \frac{1}{a\cos\theta}\frac{\partial \phi}{\partial \lambda} = 0 \tag{2.40}$$

$$\frac{\partial v}{\partial t} + 2\Omega u \sin\theta + \frac{1}{a}\frac{\partial \phi}{\partial \theta} = 0 \tag{2.41}$$

$$\frac{\partial}{\partial p}\left[\frac{1}{S_0}\frac{\partial}{\partial p}\left(\frac{\partial \phi}{\partial t}\right)\right] - \nabla \cdot \mathbf{V} = 0. \tag{2.42}$$

A lower boundary condition for (2.40-2.42) corresponds to no mass flux through the earth's surface. Then the lower boundary condition is that the linearized version of the vertical velocity ($\mathrm{d}z/\mathrm{d}t$) vanishes at a constant pressure, p_s, near the earth's surface

$$\frac{\partial}{\partial p}\left(\frac{\partial \phi}{\partial t}\right) + \frac{pS_0}{RT_0}\left(\frac{\partial \phi}{\partial t}\right) = 0 \qquad \text{at} \quad p = p_s. \tag{2.43}$$

Multiplying (2.40), (2.41) and (2.42) by u, v and $-\phi$, respectively, then summing the resulting equations, and finally integrating over the whole atmospheric mass, one obtains

$$\frac{\mathrm{d}}{\mathrm{d}t}\int\int\int_M \left[\frac{u^2+v^2}{2} + \frac{1}{2S_0}\left(\frac{\partial \phi}{\partial p}\right)^2 + \frac{\phi^2(p_s)}{2RT_0(p_s)}\right]\frac{a^2}{g}\cos\theta \;\; d\theta \; d\lambda \; dp = \int_0^{2\pi}\int_{-\pi/2}^{\pi/2}\left[\lim_{p\to 0}\omega\phi\right]\frac{a^2}{g}\cos\theta \; d\theta \; d\lambda. \tag{2.44}$$

The integral on the left-hand side of (2.44) represents the total energy, i.e., the sum of the kinetic energy and the available potential energy (APE). The following condition guarantees energy conservation

$$\lim_{p\to 0} \; \omega\phi = 0 \tag{2.45}$$

Replacing ω by its expression obtained from the linearized version of (2.37), using the hydrostatic equation and the fact that the atmosphere is considered to be bounded (i.e., $\lim_{p\to 0}\ |\phi(p)| < \infty$), the top boundary condition takes the form

$$\lim_{p\to 0}\ \frac{1}{S_0}\frac{\partial}{\partial p}\left(\frac{\partial \phi}{\partial t}\right) = 0. \tag{2.46}$$

The system (2.40)-(2.42) together with the boundary conditions (2.43) and (2.46) constitute a linearized model of the atmosphere. The solutions of this system with physical meaning should be square-integrable functions over $[0,\ p_s]$. The reason is that the atmosphere is bounded, i.e., $\lim_{p\to 0}\ |\phi(p)| < \infty$, and should have finite kinetic energy

$$\int_0^{p_s} \frac{u^2+v^2}{2}\frac{dp}{g} < \infty. \tag{2.47}$$

2.4.2 Vertical structure functions

In the system (2.40)-(2.42), the vertical coordinate appears explicitly in the operator

$$\mathbf{D} = \frac{\partial}{\partial p}\left[\frac{1}{S_0}\frac{\partial(\cdot)}{\partial p}\right], \tag{2.48}$$

which has a particular form of the Sturm-Liouville operator. Following Sneddon [1974, sec. 8.2], one may define a vertical transform

$$\mathcal{T}[f(p);\xi] = \frac{2}{p_s}\int_0^{p_s} f(p)G(p;\xi)dp, \tag{2.49}$$

which, when applied to (2.40)-(2.42), eliminates the vertical dependence on pressure. $G(p;\xi)$ denotes a prescribed function of p over the interval $]0,\ p_s]$ for each value of the parameter ξ, whose domain may be discrete or continuous.

Integrating by parts twice, it may be shown that

$$\begin{aligned}\mathcal{T}[\mathbf{D}f(p);\xi] &= \frac{2}{p_s}\lim_{p\to 0}\left\{\frac{1}{S_0}\left[f(p)\frac{dG(p;\xi)}{dp} - G(p;\xi)\frac{df(p)}{dp}\right]\right\} \\ &+ \frac{2}{p_s S_0}\left[G(p_s;\xi)\left(\frac{f(p)}{dp}\right)_{p_s} - f(p_s)\left(\frac{dG(p;\xi)}{dp}\right)_{p_s}\right] \\ &+ \frac{2}{p_s}\int_0^{p_s} f(p)\mathbf{D}G(p;\xi)dp.\end{aligned} \tag{2.50}$$

If, like $\phi(p)$, the functions $G(p;\xi)$ are bounded, i.e., $\lim_{p\to 0}|G(p;\xi)| < \infty$, and if they satisfy boundary conditions similar to (2.43) and (2.46), that is, if they satisfy the boundary conditions

$$\frac{dG}{dp} + \frac{pS_0}{RT_0}G = 0 \qquad \text{at} \quad p = p_s, \tag{2.51}$$

$$\lim_{p\to 0} \frac{1}{S_0}\frac{dG}{dp} = 0, \tag{2.52}$$

then, replacing $f(p)$ by $\partial\phi/\partial t$, the equation (2.50) reduces to

$$\mathcal{T}\left[\mathbf{D}\left(\frac{\partial\phi}{\partial t}\right);\xi\right] = \frac{2}{p_s}\int_0^{p_s}\frac{\partial\phi}{\partial t}\,\mathbf{D}G(p;\xi)dp = \frac{\partial}{\partial t}\left\{\frac{2}{p_s}\int_0^{p_s}\phi\,\mathbf{D}G(p;\xi)dp\right\}. \tag{2.53}$$

This result shows that the bounded functions $G(p;\xi)$, which satisfy boundary the conditions (2.51) and (2.52), and are eigensolutions of

$$(\mathbf{D}+\xi)G(p;\xi) = 0 \tag{2.54}$$

will be the suitable functions for the kernel of vertical transform (2.49). Applying such vertical transform to the system (2.40)-(2.42) will allow to eliminate the p-coordinate. In effect it may be shown that

$$\mathcal{T}\left[\mathbf{D}\left(\frac{\partial\phi}{\partial t}\right);\xi\right] = -\xi\frac{\partial}{\partial t}\mathcal{T}\left[\phi;\xi\right] \tag{2.55}$$

The equation 2.54 is denominated vertical structure equation (VSE) and constitutes, together with the boundary conditions (2.51) e (2.52), a singular Sturm-Liouville problem whenever $\lim_{p\to 0}\ S_0(p) = \infty$. The nature of the solutions $G(p;\xi)$ depends only on the behaviour of $S_0(p)$ in an arbitrarily small neighbourhood of $p = 0$.

Cohn and Dee [1989] have argued that the basic state atmosphere must be bounded for consistency with the shalowness approximation used in deriving the nonlinear primitive equations (2.33)-(2.37). Assuming a bounded atmosphere they obtained the following results:

- The solutions of 2.54, that satisfy the boundary conditions (2.51) and (2.52), are bounded functions (*cf.* theorem 2).

- The eigenvalues ξ are all positive and their spectrum is totally discrete (*cf.* theorem 3).

- The eigenfunctions $G(p;\xi)$ form a complete orthogonal basis for the space of functions which are square-integrable over $]0,\ p_s]$ (*cf.* theorem 3), with the inner product defined by

$$\langle f, g\rangle = \frac{2}{p_s}\int_0^{p_s} f(p)g(p)dp. \tag{2.56}$$

These results allow to conclude that, in a given point (λ,θ) and at an arbitrary instant t, the vertical dependence of the column vector $(u,v,\phi)^T$, where T denotes the transpose, may be given by the following expansion

$$(u,v,\phi)^T = \sum_{m=0}^{\infty}(\hat{u},\hat{v},\hat{\phi})_m^T G_m(p) \tag{2.57}$$

The m^{th} vector $(\hat{u},\hat{v},\hat{\phi})_m^T$ depends only on (λ,θ,t). The eigenfunctions $G_m(p) = G(p;\xi_m)$ are sorted by the increasing value of the eigenvalues ξ_m.

If the functions $G_m(p)$ have unitary norm, with the norm defined by the inner product (2.56) as $\|f\| = \sqrt{\langle f, f\rangle}$, the vector $(\hat{u},\hat{v},\hat{\phi})_m^T$ is given by

$$(\hat{u},\hat{v},\hat{\phi})_m^T = \frac{2}{p_s}\int_0^{p_s}(u,v,\phi)^T G_m(p)dp. \tag{2.58}$$

2.4.3 Horizontal structure functions

Applying the vertical transform 2.49 to the equations 2.40-2.42 and using the property 2.55 results in

$$\frac{\partial\hat{u}_m}{\partial t} - 2\Omega\hat{v}_m\sin\theta + \frac{1}{a\cos\theta}\frac{\partial\hat{\phi}_m}{\partial\lambda} = 0 \tag{2.59}$$

$$\frac{\partial\hat{v}_m}{\partial t} + 2\Omega\hat{u}_m\sin\theta + \frac{1}{a}\frac{\partial\hat{\phi}_m}{\partial\theta} = 0 \tag{2.60}$$

$$\frac{\partial\hat{\phi}_m}{\partial t} + \frac{gh_m}{a\cos\theta}\left[\frac{\partial\hat{u}_m}{\partial\lambda} + \frac{\partial}{\partial\theta}(\hat{v}_m\cos\theta)\right] = 0 \tag{2.61}$$

where $\xi_m = 1/gh_m$. The constants h_m are called equivalent depths.

This system is identical to the linearized version of the shallow-water equations. It may then be concluded that applying the vertical transform the original stratified (baroclinc) problem is reduced to the superposition of solutions of barotropic problems corresponding to the various vertical structures $G_m(p)$.

The system 2.59-2.61 describes small-amplitude motions of an incompressible, homogeneous, hydrostatic and inviscid fluid over a rotating sphere. The free oscillations (normal modes) of such a fluid may be written as

$$(\hat{u}, \hat{v}, \hat{\phi})_m^T = \exp(-i\, 2\Omega\nu t)\mathbf{C}_m(\tilde{u}, \tilde{v}, \tilde{z})_m^T \tag{2.62}$$

where $i = \sqrt{-1}$ and ν denotes a dimensionless frequency. The components of the vector $(\tilde{u}, \tilde{v}, \tilde{z})_m^T$ are also dimensionless variables, functions of (λ, θ). $\mathbf{C}_m$ is a diagonal matrix of scaling factors

$$\mathbf{C}_m = \begin{pmatrix} \sqrt{gh_m} & 0 & 0 \\ 0 & \sqrt{gh_m} & 0 \\ 0 & 0 & gh_m \end{pmatrix}$$

Replacing (2.62) in the equations 2.59-2.61, one obtains

$$\mathbf{L}_m\, \tilde{\mathbf{W}}_m = \nu \tilde{\mathbf{W}}_m, \tag{2.63}$$

where $\tilde{\mathbf{W}}_m = (\tilde{u}, \tilde{v}, \tilde{z})_m^T$, and $\mathbf{L}_m$ is the linear differential matrix operator

$$\mathbf{L}_m = \begin{bmatrix} 0 & i\sin\theta & -i\frac{\gamma_m}{\cos\theta}\frac{\partial}{\partial\lambda} \\ -i\sin\theta & 0 & -i\gamma_m\frac{\partial}{\partial\theta} \\ -i\frac{\gamma_m}{\cos\theta}\frac{\partial}{\partial\lambda} & -i\frac{\gamma_m}{\cos\theta}\frac{\partial}{\partial\theta}[\cos\theta(\cdot)] & 0 \end{bmatrix}$$

in which $\gamma_m = \sqrt{gh_m}/2\Omega a$ is a dimensionless constants. The related quantity, $\epsilon_m = \gamma_m^{-1/2}$, is called Lamb's parameter.

The domain of the operator $\mathbf{L}_m$ is considered to be the linear space, $\mathcal{F}$, of vectors $\tilde{\mathbf{W}}_m$ whose components are continuous and differentiable functions over the sphere. An inner product in this space is defined as

$$\langle \tilde{\mathbf{W}}_m^j, \tilde{\mathbf{W}}_m^k \rangle = \frac{1}{2\pi}\int_0^{2\pi}\int_{-\pi/2}^{\pi/2} \left(\tilde{\mathbf{W}}_m^j\right)^* \cdot \tilde{\mathbf{W}}_m^k \cos\theta\, d\theta\, d\lambda, \tag{2.64}$$

where $(\,)^*$ denotes the complex conjugate of the transpose. Integrating by parts over λ and θ, it may be shown that $\mathbf{L}_m$ is an Hermitian operator,

$$\langle \tilde{\mathbf{W}}_m^j, \mathbf{L}\, \tilde{\mathbf{W}}_m^k \rangle = \langle \mathbf{L}\, \tilde{\mathbf{W}}_m^j, \tilde{\mathbf{W}}_m^k \rangle. \tag{2.65}$$

Because $\mathbf{L}_m$ is Hermitian, the frequencies ν (eigenvalues) are real (i.e., the solutions (2.62) represent free oscillations), and the horizontal structure functions (eigenvectors) associated with different eigenfrequencies are orthogonal.

Because $\mathbf{L}_m$ is also linear with respect to longitude λ, the horizontal structure of the normal modes can be expressed in the form

$$\mathbf{H}_{ms}(\lambda,\theta) = \mathbf{\Theta}_{ms}(\theta)\exp(is\lambda),$$

where the vector functions $\mathbf{\Theta}_{ms}(\theta) = [U_{ms}(\theta), iV_{ms}(\theta), Z_{ms}(\theta)]^T$ represent the meridional structures. The factor i in front of $V_{ms}(\theta)$ is introduced to incorporate a phase shift of $\pi/2$. The existence of this phase shift may be easely shown if one replaces the vector $\tilde{\mathbf{W}}_m$ by $\mathbf{H}_{ms}$ in (2.63) and the system is solved for $U_{ms}(\theta)$ and $V_{ms}(\theta)$. The rationale for this can be seen by considering winds around an adjacent high and low where the maxima of zonal wind and height are in phase and the maxima of meridional wind are a quarter of wavelength behind the maxima of zonal wind or height.

Because Hough [1898] was the first to solve the normal mode problem by means of spherical harmonics, the vectors $\mathbf{H}_{ms}$ e $\mathbf{\Theta}_{ms}$ are called Hough harmonic vectors and Hough vectors, respectively.

For each Hough harmonic, $\mathbf{H}_{ms}$, associated with a given frequency ν, there is a conjugate harmonic vector $\overline{\mathbf{H}}_{ms}$ with frequency $-\nu$. This result can be seen calculating the complex conjugate of equation 2.63

$$\overline{\mathbf{L}_m\,\mathbf{H}}_{ms} = \overline{\nu\mathbf{H}}_{ms} \iff -\mathbf{L}_m\,\overline{\mathbf{H}}_{ms} = \nu\overline{\mathbf{H}}_{ms},$$

where $\overline{(\,)}$ denotes the complex conjugate.

The normal modes of (2.59)-(2.61) are partitioned into two classes of solutions [Longuet-Higgins, 1968]: solutions of class I or inertio-gravity waves and solutions of class II or Rossby (rotational) waves. Using the Helmholtz theorem in equations 2.59-2.61 and solving for the velocity potential Φ and the stream function Ψ, it may be shown that as $\gamma \to \infty$ the solutions of class I take the asymptotic form

$$\begin{aligned} \Phi &\approx AP_n^s(\sin\theta)\exp[i(s\lambda - 2\Omega\nu t)] \\ \Psi &\approx 0, \end{aligned}$$

with the frequencies given by

$$\nu \approx \pm\frac{\sqrt{n(n+1)}}{2\Omega a}\sqrt{gh_m};$$

and the solutions of class II take the asymptotic form

$$\begin{aligned} \Phi &\approx 0 \\ \Psi &\approx iBP_n^s(\sin\theta)\exp[i(s\lambda - 2\Omega\nu t)], \end{aligned}$$

with frequencies

$$\nu \approx -\frac{s}{n(n+1)}.$$

$P_n^s(\sin\theta)$ are the associated Legendre functions, and A e B are constants [cf. Longuet-Higgins, 1968, sec.4].

For the interpretation of these asymptotic solutions, it is convenient to remember that the dimensionless frequency ν must be multiplied by $2\,Omega$ to obtain its dimensional form (see eq. 2.62). In their asymptotic forms, the solutions of class I are divergent and irrotational ($\Psi = 0$) waves, with a dispersion relation similar to that of gravity waves for shallow-waters; on the other hand, the solutions of class II are rotational and non divergent ($\Phi = 0$) waves, with a dispersion relation similar to that of planetary waves.

Another important property of the horizontal structure functions is its symmetry about the equator. A function $f(\lambda,\theta)$ that is symmetric about the equator has the property $f_S(\lambda,\theta) = f_S(\lambda,-\theta)$ whereas an anti-symmetric functions has $f(\lambda,\theta) = -f(\lambda,-\theta)$. The velocity components and the geopotential can be written as a sum of symmetric and anti-symmetric functions: $\hat{u} = \hat{u}_\mathrm{S} + \hat{u}_\mathrm{A}$, $\hat{v} = \hat{v}_\mathrm{S} + \hat{v}_\mathrm{A}$ e $\hat{\phi} = \hat{\phi}_\mathrm{S} + \hat{\phi}_\mathrm{A}$. Replacing these equalities in (2.59)-(2.61) and considering that the derivative of a symmetric (anti-symmetric) function is an anti-symmetric (symmetric) function, two linearly independent systems are obtained. A system called symmetric includes symmetric $\hat{u}$ and $\hat{\phi}$ and anti-symmetric $\hat{v}$. Another system called anti-symmetric includes anti-symmetric $\hat{u}$ and $\hat{\phi}$ and symmetric $\hat{v}$. In the North Hemisphere, the motions described by the symmetric modes are the specular images of the motions in the South Hemisphere, with no flow through the equator. In the anti-symmetric case the motion at the equator is normal to the equatorial plan.

Let $\mathcal{W}_m$ be the subspace of $\mathcal{F}$, constituted by the orthogonal projections (2.58) of the solutions of the non-linearized primitive equations, 2.33, 2.34 and 2.39, onto the vertical structures $G_m(p)$, multiplied by the inverse matrix of $\mathbf{C}_m$. On other words, let $\mathcal{W}_m$ be the space of dimensionaless solutions of the system that results when the

vertical transform $\mathcal{T}$ is applied to equations 2.33, 2.34 and 2.39. Because $\mathbf{L}_m$ is an Hermitian operator and according to Eckart [1960, Cap. VI] expansion theorem for motion of a fluid on a finite volume, the Hough harmonic vectors form a complete orthogonal basis of the subspace $\mathcal{W}_m$. Then the projections $(\hat{u}, \hat{v}, \hat{\phi})^T_m$, defined by (2.58), can be expanded in the following linear combination of Hough harmonics

$$(\hat{u}, \hat{v}, \hat{\phi})^T_m = \mathbf{C}_m \tilde{\mathbf{W}}_m = \sum_{s=-\infty}^{\infty} \sum_{l=0}^{\infty} \sum_{\alpha=1}^{3} w^{\alpha}_{msl}(t) \mathbf{C}_m \mathbf{H}^{\alpha}_{msl}(\lambda, \theta), \tag{2.66}$$

The index $\alpha = 1, 2, 3$ denotes, respectively, eastward travelling inertio-gravity waves, Rossby (rotational) waves and westward travelling inertio-gravity waves. l is an integer meridional index. For rotational waves, $l = 0$ denotes the mode with the highest frequency, and for inertio-gravity waves $l = 0$ denotes the modes with the lowest frequencies. Because the meridional index is also associated with the number of nodes of the meridional profiles $U_{msl}(\theta)$, $V_{msl}(\theta)$ and $Z_{msl}(\theta)$, it may be considered as an index of the meridional scale of the motion. The frequencies of the zonal rotational modes (i.e., the rotational modes with $s = 0$) are all zero. In this case, the meridional index l sole represents the meridional scale of motion.

If the Hough harmonics have a unitary norm, and the norm is defined by the inner product 2.64, i.e., if $\|\mathbf{H}^{\alpha}_{msl}\| = \sqrt{\langle \mathbf{H}^{\alpha}_{msl}, \mathbf{H}^{\alpha}_{msl} \rangle} = 1$, the coefficients w^{α}_{msl} in the expansion 2.66 are given by

$$w^{\alpha}_{msl} = \langle \mathbf{H}^{\alpha}_{msl}, \tilde{\mathbf{W}}_m \rangle = \frac{1}{2\pi} \int_0^{2\pi} \int_{-\pi/2}^{\pi/2} \mathbf{H}^{\alpha *}_{msl} \mathbf{C}^{-1}_m (\hat{u}, \hat{v}, \hat{\phi})^T_m \cos\theta \, d\theta \, d\lambda \tag{2.67}$$

2.4.4 A basis of 3-dimensional normal modes

Replacing $(\hat{u}, \hat{v}, \hat{\phi})^T_m$ in (2.57) by the expansion (2.66) results in

$$(u, v, \phi)^T = \sum_{m=0}^{\infty} \sum_{s=-\infty}^{\infty} \sum_{l=0}^{\infty} \sum_{\alpha=1}^{3} w^{\alpha}_{msl}(t) \mathbf{\Pi}^{\alpha}_{msl}(\lambda, \theta, p), \tag{2.68}$$

The vectorial functions $\mathbf{\Pi}^{\alpha}_{msl}(\lambda, \theta, p) = G_m(p) \mathbf{C}_m \mathbf{H}^{\alpha}_{msl}(\lambda, \theta)$ define the 3-dimensional structures of the normal modes of an adiabatic atmosphere linearized about a state at rest. This vectorial functions form a complete orthogonal basis of the vector space $\mathcal{S}$ constituted by the solutions $(u, v, \phi)^T$ of the non-linearized primitive equations 2.33, 2.34 e 2.39. It must be noted that the convergence of the expansion 2.68 is defined in the mean.

The vertical index, m, represents the number of nodes of the functions $G_m(p)$ over the interval $0 \leq p \leq p_s$ [cf. Cohn and Dee, 1989, teorema 3]. Because $G_0(p)$ has no node and is approximately constant in the vertical, the modes $\mathbf{\Pi}^{\alpha}_{0sl}$ are called external or barotropic modes. The modes $\mathbf{\Pi}^{\alpha}_{msl}$ with $m \geq 1$ are called internal or baroclinic modes, and have m nodes in the vertical.

Let $\mathbf{W}_1$ and $\mathbf{W}_2$ be two vectors of the space $\mathcal{S}'$ spanned by the linear expansions 2.68, with an inner product defined by

$$\langle \mathbf{W}_1, \mathbf{W}_2 \rangle = \frac{1}{4\pi g} \int_0^{2\pi} \int_{-\pi/2}^{\pi/2} \int_0^{p_s} \mathbf{W}_1^* \cdot \mathbf{M}\mathbf{W}_2 \, \cos\theta \, dp \, d\theta \, d\lambda, \tag{2.69}$$

in which $\mathbf{M}$ is the linear differential matrix operator

$$\mathbf{M} = \frac{1}{2} \begin{bmatrix} 1 & 0 & 0 \\ 0 & 1 & 0 \\ 0 & 0 & -\mathbf{D} \end{bmatrix},$$

with $\mathbf{D}$ defined by (2.48).

The squared norm is again defined by the inner product as

$$\begin{aligned} \|\mathbf{W}\|^2 &= \langle \mathbf{W}, \mathbf{W} \rangle \\ &= \frac{1}{4\pi g} \int_0^{2\pi} \int_{-\pi/2}^{\pi/2} \int_0^{p_s} \left[\frac{u^2 + v^2}{2} - \frac{\phi}{2} \frac{\partial}{\partial p} \left(\frac{1}{S_0} \frac{\partial \phi}{\partial p} \right) \right] \cos\theta \, dp \, d\theta \, d\lambda \end{aligned} \tag{2.70}$$

Performing the vertical integration in the third term by parts and considering that ϕ (the geopotential reproduced by linear expanion (2.57)) must verify the boundary conditions (2.51) and (2.52), the square of the norm may be written as

$$\begin{aligned} \|\mathbf{W}\|^2 = \frac{1}{4\pi g} \int_0^{2\pi} \int_{-\pi/2}^{\pi/2} \int_0^{p_s} \Bigg[\frac{u^2 + v^2}{2} &+ \frac{1}{2S_0} \left(\frac{\partial \phi}{\partial p} \right)^2 \\ &+ \frac{\phi^2(p_s)}{2RT_0(p_s)} \Bigg] \cos\theta \, dp \, d\theta \, d\lambda \end{aligned} \tag{2.71}$$

Then the square of the norm is equal to the integral in the left-hand side of (2.44) divided by area of globe's surface. The contribution of the observed variance of $\phi(p_s)$ for the integral 2.71 is very small, only of the order of 1% of the jointly contributions due to the kinetic energy, K, and available potential energy, (APE). One may then conclude that the square of the norm of $\mathbf{W}$ represents very closely the mean total energy $(K + APE)$ per unit of horizontal area.

Let, now, $\mathbf{W}$ and $\mathbf{W}'$ represent two real fields defined by two pairs of complex conjugate normal modes

$$\begin{aligned} \mathbf{W} &= w^{\alpha}_{msl}\mathbf{\Pi}^{\alpha}_{msl} + w^{\alpha}_{m(-s)l}\mathbf{\Pi}^{\alpha}_{m(-s)l} \\ \mathbf{W}' &= w^{\alpha'}_{m's'l'}\mathbf{\Pi}^{\alpha'}_{m's'l'} + w^{\alpha'}_{m'(-s')l'}\mathbf{\Pi}^{\alpha'}_{m'(-s')l'} \end{aligned}$$

Because $\mathbf{W}$ and $\mathbf{W}'$ are real the coefficients verify the equality $w^{\alpha}_{m(-s)l} = (w^{\alpha}_{msl})^*$. Calculating the inner product $\langle \mathbf{W}, \mathbf{W}' \rangle$ as defined by (2.69), and considering $s, s' \geq 0$, one obtains

$$\langle \mathbf{W}, \mathbf{W}' \rangle = \frac{p_s h_m}{8} \left(w^{\alpha}_{m(-s)l} w^{\alpha'}_{m's'l'} + w^{\alpha}_{msl} w^{\alpha'}_{m'(-s')l'} \right) \delta_{mm'} \delta_{ss'} \delta_{ll'} \delta_{\alpha\alpha'}$$

This result shows the orthogonality of the vectors $\mathbf{\Pi}^{\alpha}_{msl}$. If $\alpha = \alpha'$, $m = m'$, $s = s'$ and $l = l'$, i.e., if $\mathbf{W} = \mathbf{W}'$, then

$$\|\mathbf{W}\|^2 = \frac{p_s h_m}{8} \left(|w^{\alpha}_{msl}|^2 + |w^{\alpha}_{m(-s)l}|^2 \right). \tag{2.72}$$

Finally, it may be concluded that the square of a coefficient w^{α}_{msl} is proportional to the mean total energy, per unit of horizontal area, projected onto the normal mode $\mathbf{\Pi}^{\alpha}_{msl}$.

Chapter 3

Simulation of Climatic Variability

According to the concept of a dynamical climate presented in section 2.2.1, here we have studied the free and forced variability of the general circulation during winter (DJF), simulated by the version VII.1 of the Melbourne University Atmospheric General Circulation Model (MU AGCM). With this in mind we have performed 10 independent simulations of the atmospheric general circulation, having prescribed observed SSTs and sea-ice for the 1979-88 as forcing.

The simulated fields of horizontal wind and geopotential have been projected onto a 3-dimensional normal mode basis, making it possible to analyze separately the barotropic and baroclinic components, as well as inertio-gravity waves and rotational waves. On the other hand the projection onto a normal mode base provides a method for a dynamical consistent filtering of both horizontal wind and geopotential fields, based on criteria formulated on an atmospheric linearized dynamics and on criteria based on the properties of the different temporal and spatial scales involved.

The analysis of variance described in Section 2.3.1 has been performed on the transformed space of normal mode projections. Since the anomaly patterns associated with the winter low-frequency variability of the extratropical circulation of the Northern Hemisphere present a vertical structure equivalent to the barotropic structure [Wallace and Gutzler, 1981; Kushnir and Wallace, 1989], and the same being true for the extratropical variability in both Hemispheres, associated to SST anomalies in the Tropical Pacific [Horel and Wallace, 1981; Karoly, 1989], part of the present study has been dedicated to the analysis of the variability of the barotropic normal modes.

A Complex Principal Component Analysis (CPCA), performed on the time series of the projection coefficients, has revealed global patterns of the free or forced atmos-

pheric circulation anomalies. The patterns of the vector fields $(u, v, \phi)^T$ calculated in this study present many similarities to scalar patterns documented in other studies (e.g., geopotential variability for latitudes north of 20^o N) which, although of large scale, do not have the global character of the present study. Moreover, in this study we have performed a simultaneous analysis of the horizontal wind and geopotential fields considering, implicitly, the variability of the geopotential gradient as well as the meridional variation of the Coriolis parameter.

The anomalies of the atmospheric circulation over the intertropical Pacific, associated with El Niño episodes, are characterized by an eastward shift of the related divergence pattern [Webster and Chang, 1988]. The vertical profile of divergence in synoptic systems, in regions of precipitation over the equatorial Pacific [cf. Holton, 1992, fig. 11.5], presents a structure similar to the fourth baroclinic component, $m = 4$ (fig. 3.1), in the troposphere. On the other hand, because the equivalent height associated with the vertical structure of the fourth baroclinic component is small ($h_4 = 179\,\mathrm{m}$), the horizontal modes of low meridional index are confined to the inter-tropical region [Longuet-Higgins, 1968]. Thus, due to the possibility of part of the intertropical circulation variability being projected on the fourth baroclinic component, we have also analyzed the free and forced variability of that component.

Finally, we have computed, at each grid point, the correlation between the forced Principal Components time series and the SST anomaly time series, which allows to identify the dominant modes of the forcing field.

3.1 Model description

The original version of the MU AGCM was developed based on the model described by McAvaney et al [1978], and subsequent modifications are documented by Simmonds [1985], Simmonds *et al.* [1988] and Simmonds and Lynch [1992]. The MU AGCM is a spectral model where the horizontal distribution of the prognostic variables (as well as some diagnostic variables) are expanded in spherical harmonic series with rhomboidal truncation. In version VII.1, used in this study, the series are truncated at wave number 21. This truncation corresponds, in the model, to a horizontal resolution of 64 longitude and 54 gaussian latitude transform grid points. In the vertical, the variables are discretized in 9 'sigma' levels, i.e. levels of pressure normalized by surface pressure (p/p_s), with values of 0.991, 0.926, 0.811, 0.664, 0.500, 0.336, 0.189, 0.074 and 0.009.

The version used has a seasonal cycle of 365 days and no diurnal cycle. Radiation in the top of the atmosphere is a function of the daily mean zenith angle. Radiative processes are parameterized according to the scheme of Manabe and Strickler [1964] and Manabe and Wetherald [1967]. Radiation interacts with clouds, ozone and carbon dioxide, prescribed based on climatological distributions, and with water vapour computed by the model. The seasonal cycle of clouds, which is a function of altitude (three cloud levels: low, medium and high clouds), longitude and latitude, has been obtained from the climatologies of Warren *et al.* [1988a] over land, and Warren *et al.* [1988b] over the ocean. The seasonal cycle of ozone, also prescribed and with vertical and meridional dependence, has been obtained from Dütsch [1978]. The carbon dioxide mixing ratio is kept constant with a value of $4.56 \times 10^{-4}\,\mathrm{kg\,kg^{-1}}$. Radiative calculations are performed every 12 hours and the derived heating rates applied until the next radiation calculations.

Convection is parameterized by the humid convective adjustment scheme, and the fluxes of linear momentum, latent heat and sensible heat at the surface are computed using the Monin-Obukhov similarity theory. Soil moisture content is computed by the two-layer scheme developed by Deardorff [1977].

The model distinguishes four surface types: land, ocean, ice and snow. Except for the SST fields, which are prescribed, the surface temperatures are calculated using the energy flux balance equations. The albedo of the land is constant over time, but is longitudinal and meridional dependent, and the ocean surface albedo depends on latitude and daily mean zenith angle. Ice albedo is constant for each Hemisphere, and snow albedo is constant in the Southern Hemisphere but depends on latitude in the Northern Hemisphere.

The topography of the model is spectrally analyzed from the 1^{o} lat. $\times$ 1^{o} long. topography of Gates and Nelson [1975]. At each model grid point, one standard deviation of the original ($1^{\mathrm{o}} \times 1^{\mathrm{o}}$) topography, over the respective model grid box, has been added to the mean topography. This reduces the smoothing inherent of the averaging process.

Before using an AGCM to study the atmospheric response to external forcing changes, one has to verify that the model simulates well the observed climate. For the MU AGCM, this has been shown by [Boer *et al.*, 1991, 1992].

3.2 Simulations

We have performed 10 independent atmospheric circulation simulations, for the 1979-88 period. Each simulation started on the 1st of January with an initial atmospheric state different (considered independent) from those of the remaining integrations, but forced by the same temporal evolution of the observed SST and sea-ice cover fields. A 15 minute time-step has been used.

Monthly means of SSTs and sea-ice cover data have been obtained from CSIRO (Dr. Martin Dix, personal communication) within the Atmospheric Modeling Inter-Comparison Project (AMIP). These data was originally on a 64 lon. $\times$ 56 lat. grid. The SST fields have been interpolated to the MU GCM 54 latitudes using cubic splines. After that, daily fields have been obtained by linearly interpolating in time the monthly means between day 15 of two consecutive months. With respect to the sea-ice fields the following has been done: if a grid point of the CSIRO AGCM was covered by ice, the nearest grid point of the MU GCM was considered covered by ice also.

The initial atmospheric states, consistent with the boundary conditions (SSTs) imposed, have been obtained by the following process: 10 first of January days have been randomly selected from a 30-year long control simulation previously performed by the model where the climatological seasonaly varying SSTs and sea-ice fields have been prescribed as boundary forcing. The model was integrated for the whole January of 1979 initialized with one of the 10 first of January atmospheric states. Then, the model was twice integrated with the same boundary conditions for January 1979 but initialized with the 31st of January of the previous simulation. The 11th of January of the last run has used to initialize the simulation for the whole 1979-88 period.

Finally, one should mention that, by specifying the seasonal climatological cycles of snow cover and clouds in the radiative scheme of the model, the feedback mechanisms between these variables and the atmosphere are not present [Walland and Simmonds, 1996]. This could distort the atmospheric response to the oceanic forcing.

3.3 Projections onto the basis of normal modes

In section 2.4 the atmospheric normal modes were described with the primitive equations formulated on the vertical p-coordinate. However, it is equally possible to construct a normal mode basis with the primitive equations written on the vertical coor-

dinate "sigma" [Kasahara and Puri, 1981]. This formulation was the natural choice to expand the fields $(u, v, \phi)^T$ simulated by the MU AGCM. However, because in chapter 4 we will analyze the fields $(u, v, \phi)^T$ obtained from a NCEP reanalysis data set available at isobaric levels, we have chosen to construct the normal mode basis on the p-coordinate.

The zonal and meriodional wind components were calculated from the divergence and vorticity fields in the model sigma surfaces, and interpolated to the isobaric levels by cubic splines. The geopotential fields at isobaric levels were obtained by hydrostatic interpolation of the geopotential fields simulated at sigma surfaces.

3.3.1 Vertical projection

The vertical temperature profile, T_0, of the reference state of the model atmosphere was obtained at 12 standard isobaric levels: 30, 50, 100, 150, 200, 250, 300, 400, 500, 700, 850 and 1000 hPa. These levels are the same of the FGGE IIIb data analyzed by Castanheira *et al.* [1999]. Hence the vertical structure functions were calculated by the method described in Castanheira *et al.* (see sections 2 and 4.1). The only difference is that here the temperature in levels above 30 hPa was also interpolated from the model reference atmosphere. The vertical structures of the barotropic mode, and of the 5 first baroclinic modes are presented in figure 3.1.

The projections (2.58) of the vector $(u, v, \phi)^T$ onto the vertical structure functions were calculated by gaussian quadrature method. We have considered 36 isobaric gaussian levels. The geopotential and the horizontal wind components at the gaussian levels were interpolated from the respective values on the sigma surfaces of the model. For the two gaussian levels above the 9 hPa, the anomalies of the geopotential and of the wind were considered constant, equal to their respestive values at 9 hPa level. In the case of the wind components a non-slip condition was assumed at the surface, i.e., $\mathbf{V} = \mathbf{0}$ at $p = p_s$.

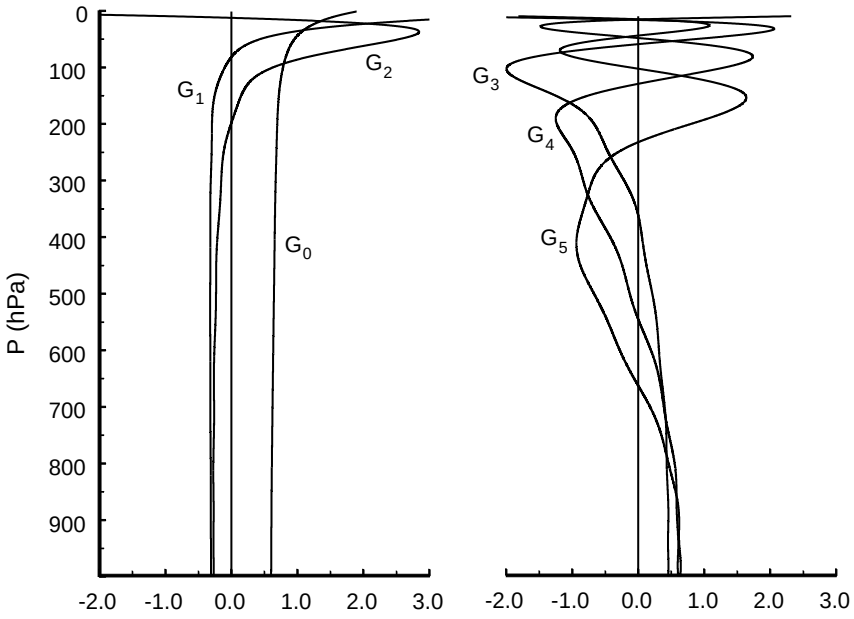

Figure 3.1: Vertical structures of the modes $m = 0, \ldots, 5$.

3.3.2 Horizontal projection

The eigenfrequencies ν and Hough harmonic vectors were numerically calculated using the method described by Swarztrauber and Kasahara [1985]. The method consists in the expansion of the eigensolutions of (2.63) in a series of spherical harmonic vectors

$$\mathbf{H}_{ms}(\lambda,\theta) = \mathbf{\Theta}_{ms}(\theta)\exp(is\lambda) = \sum_{n\geq s}\left(iA_n^s\mathbf{Y}_{n,1}^s + B_n^s\mathbf{Y}_{n,2}^s - C_n^s\mathbf{Y}_{n,3}^s\right), \tag{3.1}$$

where $\mathbf{Y}_{n,1}^s$, $\mathbf{Y}_{n,2}^s$ and $\mathbf{Y}_{n,3}^s$ are the spherical harmonic vectors defined, respectively, by

$$\mathbf{Y}_{n,1}^s = \frac{\exp(is\lambda)}{\sqrt{n(n+1)}}\begin{bmatrix} \frac{is}{\cos\theta}P_n^s \\ \frac{dP_n^s}{d\theta} \\ 0 \end{bmatrix}, \qquad \mathbf{Y}_{n,2}^s = \frac{\exp(is\lambda)}{\sqrt{n(n+1)}}\begin{bmatrix} -\frac{dP_n^s}{d\theta} \\ \frac{is}{\cos\theta}P_n^s \\ 0 \end{bmatrix},$$

$$\mathbf{Y}_{n,3}^s = \exp(is\lambda)\begin{bmatrix} 0 \\ 0 \\ P_n^s \end{bmatrix},$$

in which P_n^s denotes the associated Legendre functions.

Replacing (3.1) in the equation 2.63 results in a new problem of eigenvalues and eigenvectors. In the new problem the ν frequencies are the eigenvalues and the eigenvectors are the column vectors formed by the coefficients $(A_n^s, B_n^s, C_n^s, \cdots)$ in the expansion 3.1. In the case of $s \geq 1$, the problem reduces to computing the eigenvalues and corresponding eigenvectores of two real symmetric pentadiagonal matrices, one for symmetric Hough vectors and the other for the anti-symmetric ones. In the case of zonal modes ($s = 0$), the Hough vectors are obtained by the diagonalization of two real symmetric tridiagonal matrices.

The largest the number of terms included in the expansion 3.1, the more the frequencies ν and numerical Hough vectors approximate the exact solutions. However, for calculation purposes, the series should be truncated in a finite order, $N = n-(s-1)$, in such a way that the obtained solutions are still good approximations of the set of Hough vectors to be retained in the future analysis. Swarztrauber and Kasahara [1985] suggested that the truncation order, N, should be selected as the maximum of $\{40,\, 3L,\, 2/\gamma_m\}$, where L is the number of meridional modes of each type to be calculated, and γ_m is the parameter defined in section 2.4.3.

In this work, we have used a NAG (The Numerical Algorithms Group) package to solve the eigenvalue and eigenvector problems that result from the substitution of the expansion 3.1 in equation 2.63. As it will be confirmed by the results that we will present, the number of meridional modes of each type, retained in the analysis of the variability of the atmospheric circulation, is always ≤ 21. On the other hand, for the smallest equivalent height considered in this study, $h_4 = 179\,\mathrm{m}$, we have $2/\gamma_4 = 44.3$. The truncation order chosen for the expansion 3.1 was $N = n - (s - 1) = 76$ that results in a number of terms greater than the minimal number suggested by the Swarztrauber and Kasahara criterion. As the problem of eigenvalues can be decomposed in two problems, one for symmetric modes and another for the anti-symmetric ones, the chosen truncation order implies that the matrices to be diagonalized have the dimension $(3N/2) \times (3N/2) \equiv 114 \times 114$.

The components of Hough vectors $[U_{msl}^{\alpha}(\theta), iV_{msl}^{\alpha}(\theta), Z_{msl}^{\alpha}(\theta)]^T$ were computed at the 54 gaussian latitudes of the MU AGCM grid.

After obtaining the vertical projections of the field $(u, v, \phi)^T$ at each model grid point, its Fourier transforms were calculated for each of the 54 latitudes. Finally, the w_{msl}^{α} coefficients were obtained using the Gauss quadrature to compute the meridional

integral in (2.67).

3.4 Circulation decomposition into free and forced components

The free and forced components of the atmospheric general circulation on the winter months (DJF) were analysed based in the monthly means of the $(u, v, \phi)^T$ fields. These mean fields were projected onto the basis of normal modes of the reference model atmosphere, according to the method described in the previous section.

Before proceeding to the decomposition in free and forced components, the seasonal cycle was removed, having, for that purpose, subtracted from each coefficient the respective 'climatological' mean, calculated over the 10 years of all simulations. With this procedure we intend to guarantee that the variability of the forced components (*cf.* eq. 2.1) was due, only, to the anomalies of oceanic forcing.

For each coefficient was obtained 10 independent time series (10 simulations), each one with 30 terms in length (3 months $\times$ 10 years). These series were then decomposed on its forced and free (internal) components

$$w_\beta(i,j) = [w_\beta]_j + w'_\beta(i,j) \qquad\qquad i = 1,\ldots,10 \quad j = 1,\ldots,30 \tag{3.2}$$

where β denote a quartet of indices (α, msl); $[w_\beta]_j$ is the ensemble average of the j month (i.e. the forced component), and $w'_\beta(i,j)$ is the fluctuation due to the internal variability (i.e. the free component of the i^{th} simulation of the j month). It should be noted that, in all statistical models presented in section 2.3.1, the best estimate of the ensemble mean is the arithmetic average.

3.5 Analysis of variance

Because the w_β coefficient are complex scalars, their variances, for each j month, are defined as

$$\sigma^2_\beta(j) = E\left[w'_\beta(i,j)w'^*_\beta(i,j)\right] = E\left[\left(\Re(w'_\beta)\right)^2\right] + E\left[\left(\Im(w'_\beta)\right)^2\right], \tag{3.3}$$

where $\Re$ and $\Im$ denote, respectively, the real and imaginary parts, and $E[\,]$ is the mathematical expectation already defined.

From here on, w_{β^*} will designate the complex conjugate of the coefficient w_β, where the index β^* represents the quartet of indices $[\alpha, m(-s)l]$.

Considering the equation 2.72, the internal variance $\sigma^2_\beta(j)$ can be represented in terms of a total transient energy, $E'_{INT}(\beta, j)$, associated with the monthly mean anomalies of w_β

$$E'_{INT}(\beta, j) = \frac{p_s h_m}{c_\beta}\sigma^2_\beta(j), \tag{3.4}$$

where $c_\beta = 4$ if $s \geq 1$ or $c_\beta = 8$ if $s = 0$. The total transient energy, associated with the total variance (internal + forced), will then be given by the expression

$$E'_{TOT}(\beta) = \frac{p_s h_m}{c_\beta}\sigma^2_{TOT}(\beta), \tag{3.5}$$

with σ^2_{TOT} defined by (2.7).

For each w_β coefficient, we can form a 'total' time series of 300 terms in length with the 30 first terms corresponding to the first simulation, the second group of 30 terms corresponding to the second simulation, and so on. With such times series we can obtain an estimate of the total transient energy, associated with the total variability of each mode, through the following expression

$$E'_\beta = \frac{p_s h_m}{c_\beta}\left\{\frac{1}{299}\sum_{t=1}^{300} w_\beta(t) w^*_\beta(t)\right\} \tag{3.6}$$

.

Although this expression is not an unbiased estimate of the total variability, as it was shown in section 2.3.1, it allows, nevertheless, to identify the modes that possess considerable variability. Figure 3.2 shows the total transient energy associated with the barotropic Rossby modes, as given by 3.6. As it can be observed the modes with considerable variability have zonal wavenumbers $s \leq 10$ and meridional indices $l \leq 15$.

The barotropic gravity modes have negligible variability, excepting for the zonal Kelvin mode represented in figure 3.2 with the index (0,0).

The spectrum of total transient energy, E'_β, associated with the fourth baroclinic component, is represented in figure 3.3. As in the case of the barotropic component, only the energy associated to Rossby's modes is shown, because the variability of the graviy modes, with the exception of Kelvin modes with wavenumbers $s = 0, \ldots, 5$, is also negligible. The Rossby modes with considerable variability have zonal wavenumbers $s \leq 10$ and meridional indices $l \leq 18$.

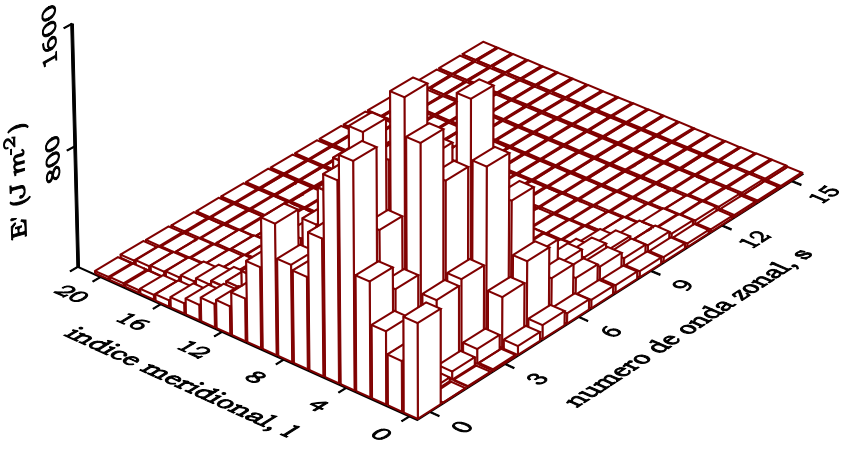

Figure 3.2: Total transient energy associated with the barotropic Rossby modes. The indices $(0, 0)$ denote the zonal Kelvin mode.

To decide which of the statistical models presented in section 2.3.1 should be used in the analysis of the internal and forced variances, some exploring tests were done on the simulated data. The tests search for the existence of correlations among ensembles and inquire about the homogeneity of the variances of ensembles. Next, we will describe the tests done, exemplifying for the case of the barotropic component.

In the first place, the dimensionality of the problem was reduced by means of a complex principal component analysis (CPCA) on the 'total' series of 300 terms, defined in expression 3.6. We have retained in the CPCA only the β modes with considerable variability [in the case of the barotropic component we have retained the Rossby modes with zonal wavenumbers $s \leq 10$ and meridional indices $l \leq 15$ and the zonal Kelvin mode (*cf.* fig. 3.2)]. We have then tested the null hypothesis of the independence of ensembles, taking all pairs of successive months, i.e., pairs constituted by Decembers and Januarys or Januarys and Februarys of a same winter. For each principal component, PC_n, and for each pair of months $(j, j+1)$, where j denotes a December or a January, we calculated the correlation coefficient $r_n(j)$ over the 10

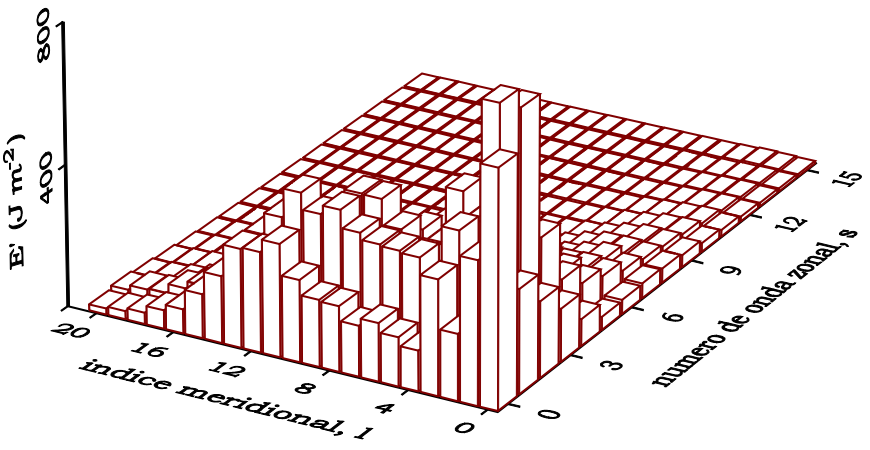

Figure 3.3: Total transient energy associated with the Rossby modes of the fourth baroclinic component. The modes with meridional index 0 and zonal wavenumbers $s = 0, \ldots, 5$ are Kelvin modes. It should be noted that the energy scale is half of respective scale in figure 3.2.

pairs $[\mathrm{PC}_n(i,j), \mathrm{PC}_n(i,j+1)]$ corresponding to the 10 simulations

$$r_n(j) = \frac{\sum_{i=1}^{10}[\mathrm{PC}_n(i,j) - \overline{\mathrm{PC}}_n(j)][\mathrm{PC}_n(i,j+1) - \overline{\mathrm{PC}}_n(j+1)]}{\sqrt{\sum_{i=1}^{10}[\mathrm{PC}_n(i,j) - \overline{\mathrm{PC}}_n(j)]^2 \sum_{i=1}^{10}[\mathrm{PC}_n(i,j+1) - \overline{\mathrm{PC}}_n(j+1)]^2}} \tag{3.7}$$

$\overline{\mathrm{PC}}_n(j)$ represents the average of the 10 values of PC_n given by the 10 simulations of j month.

Next, for each PC, we calculated the average $\overline{r}_n$ of the 19 $r_n(j)$ values corresponding to 19 $(j, j+1)$ pairs of months, formed as described in the previous paragraph. Table 3.1 shows the $\overline{r}_n$ values corresponding to the first ten PCs of the barotropic component.

The statistical significance level of each mean value $\overline{r}_n$ was calculated using a method of Monte Carlo resampling. The method tests the null hypothesis of absence of correlation between ensembles. For this purpose, the temporal order, j, of the PCs was randomly permuted, doing the same with the order i of the simulations. For each permutation the mean values, $\overline{r}_n$, of the correlations were re-calculated. Figure 3.4 shows the histogram of frequencies of the mean values of the correlations in classes of amplitude 0.025, obtained after 15000 resamplings of the PC1. The sum of the

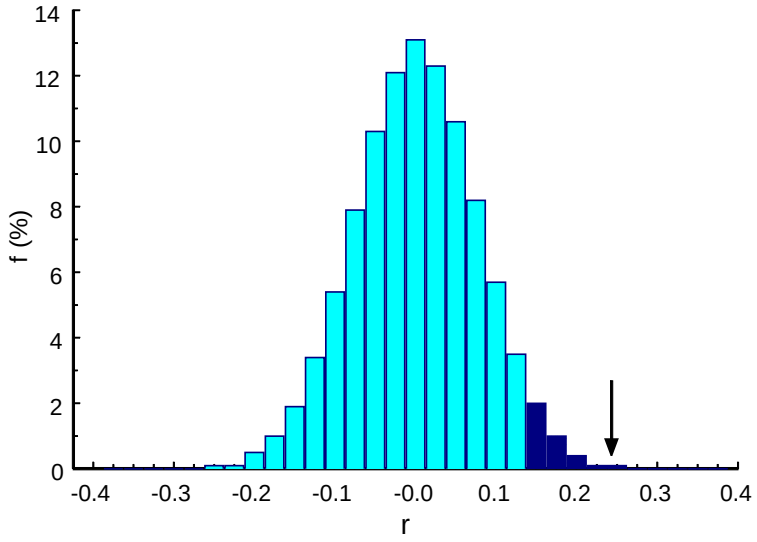

Figure 3.4: Frequencies of the mean values of the correlations in classes of amplitude 0.025, obtained after 15000 resamplings of the PC1. The sum of the frequencies corresponding to the black bars is 3.6%, and the vertical arrow indicates the 'observed' correlation value of the PC1.

frequencies corresponding to the black bars is 3.6%, and the vertical arrow indicates the 'observed' correlation value of the PC1.

Even though the joint significance levels of the correlation values were not analyzed, the results presented in table 3.1 clearly indicate that the null hypothesis of independence of ensembles should be rejected.

Finally, the homogeneity of variances of the ensembles was investigated using the Levene method [Milliken and Johnson, 1984]. The test consisted in performing an

Table 3.1: Mean correlations, $\overline{r}_n$, between ensembles associated with successive months, and the error level, p, in rejecting the null hypothesis of homogeneity of variances of the ensembles as calculated through Levene's method. The $\overline{r}_n$ values with a confidence level greater than 95% are indicated with '$*$'.

	Barotropic component ($m = 0$)									
	PC1	PC2	PC3	PC4	PC5	PC6	PC7	PC8	PC9	PC10
$\overline{r}_n$	0.24*	0.44*	0.18*	0.15*	18*	0.11	0.22*	0.02	-0.03	0.22*
$p(\%)$	81.2	15.3	82.8	8.5	42.6	14.4	37.6	89.2	6.2	7.5

analysis of variance (ANOVA) on the absolute deviations of PCs from the respective ensemble means, i.e., of the absolute values of the differences $[\mathrm{PC}_n(i,j) - \overline{\mathrm{PC}}_n(j)]$. The results obtained through the application of this method are also presented in table 3.1 and show that the null hypothesis of the homogeneity of variance can not be rejected with an error probability lower than 6% (minimal value in the case of PC9).

Even though the results of the statistical tests described in the previous paragraphs permit the acceptance of the null hypothesis of the homogeneity of variances, they demand for the rejection of the null hypothesis of the independence of ensembles. However, as it was mentioned in section 2.3.1, in the present case, where the correlation values are positive, the use of the relation 2.5, even if abusive, will lead to a small underestimate of the forced variability. Because of this, using (2.5) to estimate the forced variability does not represent any risk of appearance of climatic signals that are mere artifacts of the statistical analysis. It is then justified the procedure adopted in this work, where the internal and forced variances were estimated by the statistical model Ω_1, described in section 2.3.1, which doesn't take into account the existence of correlations between ensembles and considers the variance of the ensembles constant.

3.6 Free component of the total transient energy

The free component of total transient energy is given by the expression

$$E'_{INT}(\beta) = \frac{p_s h_m}{c_\beta} \left[\sigma^2_{INT} \left(\Re(w_\beta) \right) + \sigma^2_{INT} \left(\Im(w_\beta) \right) \right], \tag{3.8}$$

in which the internal variances are estimated by (2.3).

In the introduction to this chapter, we mentioned some results in the bibliography that raised special interest in the analysis of the variabilities of the barotropic and fourth baroclinic components. Another reason, based on the vertical spectrum of the total transient energy, can now be given for the study of those two components.

The free component of the total energy associated with a given vertical structure function , $G_m(p)$, is given by the summation of the energies associated with the free components of all Rossby modes and all inertio-gravity modes with the same vertical index m. In figure 3.5 the vertical spectrum of the free component of the total energy is presented. This spectrum presents a bimodal structure, with an energy maximum associated with the barotropic component ($m = 0$) and with another energy peak at the fourth baroclinic component ($m = 4$).

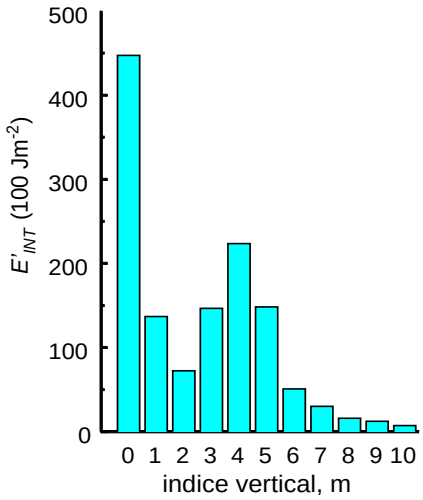

Figure 3.5: Vertical spectrum of the total transient energy associated with the internal component of the atmospheric circulation.

3.6.1 Barotropic component

Figure 3.6 shows the total transient energy associated with the free components of the barotropic Rossby modes. This figure is similar to figure 3.2. However, one may observe the relatively smaller free variability of some modes, like the Kelvin mode (0,0), the zonal Rossby modes ($s = 0, l = 5$) and ($s = 0, l = 7$) or still the Rossby mode ($s = 1, l = 5$. Even though figure 3.2 is not the representation of an unbiased estimate of the total variability, its comparison with figure 3.6 suggests that the variability of the barotropic component is dominated by the internal variability. Between the modes of smaller relative internal variability, the zonal Kelvin mode stands out. The variability of this mode is associated with an expansion or a contraction of the atmosphere, and respectively, with a greater or a smaller zonal mean speed of the zonal wind. It is then a mode sensitive to the variations of the relative angular momentum of the atmosphere.

If the variability is analyzed as a function of the meridional index, even though it is not very perceptible in the chosen projection for figure 3.6, it can be verified that the meridional index of the mode with higher variability decreases as the zonal wavenumber increases. The meridional index of the higher variability mode is $l = 5$ in the case of $s = 1$, $l = 3$ for $s = 4$ and $l = 2$ in the case of $s = 5$. This suggests that the variability in the higher latitudes is dominated by the ultralong waves ($s = 0, 1, 2$), and that the contributions of the zonal waves $s = 3, 4$ and 5 are also important in the midlle and lower latitudes. Nakamura et al [1987] achieved a similar result in a Fourier

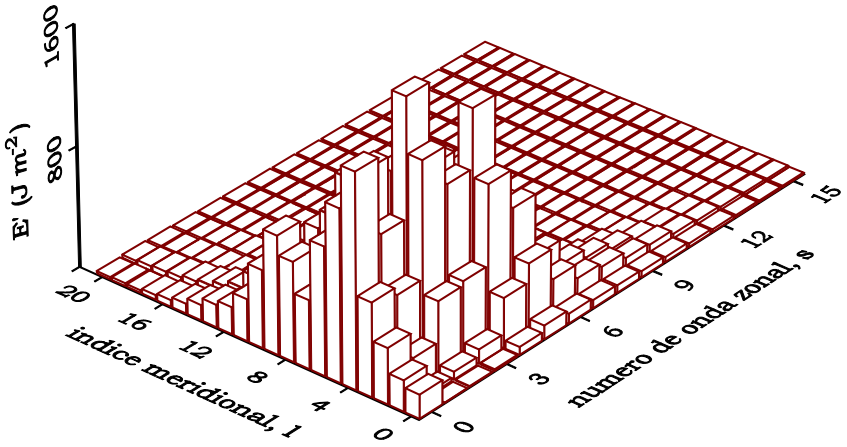

Figure 3.6: Total transient energy associated with the free components of the barotropic Rossby modes.

analysis of the horizontal structure of Northern Hemisphere wintertime teleconnection patterns of the extratropical circulation (north to 20° N).

The geographical distribution of the total transient energy associated with the free component of the barotropic circulation ($m = 0$) can be obtained calculating, at each model grid point, the internal variance of the vector

$$\sqrt{gh_0}\ \tilde{\mathbf{W}}_0 = \left(\hat{u}_m, \hat{v}_m, \frac{\hat{\phi}_m}{\sqrt{gh_m}} \right)_{m=0}^{T} . \tag{3.9}$$

$\tilde{\mathbf{W}}_\mathbf{0}$ is multiplied by $\sqrt{gh_0}$ (*cf.* eq. 2.66) to have all components with dimensions of velocity. The total transient energy, per unit of horizontal area, at a point (λ, θ), associated with the projection of the internal circulation component onto the barotropic vertical structure function is given by

$$E'_{INT}(\lambda,\theta) = \frac{p_s}{4g} \left\{ \sigma^2_{INT} \left[\hat{u}_0(\lambda,\theta) \right] + \sigma^2_{INT} \left[\hat{v}_0(\lambda,\theta) \right] + \sigma^2_{INT} \left[\frac{\hat{\phi}_0(\lambda,\theta)}{\sqrt{gh_0}} \right] \right\} . \tag{3.10}$$

In figure 3.7 it is shown the spatial distribution of the total transient energy, per unit of horizontal area, associated with the free components of the barotropic Rossby modes, including also the zonal Kelvin mode. It can be observed that the centers

of higher internal variability are located on the northeast of the Pacific and Atlantic Oceans, at the jet stream exit regions.

An indirect comparison can be made between the estimate of the free variability of the total energy, simulated by the MU AGCM, and the maps of internal variability of the 500-hPa geopotential height field, simulated by the AGCM of the Laboraroire de Météorologie Dynamique (LMD) [Harzallah and Sadourny, 1995]. In this comparison, we should have in mind that the available potential energy of the barotropic component (proportional to the square of the third component of vector 3.9) is small, when compared to the kinetic energy (proportional to the sum of squares of the first and second components of vector 3.9). In fact, the available potential energy associated with the free variability of the barotropic component presents an absolute maximum of $25.4\,\mathrm{kJm^{-2}}$ over northwest Canada (*cf.* fig. 3.10), while the total energy maximum is equal to $203\,\mathrm{kJm^{-2}}$. So, if the total energy is dominated by the parcel of kinetic energy , the variability centers of total energy should approximately coincide with the centers of the variability of the gradient of geopotential height. With this in mind, it can be verified that the meridional 'dipole' over the North Atlantic and the variability centers over the North Pacific, shown in figure 3.7, are in accordance with the disposition of the variability centers of the geopotential fields, obtained by Harzallah and Sadourny [1995].

An indirect validation of the MU AGCM simulations can be performed if we compare the simulated maps with the observed maps of the standard deviation of 30 day averages of the 500-hPa geopotential height field calculated by Blackmon *et al.* [1984, fig. 2b]. The internal variabilities simulated over the oceanic regions are in accordance to the observed variability centers. However, the highest center of variability observed by Blackmon *et al.*, located over the Siberian Arctic does not have any correspondence in the simulated barotropic variability.

For a direct validation of the simulations, we calculated the total transient energy associated with the barotropic component of the NCEP reanalyzed atmosphere. The reanalysis used in this study will be described in chapter 4. Figure 3.8 shows the transient energy associated with the barotropic Rossby modes, based on winter monthly means (DJF) of the reanalized data for the period of 1977-88. Because one can only have a sole realization (one member) of the observed atmosphere, figure 3.8 represents the total variability (free + forced), estimated by expression 3.6 with a series of 36 months.

Even though the maps in figure 3.7 represent the free component of the simulated variability, they can be compared to the maps of figure 3.8 that represent the total observed variability. In fact, the climatic variability of the barotropic component is dominated by the internal variability, and the maps of the total simulated variability (not shown) are very similar to the maps in figure 3.7.

The simulated variability reproduces fairly well the observed variability over the Pacific Ocean, in both hemispheres: the variability centers are well located, and maximum values of the total simulated variability are equal to 73 and 84% of the respective observed maxima over the Central Pacific and south of the Alaska. Over the South Pacific, the maximum value of the total energy associated with the total simulated variability is equal to 79% of the observed maximum. Over the North Atlantic Ocean, the observed transient energy map also presents a meridional dipole. Nevertheless, the simulated dipole is shifted eastward about 20° relatively to the observed dipole, and the maximum total transient energy associated with total simulated variability over the north of British isles is only 37% of the corresponding observed maximum at southeast of Greenland. These differences appear to indicate, besides possible sample related problems (only a realization of 12 years is available for reanalysis), that the model simulates better the climatic variability over the Pacific Ocean than over the Atlantic Ocean.

Figure 3.9 shows the maps of simulated and observed available potential energies associated with the total variability of the barotropic component of the extratropical Northern Hemisphere circulation. The map of available potential energy associated with the internal variability is presented in figure 3.10. Comparing the top map in figure 3.9 with the one in figure 3.10 it can be observed, as mentioned above, that the maps of internal and total simulated variabilities are very similar.

Because, in the normal mode scheme the available potential energy is proportional to the squared projections of the geopotential onto the vertical structure functions, it is now possible to make a more direct comparison between the simulated maps of the available potential transient energy and the maps of the standard deviation of the 500-hPa geopotential height obtained by Blackmon *et al.* [1984] and Harzallah and Sadourny [1995]. The internal variability simulated by the MU AGCM (fig. 3.10) presents a maximum over the Pacific, centered around 45°N, and another maximum over the Northwest Canada. This center extends to north and west, through the oriental region of Siberia, linking to another maximum over the Barents sea. This

structure presents similarities with the three centers of internal variability over the Pacific, Alaska and oriental Siberia, and the secondary maximum over the Urals simulated with the LMD AGCM [Harzallah and Sadourny, 1995, fig. 3a]. The internal variability simulated by the MU AGCM over the Atlantic presents a dipolar structure not completely separated from the other centers of variability. However this dipole is shifted eastward about 30° relatively to the dipole simulated by the LMD AGCM.

The map of the available potential energy of the NCEP reanalysis (fig. 3.9, *bottom*) reproduces the same centers of variability observed by Blackmon *et al.* [1984, fig. 2b]. However it can be seen that the reanalysis present a more pronounced dipolar structure over Greenland and the Atlantic

The available potential energy associated with the total variability simulated by the MU AGCM (fig. 3.9, *top*) presents a center of variability over the Pacific, just like the observations, even if more elongated zonally. However both centers of simulated variability over Canada and the Barents Sea, do not appear in the observations. These two centers seem to be part of a structure that is turned $\sim 60^{o}$ west relatively to the centers of observed variability over the Siberian Arctic and over Greenland.

To summarize, the MU AGCM simulates fairly well the observed variability of the total energy associated with the barotropic component over the Pacific and North American regions, being lesser the concordance over the Atlantic (*cf.* figs. 3.7 and 3.8). The differences between the simulations and the observations appear to be more important in the case of available potential energy (cf. fig.3.9), indicating that the model simulates more adequately the transient kinetic energy of the barotropic component. However it should be noted at this respect that the geopotential field intervenes in the motion dynamics only through its gradient and the gradient operator has characteristics of a high-pass filter. Due to these facts it should be expected that inaccuracies in the longest waves do not reflect, in a considerable way, in the gradient of geopotential field. Thus, the analysis of the variability of the vector $(u, v, \phi)^T$, even when the simulated ϕ component presents some discordances with the respective observed component, will certainly be more adequate to a dynamical study of atmospheric circulation variability than a more 'traditional' analysis, restricted to a study of the geopotential field at a given level.

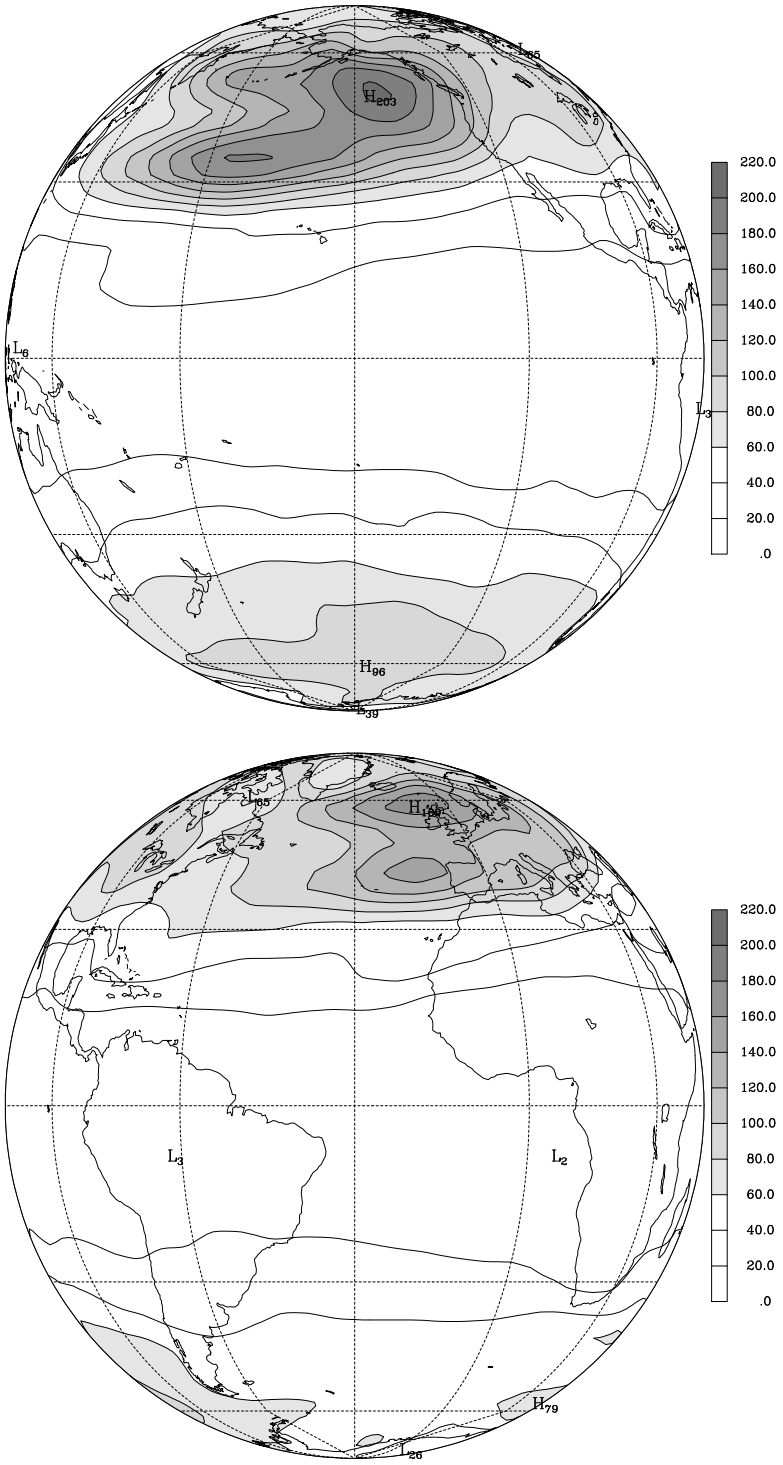

Figure 3.7: Total transient energy per unit of horizontal area ($\mathrm{kJ\,m^{-2}}$) associated with the internal variability of barotropic Rossby modes.

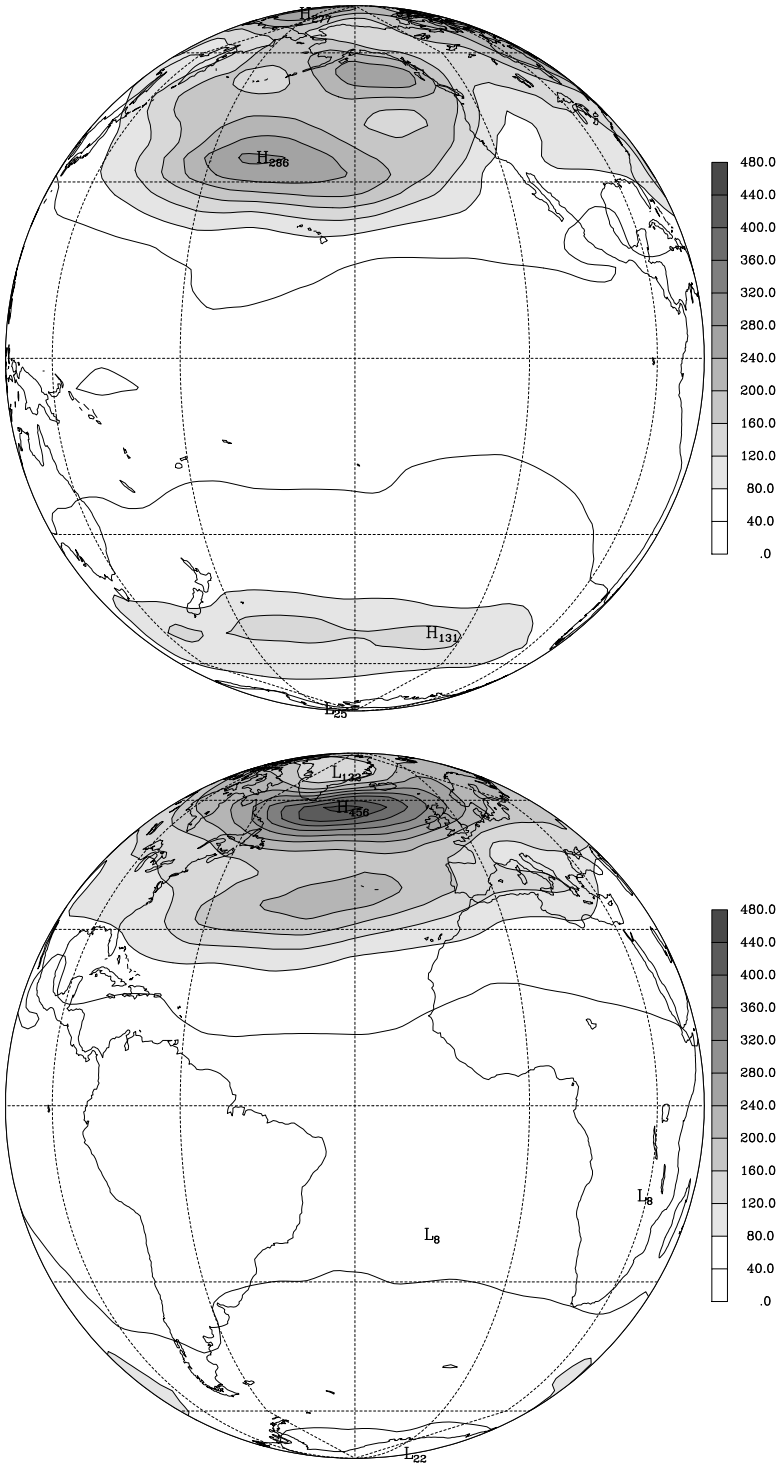

Figure 3.8: Total transient energy ($\mathrm{kJ\,m^{-2}}$) associated with the barotropic Rossby modes of NCEP reanalized atmosphere, for the period Dez/76-Fev/88.

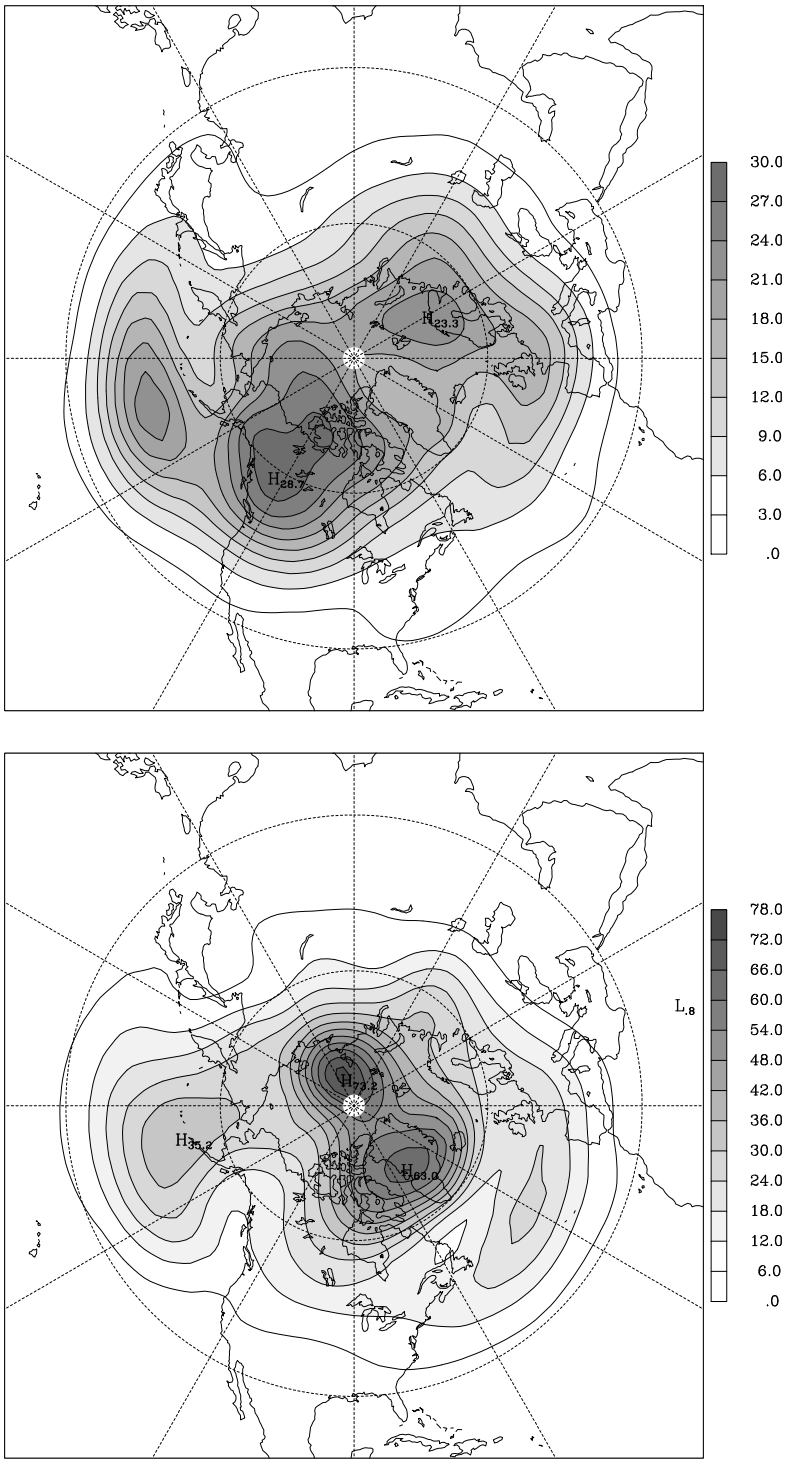

Figure 3.9: Available potential energy ($\mathrm{kJ\,m^{-2}}$) associated with the total variability of the simulated barotropic component (*top*) and the NCEP reanalysis, for the period Dez/76-Fev/88 (*bottom*). It should be noted the difference in the energy scales.

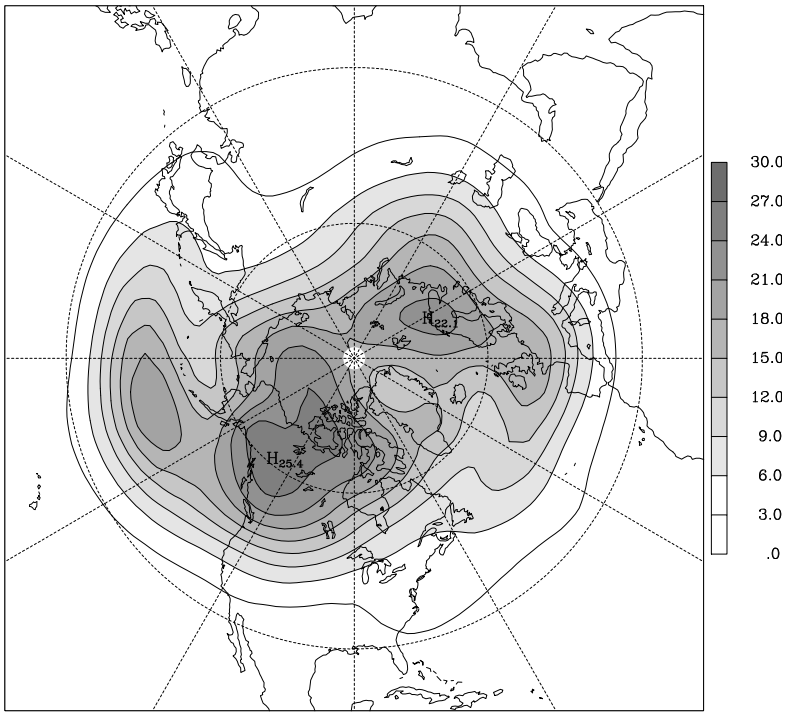

Figure 3.10: Available potential energy ($\mathrm{kJ\,m^{-2}}$) associated with the simulated internal barotropic variability.

3.6.2 Fourth baroclinic component

Figure 3.11 shows the total transient energy associated with the free variability of Rossby modes of the fourth baroclinic component. The modes with meridional index $l = 0$ and zonal wavenumbers $s = 0, ..., 5$ are Kelvin modes. Comparing this figure with figure 3.6 referring to the barotropic component, differences are visible in the energy distribution over the meridional indices. An evident difference is that the variability associated with the fourth baroclinic component projects itself onto Rossby modes of higher meridional index. This behaviour results from the fact that Hough modes of low meridional indices and associated with small equivalent heights ($h_4 = 179\,\mathrm{m} \ll h_0 = 9691\,\mathrm{m}$) are confined to the intertropical regions [Longuet-Higgins, 1968]. Hence, the variability in middle and high latitudes associated with the fourth baroclinic component should project onto different modes of higher meridional index relatively to those onto which are projected the extratropical barotropic variability.

Knowing that the Rossby modes of low meridional index and the Kelvin modes are confined to the intertropical regions, figure 3.11 suggests that the fourth baro-

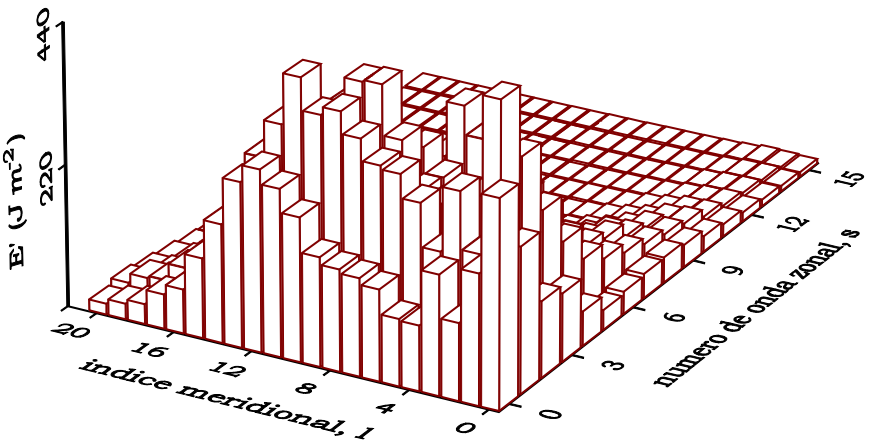

Figure 3.11: Total transient energy associated with the internal variability of Rossby modes of the fourth baroclinic component. The modes with meridional index $l = 0$ and zonal wavenumbers $s = 0, ..., 5$ are Kelvin modes.

clinic component captures intertropical variability ($l \leq 4$) and extratropical variability ($l \geq 6$). This distinction between low meridional index modes and higher index modes is also suggested by the comparison between figures 3.11 and 3.3: The internal variabilities of the modes with meridional index $l \leq 3$ have values between 50 and 70% of the respective estimates of total variability given in figure 3.3. However, the variabilities of Rossby modes with $l > 4$ are not considerably different.

The geographical distribution of the total energy associated with the free variability of the fourth baroclinic component, i.e., of the vectorial field 3.9 with $m = 4$, was calculated by an expression analogous to expression 3.10 and is represented in figure 3.12. Comparing these maps with the barotropic variability maps (fig. 3.7), it may be seen that they are approximately in quadrature, i.e., regions with higher variability of the fourth baroclinic component are located over regions of lower barotropic variability. While the centers of barotropic variability are located over the Pacific and Atlantic Oceans, the fourth baroclinic component presents a variability center over North Pacific and an extensive center of variability over North America. The center of higher variability of the fourth baroclinic component appears over the Barents Sea,

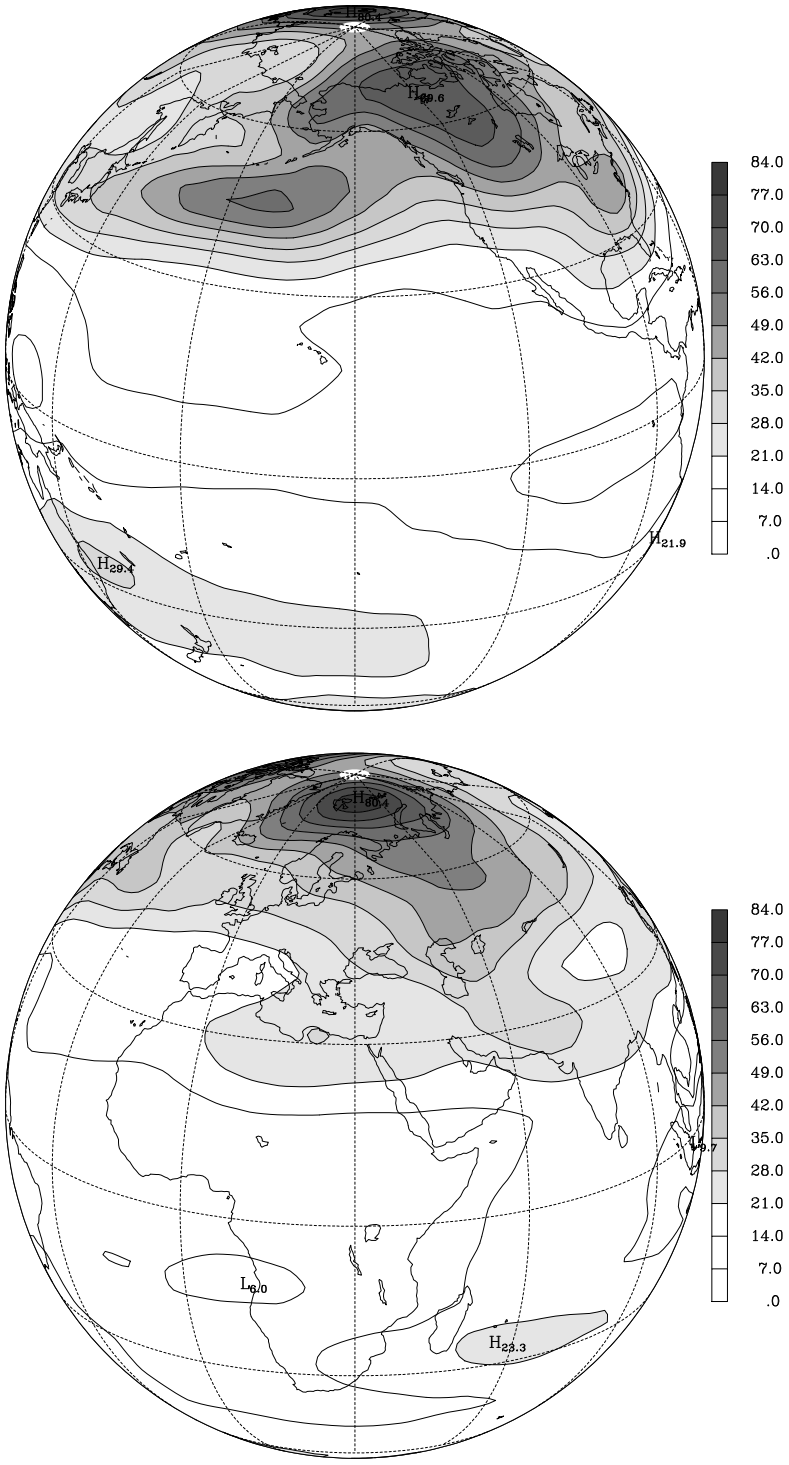

Figure 3.12: Total transiente energy ($\mathrm{kJ\,m^{-2}}$) associated with the internal variability of the fourth baroclinic component.

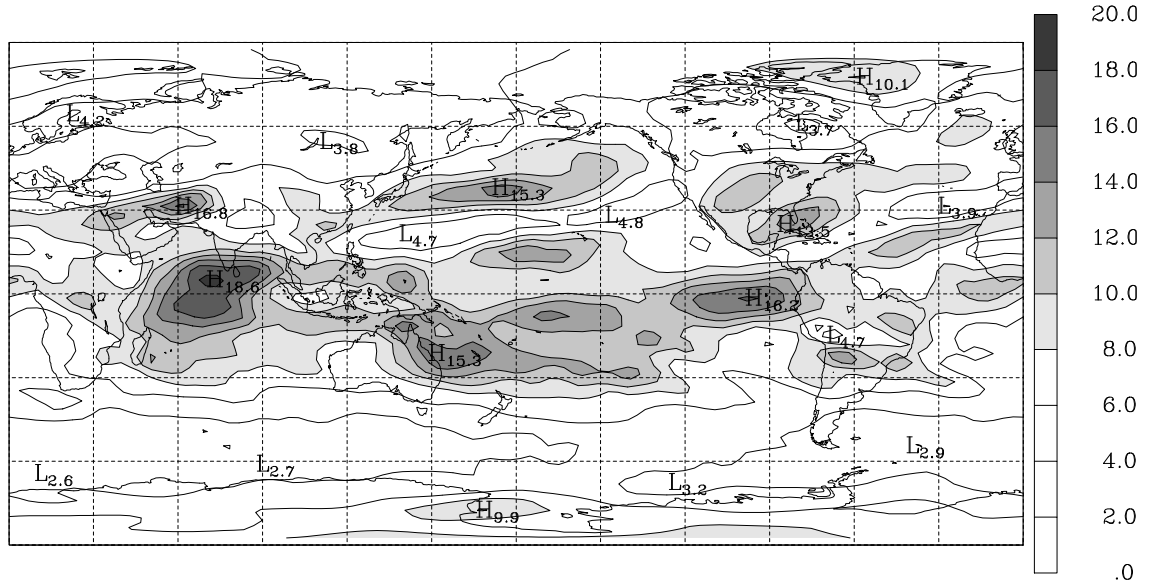

Figure 3.13: Internal variability of kinetic energy ($\mathrm{kJ\,m^{-2}}$) associated with the fourth baroclinic component.

prolonging over the Urals. This center remind the maximum standard deviation of the 500-hPa geopotential height found in the study of Blackmon *et al.* [1984].

It is important to mention that, contrary to the barotropic component, the extratropical internal variability of the fourth baroclinic component is dominated by the variability of available potential energy. This fact may be verified through the comparison of figure 3.12 with figure 3.13, that shows the internal variability field of the kinetic energy associated with the fourth baroclinic component. The comparison of the figures confirms also the two types of variability captured by the fourth baroclinic component: the extratropical variability dominated by the variability of the available potential energy and the intertropical variability dominated by the variability of the kinetic energy.

3.7 Forced component of the total transient energy

The total transient energy associated with the forced component of a given normal mode $\beta \equiv (\alpha, mls)$ is calculated by the following expression

$$E'_{SST}(\beta) = \frac{p_s h_m}{c_\beta} \left[\sigma^2_{SST} \left(\Re(w_\beta) \right) + \sigma^2_{SST} \left(\Im(w_\beta) \right) \right], \tag{3.11}$$

in which the forced variances are estimated by (2.5).

Figure 3.14 shows the vertical spectrum of the forced component of the total energy. As in the case of the internal (free) component, the vertical spectrum of the forced component of the atmospheric circulation presents a bimodal structure, with a maximum in the barotropic component ($m = 0$) and another one in the fourth baroclinic component ($m = 4$).

Comparing figures 3.5 and 3.14 it can be seen that, at all vertical indexes, the total variability

$$E'_{TOT}(m) = E'_{INT}(m) + E'_{SST}(m)$$

is dominated by the contribution due to the internal variability. The signal to noise ratio ($E'_{SST}(m)/E'_{INT}(m)$) for the barotropic component and fourth baroclinic component are 6.9% and 14.2% respectively.

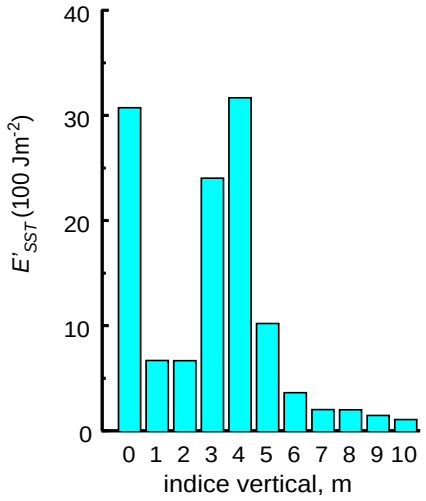

Figure 3.14: Vertical spectrum of the total transient energy associated with the forced atmospheric circulation.

3.7.1 Forced barotropic component

The total transient energy associated with the forced components of the barotropic Rossby modes is shown in figure 3.15. As it can be observed, the forced barotropic circulation projects itself on the modes associated with the larger spatial scales, i.e., with small zonal wavenumbers, s, and small meridional indices, l. The selectivity of the forcing reveals itself in two other aspects. In the first place, it should be noted the preferred forcing of symmetric Rossby modes (modes with odd meridional indices) in the case of ultralong waves ($s = 0, 1, 2$). In fact, because the zonal Kelvin mode ($s = 0, l = 0$) is also symmetric, the two perspectives of figure 3.15 clearly show that the symmetric modes associated with the waves ($s = 0, 1$ and 2) are more excited, i.e., have more energy that the anti-symmetric modes. In second place, it should be referred the relative maximum of the energy of the forced component at wavenumber $s = 4$ (the energy summed over all meridional indices).

As for the internal barotropic circulation, the geographical distribution of the total energy associated with the barotropic component of the forced circulation was estimated by the following expression

$$E'_{SST}(\lambda,\theta) = \frac{p_s}{4g}\left\{\sigma^2_{SST}\left[\hat{u}_0(\lambda,\theta)\right] + \sigma^2_{SST}\left[\hat{v}_0(\lambda,\theta)\right] + \sigma^2_{SST}\left[\frac{\hat{\phi}_0(\lambda,\theta)}{\sqrt{gh_0}}\right]\right\}. \qquad (3.12)$$

The maps of the total energy associated with the forced barotropic circulation are presented in figure 3.16. The most evident aspect of this figure is the contrast between the forcing of the circulation over the hemisphere west of 60^0 W, wich includes all the Pacific Ocean and North America, and the forcing over the complementary hemisphere. Observing the meridional distribution of the variability maxima over the Pacific Ocean, it can be discerned the tendency of the centers to occupy symmetrical positions in the relation to the equator, as should be expected due to the higher forcing of the symmetric Rossby modes (*cf.* fig. 3.15). Another important aspect is that the forced variability maps of the components ($\hat{u}_0$ e $\hat{v}_0$) of vector 3.9, i.e., the maps of the forced variability of the kinetic energy, associated the barotropic component (not shown) are practically identical to the maps in figure 3.16. In fact the contribution of the available potential energy for the total energy of the forced barotropic circulation is very small, having a maximum of $3.5\mathrm{kJ\,m^{-2}}$ over the Northwest Canada (fig. 3.17); this shows that figure 3.16 must represent, in a very good approximation, the forced variability of the horizontal wind. This forced variation of the circulation regimes, according

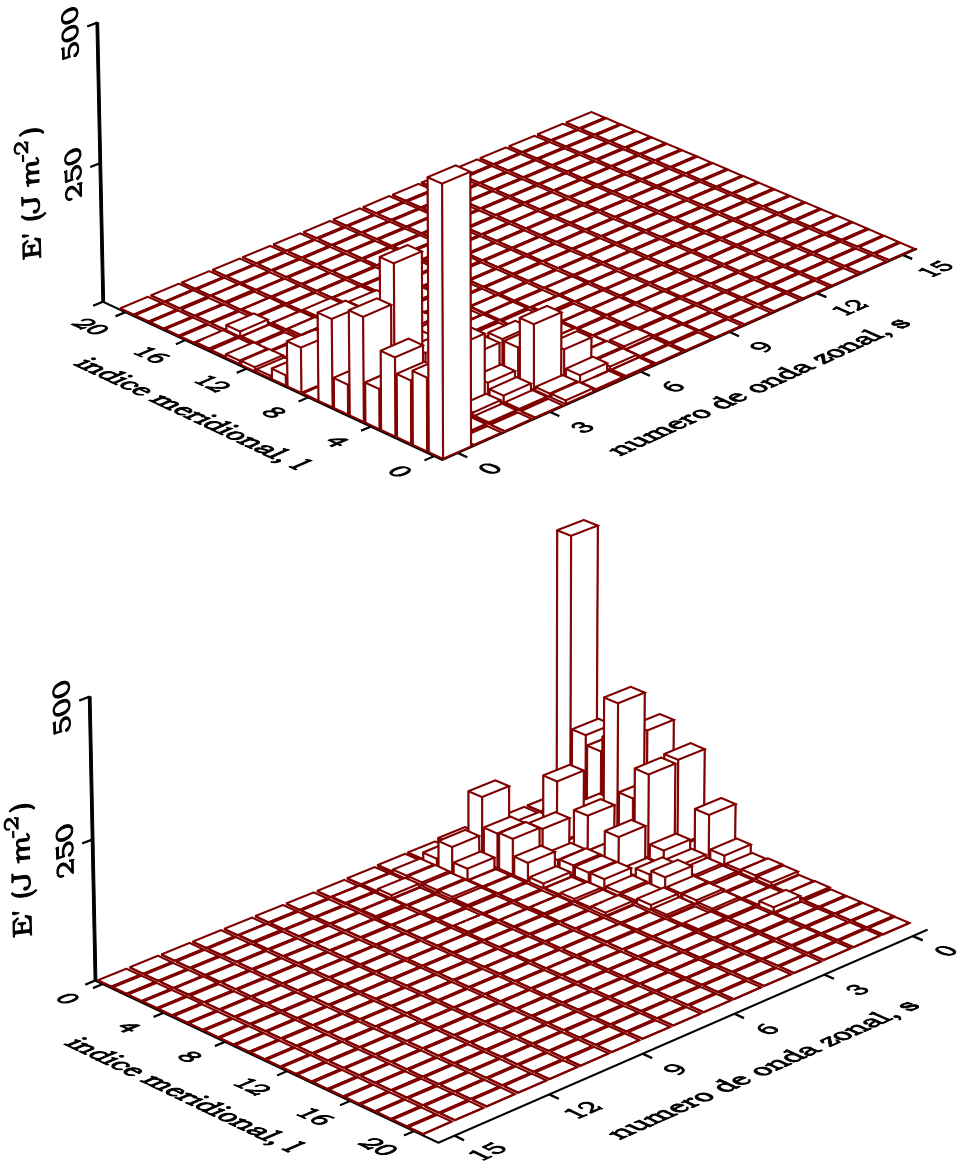

Figure 3.15: Total transient energy associated with the forced components of barotropic Rossby modes.

to the observational study of Lau [1988], can be reflected on the variability of the extratropical synoptic activity over the Pacific and North America.

The maps of the signal to noise ratio ($E'_{SST}(\lambda,\theta)/E'_{INT}(\lambda,\theta)$) for the barotropic component are presented in figure 3.18. A high fraction of the variability of the

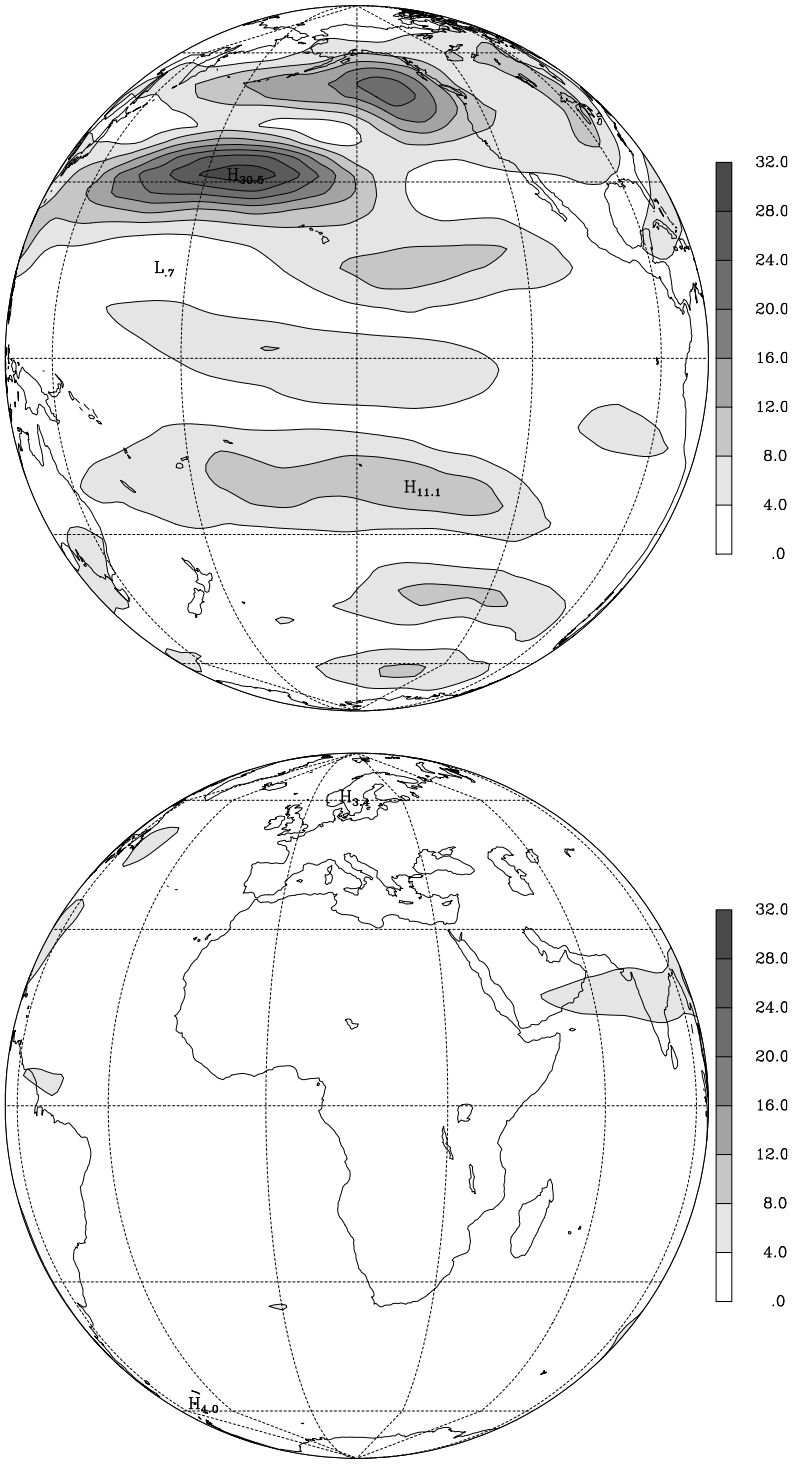

Figure 3.16: Total transient energy per unit of horizontal area ($\mathrm{k\,Jm^{-2}}$) associated with the forced barotropic Rossby modes.

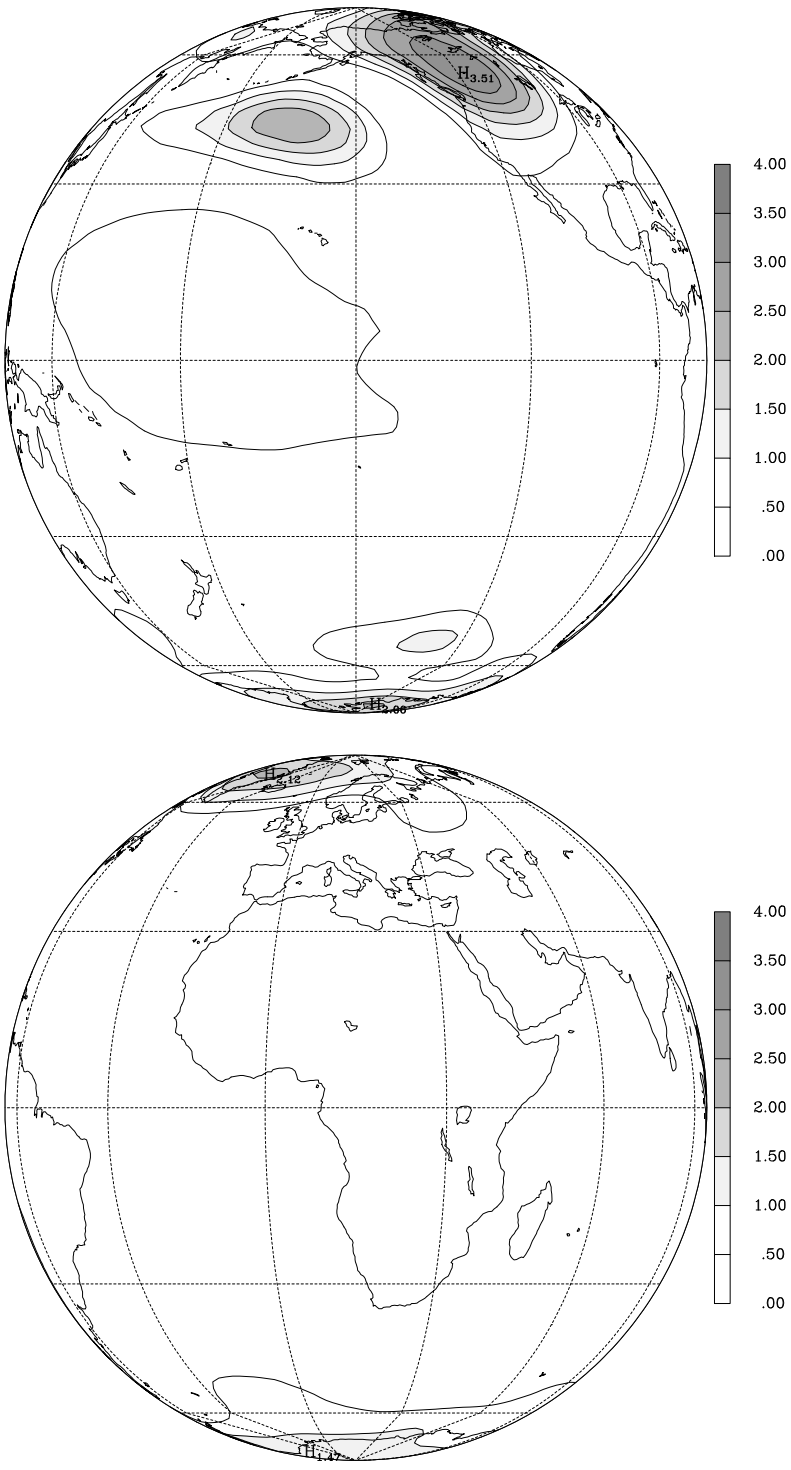

Figure 3.17: Like the figure 3.16 but respecting to the available potential energy.

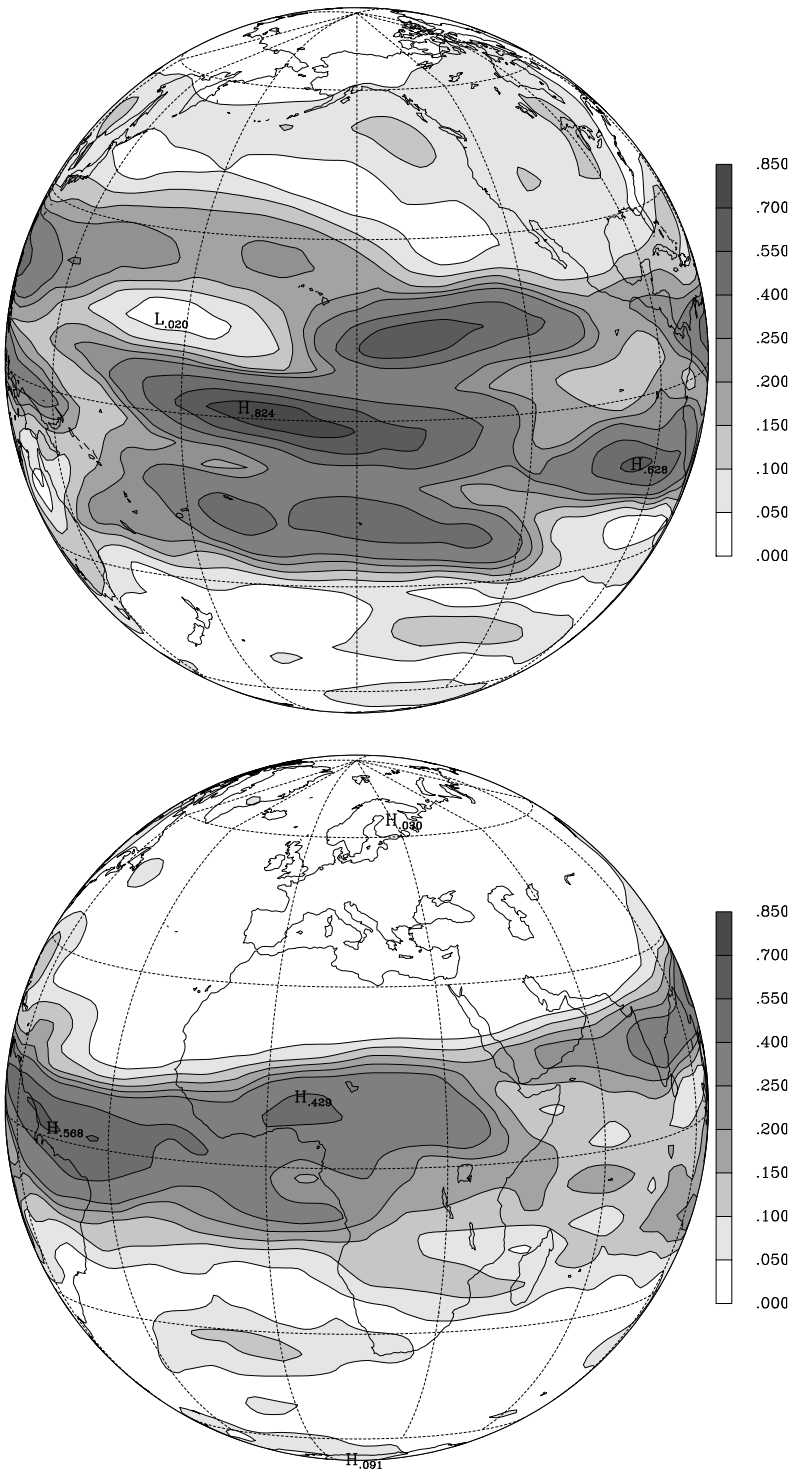

Figure 3.18: Signal to noise ratio of total transient energy associated with the barotropic circulation.

barotropic component of the intertropical circulation is related to the ocean forcing, with the signal to noise ratio achieving a maximum of 82% over the equatorial central Pacific region. This agrees with the results of observational studies [Ropelewski and Halpert, 1989; Wallace, 1996, among others] that show that great part of the inter-annual variability of the intertropical circulation is associated with SST anomalies on the tropical Pacific, through coupled atmosphere-oceanic processes clearly manifested in the El Niño-Southern Oscillation (ENSO) 'cycle'. Stern and Miyakoda [1995] analyzed an ensemble of simulations performed with the T30 version of the AGCM of the Geophysical Fluid Dynamics Laboratory, for the period 1979-88. The values they obtained for the 'reproducibility' (defined as the ratio between internal variance of each ensemble and the 'climatological' variance) also show that a high fraction of the variability of the 500-hPa geopotential height, in the intertropical region, is associated with SST variability (see their figures 7 and 10).

In the subtropical and extratropical regions of the Northern Hemisphere, the signal to noise ratio presents values greater than 15% in a extensive zonal band centered on the meridional flank of the jet stream over the Pacific, and values above 10% over the Golf of Alaska and in a center over the northern United States. These values, in spite of small, are contrasting with the much smaller values over the Atlantic, Europe and great part of Asia.

The very small forcing over the Euro-Atlantic region permits to understand some of the difficulties in developing operational schemes of seasonal forecasting for that region [Rowell, 1998]. In fact the forced variance, as calculated in this work, constitutes a measure of the response of the atmospheric circulation to oceanic forcing. However, the calculation of the mean of the squared anomalies of the forced circulation over all the temporal series may, in some cases, underestimate the intensity of the response to particular forcings. This is the case if the capacity of doing seasonal forecasts, using multiple simulations, results from atmospheric response to extreme SST anomalies, as, for example, the ones associated with El Niño or La Niña events [Barnett *et al.*, 1997]. On the other hand, as emphasized by Anderson and Stern [1996], the mean and the variance of ensembles are not the sole measures of the predictive utility of ensemble integrations.

3.7.2 Fourth baroclinic component of the forced circulation

The total transient energy associated with the Rossby and Kelvin ($l = 0,\ s = 0, \ldots, 5$) modes of the 4^{th} baroclinic component of the forced circulation is shown in figure 3.19.

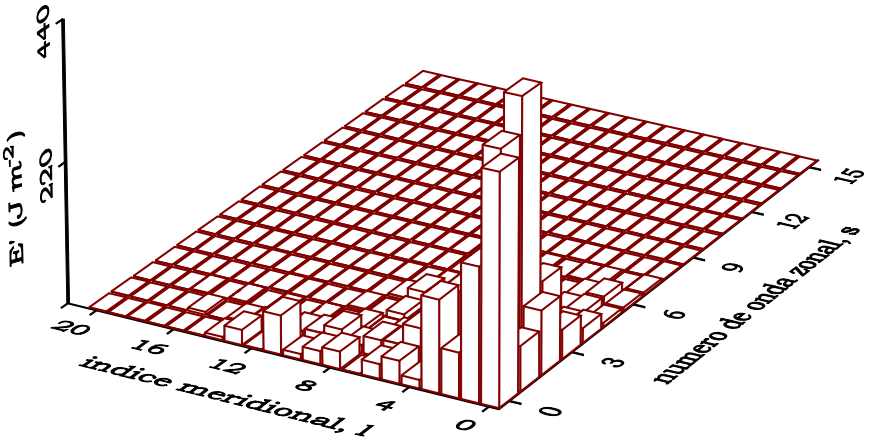

Figure 3.19: Total transient energy associated with the Rossby and Kelvin ($l = 0,\ s = 0, \ldots, 5$) modes of the 4^{th} baroclinic component of the forced circulation.

As suggested in section 3.6.2, the forced variability of the fourth baroclinic component is dominated by the modes with meridional index $l < 4$. Hence the forced energy associated with this component is dominated by the forced variability of the intertropical circulation, as it may be observed in figure 3.20.

It was also seen in section 3.6.2, that the internal variability of the fourth baroclinic component, in the extratropical regions is dominated by the variability of the available potential energy while the parcel of kinetic energy is higher in the intertropical regions. In the case of the forced variability, the contributions due to the kinetic and available potential energies are equally important over the intertropical region, as it can be observed in figure 3.21.

It should be finally noted that the variance of the 200-hPa geopotential height is often used to evaluate the response of the upper troposphere to tropical SST anomalies

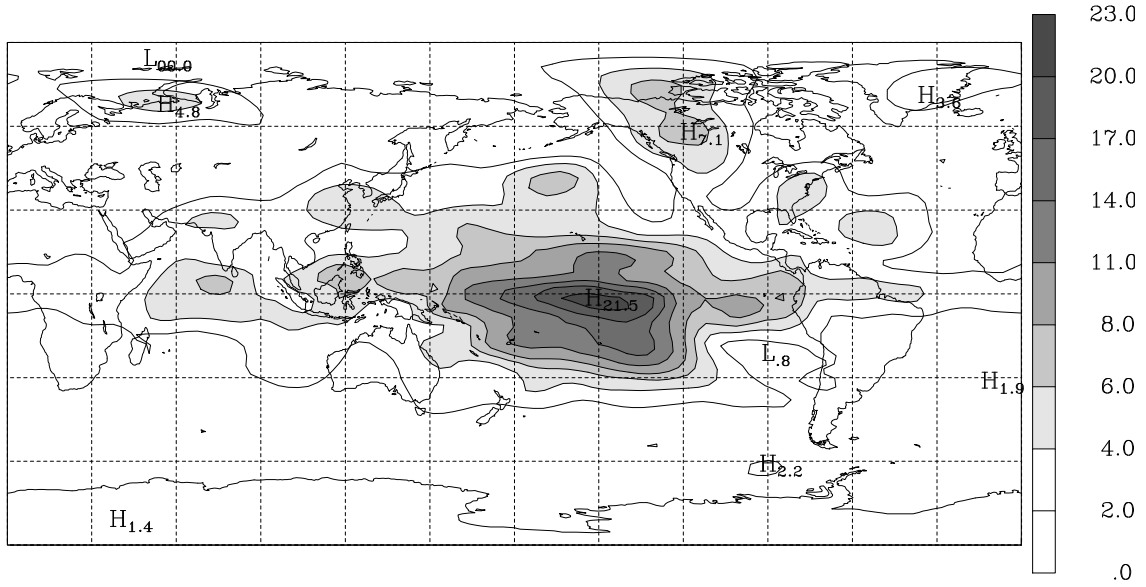

Figure 3.20: Total transient energy ($\mathrm{kJ\,m^{-2}}$) associated with the 4$^{\mathrm{th}}$ baroclinic component of the forced circulation.

[Horel and Wallace, 1981; Kawamura *et al.*, 1995]. As it can be seen in figure 3.1, the vertical structure of the mode $m = 4$ presents a maximum close to the 200 hPa level, hence being sensitive to the anomalies of the geopotential in the upper troposphere. In fact, figure 3.22 shows a pattern of the signal to noise ratio of the available potential energy of the 4$^{\mathrm{th}}$ baroclinic component very similar to figure 9 in an article of Kawamura *et al.* [1995]. In that article they calculated the ratio between the standard deviations of the 200-hPa geopotential height fields simulated by the T42/L21 AGCM version of the Japanese Meteorological Agency forced with observed and climatological SSTs. The simulation forced with climatological SSTs was used to estimate the internal variability. However, it should be mentioned to this purpose, that the results of Harzallah and Sadourny [1995] indicate differences between the internal variability estimated by an integration forced with climatological SSTs and the internal variability estimated by a set of simulations (ensemble) forced with SSTs that include the interannual variability.

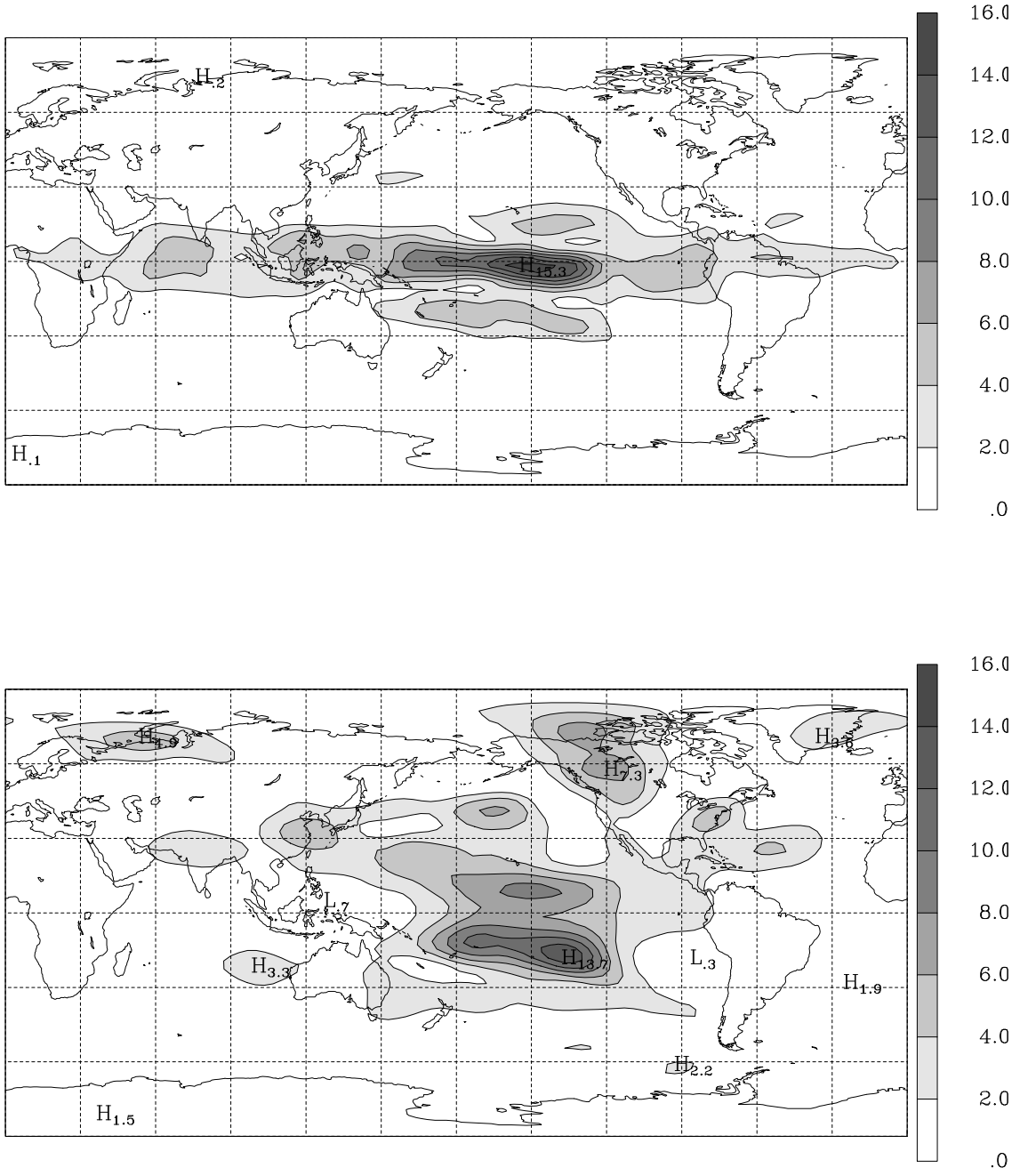

Figure 3.21: Kinetic energy (*top*) and available potential energy (*bottom*) associated with the forced variability of the 4$^{\text{th}}$ baroclinic component.

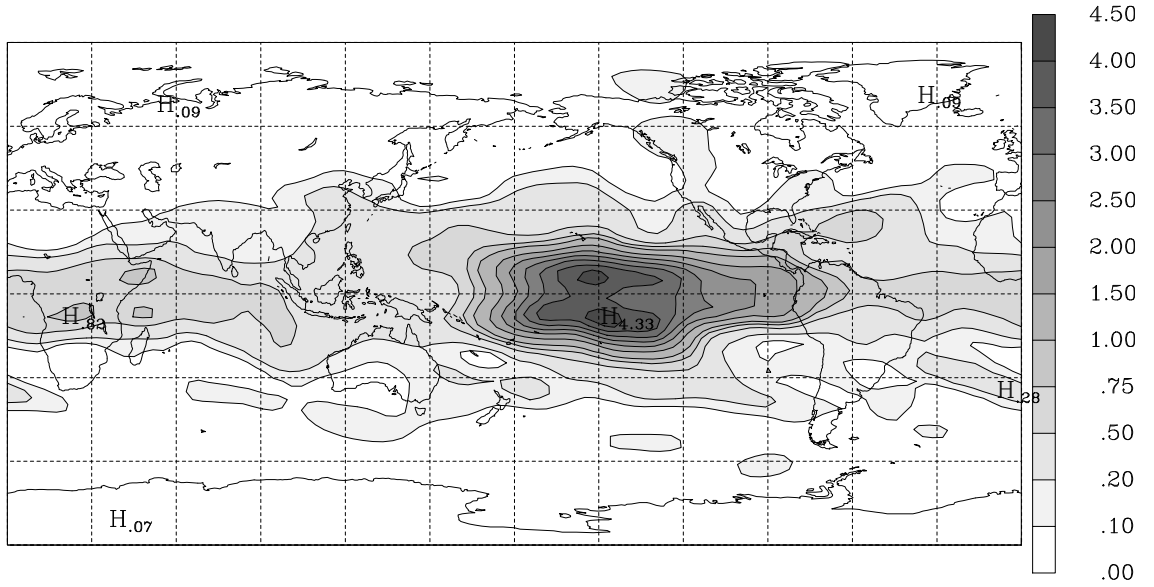

Figure 3.22: Signal to noise ratio of the variability of the available potential energy of the 4$^{\text{th}}$ baroclinic component.

3.8 Patterns of internal variability

The method for the identification of the principal patterns of internal variability of the circulation projected onto a given vertical structure, m, consisted in the realization of a complex principal component analysis (CPCA) on the $w_{\alpha,msl}$ coefficients. Because coefficients are complex, the adequate formulation of the problem of eigenvectors and eigenvalues is

$$\sum_{\beta'} S_{\beta\beta'} e_k(\beta') = \lambda_k e_k(\beta) \tag{3.13}$$

where $\hat{e}_k$ is the complex EOF ande λ_k its associated eigenvalue. $S_{\beta\beta'}$ are the elements of the internal variance and covariance matrix, $\mathbf{S}$, defined by

$$S_{\beta\beta'} = \frac{1}{N(M-1)} \sum_{j=1}^{N} \sum_{i=1}^{M} w'_{\beta}(i,j) {w'_{\beta'}}^{*}(i,j) \tag{3.14}$$

where β and β' denotes two quartet of indices α, msl and $\alpha', ms'l'$; $M = 10$ is the number of simulations, and $N = 30$ is the number of winter months (DJF) in each simulation.

The vectors $\hat{e}_k$ satisfy the following orthonormality condition

$$\sum_{\beta} \hat{e}_j(\beta) \hat{e}^*_k(\beta) = \delta_{jk}. \tag{3.15}$$

The w'_β coefficients can be expanded as

$$w'_\beta(i,j) = \sum_k z_k(i,j)e_k(\beta), \tag{3.16}$$

where $z_k(i,j)$are the principal components (PCs), which are determined from

$$z_k(i,j) = \sum_\beta w'_\beta(i,j)e^*_k(\beta) \tag{3.17}$$

Because the fields projected onto the normal modes basis are real, for each w'_β coefficient we have a complex conjugate ${w'_\beta}^* = w'_{\beta^*}$, where $\beta^* = (\alpha, m(-s)l)$. Then, if in the column vector

$$\begin{bmatrix} w'_1(i,j) \\ w'_2(i,j) \\ \vdots \\ w'_q(i,j) \end{bmatrix}, \tag{3.18}$$

where q is the number of modes retained in the CPCA, the coefficients $w'_\beta(i,j)$ and $w'_{\beta^*}(i,j)$ are permuted, and the variance-covariance matrix calculated again, one obtains a new matrix , $\mathbf{S}'$, that is the complex conjugate of the original matrix $\mathbf{S}$. Since $\mathbf{S}'$ is Hermitian, its eigenvalues are real and equal to the eigenvalues of $\mathbf{S}$, and one its basis of eigenvectores, $\hat{e}'_j$, may be given by the complex conjugate of the eigenvectores of $\mathbf{S}$, i.e.,

$$e'_j(\beta) = e^*_j(\beta). \tag{3.19}$$

On the other hand, because the new matrix $\mathbf{S}'$ results only from the change of components β and β^* in the column vector 3.18, the $\hat{e}''_j$ vectors whose components are given by

$$e''_j(\beta) = e_j(\beta^*) \tag{3.20}$$

form also one basis of eigenvectors of the matrix $\mathbf{S}'$.

If λ_j is a nondegenerate eigenvalue then eigenvectors $\hat{e}'_j$ and $\hat{e}''_j$ can only differ on a phase factor, i.e.,

$$\hat{e}'_j = \exp(i\varphi)\hat{e}''_j. \tag{3.21}$$

Replacing equalities 3.19 and 3.20 in equation 3.21, one obtains

$$e^*_j(\beta) = \exp(i\varphi)e_j(\beta^*) \tag{3.22}$$

and multiplying both members of (3.22) by $\exp(-i\varphi/2)$ results in

$$\left[\exp\left(i\frac{\varphi}{2}\right)e_j(\beta)\right]^* = \exp\left(i\frac{\varphi}{2}\right)e_j(\beta^*) \tag{3.23}$$

Equation 3.23 shows a relation between the components of the vector $[\exp(i\varphi/2)\,\hat{e}_j]$. Then, at least in the nondegenerated case, another condition can be imposed to the normalization of the eigenvectors $\hat{e}_k$

$$e_k^*(\beta) = e_k(\beta^*). \tag{3.24}$$

Imposing this normalization condition to the eigenvectors, one may demonstrate that the PCs defined by (3.17) are real.

The EOFs are column vectors whose components are the complex variability 'amplitudes' associated with each w'_β coefficient. Substituting the components of the EOFs in the expansion 2.66 one obtains the internal variability patterns in the (λ, θ, p) coordinates. If in that expansion the following matrix of scale factors is used

$$\mathbf{C}'_m = \begin{pmatrix} \sqrt{gh_m} & 0 & 0 \\ 0 & \sqrt{gh_m} & 0 \\ 0 & 0 & h_m \end{pmatrix},$$

instead of $\mathbf{C}_m$, the geopotential will be given in geopotential meters (gpm).

Finally, it should be noted that the normalization condition 3.24 also guarantees that the (u, v, ϕ) components of the circulation patterns are real.

3.8.1 Barotropic component

Only the modes with considerable variability are retained in the CPCA performed on each vertical component. Hence, in the case of the barotropic component, the CPCA was performed on the Rossby modes with zonal wavenumber $s < 10$ and meridional index $l < 15$, also including the Kelvin zonal mode (*cf.* figure 3.6).

The first four patterns of internal variability of the barotropic circulation are shown in figures 3.23-3.25. Henceforth, the pattern of internal variability associated with the n^{th} PC will be briefly designated by EOFn-I, and the forced EOFs will be designed by EOFn-F.

For the interpretation of the circulation patterns we should have in mind that they were obtained based on monthly means, therefore representing intraseasonal and

interannual variability [Kushnir and Wallace, 1989, fig. 1]. In fact, the total transient energy associated with the Rossby barotropic modes, based on the monthly means, is $41.4\,\mathrm{kJm^{-2}}$, while the same kind of energy calculated from the winter means is $16.7\,\mathrm{kJm^{-2}}$.

The EOF1-I (fig.3.23) explains 13% of the internal variability of the global barotropic circulation and clearly reproduces the Pacific/North America (PNA) teleconnection pattern [Wallace and Gutzler, 1981]. Performing the CPCA on the winter means, we obtained a PNA pattern similar to the one in figure 3.23, explaining in this case, 17% of the interannual variance.

The EOF2-I and EOF3-I (fig. 3.24) explain, respectively, 6.9% and 6.4% of the internal variance of the barotropic circulation and present several characteristics in common. In the Southern Hemisphere, they have similar structures, but of opposite sign. In the Northern Hemisphere, the patterns present similar wave structures, approximately in quadrature, with the exception of the anticyclonic circulation centered over the Labrador Peninsula. The main difference between the two patterns is due, in the case of the EOF2-I, to the presence of a circumpolar current over which it is superimposed the wave structure mentioned above.

The variability patterns that present similar but out of phase structures explaining almost equal amounts of variability , as it is the case of EOF2-I and EOF3-I, can be interpreted as a basis of a continuous set of variability patterns [Kushnir and Wallace, 1989]. This interpretation is consistent with the patterns obtained for the second and third PCs of the winter means, which represent, respectively, 10% and 8% of the interannual variability. In fact, the dominating characteristics of the variability represented by the second and third EOFs based on the monthly means (fig. 3.24) are reproduced in the second and third EOFs based on the winter means (fig. 3.26). The most apparent difference between the two pairs of EOFs is that, in the case of monthly means both EOFs explain variability in the Southern and Northern Hemisphere, while, in the case of the winter means, the second EOF explains more variability in the Southern Hemisphere, and the third EOF explains more variability in the Northern Hemisphere.

The EOF4-I (fig. 3.25) explains 5% of the internal variance of the monthly means and reveals a pattern associated the North Atlantic Oscillation (NAO) [Wallace and Gutzler, 1981; Kushnir and Wallace, 1989]. Unlikely to figure 4 of Wallace and Gutzler [1981], the EOF4-I shows circulation anomalies over the southwest of the British Isles

and opposite phase anomalies over the central North Pacific. However, the pattern associated with the NAO, obtained by Kushnir and Wallace [1989, fig. 12b], also shows a variability center of small amplitude over the Pacific with opposite phase to that of the circulation anomalies over the Atlantic.

In the case of the EOF4-I, the relatively high amplitude circulation anomalies over the central North Pacific must be related to the fact that the variability simulated by the MU AGCM over the Atlantic is much smaller than the observed, while the variability over the Pacific seems to be fairly well simulated (*cf.* figs. 3.7 and 3.8).

As for the PNA (EOF1-I), when the CPCA was performed on the winter means we also obtained a pattern associated with the NAO similar to that of EOF4-I. However, in this case, the NAO type pattern is associated with the fifth PC and explains 5.6% of the interannual variability.

Concluding this section we must emphasize that both the PNA and NAO type patterns appear as internal modes of the interannual variability of the global barotropic circulation.

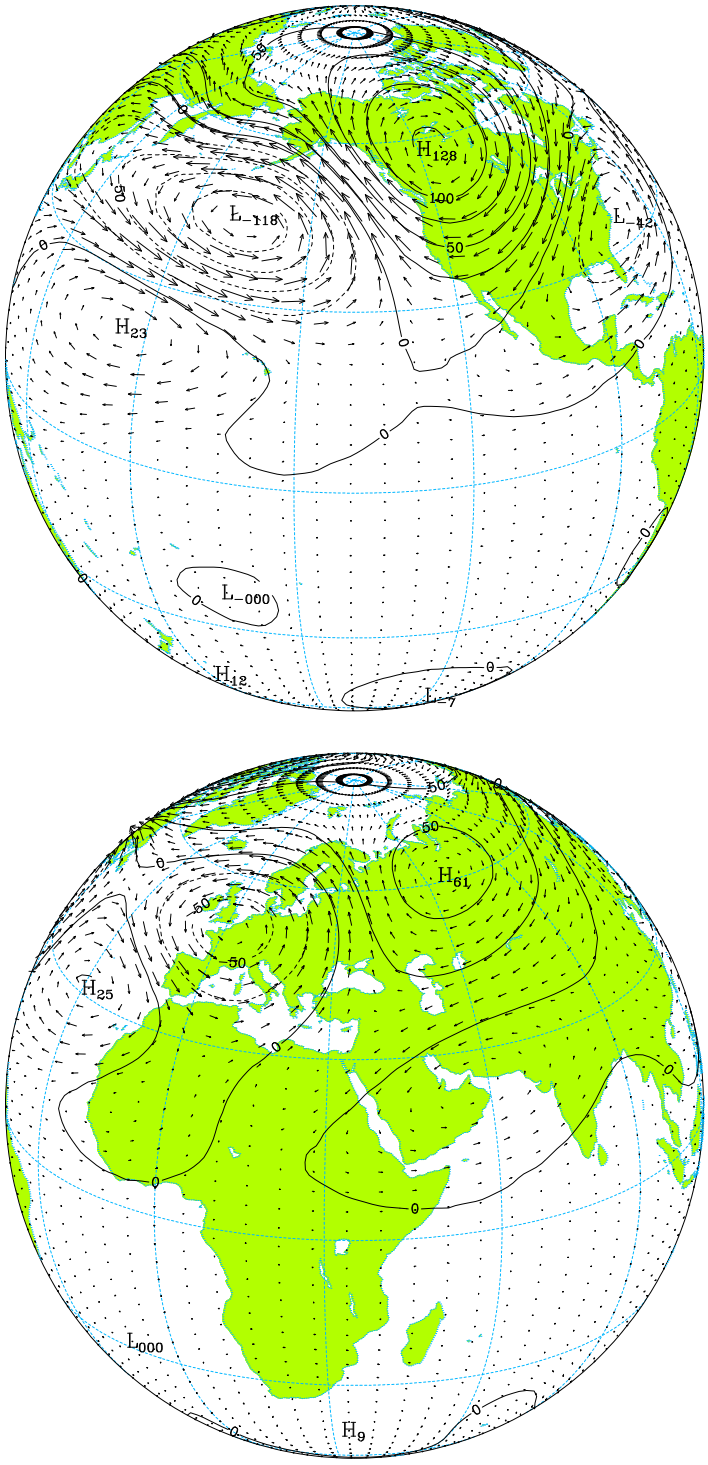

Figure 3.23: Pattern associated with the first PC of internal variability of the barotropic circulation. The units of the geopotential and wind velocity are gpm and $\mathrm{m\,s^{-1}}$, respectively. The maximum velocity is $v_{max.} = 10.2\,\mathrm{m\,s^{-1}}$.

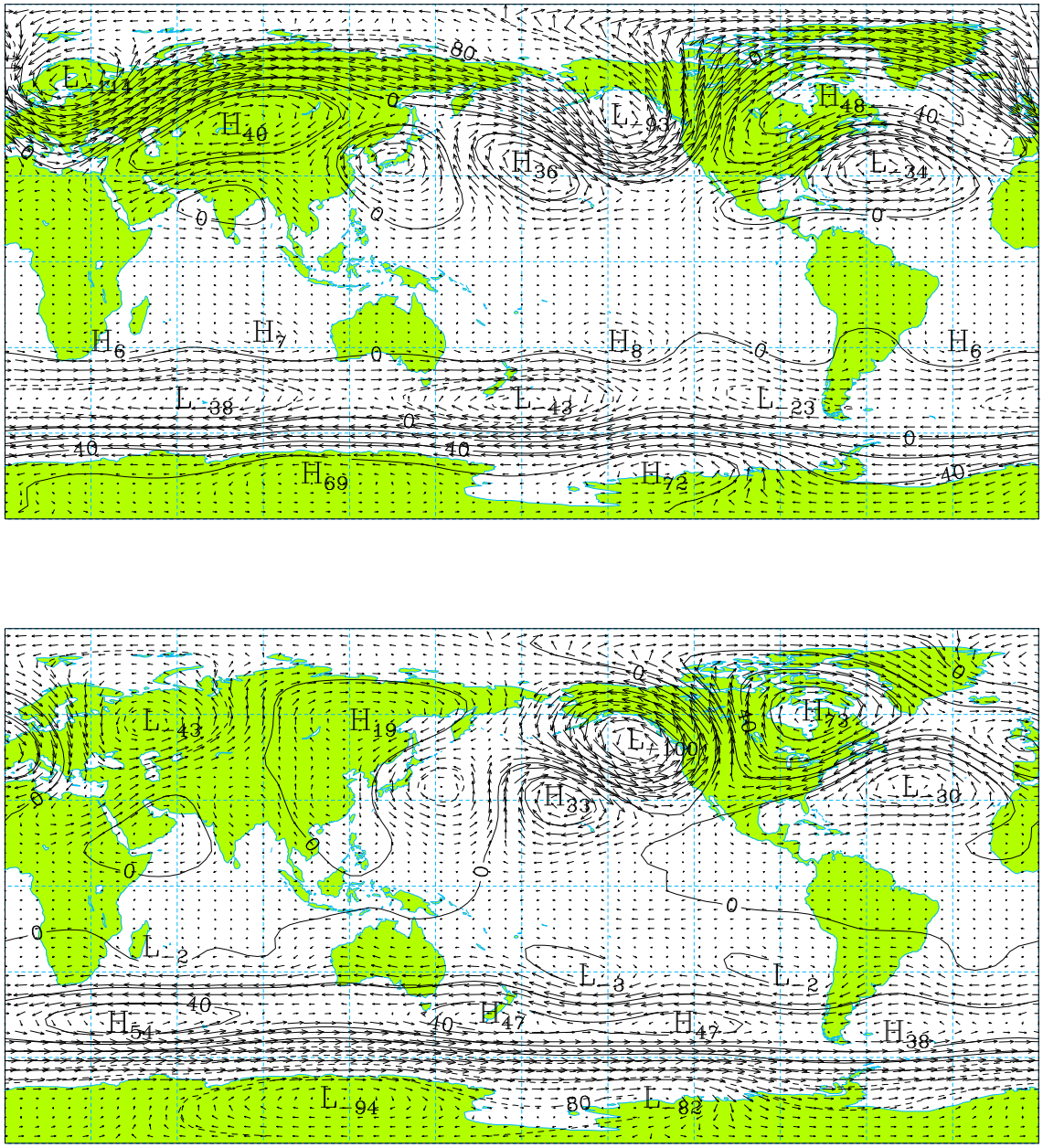

Figure 3.24: As in figure (3.23) but for the second PC (*top*, $v_{max.} = 6.7\,\mathrm{m\,s^{-1}}$) and the third PC (*bottom*, $v_{max.} = 7.6\,\mathrm{m\,s^{-1}}$).

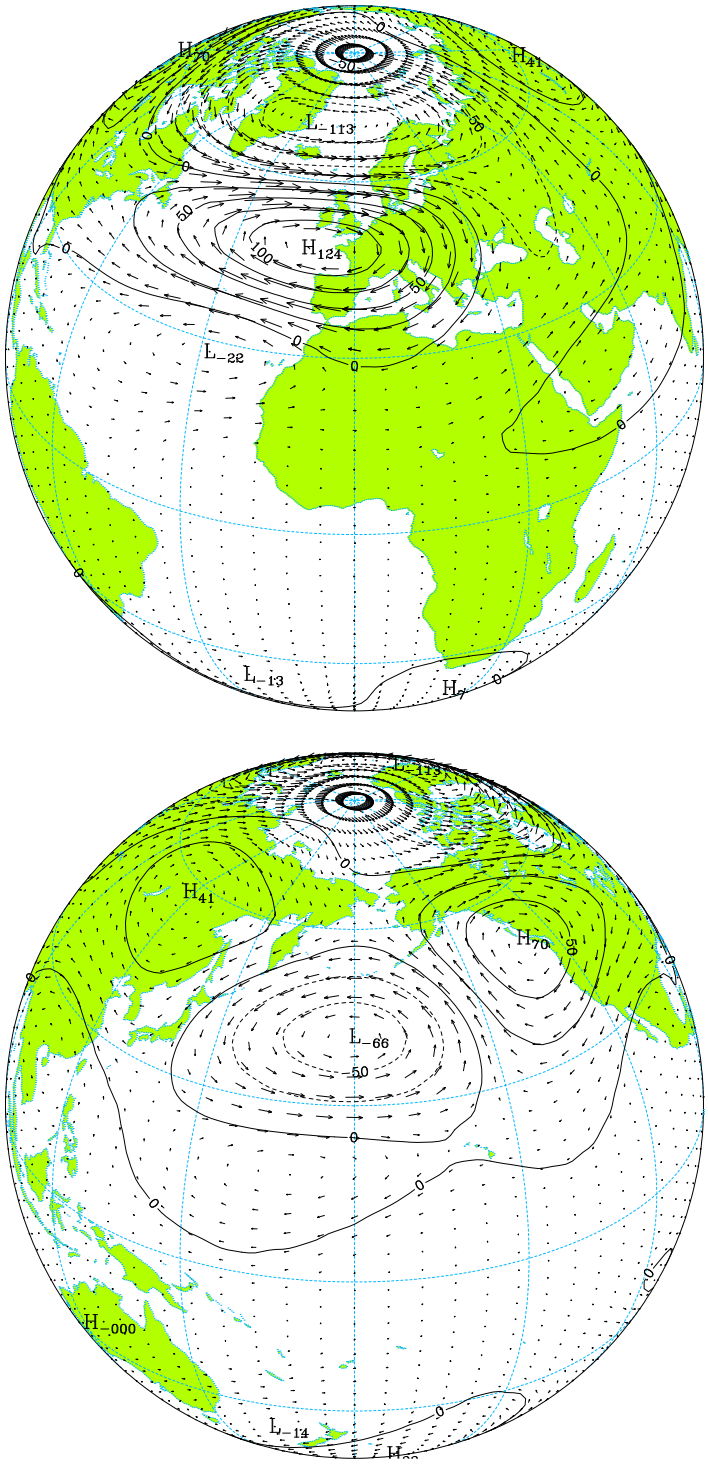

Figure 3.25: As in figure (3.23) but for the fourth PC ($v_{max.} = 12.3\,\mathrm{m\,s^{-1}}$).

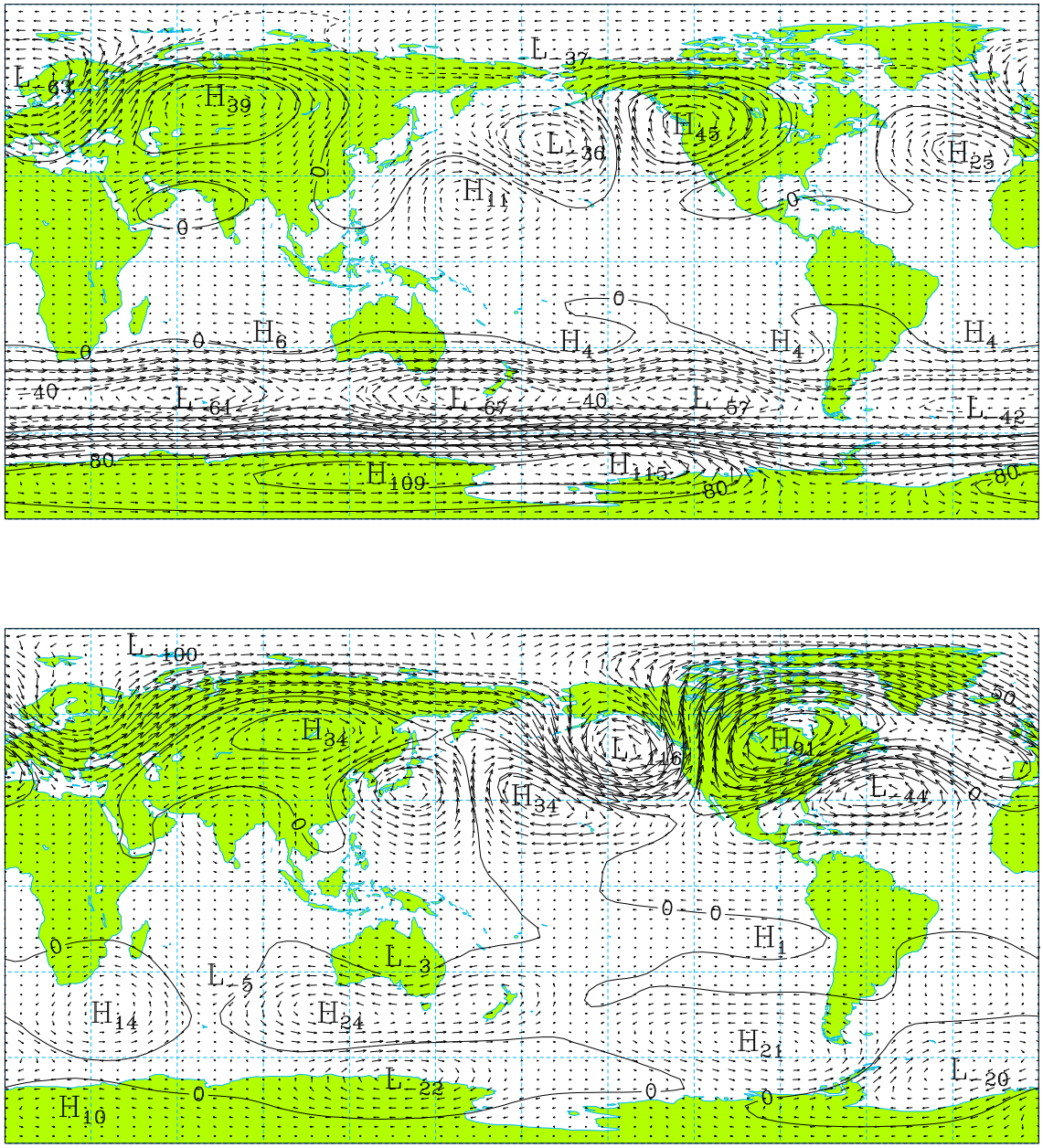

Figure 3.26: Patterns associated with the second (*top*, $v_{max.} = 7.6\,\mathrm{m\,s^{-1}}$) and third (*bottom*, $v_{max.} = 8.2\,\mathrm{m\,s^{-1}}$) PCs of the winter mean barotropic circulation.

3.8.2 Fourth baroclinic component

In the CPCA performed on the 4^{th} baroclinic component, we have retained the Rossby modes with zonal wavenumbers $s \leq 7$ and meridional indices $l \leq 17$, and the Kelvin modes with zonal wavenumbers $s \leq 5$ (*cf.* fig. 3.11).

The first PC of the fourth baroclinic component explains 9.2% of its internal variability, and the associated pattern (fig. 3.27) presents a structure very similar to that of EOF1-I of the barotropic component (fig. 3.23), i.e., to the structure of the PNA. On the other hand, the patterns associated with PCs 2 to 7, that together explain 28% of the internal variance, do not present simple structures that remind familiar patterns in the literature.

The barotropic vertical structure function, G_0, presents a small variation between surface ($p_s = 1010.5$ hPa) and the 200-hPa level [$G_0(p_s) = 0.60$, $G_0(200) = 0.69$, *cf.* fig. 3.1]. Because G_0 is approximately constant, in the normal mode scheme the barotropic component of the circulation represents approximately an arithmetic vertical mean of the tropospheric circulation. On the other hand, the northern winter low frequency variabilitiy of the extratropical circulation, in both Hemispheres, presents vertical structures equivalent to the barotropic structure [Wallace and Gutzler, 1981; Karoly, 1989], i.e., the anomalies are centered on the same vertical but their amplitudes increase with height. So we may expect that part of such a variability should be projected onto other vertical structures besides G_0.

Perlwitz and Graf [1995] performed a canonical correlation analysis (CCA) between the stratospheric and tropospheric circulation of the Northern Hemisphere in winter. In their analysis they identified two important modes of variability. The tropospheric circulation pattern associated with the first pair of canonical variables ($r = 0.70$) was identified with NAO, presenting baroclinic characteristics. The tropospheric circulation pattern associated to the second pair of canonical variables ($r = 0.69$) was identified with the PNA, presenting an equivalent barotropic structure.

The same modes of stratospheric and tropospheric covariance was identified by a singular value decomposition of stratospheric and tropospheric geopotential height fields [Graf *et al.*, 1997]. The two modes together explain more than 80% of total covariance, and were identified in observation as well in climatological simulations performed with the T21 and T42 versions of the ECHAM3 GCM of the Max-Planck Institut für Meteorologie.

The 4$^{\text{th}}$ baroclinic vertical structure function, G_4, presents a node at the 540 hPa level, that separates the negative values in the upper troposphere from the positive ones in the lower troposphere (*cf.* fig. 3.1). Hence we may consider that the 4$^{\text{th}}$ baroclinic component of the atmospheric circulation (see eq. 2.58) corresponds to an weighted difference between the circulations in the upper and lower troposphere.

In this work, we investigate whether the vertical structures of the 3-dimensional patterns of the PNA and NAO have only an equivalent barotropic structure or, on the contrary, they have baroclinic characteristics, i.e., whether the anomalies are centered on axes tilted to the vertical and the horizontal wind turns with height.

The used method consisted in performing a combined CPCA on the barotropic and 4$^{\text{th}}$ baroclinic components. The CPCA is then performed on the vectors

$$\begin{aligned}&\Big[h_0 w'_1(i,j), h_0 w'_2(i,j), \ldots, h_0 w'_p(i,j),\\ &\ h_4 w'_{p+1}(i,j), h_4 w'_{p+2}(i,j), \ldots, h_4 w'_{p+q}(i,j)\Big]^T ,\end{aligned} \tag{3.25}$$

where p and q denote the number of barotropic and 4$^{\text{th}}$ baroclinic modes retained in the analysis, respectively. Each $w'_\beta(i,j)$ coefficient was previously multiplied by the respective equivalent height to reduce the variances (total energies) of the barotropic and baroclinic modes to the same units.

If the NAO and PNA patterns appear in both vertical components, we can compare the location as well as the wind direction of the corresponding centers of variability. From this comparison we can gain some insight into the vertical structures of those patterns. On the other and, the total energy associated with each variability pattern can be partitioned into the contributions due to the barotropic and 4$^{\text{th}}$ baroclinic components. The computations for each EOF proceeds as follows. As the EOFs have unitary norm, the sum of squares of the first p components of an EOF gives the energy fraction associated with the barotropic component, and the sum of squares of the remaining q components of the same EOF gives the energy fraction associated with the 4$^{\text{th}}$ baroclinic component.

The described method presents some analogies to that used by Schubert [1986] in a study of the vertical structures of the variability patterns identified by a principal component analysis of the 500-hPa stream function. Schubert performed a PCA on the differences between the 200 hPa and 700 hPa stream functions, to obtain the vertical

structures of the variability patterns. However, it should be noted that Schubert calculated separately the EOFs of 500-hPa stream function from that of 200-hPa and 700-hPa differences.

Figures 3.28 and 3.29 show the barotropic and 4$^{\text{th}}$ baroclinic components of a PNA type mode of variability. These patterns are associated with the first PC of the vector 3.25, explaining 11.3% of the joint variance of those two vertical components. The barotropic component represents 76.6% of the total energy associated with this PNA mode, and the remaining 23.4% are associated with the 4$^{\text{th}}$ baroclinic component. The depression over the United States coast presents a slight axis tilting to northwest, and the same can be said about the anticyclonic circulation over the Tropical Pacific, that has a not well defined center on the fourth component. However, in both cases the axes tiltings are not accompanied by an apparent rotation of the wind with height. The anticyclonic circulation over the northwest Canada as well as the depression south of the Aleutians present also equivalent barotropic structures.

One should note that for the comparison of the amplitudes of the anomalies in both vertical components, it should be taken into account the ratio between the respective vertical structure functions: $G_4(850)/G_0(850) = 0.95$ and $G_4(250)/G_0(250) = -1.42$.

Figures 3.30 and 3.31 show the barotropic and 4$^{\text{th}}$ baroclinic components of a NAO type mode of variability. These patterns appear associated with the fourth PC, and explain 4.9% of the joint variance. The barotropic component represents 78.6% of the total energy associated with this NAO mode, and the remaining 21.4% are associated with the 4$^{\text{th}}$ baroclinic component. The anticyclonic circulation over the Euro-Atlantic region and the depression north of Iceland present baroclinic characteristics with the axes tilted respectively to northwest and southwest. The axes tiltings are, in this case, accompanied by a rotation of the wind with height over the north of the Atlantic and Europe. The depression over North Pacific presents an equivalent barotropic structure.

Finally, it should be noted that part of the variability of the jet stream over the North of Africa and Middle East projects itself onto the fourth baroclinic component.

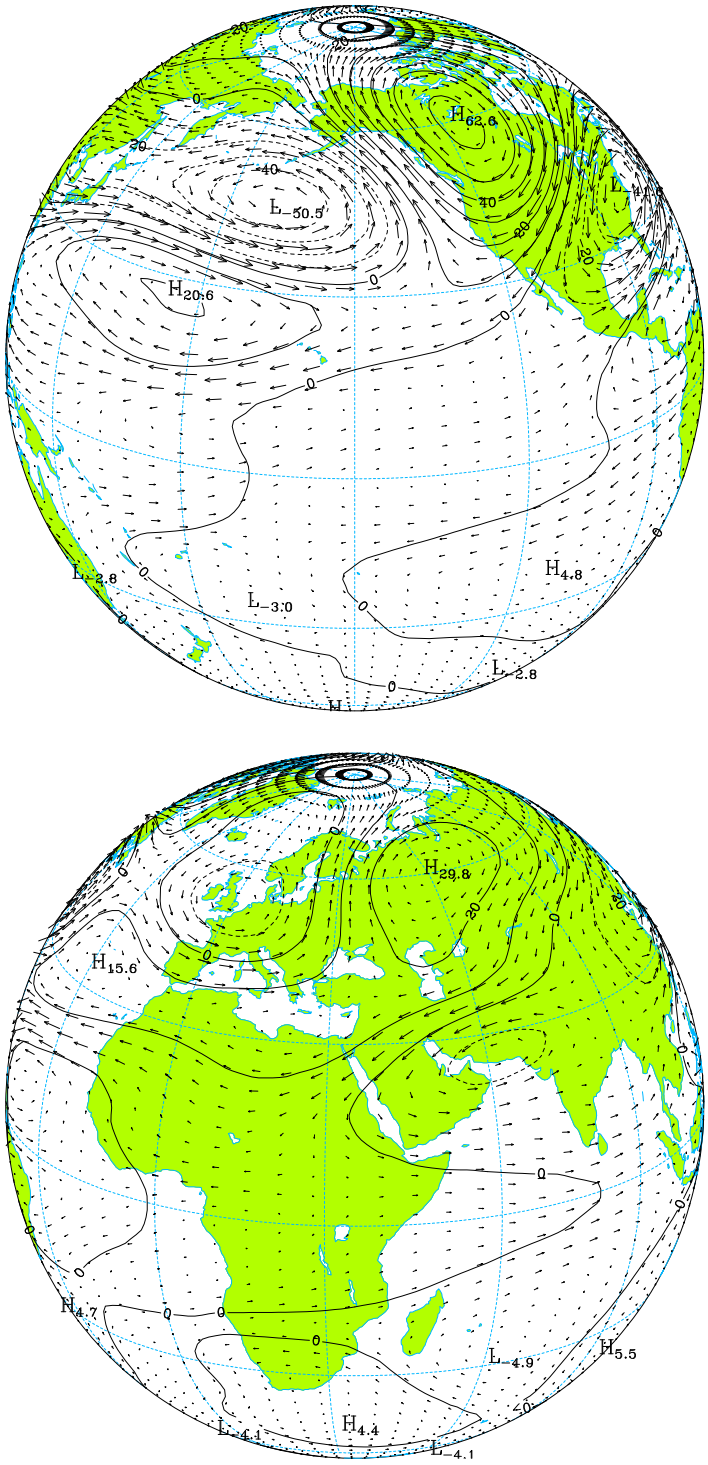

Figure 3.27: Pattern associated with the first PC of the internal variability of the 4$^{\text{th}}$ baroclinic component ($v_{max.} = 5.8\,\mathrm{m\,s^{-1}}$).

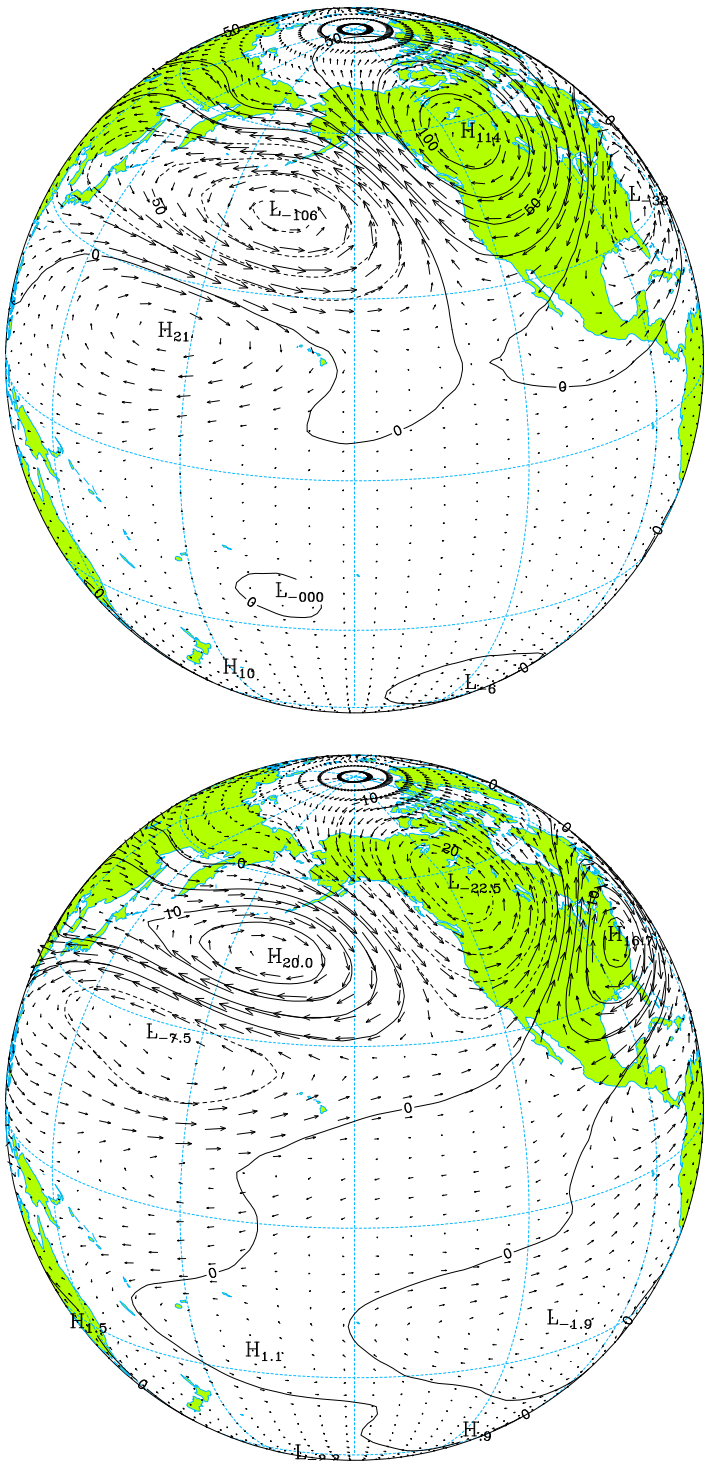

Figure 3.28: Barotropic (*top*, $v_{max.} = 9.1\,\mathrm{m\,s^{-1}}$) and 4$^{\mathrm{th}}$ baroclinic (*bottom*, $v_{max.} = 2.3\,\mathrm{m\,s^{-1}}$) components of the PNA.

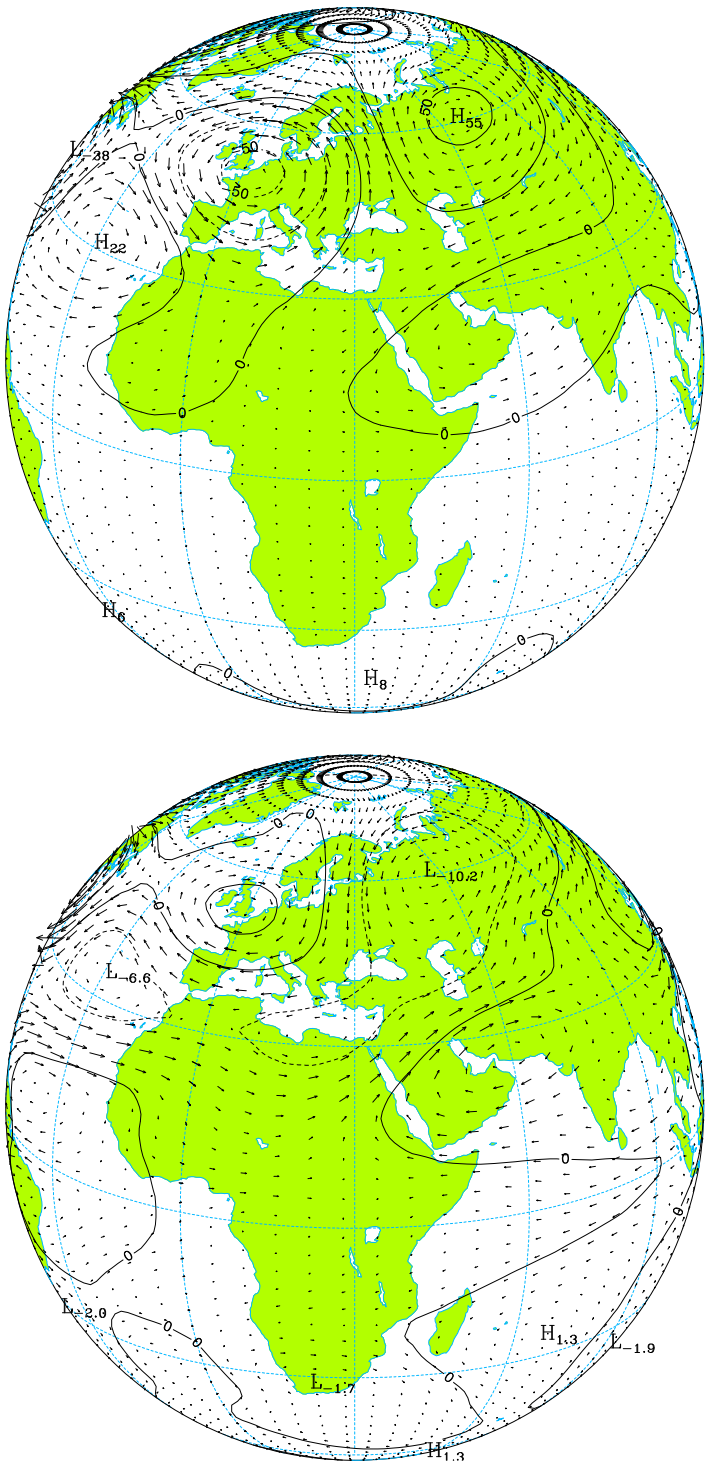

Figure 3.29: As in figure 3.28 but for the other hemisphere.

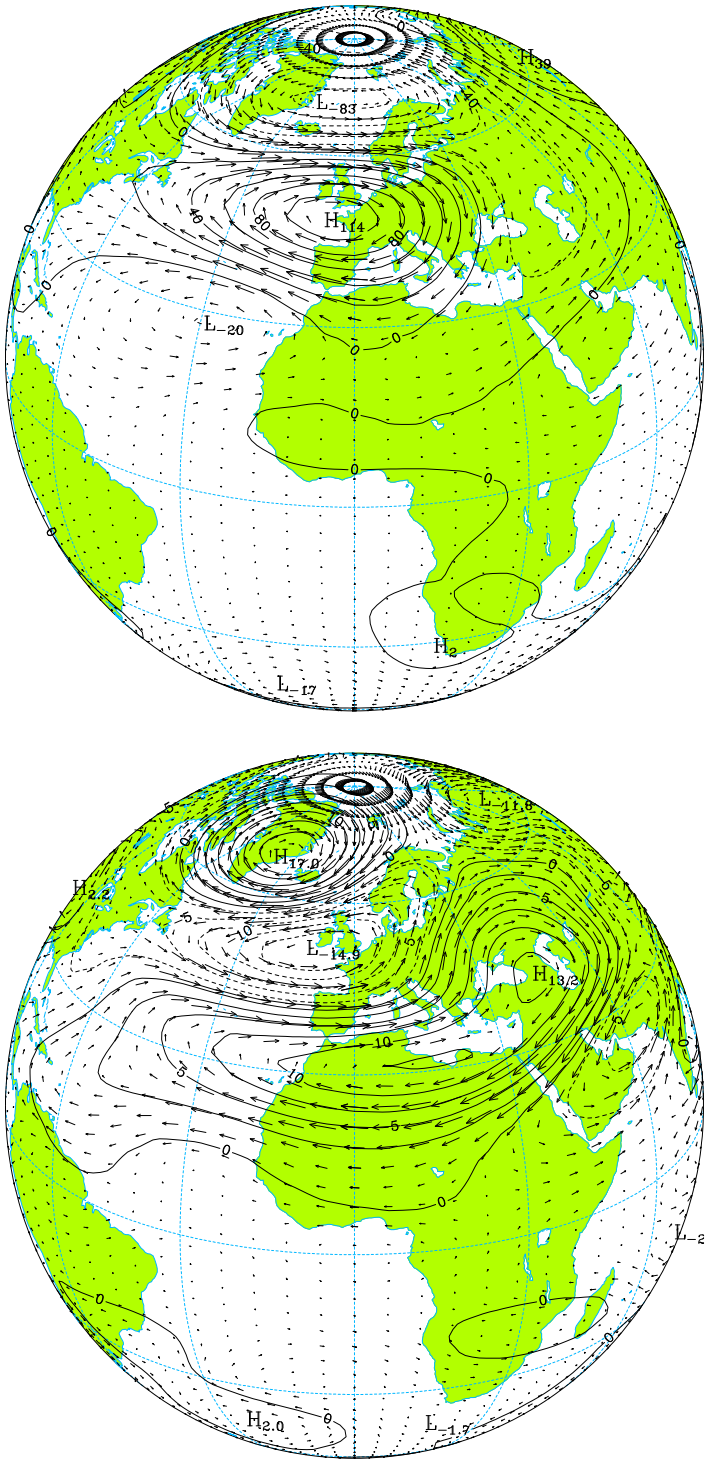

Figure 3.30: Barotropic (*top*, $v_{max.} = 10.2\,\mathrm{m\,s^{-1}}$) and 4$^{\mathrm{th}}$ baroclinic (*bottom*, $v_{max.} = 1.9\,\mathrm{m\,s^{-1}}$) components of the NAO.

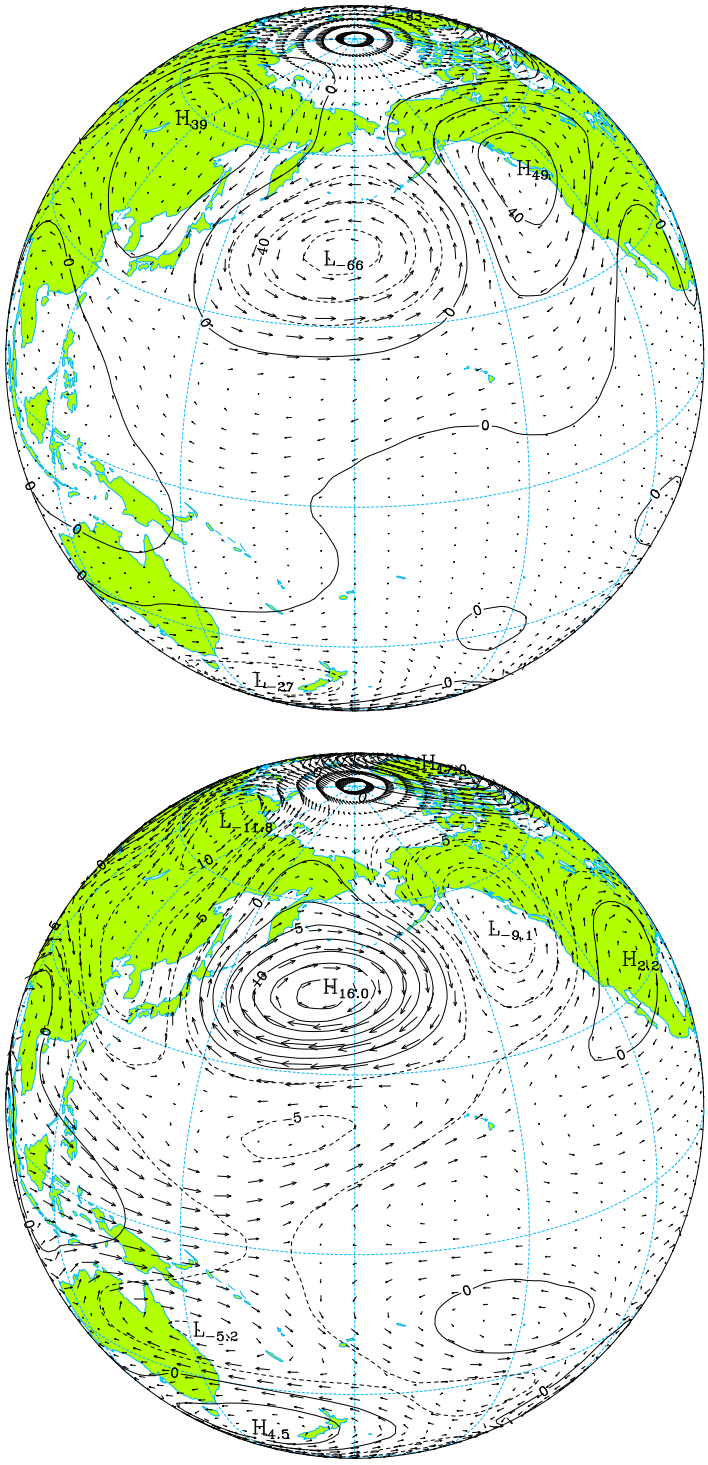

Figure 3.31: As in figure 3.30 but for the other hemisphere.

3.9 Patterns of forced variability

The atmospheric circulation patterns associated with anomalies of the SST fields were obtained through a CPCA performed on the ensemble means, $[w_\beta]_j$. An unbiased estimate of the variance-covariance matrix is given by

$$S^{SST}_{\beta\beta'} = \frac{\hat{\sigma}_{SST}(\beta)\hat{\sigma}_{SST}(\beta')}{\sigma_{EM}(\beta)\sigma_{EM}(\beta')} \frac{\sum_{j=1}^{N}[w_\beta]_j[w_{\beta'}]^*_j}{N-1} \tag{3.26}$$

where σ_{EM} is the standard deviation of the ensemble means calculated as

$$\sigma_{EM}(\beta) = \sqrt{\frac{1}{N-1}\sum_{j=1}^{N}[w_\beta]_j[w_\beta]^*_j} \tag{3.27}$$

Equation 3.26 is formally identical to equation 3 of Harzallah and Sadourny [1995] but with the standard deviation $\sigma_{SST}(\beta)$ associated with the oceanic forcing defined by the expression

$$\sigma_{SST}(\beta) = \sqrt{\sigma^2_{SST}\left(\Re(w_\beta)\right) + \sigma^2_{SST}\left(\Im(w_\beta)\right)}, \tag{3.28}$$

in which the variances $\sigma^2_{SST}\left(\Re(w_\beta)\right)$ and $\sigma^2_{SST}\left(\Im(w_\beta)\right)$ were estimated by (2.5).

3.9.1 Barotropic component

In the CPCA performed on the forced barotropic component, we retained the Rossby modes with zonal wavenumbers $s \leq 5$ and meridional indices $l \leq 10$ and the zonal Kelvin mode (*cf.* fig. 3.15). The pattern associated with the first PC of the forced barotropic circulation is shown in figure 3.32. This pattern explains 46% of the forced variance of the barotropic component. It is very similar to the schematic illustrations of the global pattern of middle and upper tropospheric anomalies, during the mature stage of an ENSO event in NH winter (DJF), as were been proposed by Horel and Wallace [1981] e Karoly [1989]. In fact the correlation coefficient between the PC1 and the *cold tongue index* (defined as the averaged SST anomalies over the region 6^0N $-$ 6^0S, $90^0 - 180^0$W) presents a high value of 0.92. The correlation coefficient was calculated for a small period (1979-88), that includes the strong El Niño event in the winter of 1982/83. However, as it can be seen in figure 3.33 the high value of the correlation does not result from one or two pairs of extremely high anomalies.

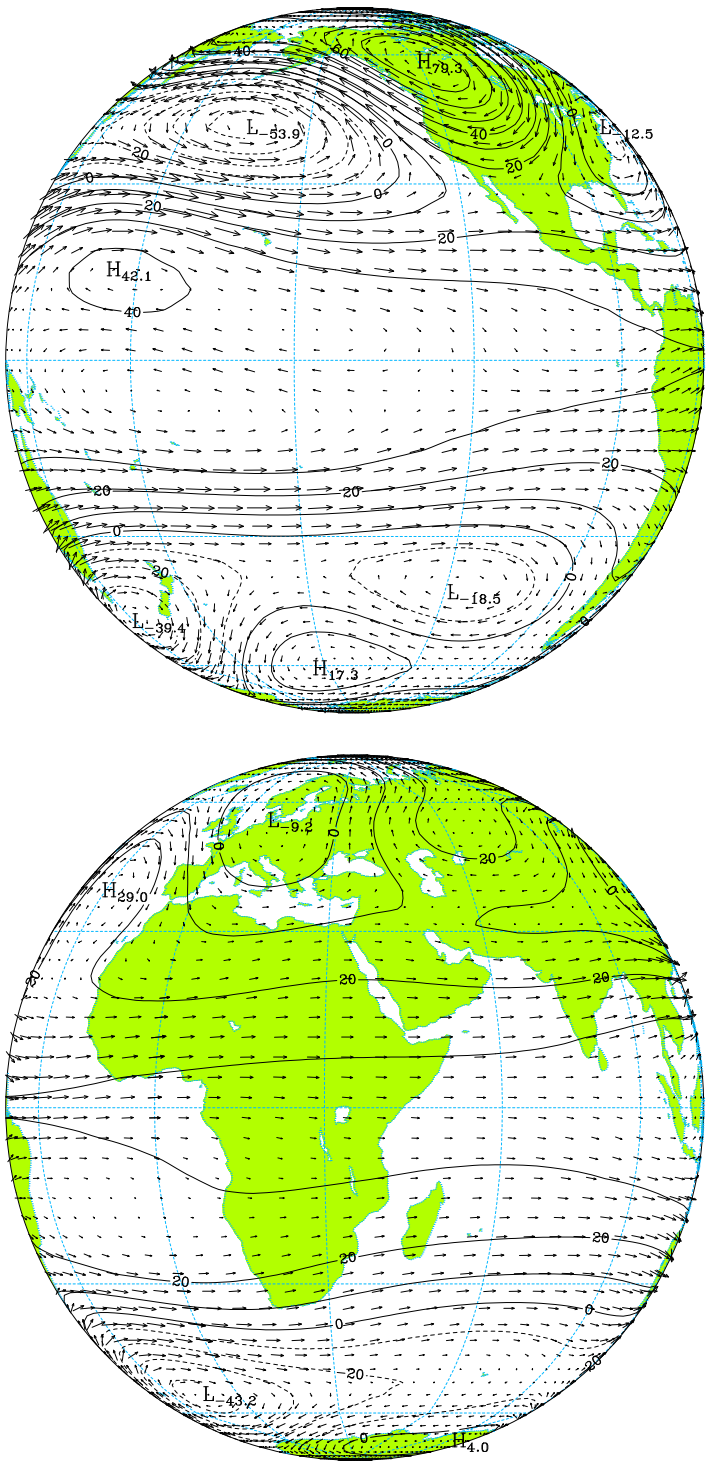

Figure 3.32: Pattern associated with the first PC of the forced barotropic circulation ($v_{max.} = 6.6\,\mathrm{m\,s^{-1}}$).

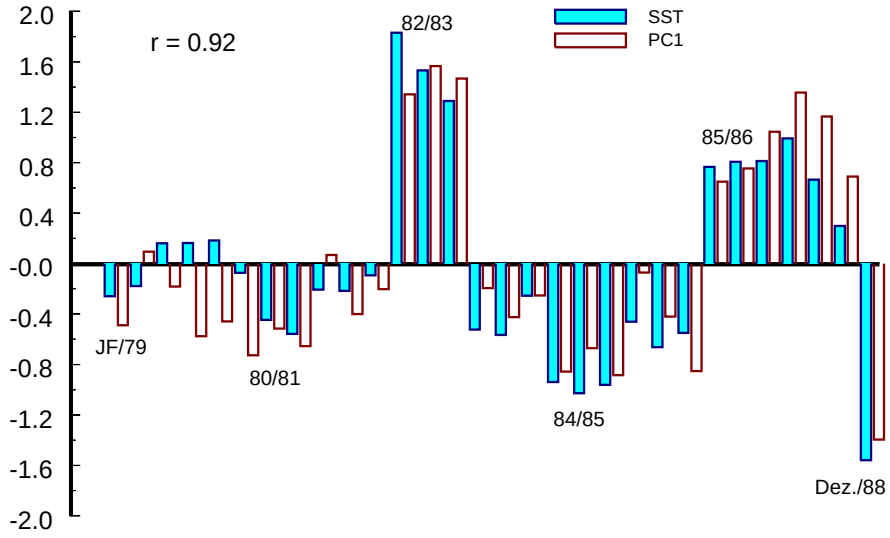

Figure 3.33: Time series of the *cold tongue index* (K) and of PC1 of the forced barotropic circulation. The PC was multiplied by 2.5.

It is also interesting to refer the similarity between the pattern of EOF1-F and the pattern obtained by linearly regressing monthly time series of vertical averaged tropospheric temperatures (surface - 300 hPa) upon a normalized time series of the *cold tongue index*, in the period of 1979-92 [Wallace, 1996, cap. 2, fig. 23]. The observed pattern of anomalies of the vertical averaged tropospheric temperatures and the simulated pattern for the field $(u, v, \phi)^T$ (fig. 3.32) show, however, some differences. Over the tropical Pacific, the simulated pattern presents a pair of anticlyclones that is shifted westward about 30º relatively to the observed pair. Regarding the extratropical circulation, although the regression patterns present positive anomalies over Canada and negative anomalies over the Pacific southwest of the Aleutians and over the south of the United States, they do not reproduce a PNA teleconnection pattern as well defined as the simulated pattern. These differences can be due, at least partly, to the fact that the regression pattern [Wallace, 1996] was calculated including monthly means for the whole seasonal cycle, whereas the simulated pattern represents only the forced variability of the winter circulation, when the influence of the tropical circulation over the extratropical is more intense, due to the strongest meridional gradients of potential-vorticity.

The second PC explains only 11.4% of the forced variance of the barotropic circulation, and the respective pattern is not easily interpretable.

3.9.2 Fourth baroclinic component

The patterns of forced variability of the 4$^{\text{th}}$ baroclinic component were obtained performing the CPCA on the Kelvin and Rossby modes with $s \leq 4$ e $l \leq 5$ (*cf.* fig. 3.19).

Figure 3.34 shows the patterns associated with PC1 and PC2, which explain, respectively, 42% and 22% of the forced variance of the 4$^{\text{th}}$ baroclinic component.

The EOF1-F presents many similarities with a composite of the wind at 200 hPa, based on observations for the months of October to December of years 1970, 1973 and 1975, characterized by a high index phase of the Southern Oscillation [Ropelewski and Halpert, 1989, fig. 17c]. In fact, as for the PC1 of the forced barotropic circulation, the correlation coefficient between the PC1 of the 4$^{\text{th}}$ baroclinic component of the forced circulation and the *cold tongue index* presents a high value of 0.95.

The patterns of EOF1-F and EOF2-F are clearly associated with the anomalies of the Walker circulation [Webster and Chang, 1988], and this association can be seen in the maps of figure 3.35, which show the fields of divergence for the EOF1-F the EOF2-F. The divergence field of EOF1-I shows a weakening of the convergence over the regions of Indonesia and the north of South America, accompanied by an weakening of the divergence over the central and eastern Pacific, the Gulf of Guinea, and over the west region of the Indian Ocean. These are characteristic anomalies during El Niño events. The map associated with the EOF2-F shows an increase of the convergence over the western Pacific and the east region of the Indonesian archipelago and a small increase of convergence over the southeast Africa, accompanied by an increase of divergence over eastern Indian ocean.

Although, in this chapter, special attention has been given to the barotropic and fourth baroclinic components, we may see in figure 3.14 that the third baroclinic component represents also an important component of the forced circulation. A principal component analysis performed on the third baroclinic component revealed patterns of forced circulation similar to the ones presented in figure 3.34. The same analysis, performed jointly on the third and fourth baroclinic components, revealed also covariability patterns similar to the ones represented in figure 3.34. These results indicate that the anomalies of the divergence field, associated with the EOFs of the third baroclinic component, reinforce the divergence patterns represented in figure 3.35.

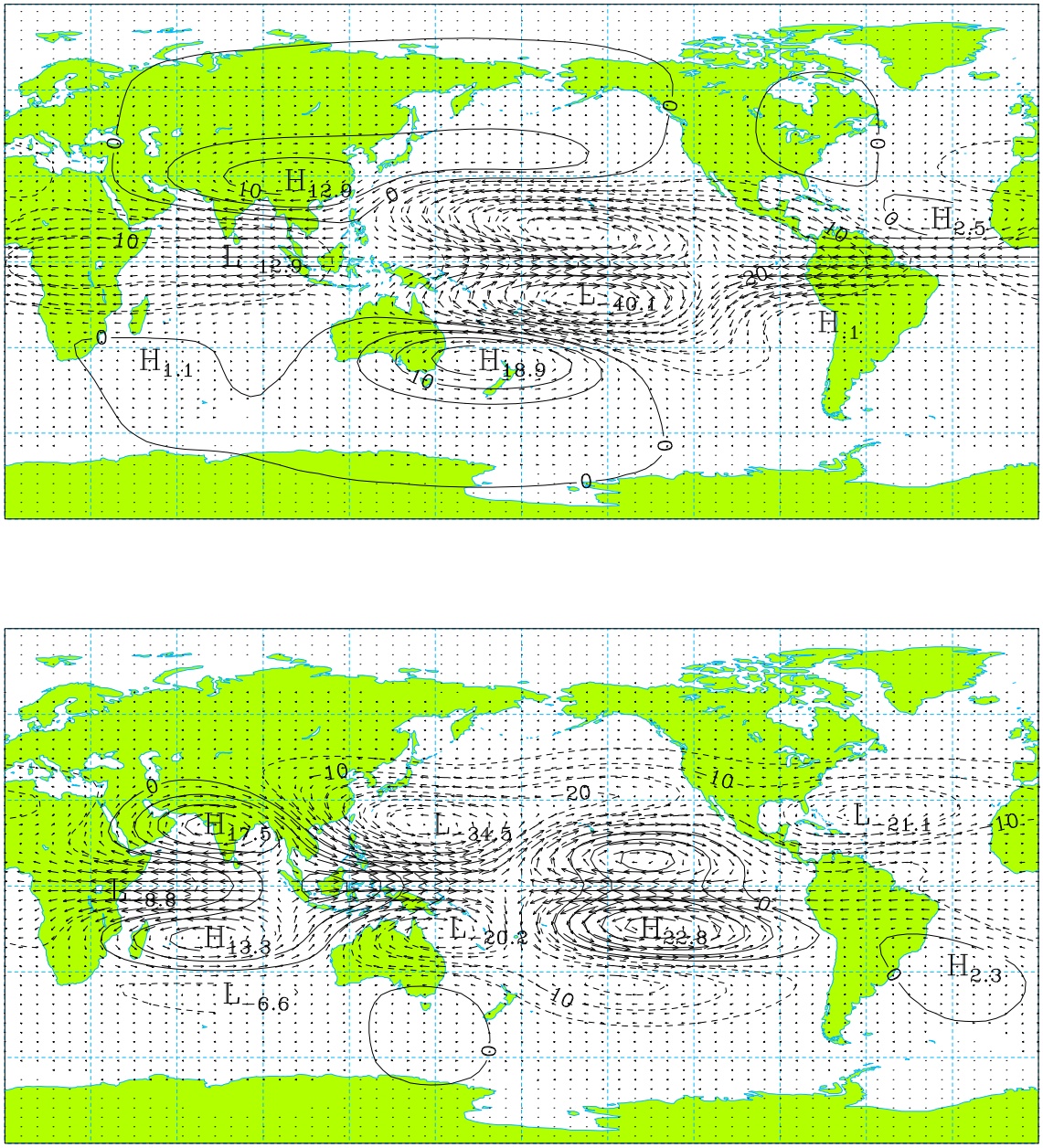

Figure 3.34: Patterns associated with the first (*top*, $v_{max.} = 8.1\,\mathrm{m\,s^{-1}}$) and second (*bottom*, $v_{max.} = 8.9\,\mathrm{m\,s^{-1}}$) PCs of the 4$^{\mathrm{th}}$ baroclinic component of the forced circulation.

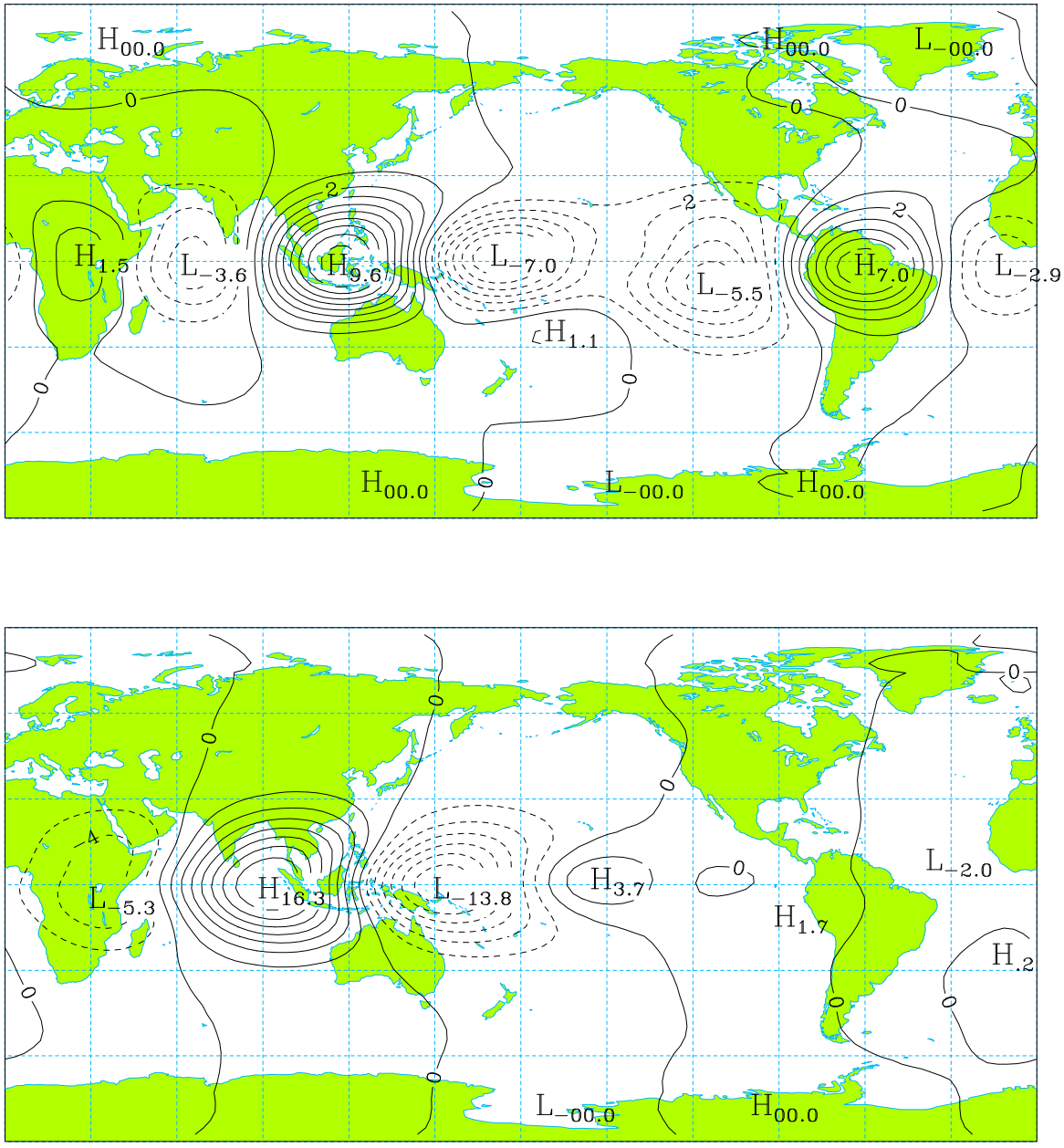

Figure 3.35: Divergence fields ($10^{-7}s^{-1}$) associated with the EOF1-F (*top*) and EOF2-F (*bottom*) of the 4$^{\text{th}}$ baroclinic component of the forced circulation.

3.9.3 Correlation maps of the forced PCs with the global SSTs

To determine the global SST patterns associated with the patterns of forced circulation, we calculated the correlation of each forced PC with the time series of SST anomalies at each grid point of the forcing field.

Figure 3.36 shows the correlation maps respecting to the PC1 of forced barotropic circulation and the PC2 of the 4^{th} baroclinic component of the forced circulation. The correlation map for the PC1 of the 4^{th} baroclinic component of forced circulation is practically identical to that of PC1 of the forced barotropic circulation. These maps show that the positive values of the PC1-F of the barotropic component and PC1-F of the 4^{th} baroclinic component are associated with a pattern of SST anomalies very similar to that of the SST anomalies during the mature stage of an El Niño event. The correlation map of the PC2-F of the 4^{th} baroclinic component shows that the positive values of this PC are associated with positive SST anomalies in the west and central Tropical Pacific, Tropical Atlantic and South Atlantic. This map also shows a reminiscent pattern (symmetric) of the El Niño anomalies in the eastern tropical Pacific.

While the correlation maps for the first PCs of the barotropic and 4^{th} baroclinic components of forced circulation reflect a robust structure, well documented in the bibliography (see, for example, the maps presented by Philander, S. G. [1990, cap. 1, fig. 1.19(c)], Harzallah and Sadourny [1995, fig. 11a] or Renshaw *et al.* [1998, fig. 6b,c]), one must be very cautious about the physical significance of the map respecting to the PC2 of 4^{th} baroclinic component, because the correlations were based only on 10 years long time series. However, it should be noted that the positive SST anomalies in the western Pacific are consistent with an increase of convective activity in that region, and consequently, with the increase of the circulation convergence, shown in the map of the divergence associated with the PC2 of the 4^{th} baroclinic component.

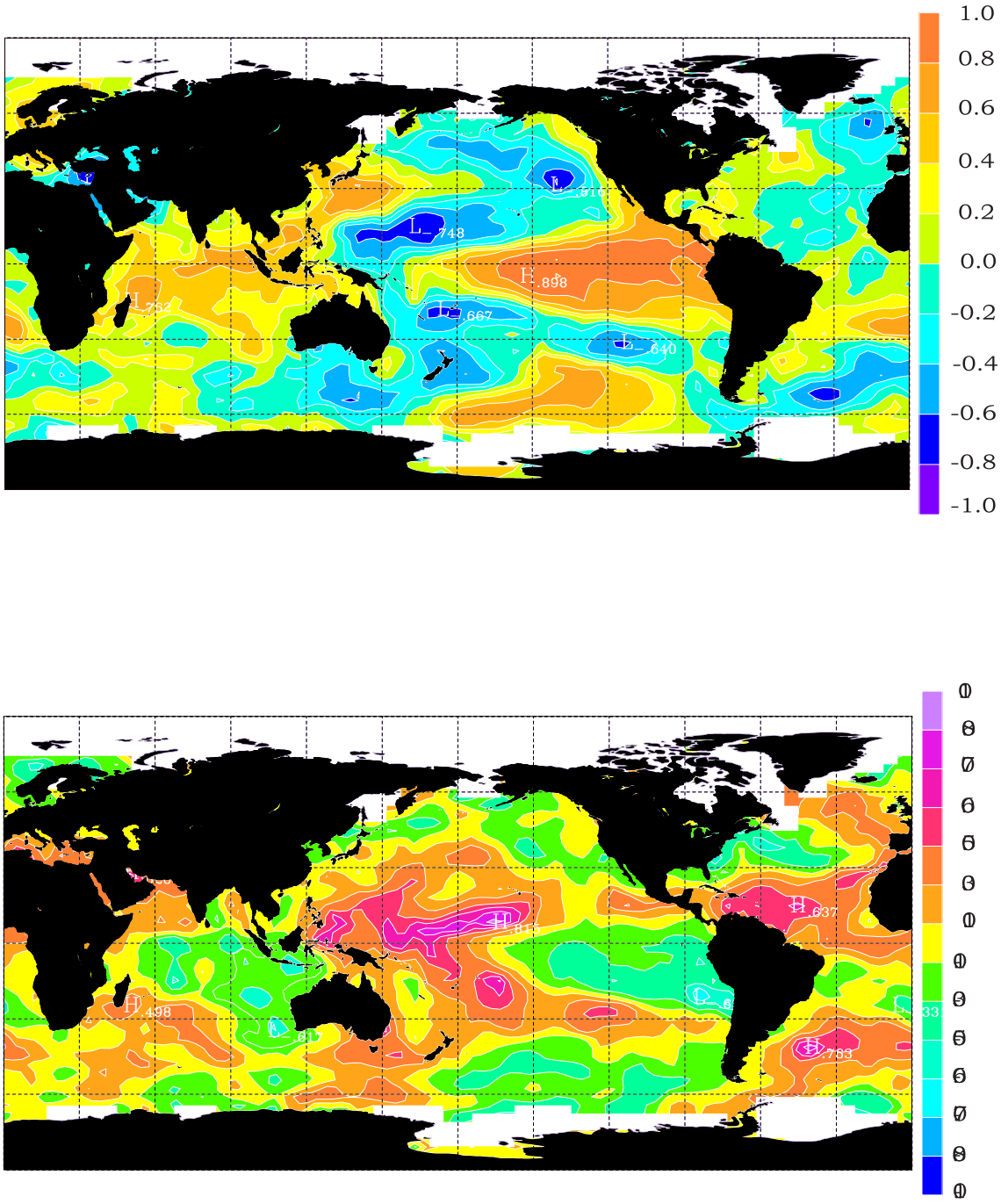

Figure 3.36: Correlation maps between the PC1 of the forced barotropic circulation (*top*), the PC2 of the 4th baroclinic component of the forced circulation (*bottom*) and the SST anomalies.

3.10 Projections of NCEP reanalysis onto simulated forced patterns

The patterns associated with the first PCs of the barotropic and 4^{th} baroclinic components of the forced circulation may be interpreted as responses of the simulated atmospheric circulation to SST anomalies associated with the ENSO cycle. We can test these patterns projecting onto them the observed atmosphere and then correlating the time series of projections with an observed El Niño index.

Figures 3.37 and 3.38 show the winter means values of the projections of NCEP reanalysis, for the period 1973-96, onto the EOF1-F of the forced barotropic circulation and EOF1-F of the 4^{th} baroclinic component of the forced circulation, respectively. It is also shown the time series of the Niño3.4 index, defined as the averaged SST anomalies over the region 5^0N $- 5^0$S, $120^0 - 170^0$W).

The values of the correlation coefficients of the Niño3.4 index with the time series of the projections onto EOF1-Fs of the barotropic and 4^{th} baroclinic components are 0.78 and 0.93, respectively. These high values of correlation shown that a large fraction of the observed atmospheric circulation variability projected onto the simulated forced patterns is linearly associated with the SST anomalies in the tropics. Hence the projected anomalies may also be interpreted as responses to oceanic forcing.

The smaller value of the correlation, in the case of the projections onto the EOF1-F of the simulated barotropic component, is due, at least in part, to the fact that the EOF1-I (the free PNA) is not orthogonal to the EOF1-F. As a consequence, the observed internal variability associated with the free PNA has a non null projection onto the EOF1-F, and vice versa, part of the forced variability associated with EOF1-F is projected onto EOF1-I. In fact, the time series of the projections of the NCEP reanalysis onto EOFs 1-I and 1-F of the simulated barotropic circulation have a correlation of 0.78. However, it should be noted that while the correlation of the projections onto the EOF1-F with the index Niño3.4 is 0.78, the correlation of the projections onto the EOF1-I with the same El Niño index is only 0.43.

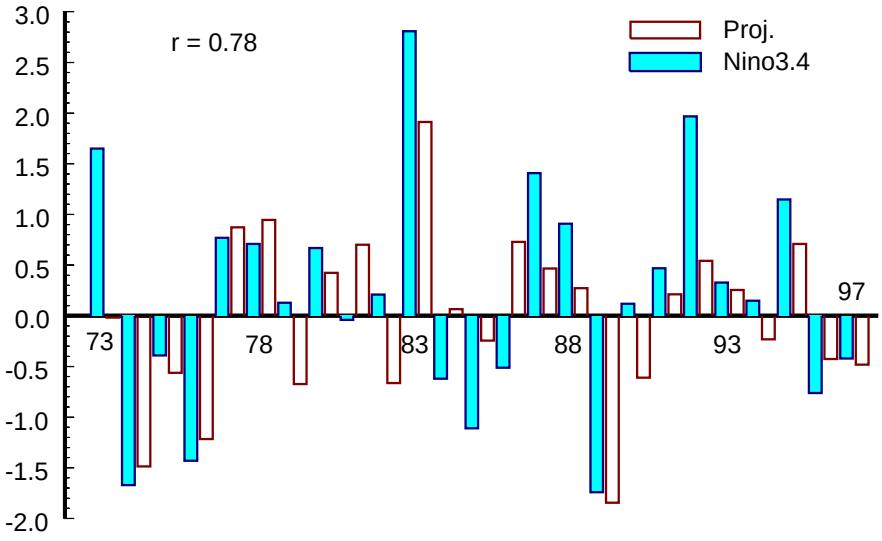

Figure 3.37: Time series of the index Niño3.4 (K) and the projections of the NCEP reanalysis onto the EOF1 of the simulated forced barotropic circulation. The projections were multiplied by 1.5.

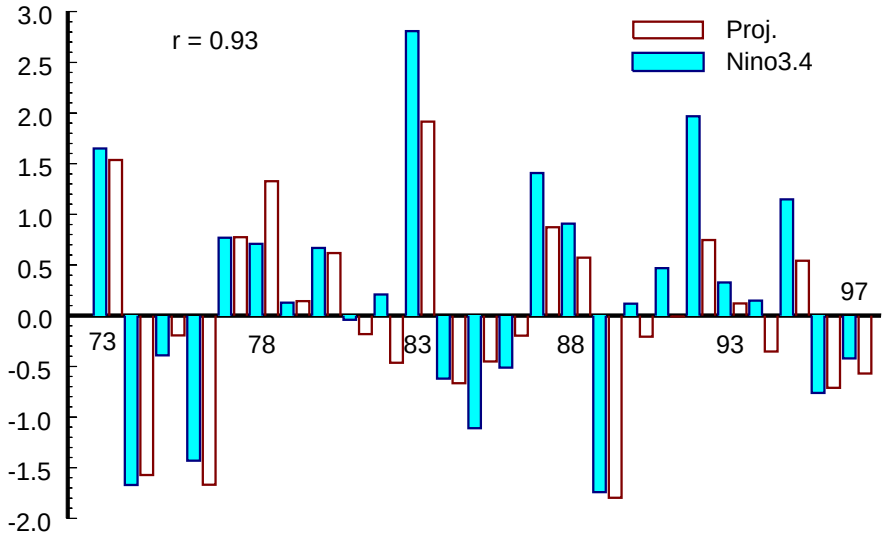

Figure 3.38: As in figure 3.37 but respecting to the 4^{th} baroclinic component of the forced circulation. The projections were multiplied by 3.

Chapter 4

Climatic Variability in the NCEP Reanalysis

In this chapter, we present a study of the intraseasonal and interannual variability of the winter (DJF) global atmospheric circulation based on a NCEP reanalysis data set for the period of January 1973 to December 1996. The used data consisted of monthly means (DJF) of the vector $(u, v, \phi)^T$ and virtual temperature, available at 17 standard pressure levels (1000, 925, 850, 700, 600, 500, 400, 300, 250, 200, 150, 100, 70, 50, 30, 20 e 10 hPa) with an horizontal grid resolution of 2.5° lat. × 2.5° long.. Henceforth we will refer the reanalysis as the NCEP atmosphere or, simply, as observations.

4.1 Normal modes of the NCEP atmosphere

The vertical profile of the virtual temperature, $T_0(p)$, of the reference state for the NCEP atmosphere was obtained as the global isobaric means of the virtual temperature fields, averaged over the 72 winter months from Janury 1973 to December 1996. This profile was then replaced in equation 2.38 to obtain the static stability parameter of the atmospheric reference state.

The vertical structure functions of the NCEP atmosphere were calculated by the method described by Castanheira *et al.* [1999, secs. 2 and 4]. Figure 4.1 shows the vertical structures of the barotropic and first 5 baroclinic components of the NCEP atmosphere.

Comparing figures 3.1 and 4.1, it can be observed that the vertical structure of the NCEP atmosphere have the nodes less spaced, hence giving a greater resolution of the

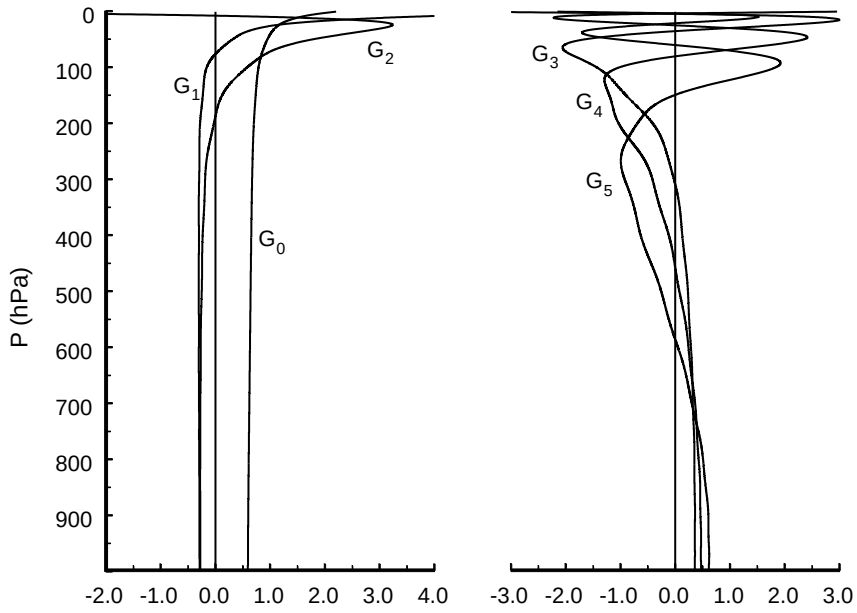

Figure 4.1: Vertical structures of the modes $m = 0, \ldots, 5$ of the NCEP atmosphere.

lower stratosphere and upper troposphere. This greater resolution is a consequence of the greater vertical discretization (17 levels) of the reanalysis, especially in the lower stratosphere [Castanheira *et al.*, 1999, secção 4.2]. It should be remembered that the MU AGCM has only two stratospheric sigma levels (0.074 and 0.009).

The barotropic structure functions of the observed and simulated atmospheres are almost identical, allowing a direct comparison between the observed and simulated barotropic circulation patterns. On the other hand, as a consequence of the greater resolution of the NCEP atmosphere, it may happen that patterns similar to the ones obtained for the simulated 4^{th} baroclinic component appear now associated with the 4^{th} and/or 5^{th} baroclinic components of the NCEP atmosphere.

The vertical projections 2.58 of the observations onto the vertical structure functions were calculated using guassian quadrature, as for the simulations, but in this case the (u, v, ϕ) fields were interpolated by cubic splines for 41 gaussian levels. Above the 10 hPa level, the anomalies of $\mathbf{V}$ and ϕ were considered constant and equal to their respective values at that level. At gaussian levels between the surface, $p_s = 1011.3\,\text{hPa}$, and the 1000 hPa level, the geopotencial anomalies are obtained by hydrostatic extrapolation, using the observed anomalies and the virtual temperatures at the 1000 hPa level. For the horizontal wind we assumed again a non-slip condition at the surface.

The Hough harmonic vectors associated with each vertical structure function were

calculated by the method described in section 3.3.2.

The projections of the vertical transforms of the reanalyzed fields onto the Hough harmonics vectors were performed by the same method used for the simulations, but the meridional integral in (2.67) was calculated with 72 gaussian latitudes.

4.2 Vertical spectrum of the total transient energy

The observed atmosphere may be considered as a member of a theoretical ensemble of atmospheres all subjected to the same external influences, and each going trough normal weather fluctuations independently of all others [Leith, 1978].

Having only one member it is not possible to perform the decomposition 3.2 of the projections onto a given mode $\beta = (\alpha, msl)$ on the fluctuations due to the internal variability and the response to the external forcing. Therefore, it is not possible to obtain the estimates 3.8 and 3.11 of the total transient energies associated, respectively, with the free and forced variabilities.

An unbiased estimate of the total transient energy associated with the total (internal+forced) variability is given by the following expression

$$E'_\beta = \frac{p_s h_m}{c_\beta} \frac{1}{N-1} \sum_{t=1}^{N} w_\beta(t) w^*_\beta(t) \tag{4.1}$$

where $N = 72$ is the number of winter months (DJF) in the period 1973-96.

One should note that, apparently, there is a contradiction when saying that expression 3.6 is a *biased* estimate of the total simulated variability, and on the other hand, that expression 4.1 is an *unbiased* estimate of the total observed variability. In fact, the contradiction is only apparent. The reason for the distinction of the estimates is that (3.6) fails to account for the impact that the make-up of the that has on the number of degrees of freedom [Rowell *et al.*, 1995]. The estimator 4.1 is used on a time series that contains only one realization of the fluctuations, ε_{1n}, due to the internal variability, and one realization of the climatic signal, β_n, due to the external forcing (*cf.* eq. 2.1). On the other hand, the estimator 3.6 is applied on a time series constructed by a succession of 10 independent realizations of the fluctuations, ε_{mn}, due to the internal variability, added to 10 successive repetitions of the climatic signal, β_n, due to the external forcing in the period 1979-88. The estimator 3.6 does not account for the repetitions of the climatic signal.

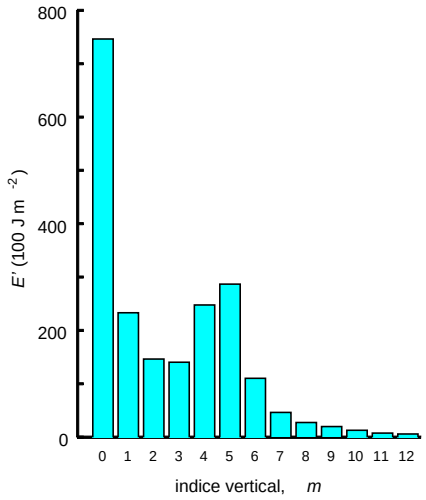

Figure 4.2: Vertical spectrum of total transient energy of the NCEP atmosphere for the period 1973-96.

Figure 4.2 shows the vertical spectrum of the total transient energy of the winter monthly means of the NCEP atmosphere. As described in section 3.6, the energy associated with each vertical structure function , G_m, was calculated adding the energies associated with all the horizontal modes with the same vertical index m.

Comparing figure 4.2 to figures 3.5 and 3.14 it can be verified that the total transient energy simulated by the MU AGCM is smaller than the observed one. In fact, in the case of the simulated atmosphere, the sum of the energies associated with all the vertical indices, i.e., the energy integrated over the whole atmospheric mass is only equal to 71% of the total observed energy.

The observed vertical energy spectrum presents a bimodal structure as in the case of the simulated spectrum. However, in the case of the observed atmosphere, the second energy peak appears in the 5^{th} baroclinic component instead of the 4^{th} baroclinic component. But the difference between the values of the energies associated with the fourth and fifth components is relatively small.

It should be noted that, in the case of the simulated atmosphere, the fact that the second energy maximum appears associated with the fourth component results only of the lesser vertical discretization of the model [Castanheira *et al.*, 1999]. In fact, the equivalent height associated with the 4^{th} baroclinic component of the simulated atmosphere ($h_4 = 179\,\text{m}$) is the one that presents a closer value to the equivalent height of the 5^{th} baroclinic component of the NCEP atmosphere ($h_5 = 145\,\text{m}$). On the

other hand, the relatively small difference between the energies associated with the 4^{th} and 5^{th} baroclinic components of the observed atmosphere suggests the possibility, already anticipated in section 4.1, that the 3-dimensional variability patterns of the atmospheric circulation, associated with the 4^{th} baroclinic component of the simulated atmosphere, may appear, in the case of the observed atmosphere, associated with the fourth and/or fifth baroclinic components.

4.3 Barotropic component

Figure 4.3 shows the horizontal spectrum of the total transient energy associated with the Rossby barotropic modes, including the zonal Kelvin mode, and figures 4.4 and 4.5 show the spectra of the energies associated with the westward and eastward barotropic gravity modes, respectively.

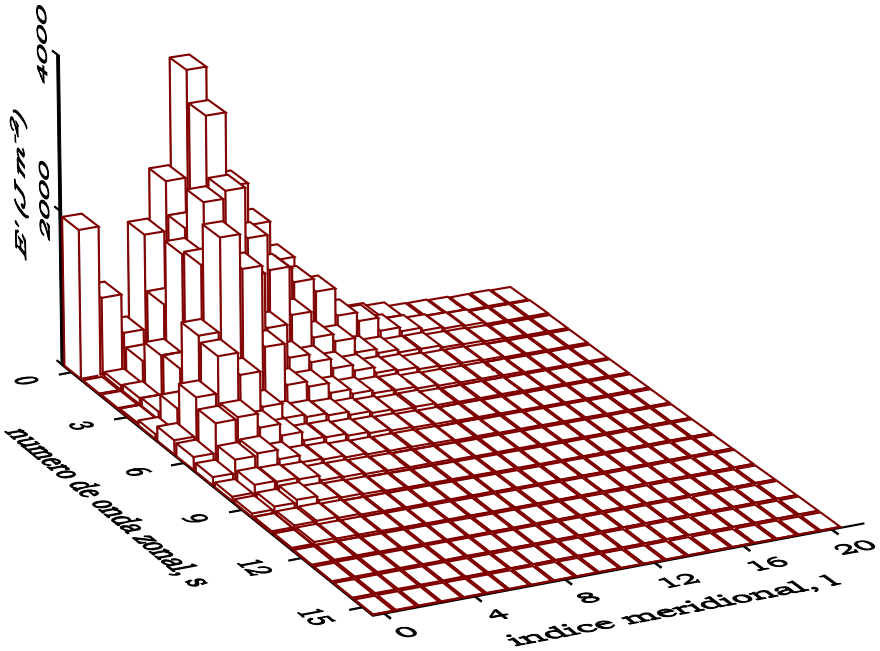

Figure 4.3: Total transient energy associated with the barotropic Rossby modes and zonal Kelvin mode ($s = 0,\ l = 0$).

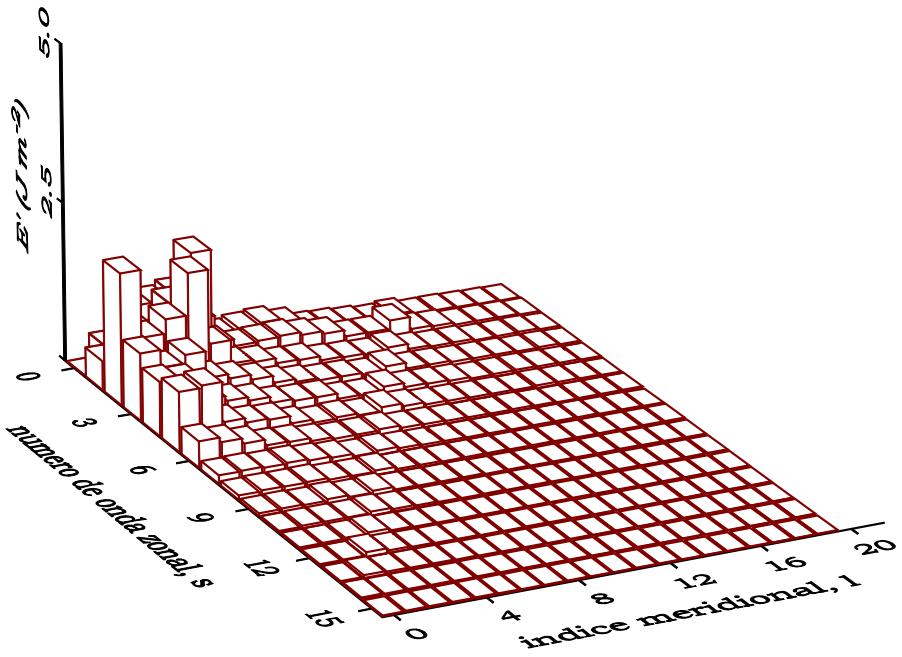

Figure 4.4: Total transient energy associated with the westward barotropic gravity modes.

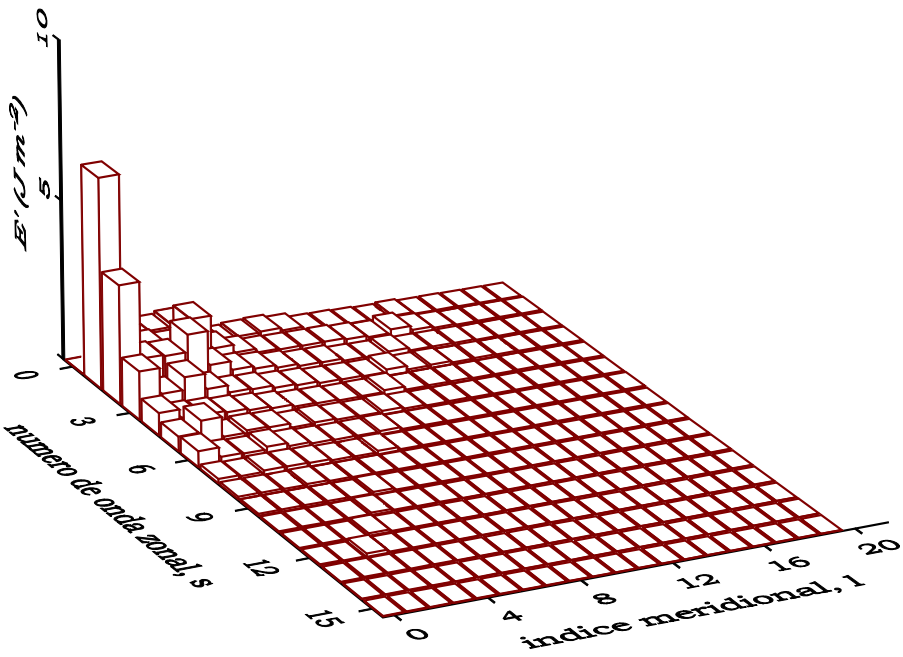

Figure 4.5: Total transient energy associated with the eastward barotropic gravity modes.

The values of the energy associated with the barotropic gravity modes are three orders of magnitude smaller than those of the Rossby barotropic modes. So, as in the case of the simulations, for the analysis of the variability of the observed barotropic circulation we considered only the Rossby modes and the zonal Kelvin mode.

In figure 4.3 one can see that, as the zonal wavenumber increases, the meridional maximum of the variability appears associated with smaller indices l. This fact was referred in section 3.6.1 and indicates that the variability in high latitudes is dominated by the waves $s = 0$, 1 and 2 and the contribution of the waves $s = 3$, 4 and 5 becomes also important in the middle and low latitudes [Nakamura et al, 1987].

The geographical distribution of the total transient energy associated with the barotopic circulation is given by

$$E'(\lambda,\theta) = \frac{p_s}{4g}\left\{\sigma^2\left[\hat{u}_0(\lambda,\theta)\right] + \sigma^2\left[\hat{v}_0(\lambda,\theta)\right] + \sigma^2\left[\frac{\hat{\phi}_0(\lambda,\theta)}{\sqrt{gh_0}}\right]\right\}, \tag{4.2}$$

where the variances σ^2 are calculated by the estimator 4.1, applied in this case to real variables.

Figure 4.6 shows the spatial distribution of the total transient energy of the observed barotropic circulation, and figure 4.7 shows the contributions due to the kinetic and available potential energies of the extratropical circulation of the Northern Hemisphere, for the period 1973-96. The maps of the total energy and available potential energy are similar to the respective maps of figure 3.8 and the bottom map in figure 3.9, calculated for the period Dec/76-Feb/88. However, it should be noted that the dipolar structure over the Atlantic in figures 4.6 and 4.7 does not appear as well defined as in figures 3.8 and 3.9.

A justification should be presented here for the comparison of the transient energy of the simulated barotropic circulation with the transient energy of the observed barotropic circulation in the period of Dec/76 to Feb/88, although there were available observations for the longer period of 1973-96. The reason has to do with the occurrence of an anomalous circulation regime during the period Dec/76-Feb/88, including the ten year period of the simulations, as it will be described in section 4.3.2.

Going back to figures 4.6 and 4.7, one can see, as referred in section 3.6.1 for the simulations, that the total transient energy associated with the observed barotropic circulation is dominated by the parcel of the kinetic energy. The maps of figure 4.7 also confirm that the maxima of the kinetic transient energy tend to locate over the

minima of the available potential energy, as would be expected from the approximate geostrophic motion in the middle and high latitudes.

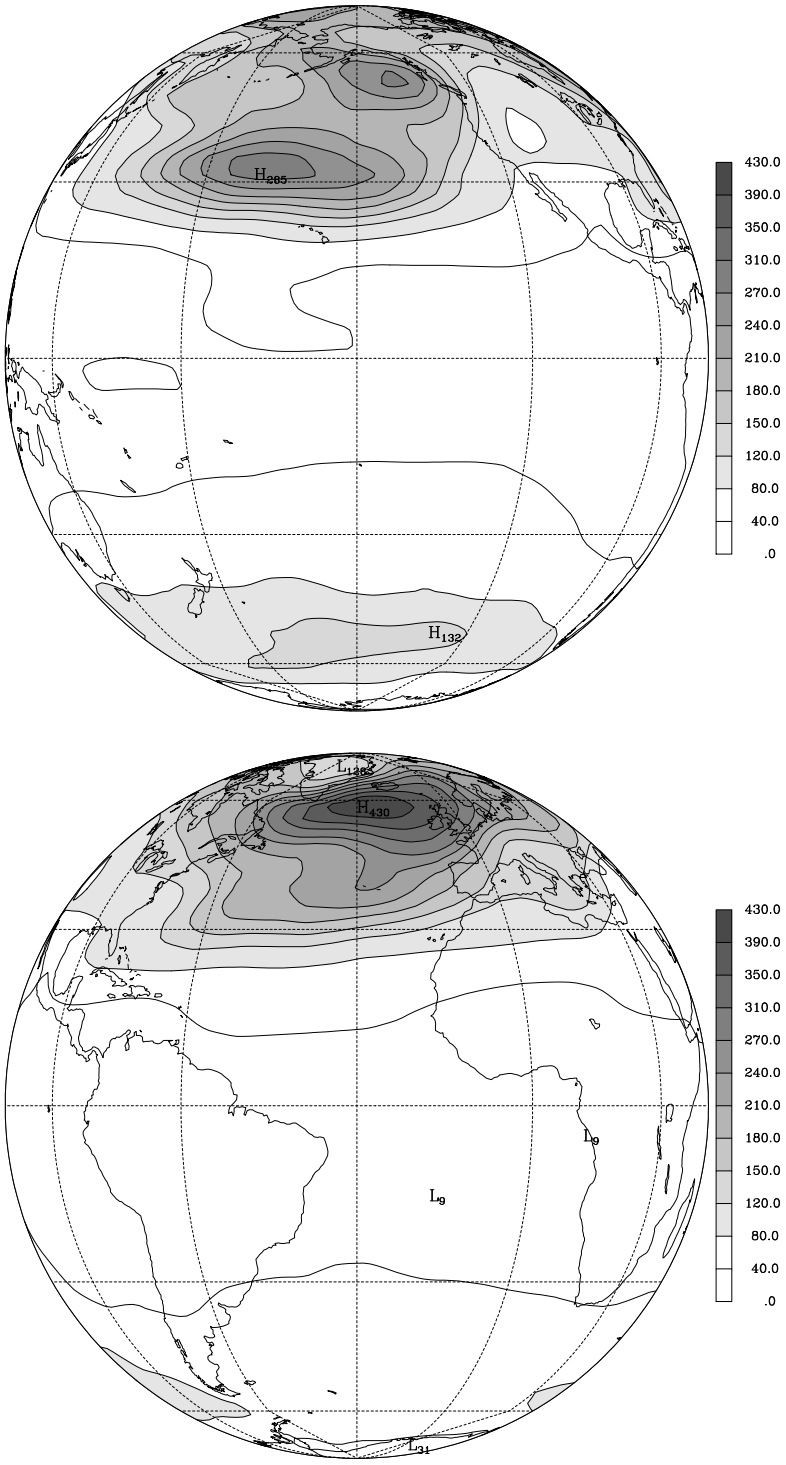

Figure 4.6: Total transient energy per unit of horizontal area ($\mathrm{kJ\,m^{-2}}$) associated with the barotropic Rossby modes of the NCEP atmosphere.

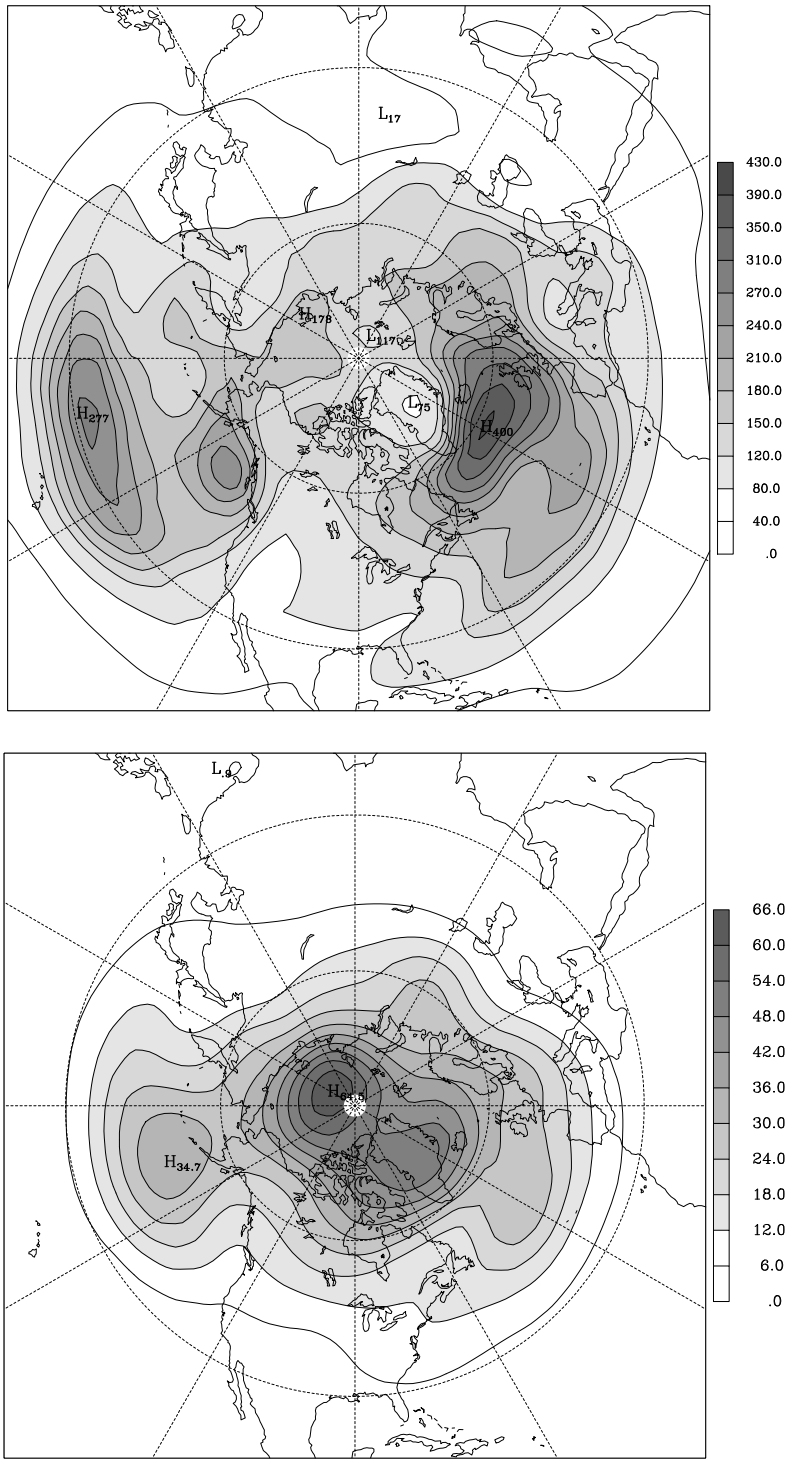

Figure 4.7: Kinetic transient energy (*top*) and available potential energy (*bottom*) associated with the extratropical barotropic circulation of the NCEP atmosphere. The units are kJ m^{-2}.

4.3.1 Variability patterns

The variability patterns of the observed circulation projected onto a given vertical component, m, were obtained through the diagonalization of the variance-covariance matrix, whose elements are estimated by

$$S^{O}_{\beta\beta'} = \frac{1}{N-1}\sum_{t=1}^{N} w'_{\beta}(t)w'_{\beta'}{}^{*}(t) \tag{4.3}$$

where the indices β e β' have the meaning defined in section 3.8, i.e., $\beta \equiv (\alpha, msl)$ e $\beta' \equiv (\alpha', ms'l')$. The expression 4.3 gives an unbiased estimate of the total (internal+forced) variance-covariance matrix and the theory presented in section 3.8 is entirely applicable to the diagonalization of this matrix. In the future, according to the notation used in chapter 3 and when the context is clear, the variability pattern associated with the PC of order n will be designated, shortly, by EOFn.

For the CPCA on the observed barotropic circulation, we have retained the zonal Kelvin mode and the Rossby modes with zonal wavenumbers $s \leq 5$ and meridional indices $l \leq 10$ (*cf.* fig. 4.3). Figures 4.8, 4.9 and 4.10 show, respectively, the circulation patterns associated with the first, second and third PCs. The energy values associated with these PCs represent, respectively, 15.9%, 10.9% and 7.8% of the total transient energy of the observed barotropic circulation.

The circulation pattern of the first PC (fig. 4.8) is associated with the strength of the depression southwest of the Aleutians, and, over the Atlantic, with a meridional oscillation of the atmospheric mass between a region centered in Greenland and an extensive zonal band around latitude 45° N, from the eastern coast of the United States to the northern Europe.

Saravanan [1998] performed a principal components analysis on the winter monthly means (December to March) of the 500-hPa geopotential height fields, based on the NCEP reanalysis for the period 1973-95. In his study, Saravanan calculated the PCs over the Pacific region and in a separate analysis the PCs over the Atlantic. The pattern associated with our first PC of the barotropic circulation (see fig. 4.8) captures simultaneously the variabilities represented by the first EOF over the Pacific and by the first EOF over the Atlantic, obtained by Saravanan.

The second EOF of the observed barotropic circulation (fig. 4.9) represents also a meridional oscillation of the atmospheric mass over the North Atlantic, with a structure

similar to the fourth internal EOF (fig. 3.25) of the barotropic circulation simulated by the MU AGCM. However, the center of anticyclonic circulation in the simulated pattern is shifted eastward about 20º relatively to the observed center. Over the Pacific and North America region the EOF2 presents a reminiscent structure of the PNA.

The pattern associated with the third EOF (fig. 4.10) reminds the teleconnection pattern of the East Atlantic (EA) of Wallace and Gutzler [1981]. However, the pattern here presented is in approximate quadrature with the EA pattern, as it can be verified by the comparison of the figure 4.11 with figures 12 and 13 of Wallace and Gutzler [1981].

The teleconnection patterns of the PNA and NAO appear, in the literature and in the results obtained with the MU AGCM simulations, as two distinct modes that represent the highest fractions of variability of the extratropical circulation over the Pacific/North America region and over the Euro-Atlantic region, respectively. However, among the EOFs of the barotropic component of the NCEP atmosphere no pattern was found that represented individually the PNA. Nevertheless, we can observe that the bottom maps in figures 4.8 and 4.9 present characteristics of the PNA pattern.

The first and second EOFs of the barotropic component represent meridional oscillations of atmospheric mass associated with changes in the westerlies across the Northern Atlantic onto Europe, characteristic of the NAO. Regarding the PNA, it appears reproduced on EOF1 (fig. 4.8, *bottom map*), but with the teleconnection center over northwest Canada not well defined (*cf.* fig. 3.23). The association between the EOF1 and the PNA are more evident in the correlation map between the PC1 and the time series of the temperature anomaly fields at the 850 hPa level (fig. 4.12). This correlation map show in the upper panel a pattern that is characteristic of advective temperature anomalies of the NAO. The lower panel show the PNA teleconection centers, and it should also be noted the existence of a negative correlation over the Tropical Pacific. Considering that the 850 hPa temperature field reflects the surface temperature, the correlation over the Tropical Pacific is an indication of the teleconnection between the SST anomalies in that region and the PNA. It also should be noted that while the correlation map of the PC1 over the Northern Atlantic presents advective characteristics, over the Pacific and North America the anomalies of the temperature field tend to be coincident with the geopotential anomalies, indicating, in this case, a vertical structure equivalent to the barotropic. The EOF2 presents also a reminiscent structure of the PNA with an anticyclonic circulation well defined

over Canada. The correlation map between the PC2 and the 850 hPa temperature anomalies (fig. 4.13) shows, yet, a reminiscent structure of the PNA and, over the Euro-Atlantic region, an anomaly pattern that is similar to the characteristic pattern associated with the NAO.

The observations in the above paragraph suggest that the teleconnection patterns of the PNA and the NAO, that weren't individualized by the CPCA, are jointly present in both first two EOFs, and may eventually be obtained separately through an adequate linear combination of those two EOFs. In fact, in many studies [e.g., Kushnir and Wallace, 1989; Renshaw *et al.*, 1998] the variability patterns of the atmospheric circulation were revealed using a method of rotation of the EOFs or the PCs. In a revision article, Richman [1986] presented several rotation methods for the PCs and the EOFs, discussing the merits of each one. In a more recent study, Cheng *et al.* [1995] argued that the rotated EOFs are less sensitive to statistic fluctuations of sampling than the corresponding unrotated EOFs, and suggested that the rotated EOFs are more efficient in isolating circulation patterns with physical meaning.

Figures 4.14 and 4.15 show, respectively, the circulation patterns associated with the following linear combinations of the first two EOFs

$$\frac{1}{\sqrt{2}}\,(\mathrm{EOF2} + \mathrm{EOF1}) \tag{4.4}$$

$$\frac{1}{\sqrt{2}}\,(\mathrm{EOF2} - \mathrm{EOF1})\,. \tag{4.5}$$

Figure 4.14 shows the teleconnection pattern of the NAO, and figure 4.15 reproduces now a teleconnection pattern of the PNA similar to the one obtained with the MU AGCM (*cf.* fig. 3.23).

The projections (PCs) of the barotropic circulation onto the patterns 4.4 and 4.5 are given, respectively, by the expressions

$$\frac{1}{\sqrt{2}}\,(\mathrm{PC2} + \mathrm{PC1}) \tag{4.6}$$

$$\frac{1}{\sqrt{2}}\,(\mathrm{PC2} - \mathrm{PC1})\,. \tag{4.7}$$

Figure 4.16 and 4.17 show, respectively, the correlation maps between the 850 hPa temperature anomalies and both the PCs 4.6 and 4.7. Figure 4.16 shows the characteristic pattern of the temperature anomalies resulting from the advection by circulation anomalies associated with the NAO. The map in figure 4.17 shows the temperature anomalies associated with the PNA. It should be noted, by the location of the centers

of temperature anomalies that the PNA must have an equivalent barotropic structure. These results agree with the results obtained for the simulated atmosphere (*cf.* sec. 3.8.2) which indicate that the vertical structure of the PNA must be equivalent to the barotropic, while the NAO must have baroclinic characteristics [Perlwitz and Graf, 1995].

The patterns given by the linear combinations 4.4 and 4.5 are orthogonal, and the total transient energy associated with the circulation projected onto each pattern is given by the variance of the respective PC. Thus, the total transient energy of the barotropic circulation is still given by the sum of the energies associated with each of two rotated PCs and the energies associated with the unrotated PCs of higher order than the second. Therefore, the PCs 4.6 and 4.7 have the same physical meaning of the unrotated PCs but loose the temporal orthogonality between them.

Finally, it should be noted that although figures 4.14 and 4.15 represent circulation patterns of higher physical meaning, the linear combinations 4.4 and 4.5 were obtained from the visual inspection of figures 4.8 and 4.9, so they are not based in an objective criterion of rotation.

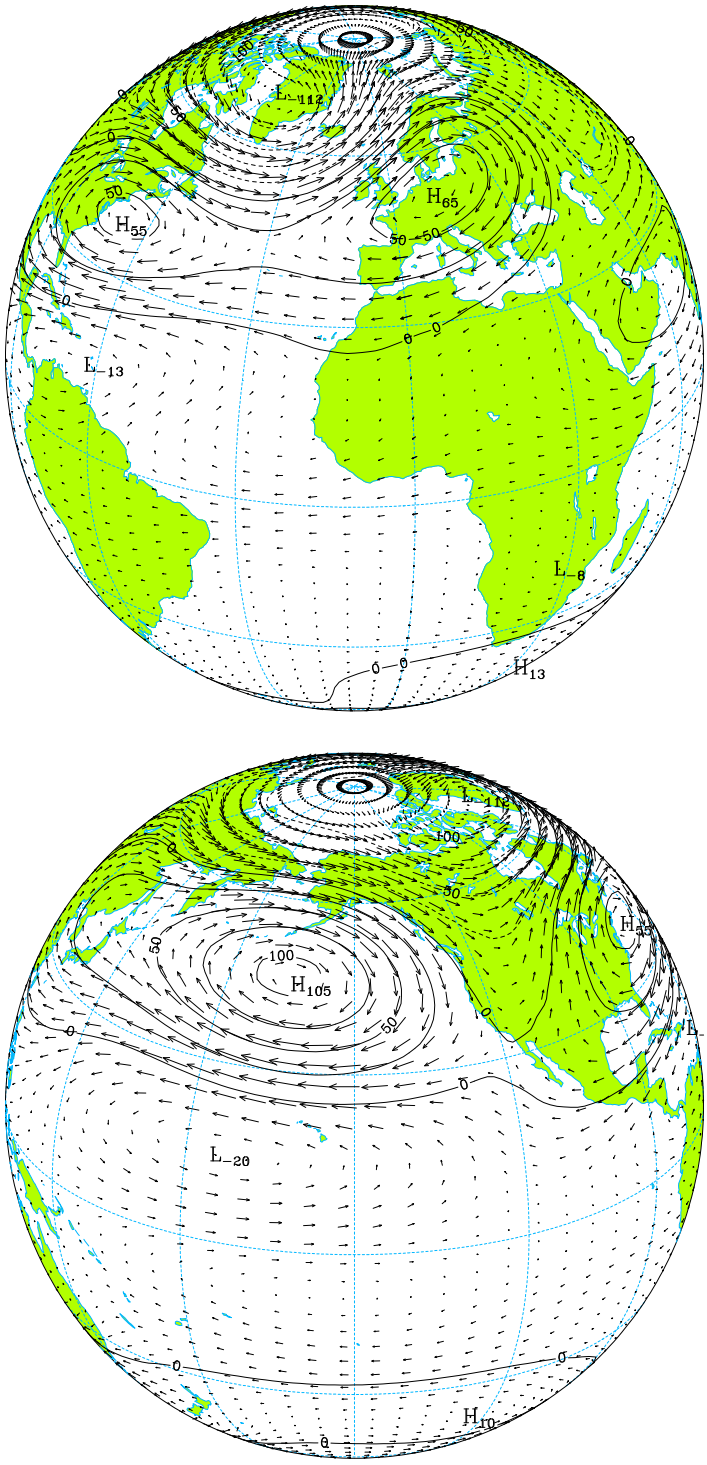

Figure 4.8: Pattern associated with the first PC of the barotropic circulation of the NCEP atmosphere. The geopotential and wind speed units are gpm and $\mathrm{m\,s^{-1}}$, respectively. The maximum speed is $v_{max.} = 7.8\,\mathrm{m\,s^{-1}}$.

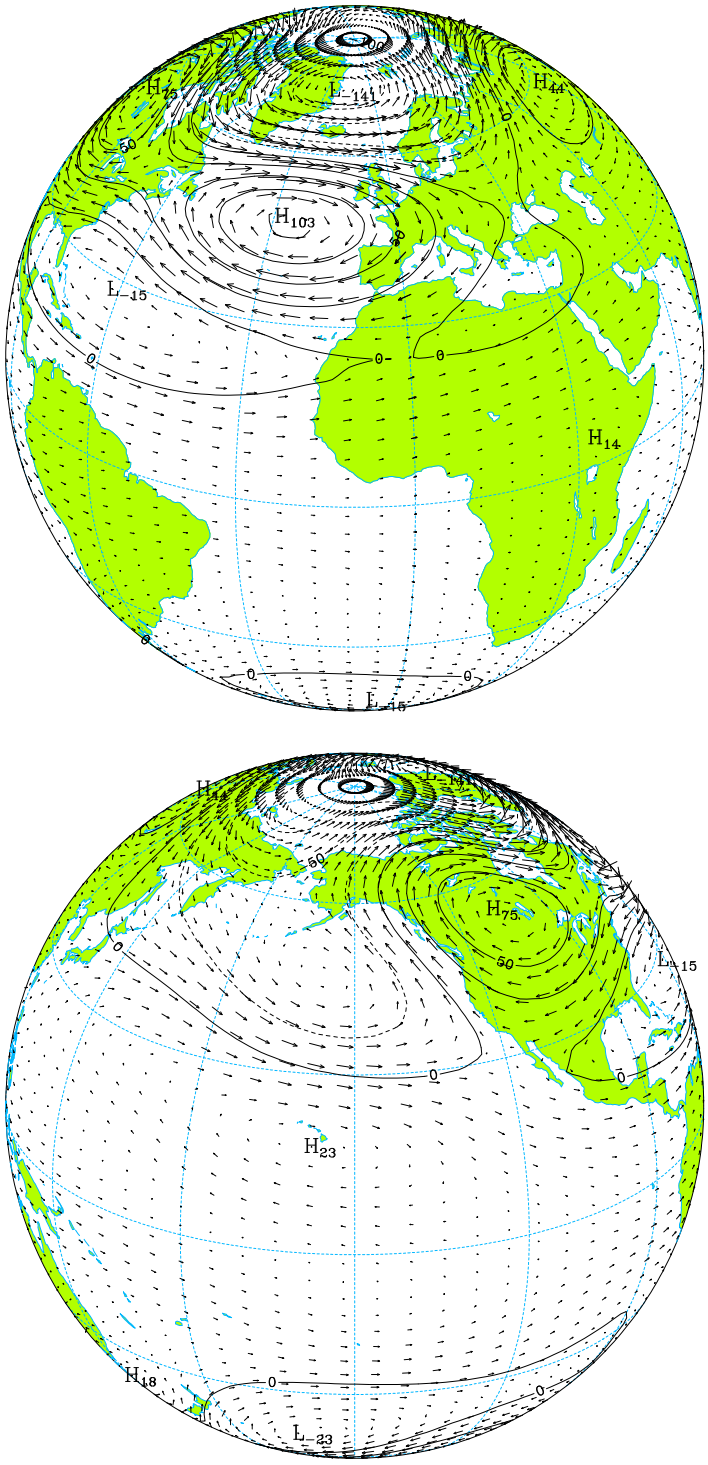

Figure 4.9: As in figure 4.8 but respecting to the second PC ($v_{max.} = 10.2\,\mathrm{m\,s^{-1}}$).

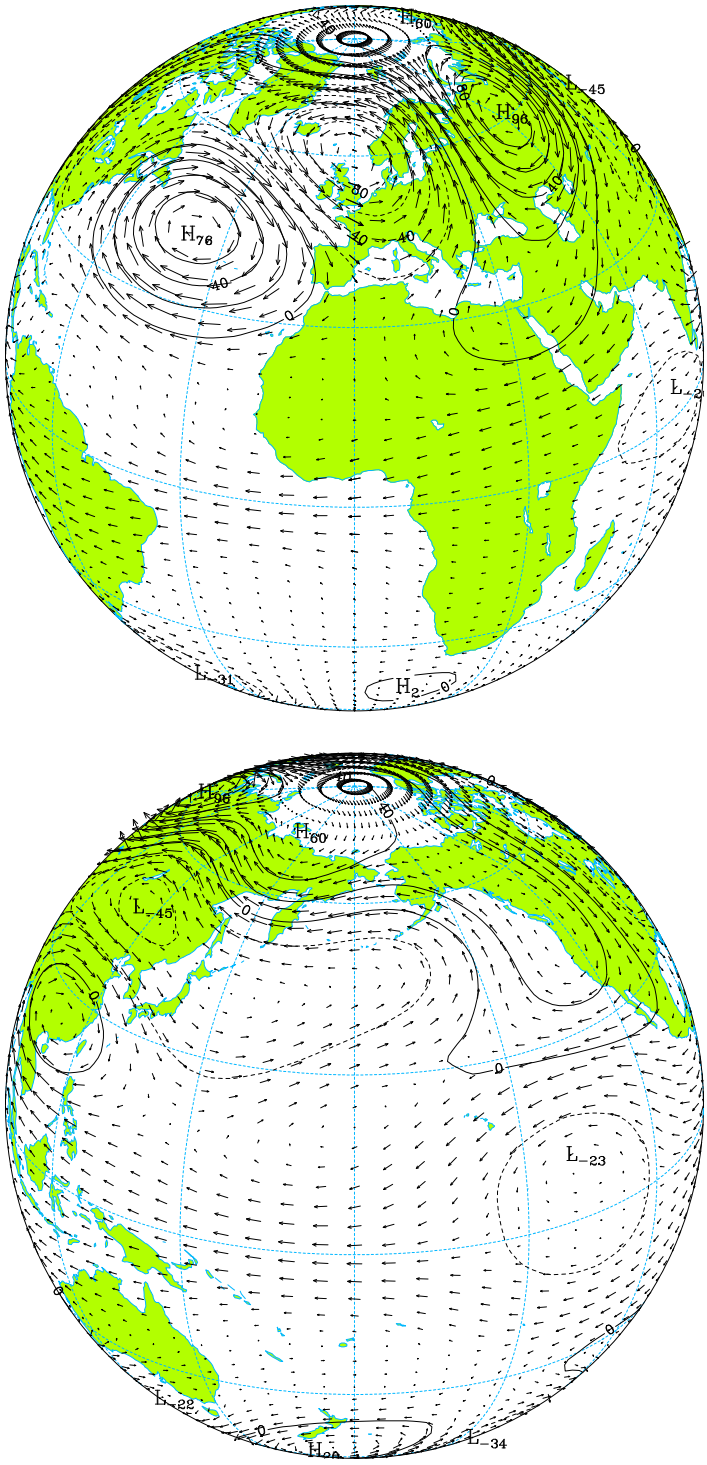

Figure 4.10: As in figure 4.8 but respecting to the third PC ($v_{max.} = 8.0\,\mathrm{m\,s^{-1}}$).

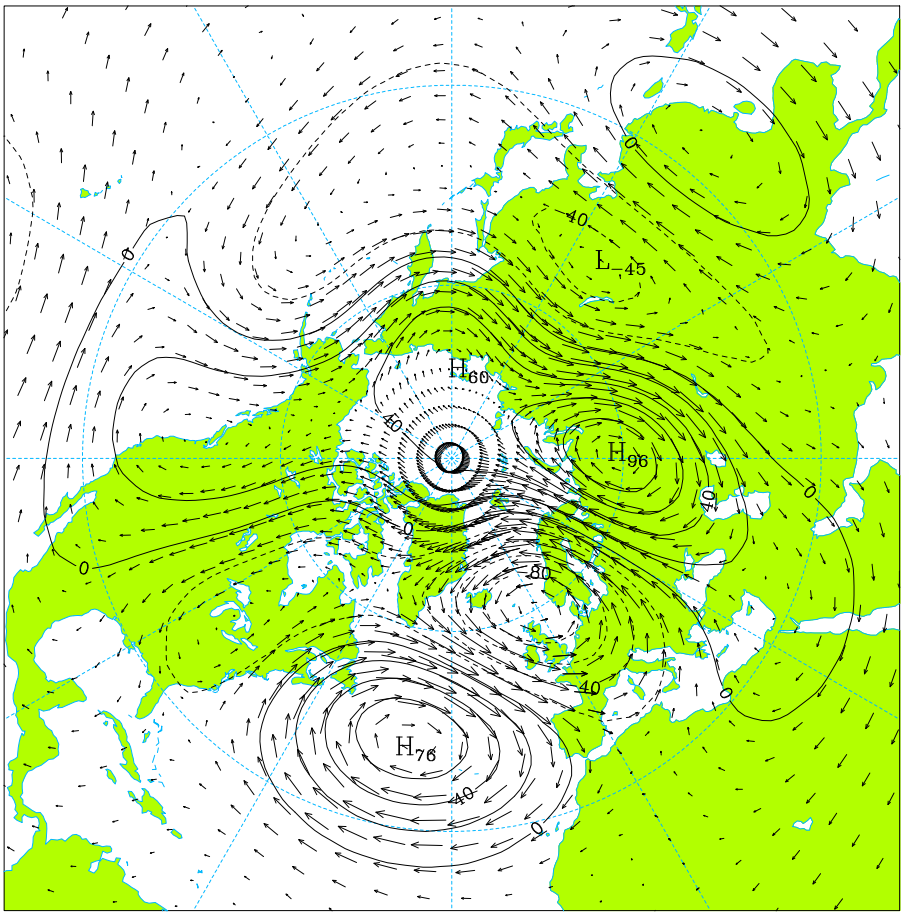

Figure 4.11: Polar stereographic projection of the Northern Hemisphere extratropical circulation associated with the third EOF of the barotropic component of the NCEP atmosphere.

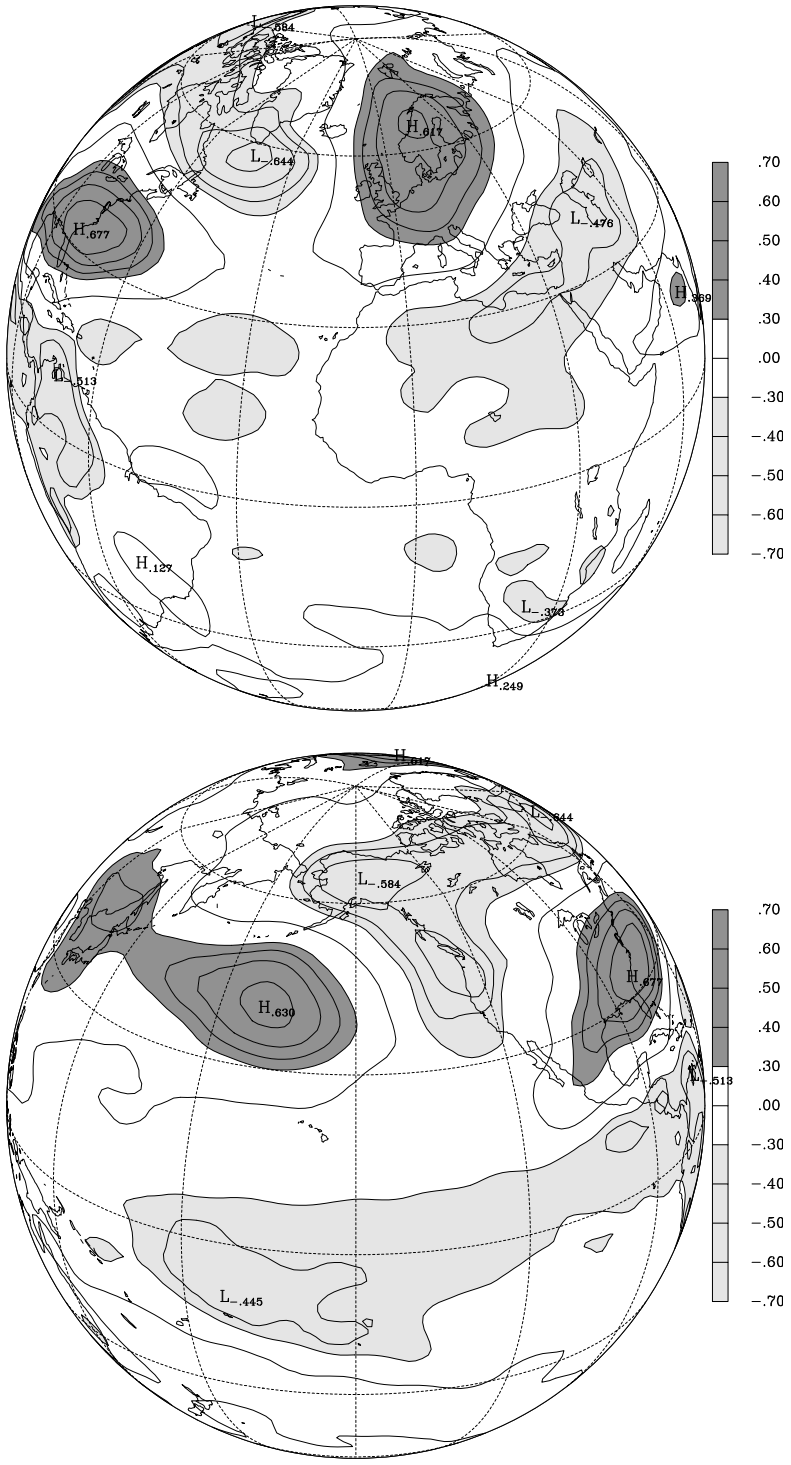

Figure 4.12: Correlation map between the PC1 of the barotropic circulation and the 850 hPa temperature anomaly fields.

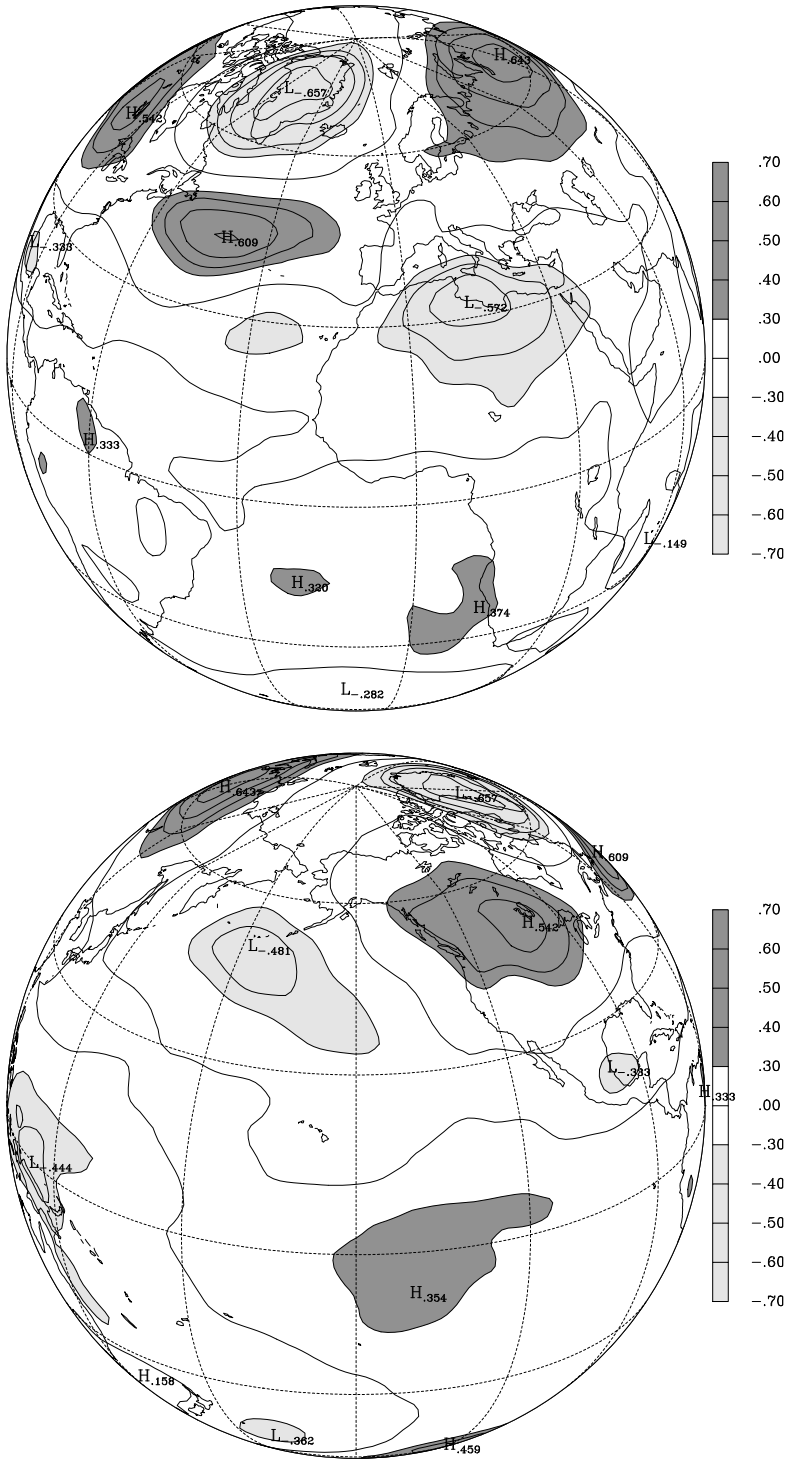

Figure 4.13: As in figure 4.12 but referring to the PC2.

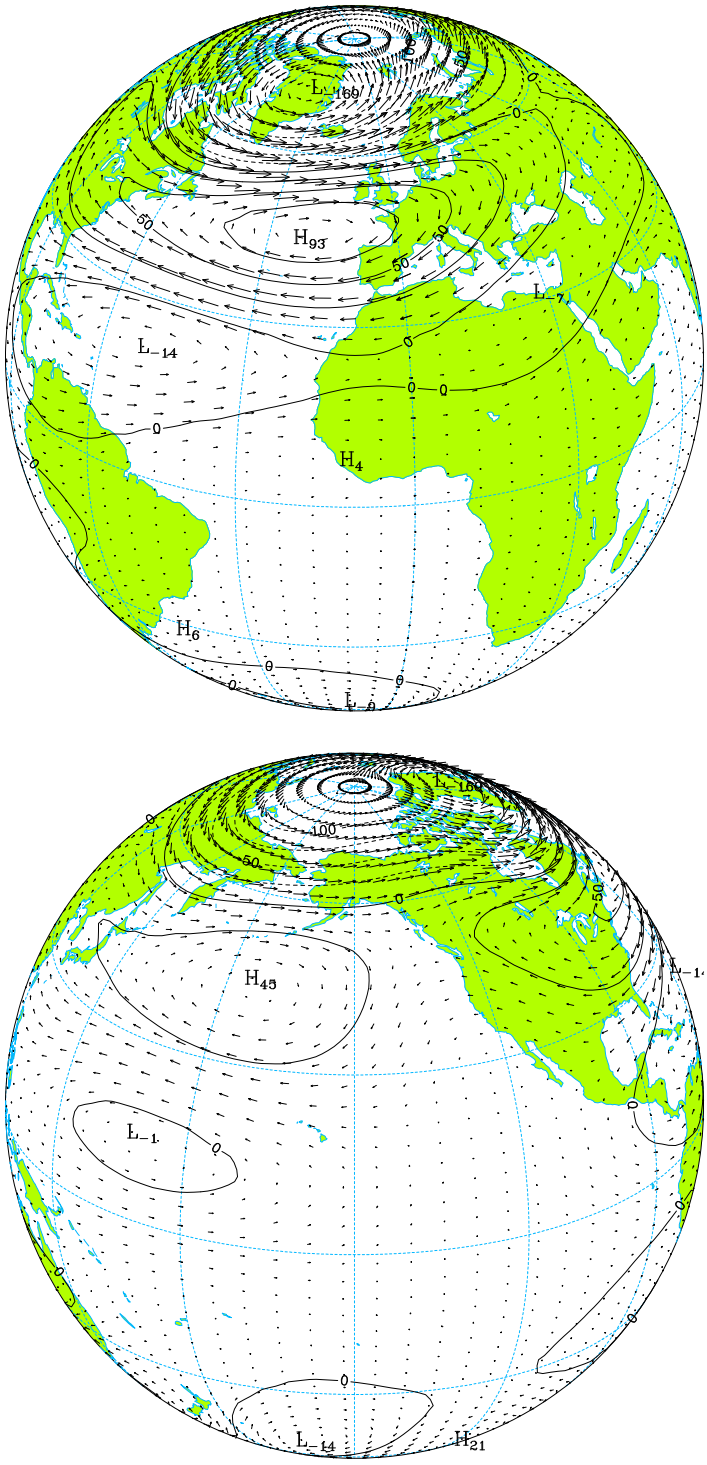

Figure 4.14: Pattern associated with the linear combination $\left(1/\sqrt{2}\right)\{\mathrm{EOF2}+\mathrm{EOF1}\}$ ($v_{max.} = 11.2\,\mathrm{m\,s^{-1}}$).

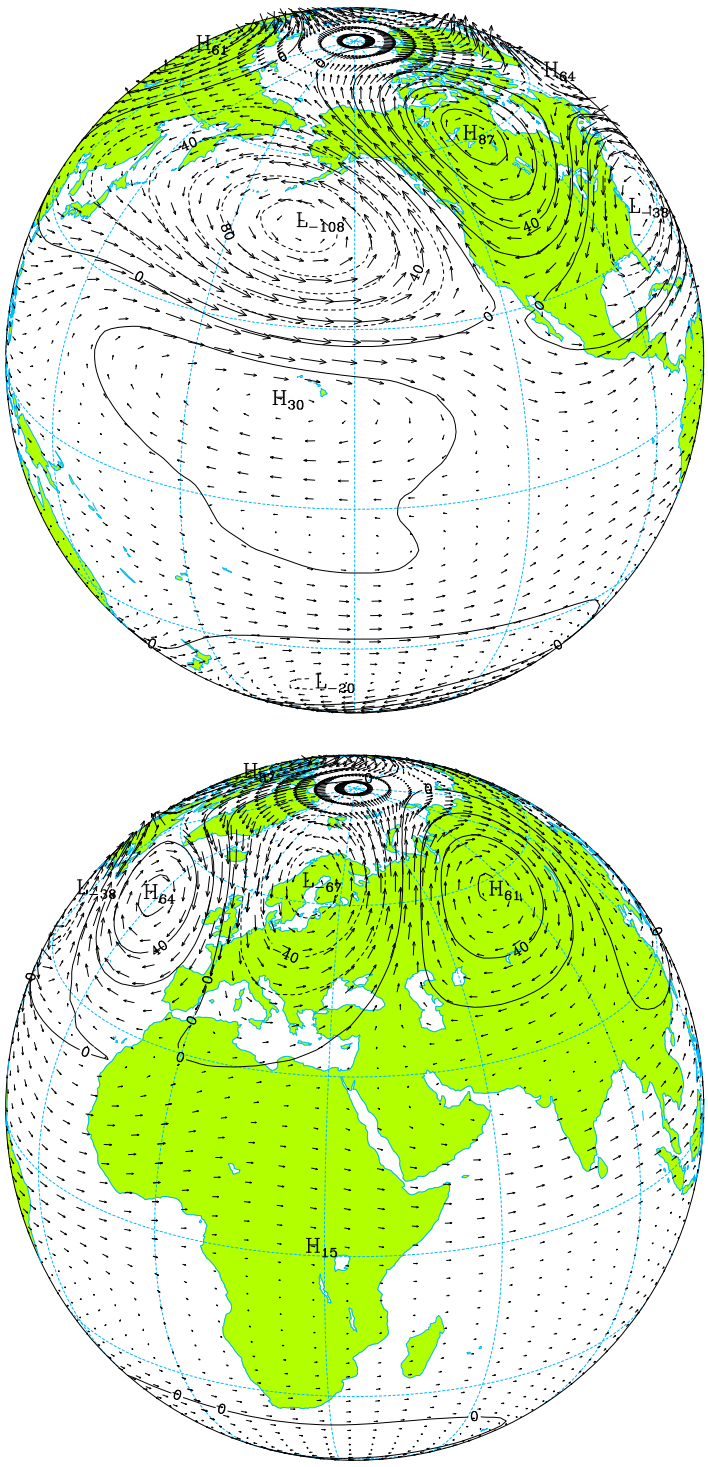

Figure 4.15: Pattern associated with the linear combination $\left(1/\sqrt{2}\right)\{\mathrm{EOF2}-\mathrm{EOF1}\}$ ($v_{max.} = 8.7\,\mathrm{m\,s^{-1}}$).

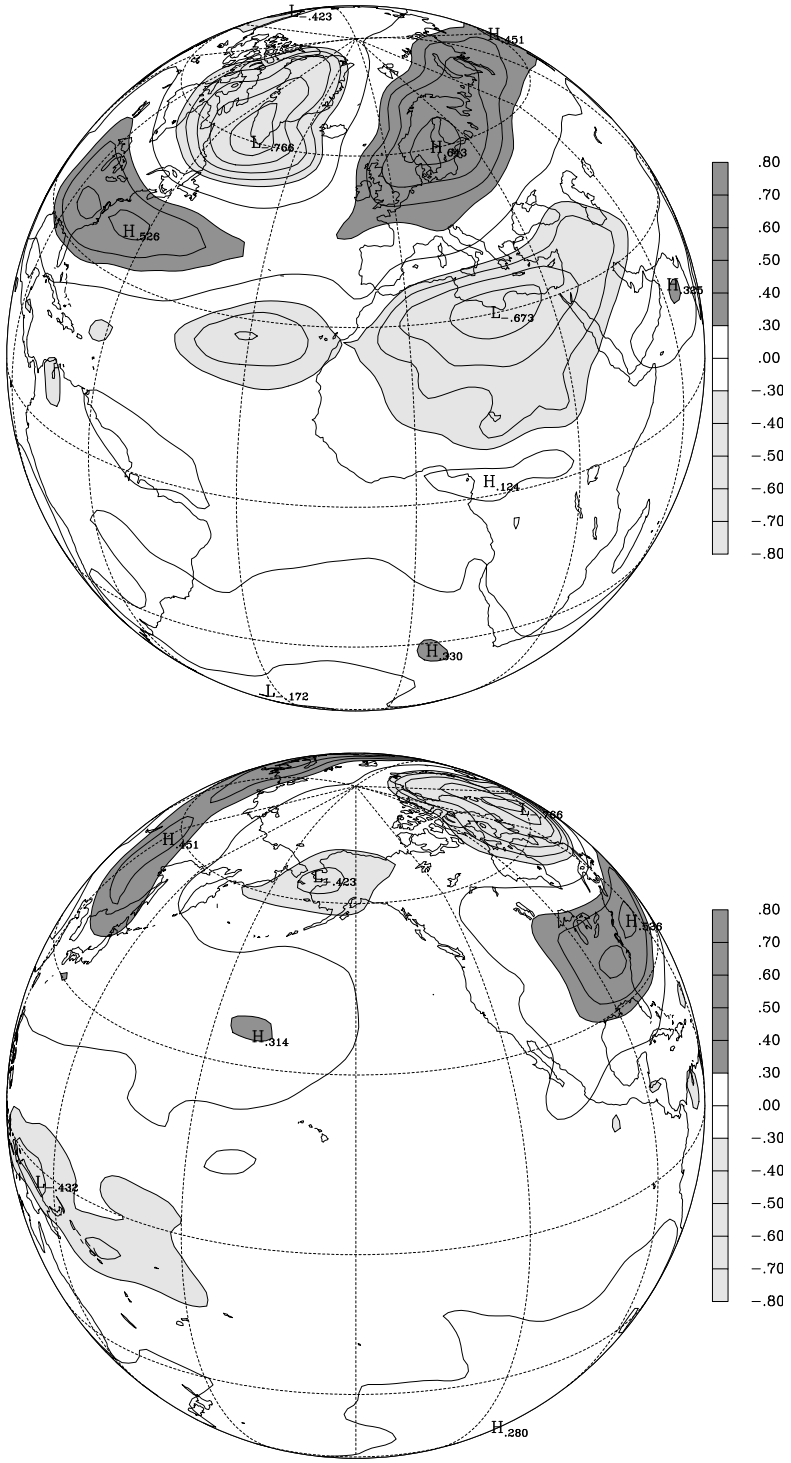

Figure 4.16: Correlation map between the time series of the projections 4.6 and the time series of the 850 hPa temperature anomaly fields.

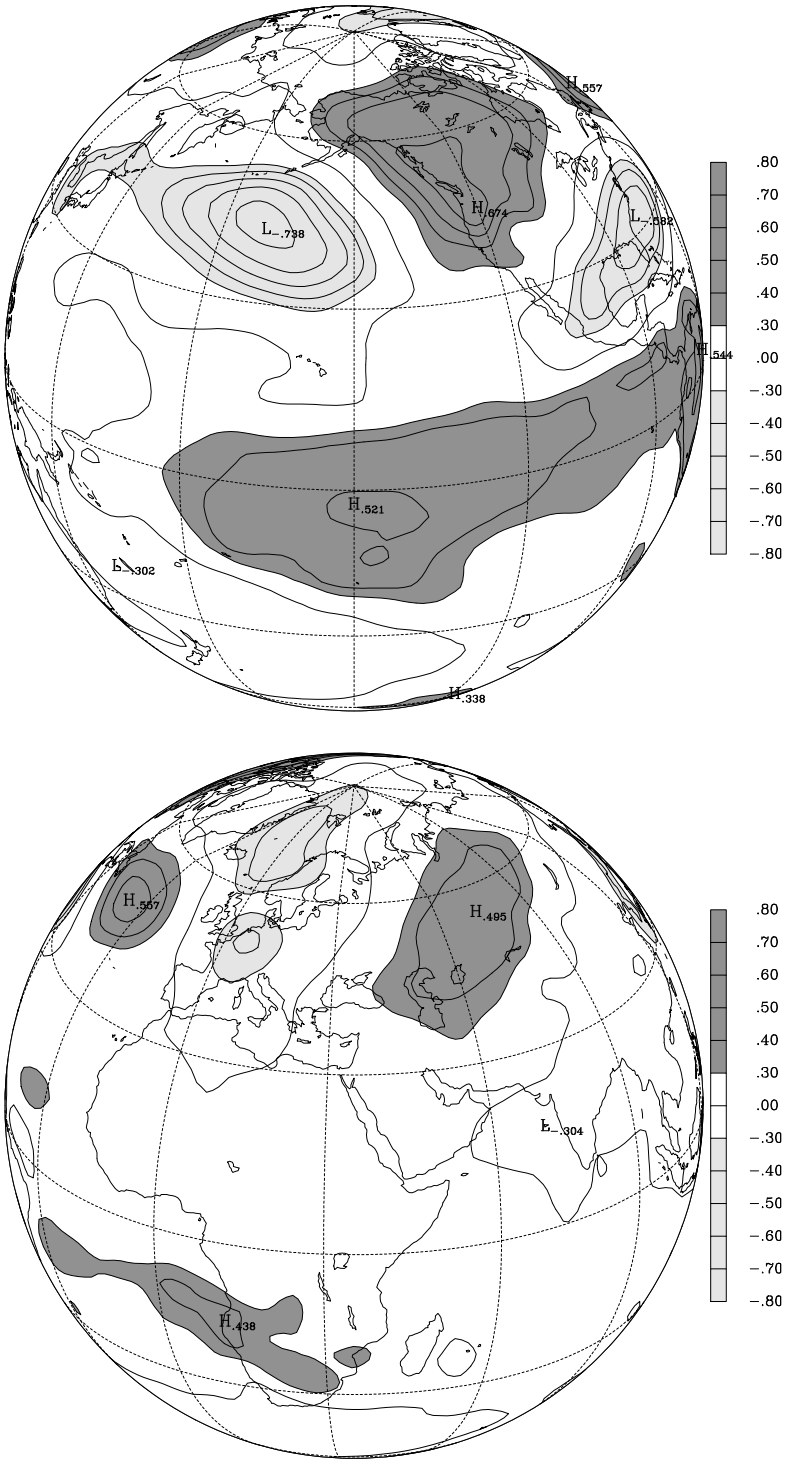

Figure 4.17: As in figure 4.16 but respecting to the linear combination 4.7.

4.3.2 Circulation patterns for the period Dec/76-Feb/88

The time series of the PC1 of the barotropic circulation of NCEP atmosphere is shown in figure 4.18. From Dec/76 to Fev/88 the PC predominantly presents a negative polarity. Considering the winter mean values, it presents only a positive but small value in the winter of 1981/82, and another positive value in the winter of 1983/1984. A t-student test shows that the mean value of the PC over the period Dec/76-Feb/88 is statistically different of the mean value calculated over the remaining time intervals, with a significance level superior to 99%.

The period between the winters of 1976/77 and 1987/88 is often referred as a period in which the atmospheric circulation had a anomalous regime over North Pacific [Renshaw *et al.*, 1998]. The most evident characteristic of that anomalous regime was a deepening of the depression southwest of the Aleutians. Renshaw *et al.* identified that period of anomalous circulation using the time series of winter means (JFM) of the PCs associated with the simulated and observed PNA, previously filtered to remove fluctuations on timescales of less than 8 years.

All the winter months simulated with the MU AGCM, with an exception of December 1988, are included in the period from Dec/76 to Feb/88, when the referred anomalous circulation regime occurred. As already mentioned in section 4.2 this was the reason to use only the period Dec/76-Feb/88 to validate the transient energy

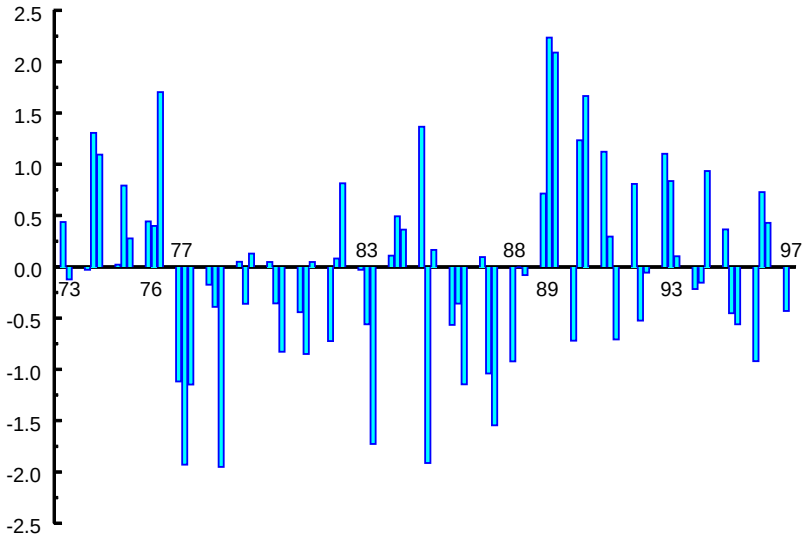

Figure 4.18: Time series of the PC1 of the barotropic circulation of NCEP atmosphere. Each winter is referred by the year where the January month belongs.

simulated by the MU AGCM.

As the CPCA performed on the observed atmosphere did not produce distinct patterns for the PNA and the NAO, as happened with the atmosphere simulated by the MU AGCM. The facts described above arose the question of knowing whether not obtaining distinct patterns was due only to statistical fluctuations of sampling, or whether, on the contrary, it might have also been a consequence of circulation fluctuations on timescales greater than the interannual scale. To explore the reasonableness of the question posed, the EOFs of the barotropic circulation of the NCEP atmosphere were recalculated based on the reanalysis for the period from Dec/76 to Feb/88.

Figures 4.19 and 4.20 show the patterns of the first and second EOFs of the barotropic circulation, based on the NCEP reanalysis for the period Dec/76-Feb/88. These EOFs reproduce, now separately, the teleconnection pattern of the NAO (EOF1) and the teleconnection pattern of the PNA (EOF2), explaining 15.8% and 12.9% of the variability of the barotropic circulation, respectively.

Finally, it should be noted some differences between the simulated and the observed patterns. In the first place, contrary to what happens with the simulated atmosphere of the MU AGCM, the NAO appears as the pattern of highest variability of the observed barotropic circulation. Another difference, already referred, is that the simulated meridional dipole appears shifted eastward relatively to the observed pattern. These differences reflect that the variability simulated by the model is more underestimated over the Atlantic than over the Pacific, and the eastward shifting of total transient energy maxima over the Atlantic (*cf.* figs. 3.7 and 3.8). With respect to the PNA the observed and simulated patterns are similar, although the simulated pattern is shifted westward relatively to the observed one, especially the subtropical anticyclone.

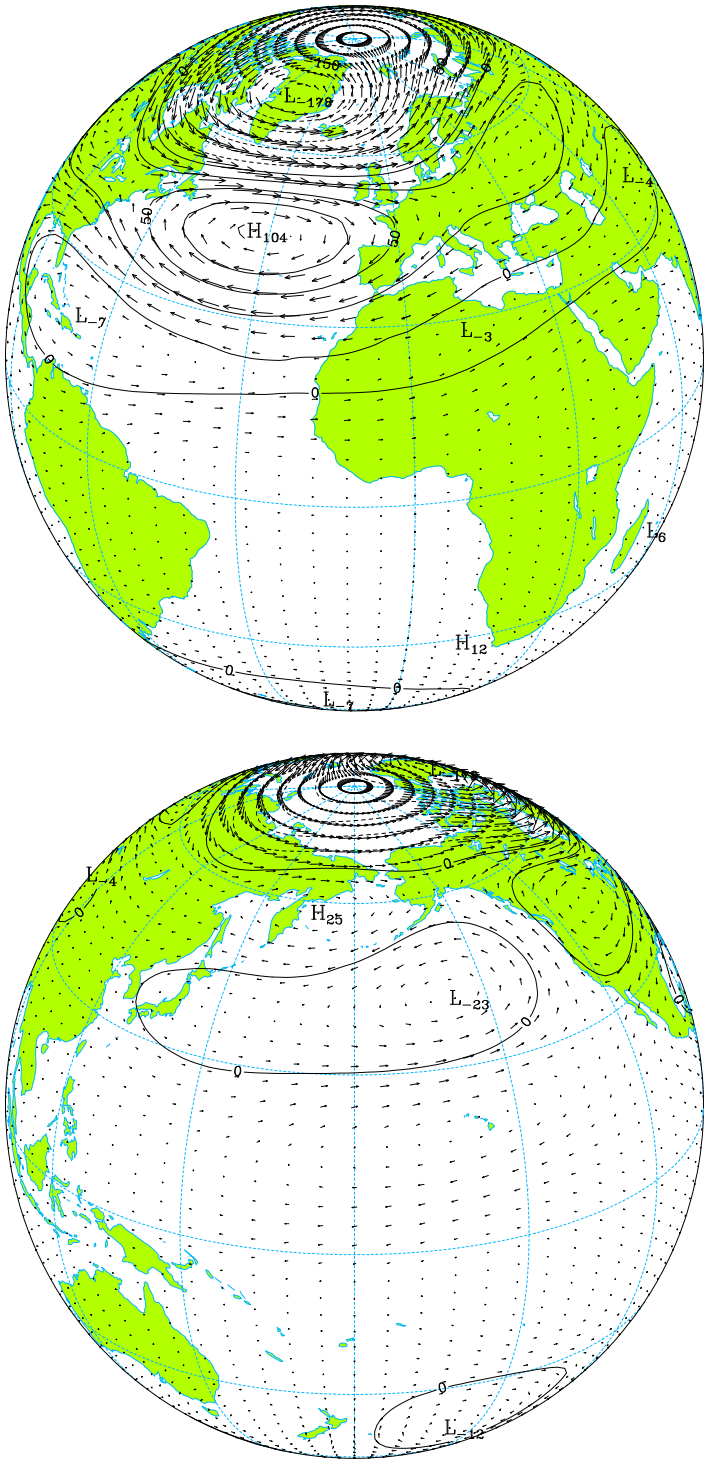

Figure 4.19: Pattern associated with the first EOF of the barotropic circulation, based on the period Dec/1977-Feb/88 ($v_{max.} = 12.0\,\mathrm{m\,s^{-1}}$).

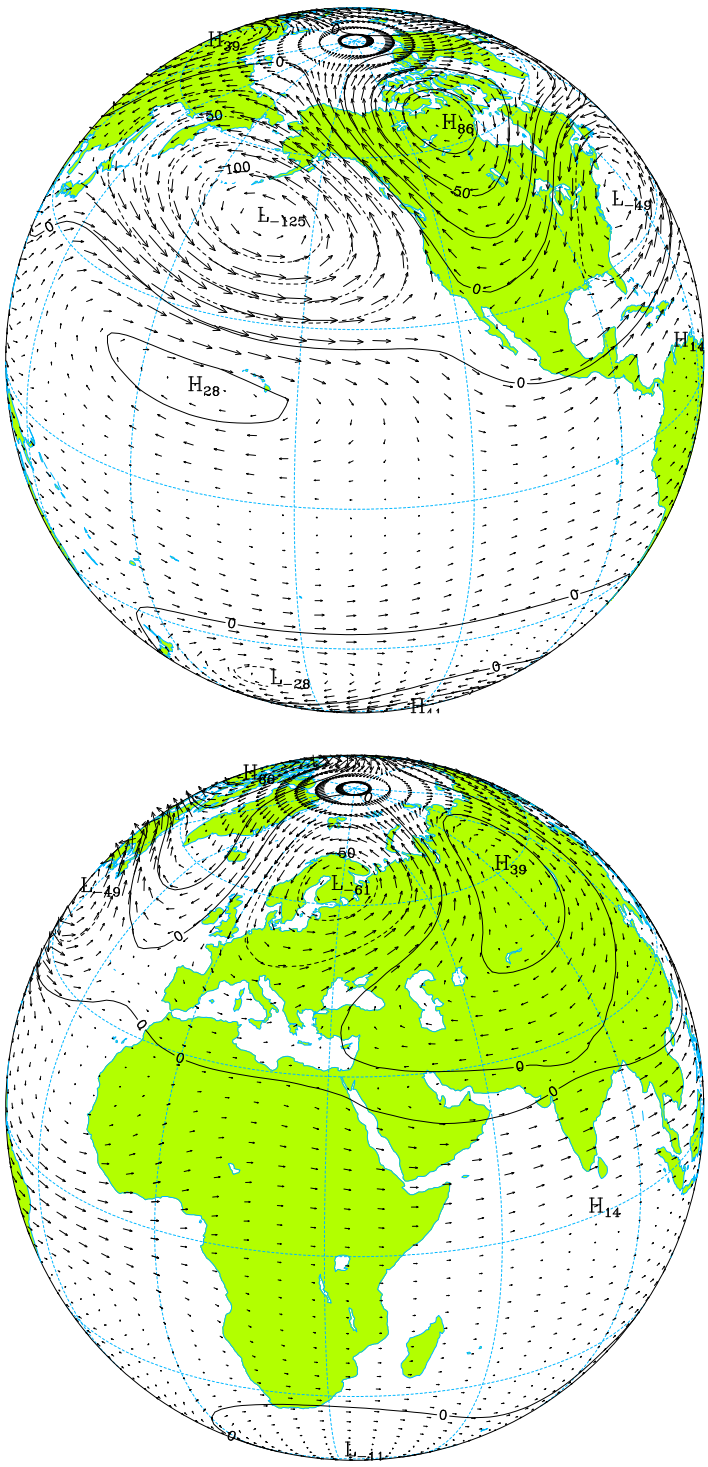

Figure 4.20: As in figure 4.19 but respecting to the second EOF ($v_{max.} = 9.3\,\mathrm{m\,s^{-1}}$).

4.3.3 Canonical correlation pattern

The first pattern of the forced barotropic circulation simulated by the MU AGCM was associated with the SST anomalies in the tropical Pacific (*cf* sec. 3.9.3). To confront the simulated pattern with the observations, a canonical correlation analysis (CCA) was performed between the time series of the observed barotropic circulation field and a time series of the index Niño3.4.

The CCA was performed in the space of the PCs, retaining in the analysis only the PCs 1,2,3,4,6 and 8 [Bretherton *et al.*, 1992]. These PCs are chosen because the values of the single correlation coefficients between each PC and the time series of the index Niño3.4 are all above the level of statistical significance of 95%, except for the PC4 which has a correlation value only above the level of statistical significance of 80%. The values of the single correlation coefficients between the PCs 5, 7, and 9 and the index Niño3.4 are all inferior to the level of statistical significance of 60%. The PCs retained for analysis represent together 54.4% of the variability of the observed barotropic circulation.

We obtained a multiple (canonical) correlation coefficient of 0.83, and the barotropic circulation pattern associated with the pair of canonical variables is represented in figure 4.21. The total transient energy associated with this circulation pattern is equal to 9.4% of the total transient energy associated with the observed barotropic circulation.

The canonical pattern is very similar to the pattern of the first EOF of the forced barotropic circulation simulated by the MU AGCM, confirming that the SST anomalies in the Tropical Pacific force the barotropic atmospheric circulation, essentially over the Pacific Ocean and North America. The SST anomalies in the Tropical Pacific do not appear to have a significant influence on the barotropic atmospheric circulation over the Euro-Asiatic region.

It should be noted that the centers of forced variability simulated by the MU AGCM are shifted westward about 15 to 30° relatively to the respective centers in the observed canonical pattern. Li [1999] obtained the same type of deviation in the position of the forced pattern simulated with a recent version of the LMD AGCM, for the period 1979-96. Li calculated the forced circulation patterns by linearly regressing the simulated and observed 200-hPa geopotential height fields upon a time series of the index Niño3. In the same study, Li performed also a singular value decomposition of the Northern Hemisphere 500-hPa geopotential height and the tropical Pacific

SST fields, again obtaining the same type of displacement between the simulated and observed geopotential patterns. As an hypothesis to explain the westward shifting of the simulated patterns, Li suggested that there are inaccuracies in the LMD AGCM convection parameterization, which may not respond correctly to the SST anomalies in the eastern Pacific.

Finally, it should be noted that the displacement between the simulated and observed patterns, found in our work, it is not due to the fact that the simulated and observed patterns were based in different temporal periods. In fact, recalculating the CCA with the PCs based on the period Dec/76 to Feb/88, we obtained a canonical correlation pattern ($r = 0.76$, fig. 4.22) similar to that of figure 4.21, presenting the same spatial shift with respect to the simulated pattern. In this CCA we retained only the PCs 2 to 5. The selection of the PCs was also based in the correlation coefficients between each PC and the time series of the index Niño3.4. All retained PCs have values of the correlation coefficient above the statistical significance level of 77.5%. The PC1 (NAO) was not included in the analysis because its correlation value is small, inferior to the level of statistical significance of 55%.

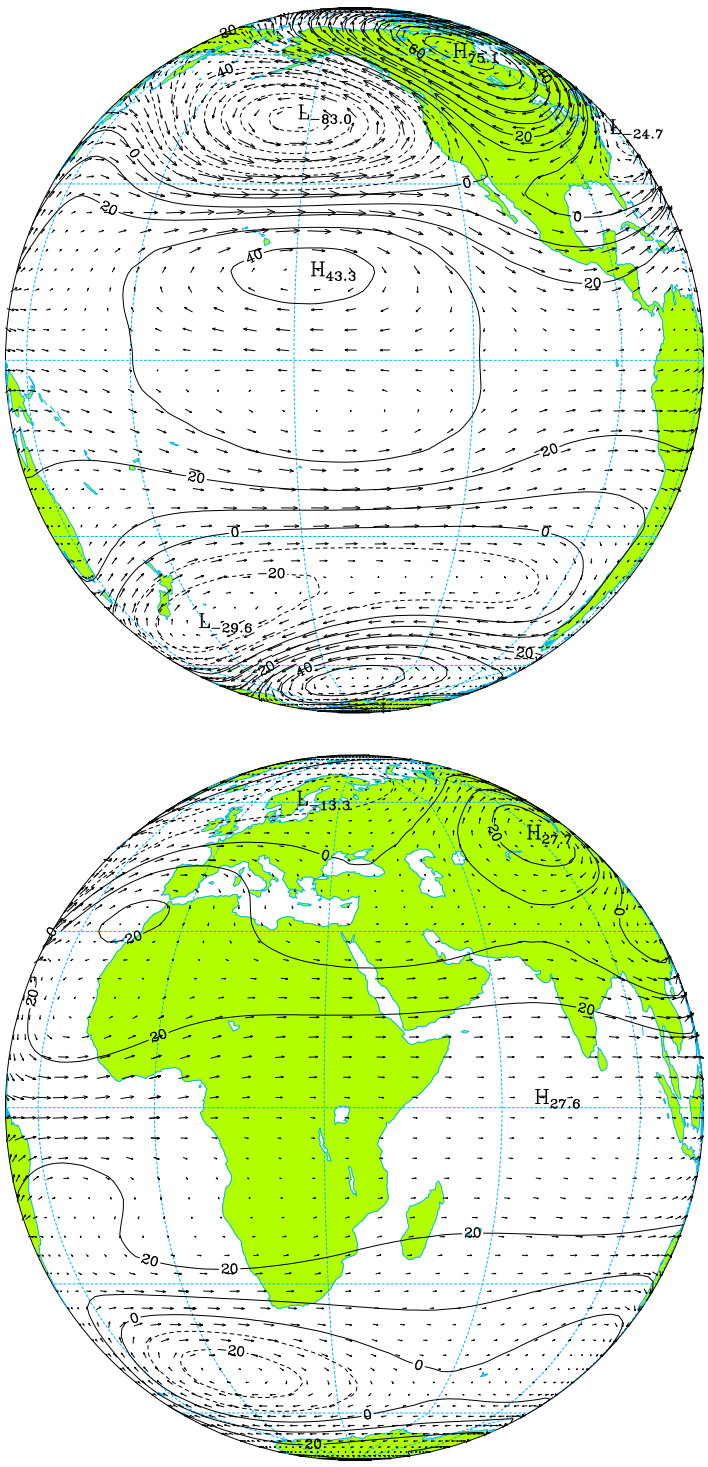

Figure 4.21: Canonical pattern of the observed barotropic circulation associated with the index Niño3.4 ($v_{max.} = 9.2\,\mathrm{m\,s^{-1}}$). See in the text how this pattern was obtained.

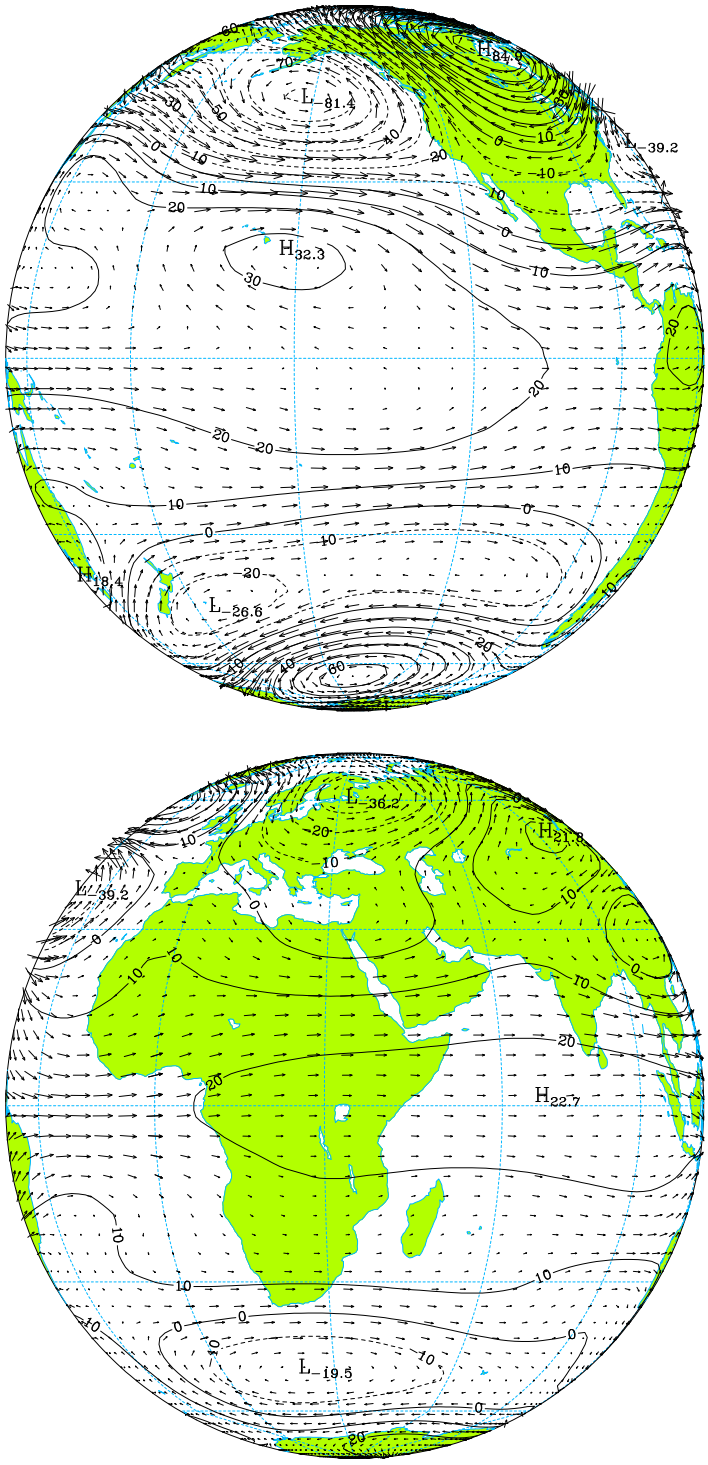

Figure 4.22: As in figure 4.21 but with the CCA based on the period Dec/76-Feb/88 ($v_{max.} = 7.0\,\mathrm{m\,s^{-1}}$).

4.4 Fourth baroclinic component

The total transient energy associated with the 4$^{\text{th}}$ baroclinic component of the NCEP atmosphere presents a value close to the peak at the 5$^{\text{th}}$ baroclinic component (*cf.* fig. 4.2). On the other hand, the 4$^{\text{th}}$ baroclinic vertical structure function is positive in the lower troposphere (below 460 hPa) and negative in the upper troposphere. Such vertical structure with opposite signs in the upper and lower troposphere has the adequate characteristics to capture the variability of the intertropical atmosphere associated with the ENSO cycle.

Figure 4.23 shows the horizontal spectrum of the total transient energy associated with the Rossby modes and the Kelvin modes ($s \leq 3,\ l = 0$) of the fourth baroclinic component. As it can be observed the higher energy values are associated with modes of meridional indices $l \leq 3$, i.e., with intertropical modes. Remember that for small equivalent heights, the modes of low meridional indices are confined to the intertropical region; and the value of the equivalent height associated with the 4th baroclinic vertical structure function is $h_4 = 279\,\text{m}$.

The maps of figure 4.24 show the spatial distributions of the total and kinetic tran-

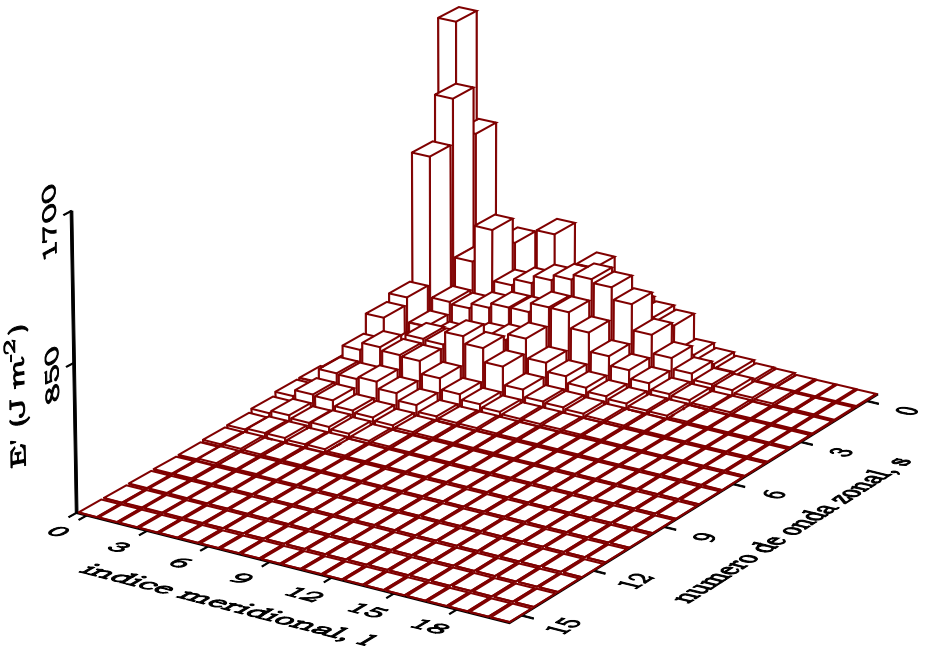

Figure 4.23: Total transient energy associated with the Rossby modes and Kelvin modes ($s \leq 3,\ l = 0$) of the 4$^{\text{th}}$ baroclinic component of the NCEP atmosphere.

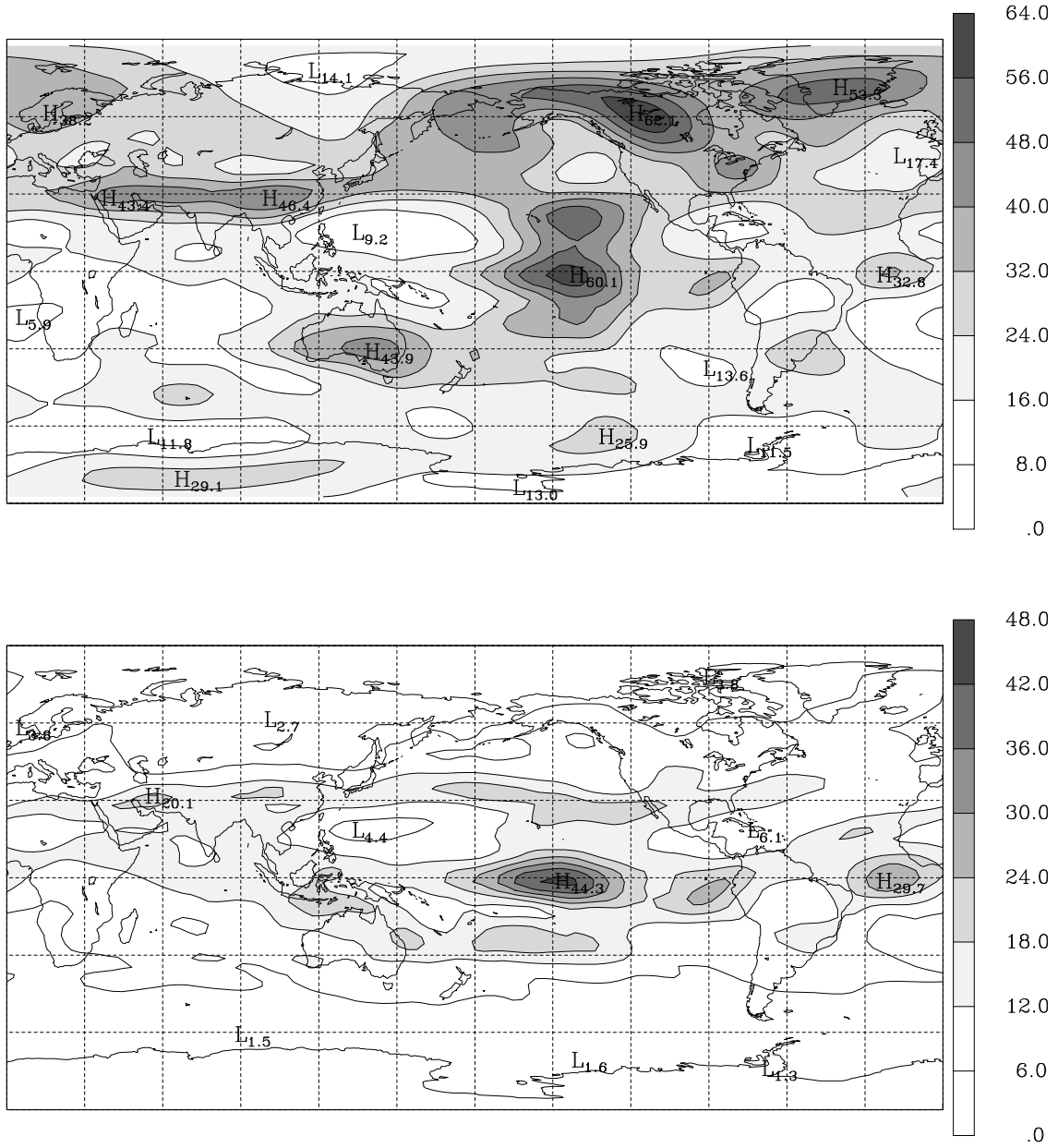

Figure 4.24: Spatial distribution of the total (*top*) and kinetic (*bottom*) transient energies associated with the 4$^{\text{th}}$ baroclinic component of the NCEP atmosphere. The units are kJ m^{-2}.

sient energies associated with the 4$^{\text{th}}$ baroclinic component of the NCEP atmosphere. As in the case of the simulated atmosphere, one can observe that the available potential energy (i.e. the geopotential variability) is the dominant parcel of the extratropical variability of the circulation projected onto the 4$^{\text{th}}$ baroclinic component, whereas the kinetic energy is the dominant contribution over the equatorial region.

4.4.1 Variability patterns

The variability patterns of the circulation projected onto the fourth baroclinic component were obtained performing the CPCA on the Kelvin modes ($s \leq 3$) and Rossby modes with zonal wavenumbers $s \leq 5$ and meridional indices $l \leq 11$ (*cf.* fig. 4.23).

The PC1 explains 19.3% of the variability of the fourth baroclinic component, and the respective pattern is shown in the top panel of figure 4.25. In the intertropical region, this pattern is very similar with the one associated with the PC1-F of the fourth baroclinic component of the forced circulation simulated by the MU AGCM (*cf.* fig. 3.34, *top panel*). The similarities between the patterns are even bigger if the CPCA is performed only on the intertropical modes ($s \leq 4, l \leq 5$) as it was done in the case of the CPCA of the 4^{th} baroclinic component of the forced circulation simulated by the MU AGCM. In figure 4.25 the bottom map represents the pattern associated with the PC1 of the intertropical modes of the fourth baroclinic component of the NCEP atmosphere. It is important to notice that this PC explains 29.2% of total transient energy projected onto the intertropical modes of the 4^{th} baroclinic component. Another point is that the energy associated with the PC1 of the intertropical modes is equal to 90% of the energy associated with the PC1 calculated retaining all the modes with $s \leq 5$ and $l \leq 11$.

As it was observed in the case of the barotropic component, the EOF1-F of the simulated 4^{th} baroclinic component presents a westward shift of about 15 a 30º relatively to the observed pattern. However, in the present comparison it should be taken into account that the observed EOF may contain a fraction of internal variability.

The top panel of figure 4.26 shows the divergence field associated with the EOF1 of the intertropical modes. This map represents a divergence pattern of the Walker Circulation anomalies associated with the ENSO cycle. This divergence pattern is similar to the respective pattern associated with the EOF1 of the fourth baroclinic component of the forced circulation simulated by the MU AGCM (*cf.* fig. 3.35). It should be noted also the westward shift of the simulated divergence field with respect to the observed field, as referred before for the patterns of the respective EOFs.

The results obtained with the MU AGCM suggest that the first EOF of the 4^{th} baroclinic component of the NCEP atmosphere should essentially represent forced circulation. The existence of an oceanic forcing pattern associated with that EOF was investigated. With this purpose, the PC1 of the intertropical modes of the 4^{th}

baroclinic component of the NCEP atmosphere was correlated with the SST anomalies over all the oceans. The SSTs were obtained from the *Global sea-Ice and Sea Surface Temperature (GISST)* data set of the Hadley Centre. The bottom panel in figure 4.26 shows the correlation map between the PC1 and the winter (DJF) mean SST anomalies for the period 1973-94. This map represents a forcing pattern associated with the ENSO cycle, practically identical to the one obtained for the PC1-F of the 4^{th} baroclinic component of the forced circulation simulated by the MU AGCM (*cf.* fig. 3.36). One should remember that the correlation map of PC1-F of the barotropic component and that of the PC1-F of the fourth baroclinic component are identical (*cf.* sec. 3.9.3).

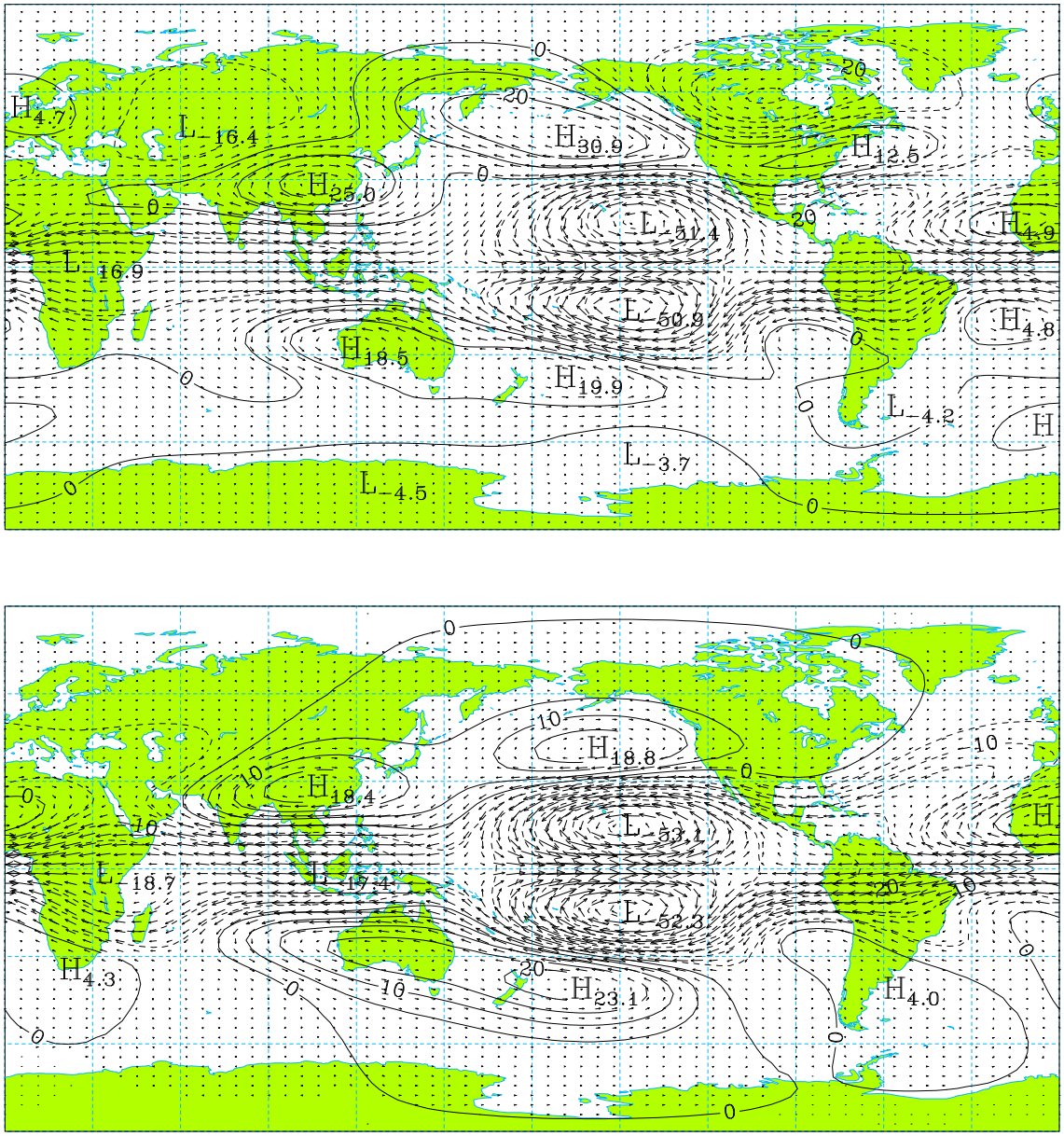

Figure 4.25: Patterns associated with the PC1 of the 4$^{\text{th}}$ baroclinic component of the NCEP atmosphere, retaining in the CPCA the Kelvin modes ($s \leq 3$) and the Rossby modes with $s \leq 5$ and $l \leq 11$ (*top*, $v_{max.} = 9.3\, m\, s^{-1}$), and retaining only the intertropical modes (*bottom*, $v_{max.} = 9.2\, m\, s^{-1}$).

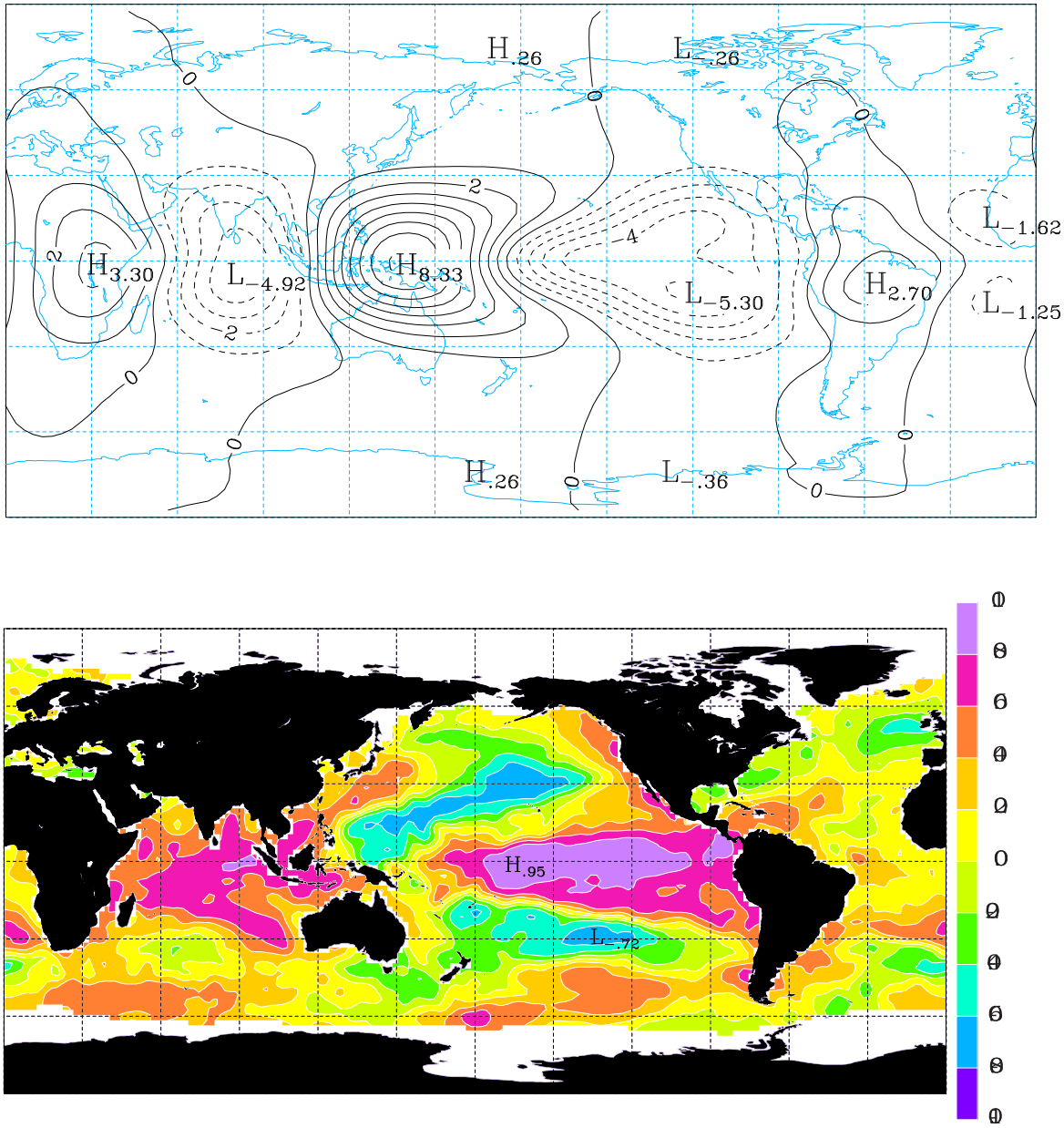

Figure 4.26: Divergence pattern associated with the EOF1 (*top*, units $10^{-7}\,s^{-1}$) and the correlation map between the respective PC and the SST anomalies (*bottom*). These maps were obtained retaining in the CPCA only intertropical modes of the 4$^{\text{th}}$ baroclinic component of the NCEP atmosphere.

4.5 Fifth baroclinic component

The horizontal spectrum of the total transient energy associated with the Rossby modes and the Kelvin modes ($s \leq 2,\ l = 0$) of the fifth baroclinic component of the NCEP atmosphere is shown in figure 4.27. Comparing to the spectrum of the fourth baroclinic component (fig. 4.23), it can be observed that the highest values of the total transient energy are now associated with modes of higher meridional indices. This fact suggests that the 5$^{\text{th}}$ baroclinic component must capture essentially extratropical variability, as it can be observed in the map of total transient energy presented in figure 4.28.

The total transient energy of the extratropical circulation projected onto the 5$^{\text{th}}$ baroclinic component is dominated by the contribution due to the available potential energy, as it can be concluded by the comparison of the map of total energy with that of kinetic transient energy, which is also shown in figure 4.28.

The highest variability center in the map of the total transient energy is located over northwestern Canada, extending over the Alaska. Over the Atlantic appears a dipolar structure as for the barotropic component, although, in the present case, the

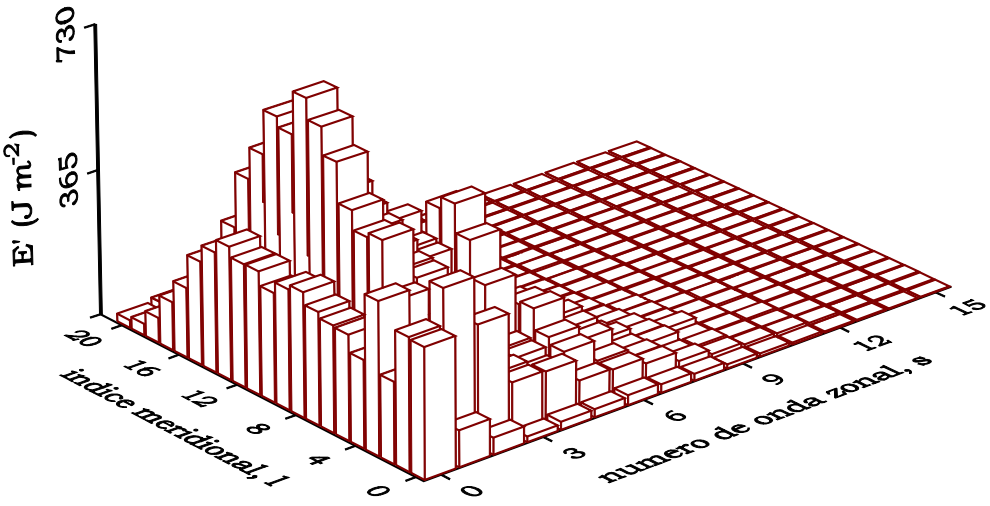

Figure 4.27: Total transient energy associated with the Rossby modes and the Kelvin modes ($s \leq 2,\ l = 0$) of the 5$^{\text{th}}$ baroclinic component of NCEP atmosphere.

dipole is more well defined and is located northwest of the respective centers of the barotropic component.

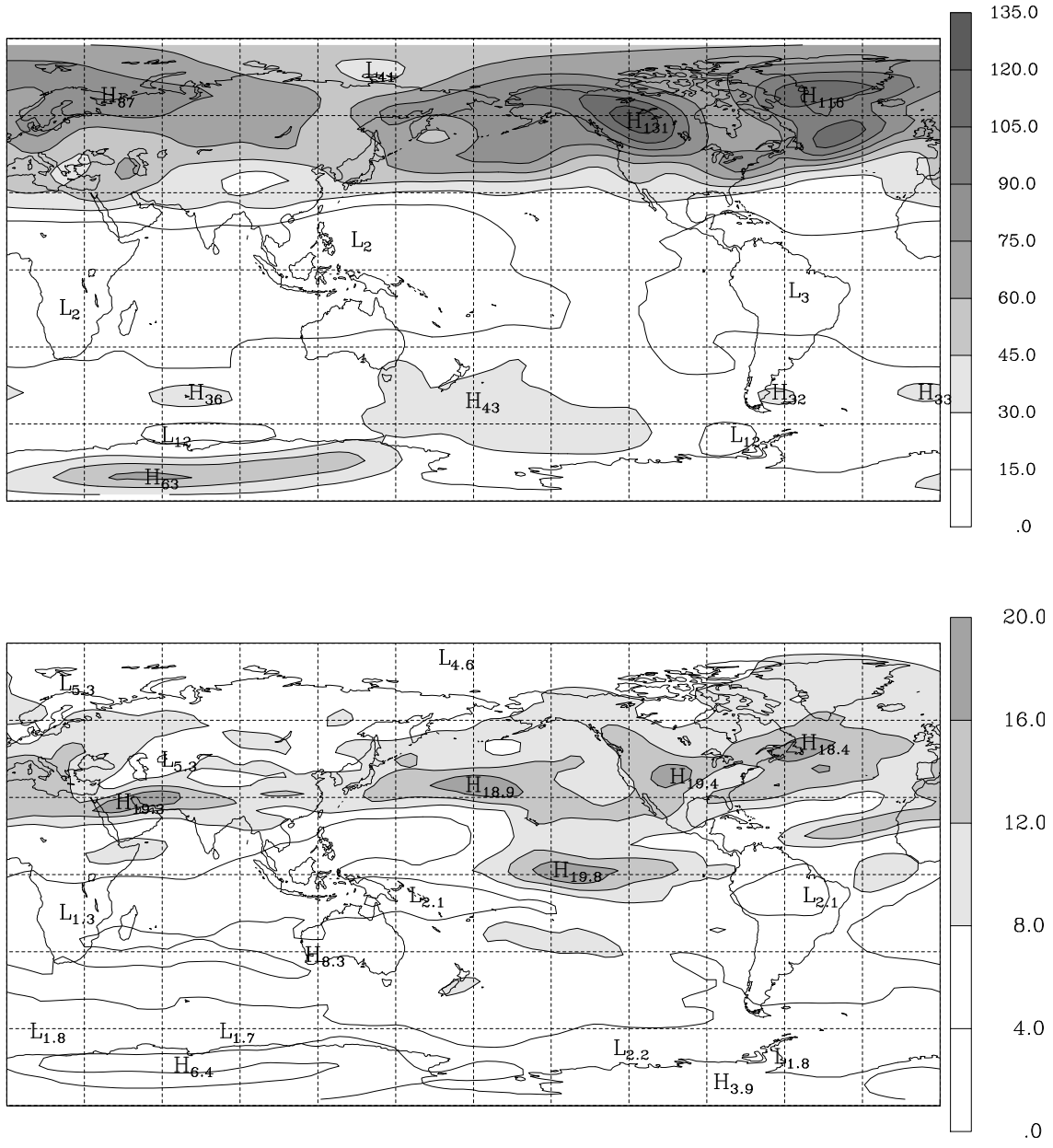

Figure 4.28: Total (*top*) and kinetic (*bottom*) transient energies associated with the 5^{th} baroclinic component of NCEP atmosphere. The units are $\mathrm{kJ\,m^{-2}}$.

4.5.1 Variability patterns

In the CPCA performed on the fifth baroclinic component, we retained the Kelvin modes ($s \leq 2$) and the Rossby modes with zonal wavenumbers $s \leq 5$ and meridional indice $l \leq 17$ (*cf.* fig. 4.27).

PCs 1 and 2 explain, respectively, 12.4% and 9.4% of the variability of the circulation projected onto the 5$^{\text{th}}$ baroclinic component of NCEP atmosphere. The pattern of the EOF1 (fig. 4.29) presents the familiar structure of the PNA teleconnection pattern. The pattern of the EOF2 (fig. 4.30) presents a more complex structure with a zonal depression band around latitude 45$^{\text{o}}$ N extending from the eastern North America to the Europe, and prolonging to northeast with a centre over the Urals. At north of this depression band an anticyclonic circulation is present, centered over the southwestern Greenland. The location of this anticyclonic circulation may be related to a southwestward axis tilt of the depression in the NAO structure, as it was verified in the case of the NAO simulated by the MU AGCM.

As it was previously mentioned, the fifth baroclinic component represents mainly extratropical variability. On the other hand, the projection of the tropospheric circulation onto the 5$^{\text{th}}$ baroclinic vertical structure, $G_5(p)$, corresponds to a weighted difference between the circulations at the upper and lower troposphere (*cf.* fig. 4.1). Considering these facts and that the pattern of the EOF1 reproduces the PNA teleconnection pattern, and the pattern of the EOF2 presents characteristics that may be associated with the NAO, we performed a combined CPCA on the barotropic and 5$^{\text{th}}$ baroclinic components. These calculations are identical to the ones described in section 3.8.2 with the goal to investigate whether the PNA and the NAO have vertical structures equivalent to the barotropic, or whether, on the contrary, they have baroclinic characteristics, i.e., whether the geopotential anomalies are centered on axes tilted to the vertical and the horizontal wind changes the direction with the height.

As the CPCA performed on the barotropic component only revealed distinct patterns of the PNA and the NAO for the period Dec/76-Feb/88, the combined CPCA on the barotropic and 5$^{\text{th}}$ baroclinic components was also performed for that period.

Figure 4.31 shows the total transient energy of the circulation projected onto the 5$^{\text{th}}$ baroclinic component, for the period from Dec/76 to Feb/88. As already mentioned this baroclinic component presents a peak in the observed vertical energy spectrum like the fourth baroclinic component in the case of the simulated vertical energy spectrum.

It is also interesting to notice the similarity of the maps of the total transient energies associated with those two baroclinic components (*cf.* figs. 3.12 and 4.31).

The patterns of the combined EOF1 associated with the barotropic and fifth baroclinic components are presented in figures 4.32 and 4.33, and the patterns corresponding to EOF2 are presented in figures 4.36 and 4.37.

The NAO structure (figs. 4.32 and 4.33) is similar to the structure simulated by the MU AGCM (figs. 3.30 and 3.31). However it should be noted that in the simulated pattern for the NAO, besides the already mentioned eastward shift on the position of the circulation centers, there is an anticyclonic circulation over the Caucasian region associated with the fourth baroclinic component. This difference may result from one or more of the following causes: a) from the difference between the vertical structures of the simulated fourth baroclinic component and of the fifth baroclinic component of the NCEP atmosphere; b) of considering only one series of 12 years for the observations; c) and/or deficiency of the model.

The NAO explains 14.2% of the intraseasonal and interannual variability of the circulation projected onto the barotropic and 5^{th} baroclinic components of the NCEP atmosphere. The barotropic component contributes with 77.4% of the total energy of the circulation projected onto the NAO, and the remaining 22.6% are due to the fifth baroclinic component.

The barotropic and fifth baroclinic components of the extratropical circulation associated with the NAO are shown in figure 4.34, using polar stereographic projections. These projections allow an easier comparison of the positions of the variability centers.

The depression over Greenland has the axis tilted to southwest and the wind over the Iceland and Greenland Sea region presents a anti-clockwise rotation with height, and over Canada a clockwise rotation. The axis of the anticyclonic circulation over the Atlantic presents an westward tilting but the wind doesn't rotate with height. The depression southwest of the Aleutians and the anticyclonic circulation over the western North America present equivalent barotropic vertical structures.

Admitting that the barotropic and fifth baroclinic components capture almost all of the 3-dimensional variability of the NAO and the PNA, one may obtain the patterns of these variability modes, in any isobaric level, through the following linear combination

$$(u'(p), v'(p), \phi'(p))_i^T = G_0(p) \cdot \text{EOF}i_{m=0} + G_5(p) \cdot \text{EOF}i_{m=5}, \tag{4.8}$$

where $m = 0$ and $m = 5$ denote, respectively, the barotropic and fifth baroclinic com-

ponents of the 3-dimensional fields $(u, v, \phi)_i^T$ associated with the combined EOFi. Thus the equation 4.8 can be used to determined the anomalies of the thermal wind,$\mathbf{V}_T$, and of thickness of a layer between two isobaric levels. Because the barotropic vertical structure is approximately constant, it must be expected that thermal wind and thickness anomalies are similar to the pattern associated with the fifth baroclinic component of the respective EOF. The top panel in figure 4.35 shows the thermal wind and thickness anomalies between the levels of 300 hPa and 850 hPa associated with the NAO. As an example, taking a point over Iceland, the module of the anomaly of the thermal wind between the 300 hPa and the 850 hPa is $|\mathbf{V}_T| = 1.2\ \mathrm{m\,s^{-1}}$ and the anomalies of the horizontal wind turn $\sim 23^{\mathrm{o}}$ between the two levels.

The bottom panel in figure 4.35 shows the correlation map between PC1 of the combined CPCA and the anomalies of the 850 hPa temperature field. As it can be seen by comparison of the maps in figure 4.35, the wind rotation with height is consistent with the orientation of the horizontal gradients of the temperature anomalies associated with the NAO.

The PC2 explains 12.5% of the variability of the circulation projected onto the barotropic and fifth baroclinic components of the NCEP atmosphere. The barotropic component contributes to 74.4% of the total transient energy associated with this PC, and the remaining 25.6% are due to the fifth baroclinic component. The patterns associated with the combined EOF2 (figs. 4.36 and 4.37) show characteristics similar to the PNA but, in the barotropic component, the anticyclonic circulation over North America is dislocated to northeast relatively to the respective center in figure 4.20. The difference is yet bigger if we compare the position of the anticyclonic center with that of the maximum teleconnection of the PNA over Canada ($55^{\mathrm{o}}\,\mathrm{N}, 115^{\mathrm{o}}\,\mathrm{W}$) [Wallace and Gutzler, 1981]. The same observation can be made in relation to the depression over the eastern coast of the United States.

As it was done for the combined EOF1, the stereographic projections of the two vertical components of the combined EOF2 are shown in figure 4.38, for an easier comparison of the positions of the variability centers. The axis of the depression over the Atlantic coast of the United States has an westward tilting, and the axis of the depression south of the Aleutians has a slight tilting to southwest. The anticyclonic circulation over Canada has the axis tilted to southwest and the horizontal winds present a clockwise rotation with height, over the north of the Alaska, and an anti-

clockwise rotation over the Greenland sea and Iceland region. The map of the thermal wind and thickness anomalies of the layer between levels 850-300 hPa associated with the combined EOF2, as well as the correlation map between the PC2 and the anomalies of the 850-hPa temperature field are shown in figure 4.39. As it can be observed in the figure, the wind rotation with height is consistent with the orientation of the horizontal gradients of the temperature anomalies associated with the PC2.

As referred in section 3.8.2, Perlwitz and Graf [1995] and Graf *et al.* [1997] obtained results indicating an equivalent barotropic vertical structure for the PNA, whereas the NAO seems to possess baroclinic characteristics. The results obtained with the simulations of the MU AGCM agree with the conclusions of Perlwitz and Graf and Graf *et al.*, and the results for the observed NAO are also in concordance with the same conclusions. With respect to the EOF2 of the NCEP atmosphere, which has a pattern similar to the PNA, it appears to have baroclinic characteristics. The baroclinicity of this pattern may result from the 'wrong' location of the circulation centers over Northwest Canada and over the eastern cost of the United States. In other words, the apparent baroclinicity of the EOF2 may result from the fact that it doesn't represent only the variability associated with the teleconnection pattern of the PNA.

Finally, it should be noted that we have performed the combined CPCA on the barotropic and fifth baroclinic components for the period of Dec/76 to Feb/88, because it was for this period that we obtained distinct teleconnection patterns of the PNA and the NAO. However, as it can be observed in figures 4.40 and 4.41, performing the combined CPCA on the barotropic and fifth baroclinic components for the whole period from 1973 to 1996, we obtained patterns similar to the ones based on the period from Dec/76 to Feb/88. Note that for the whole period from 1973 to 1996 the combined EOFs have an inverse order.

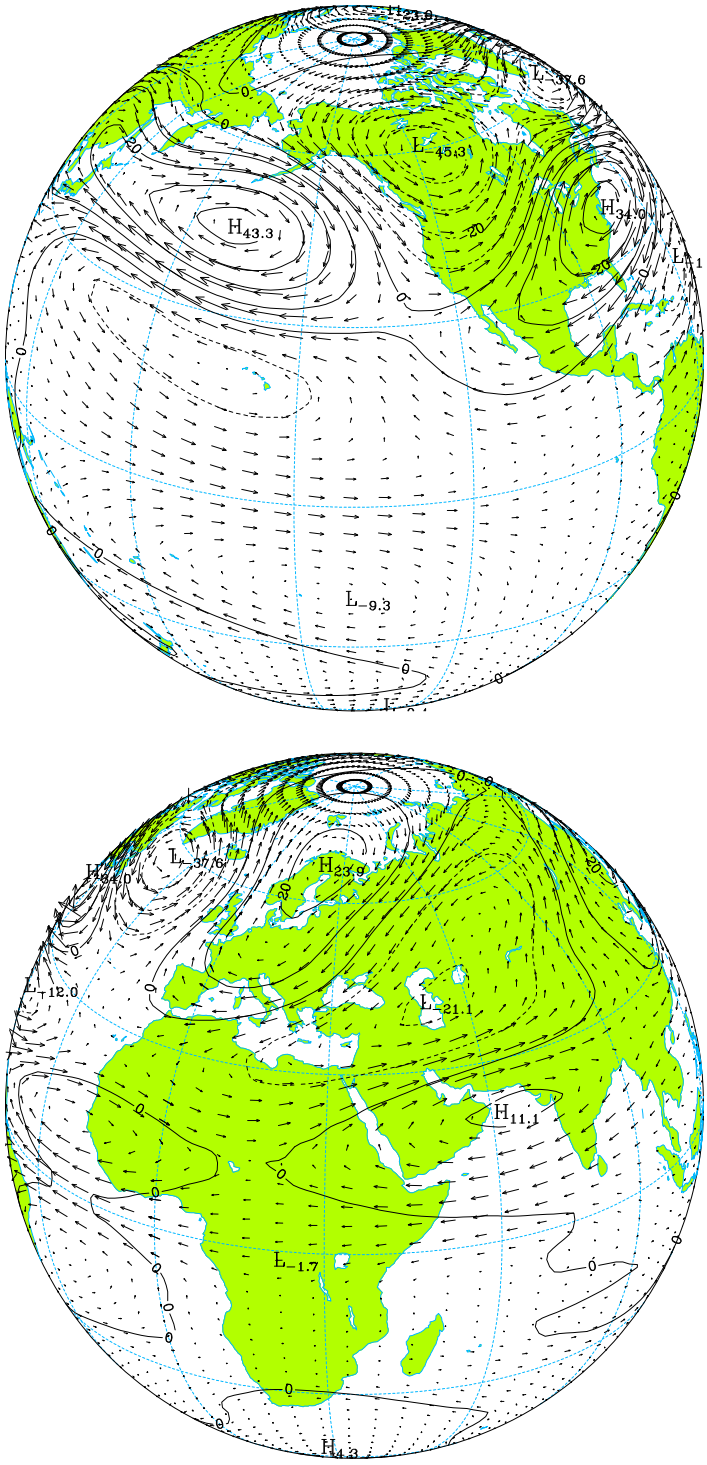

Figure 4.29: Pattern associated with the first EOF of the 5$^{\text{th}}$ baroclinic component of the NCEP atmosphere ($v_{max.} = 4.5\,\mathrm{m\,s^{-1}}$).

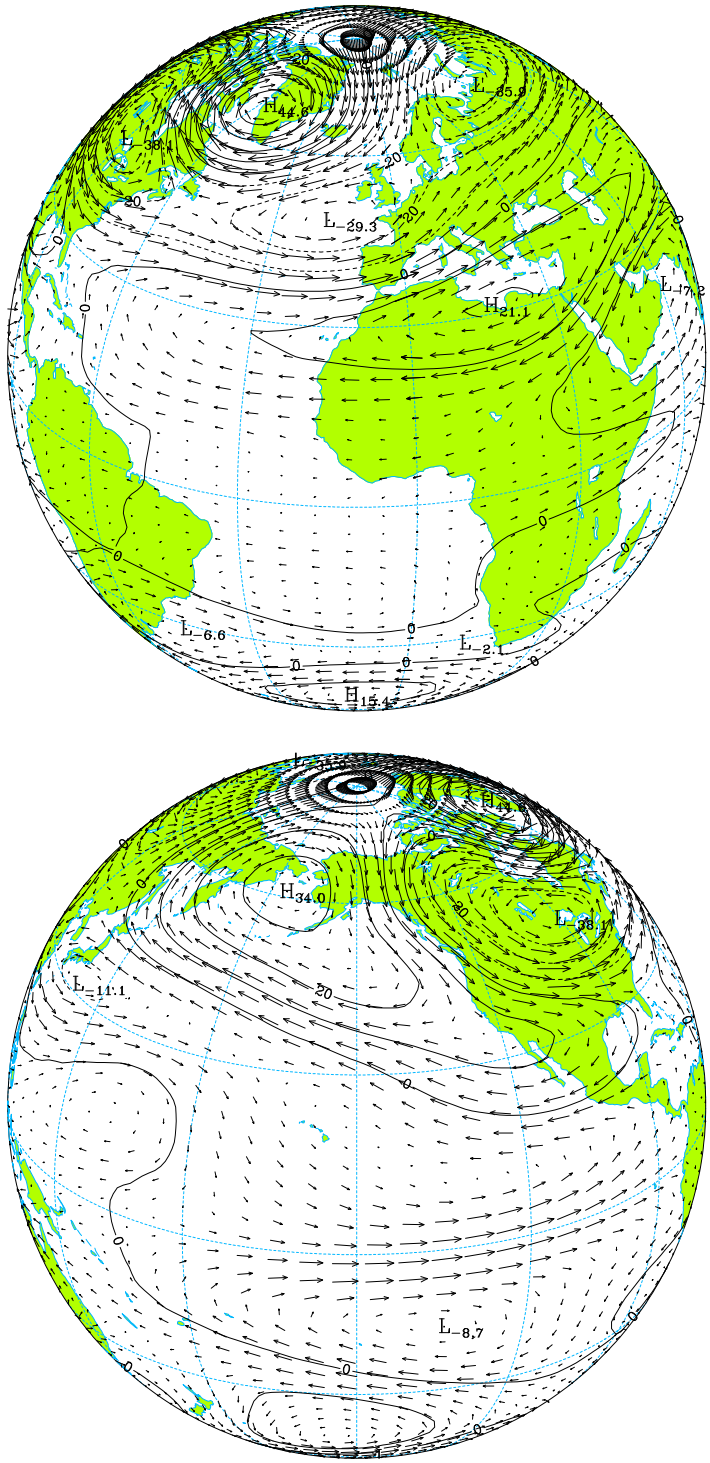

Figure 4.30: As in figure 4.29 but respecting to the EOF2 ($v_{max.} = 3.6\,\mathrm{m\,s^{-1}}$).

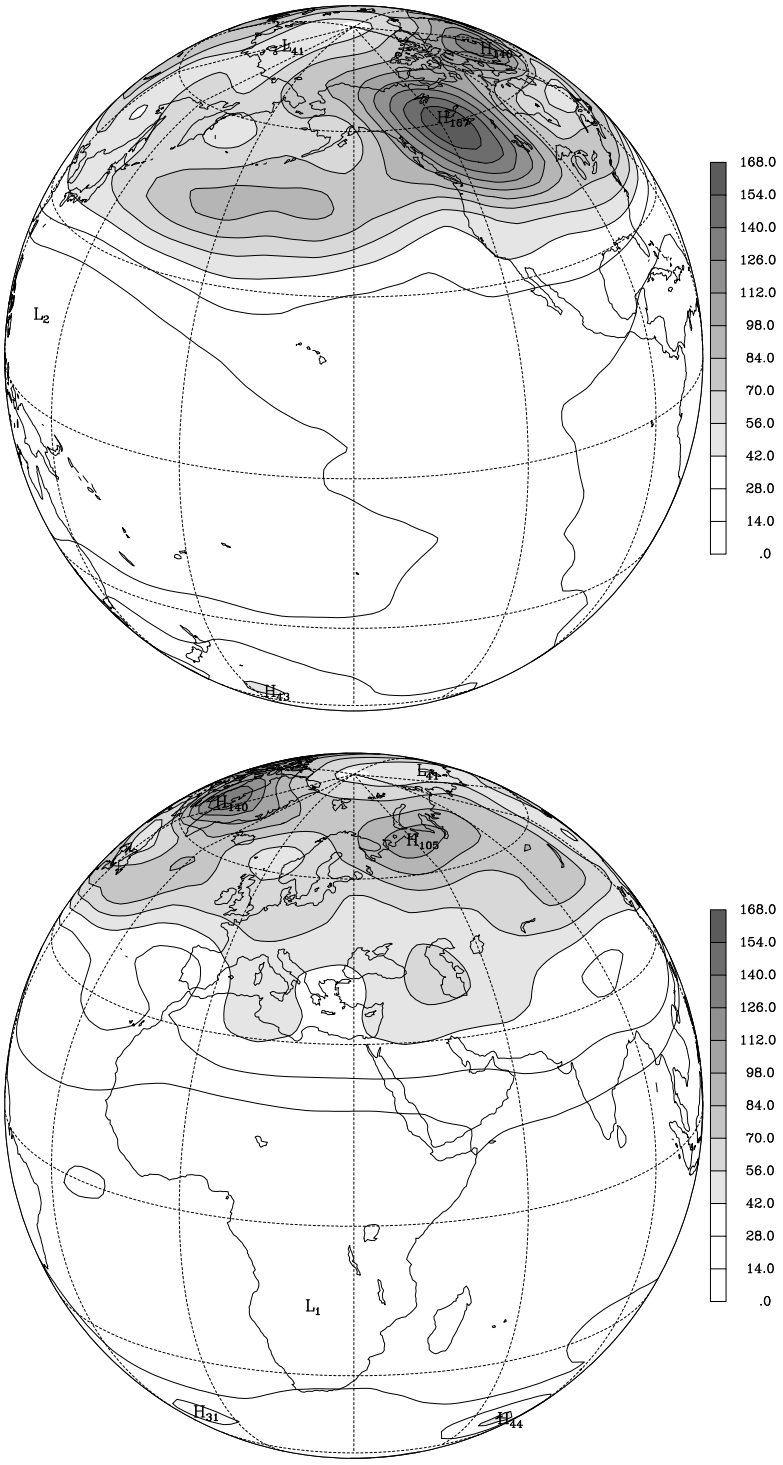

Figure 4.31: Total transient energy ($\mathrm{kJ\,m^{-2}}$) of the circulation projected onto the 5^{th} baroclinic component of the NCEP atmosphere, for the period from Dez/76 to Fev/88.

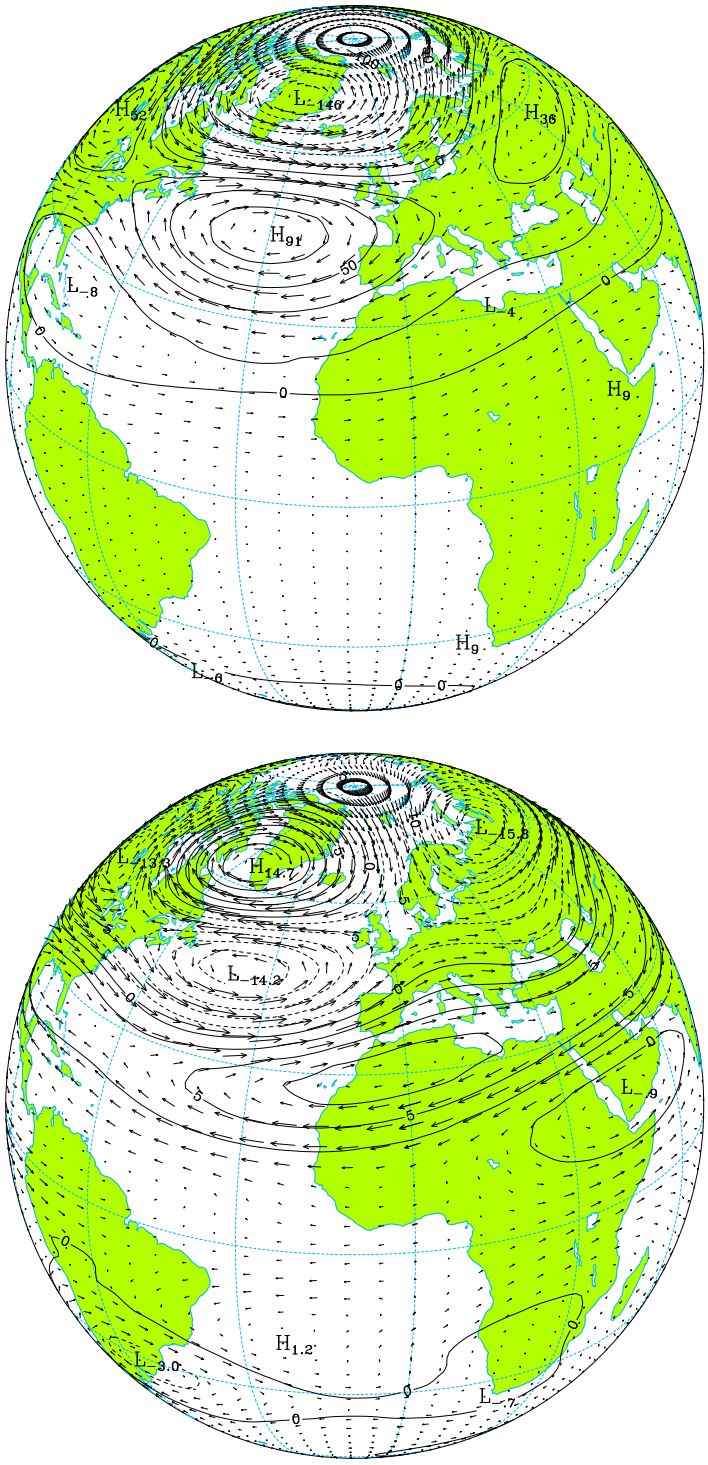

Figure 4.32: Barotropic (*top*, $v_{max.} = 10.2\,\mathrm{m\,s^{-1}}$) and 5$^{\mathrm{th}}$ baroclinic (*bottom*, $v_{max.} = 1.7\,\mathrm{m\,s^{-1}}$) components of the NAO, based on the period Dez/76-Fev/88.

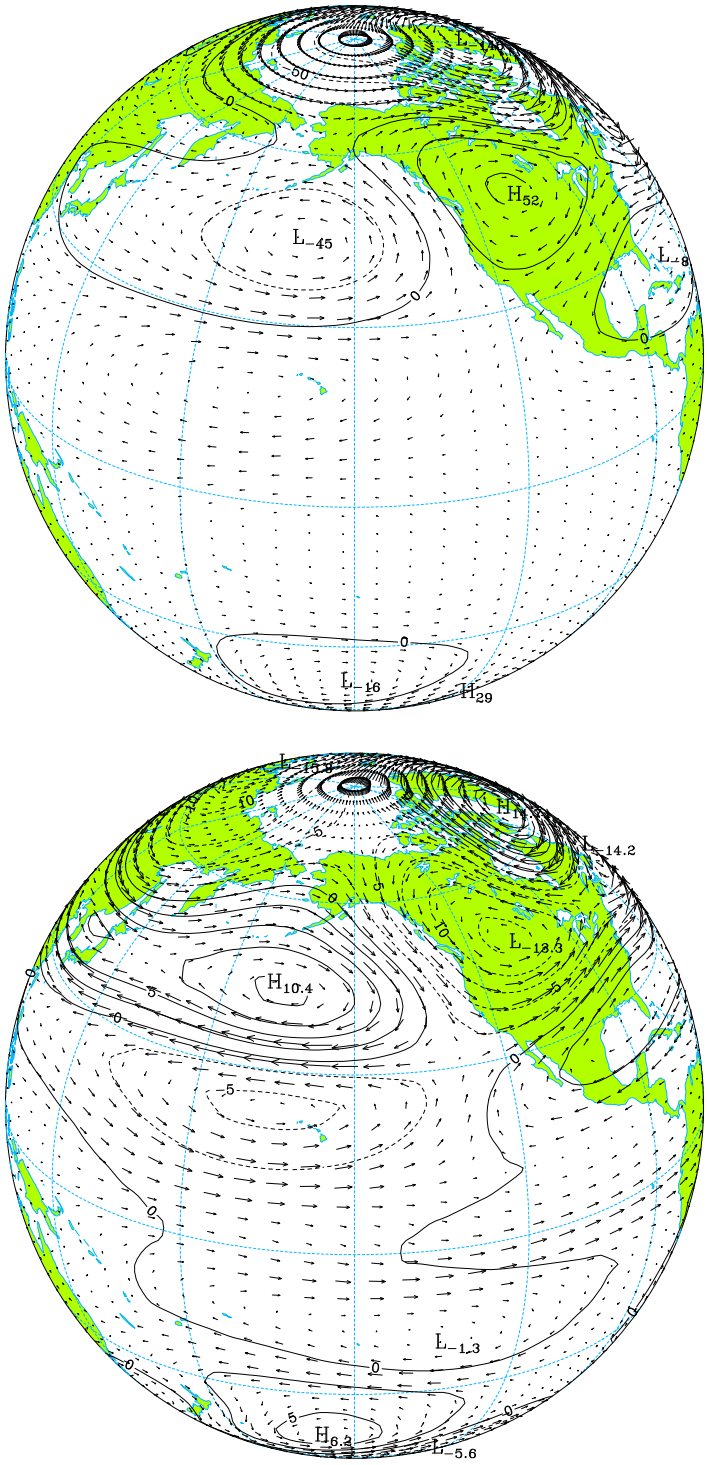

Figure 4.33: As in figure 4.32 but for the other Hemisphere.

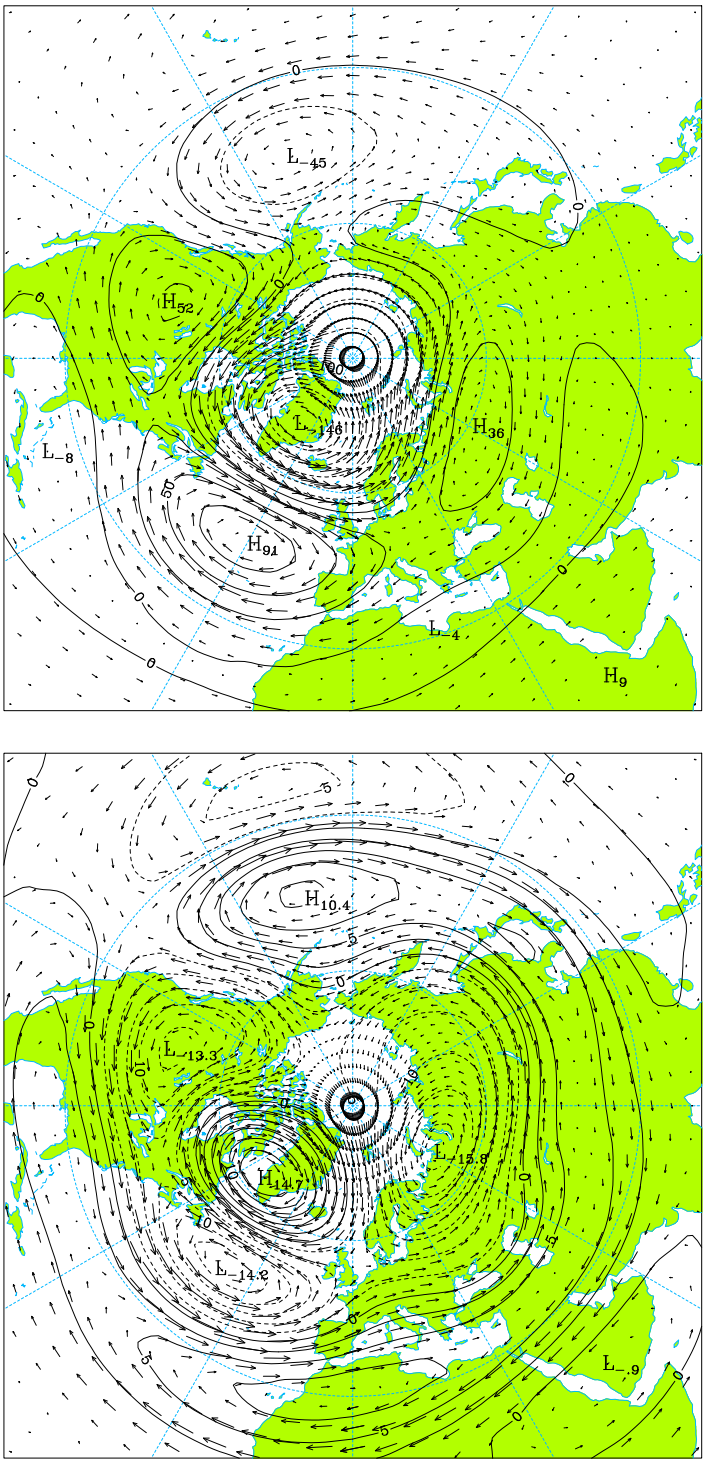

Figure 4.34: Polar stereographic projections of the barotropic *(top)* and 5$^{\text{th}}$ baroclinic *(bottom)* components of the NAO.

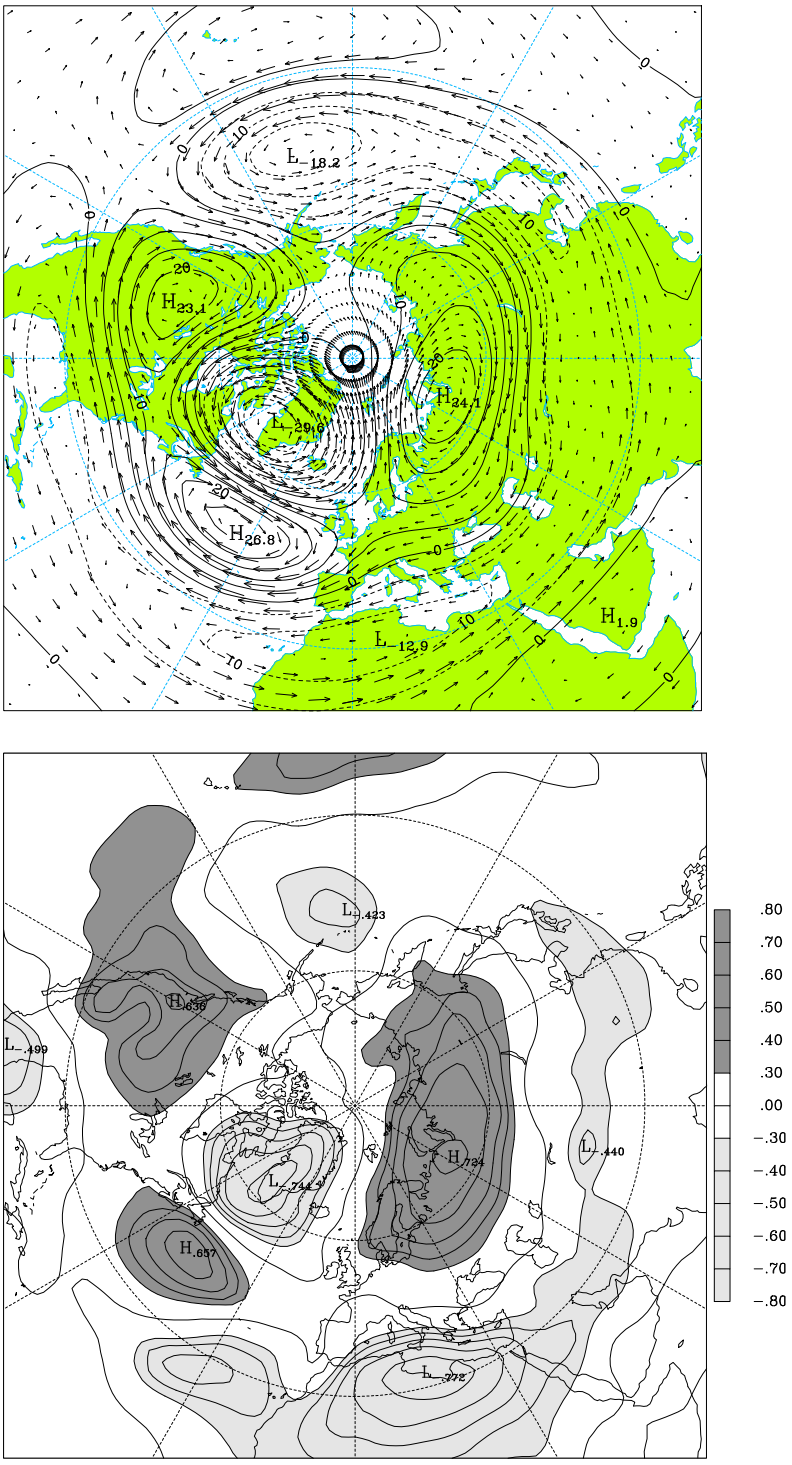

Figure 4.35: Thermal wind and thickness anomalies associated with the NAO for the layer 850-300 hPa (*top*, $v_{max.} = 3.2\,\mathrm{m\,s^{-1}}$), and correlation map between the combined PC1 and the 850 hPa temperature anomalies (*bottom*).

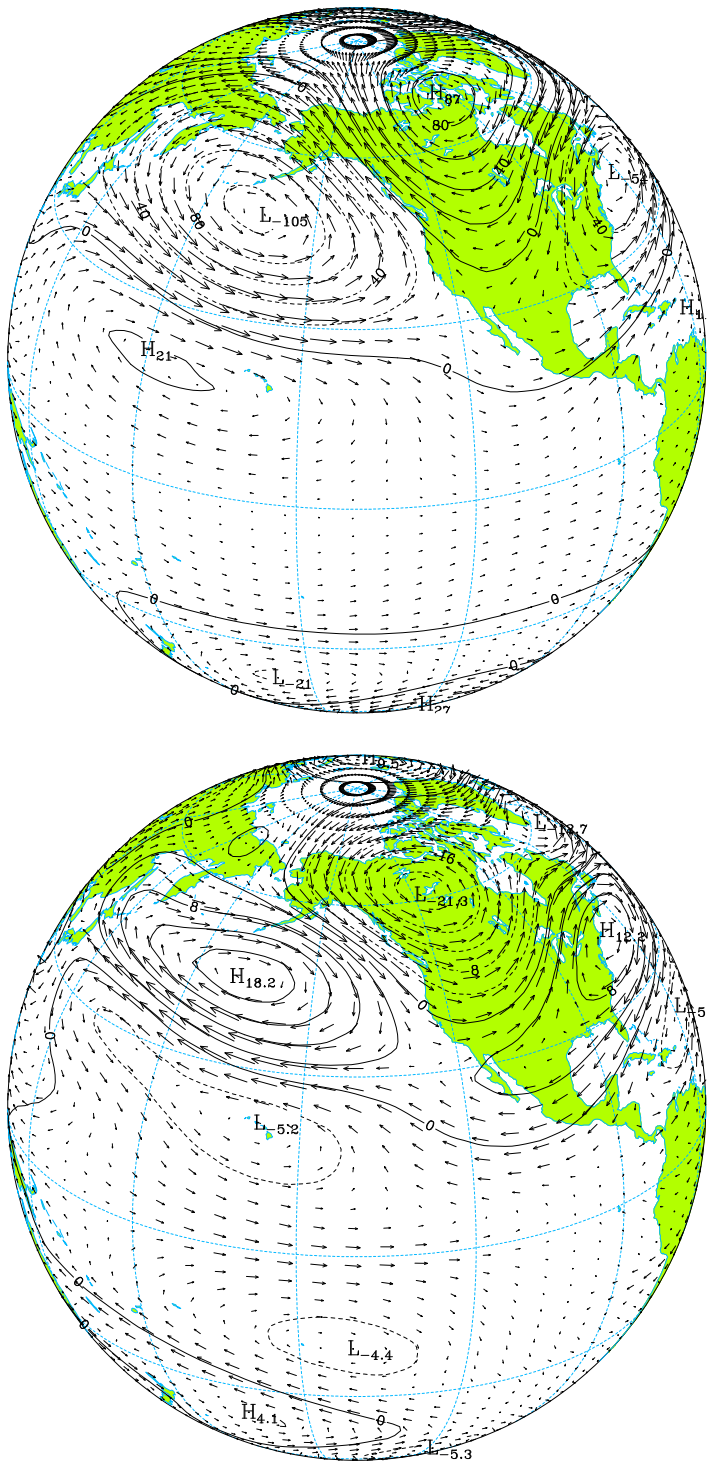

Figure 4.36: Barotropic (*top*, $v_{max.} = 7.5\,\mathrm{m\,s^{-1}}$) and 5$^{\mathrm{th}}$ baroclinic (*bottom*, $v_{max.} = 1.9\,\mathrm{m\,s^{-1}}$) components of the combined EOF2, based on the period Dez/76-Fev/88.

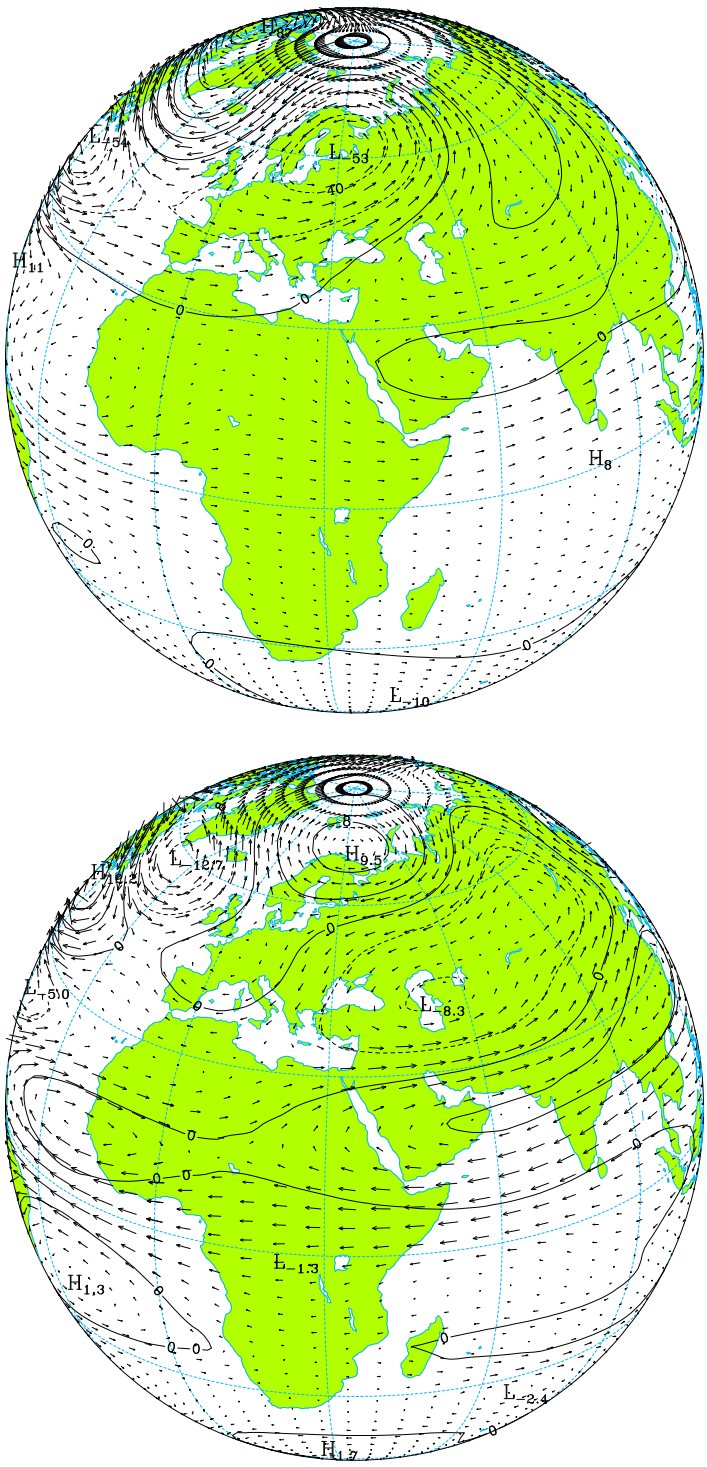

Figure 4.37: As in figure 4.36 but for the other Hemisphere.

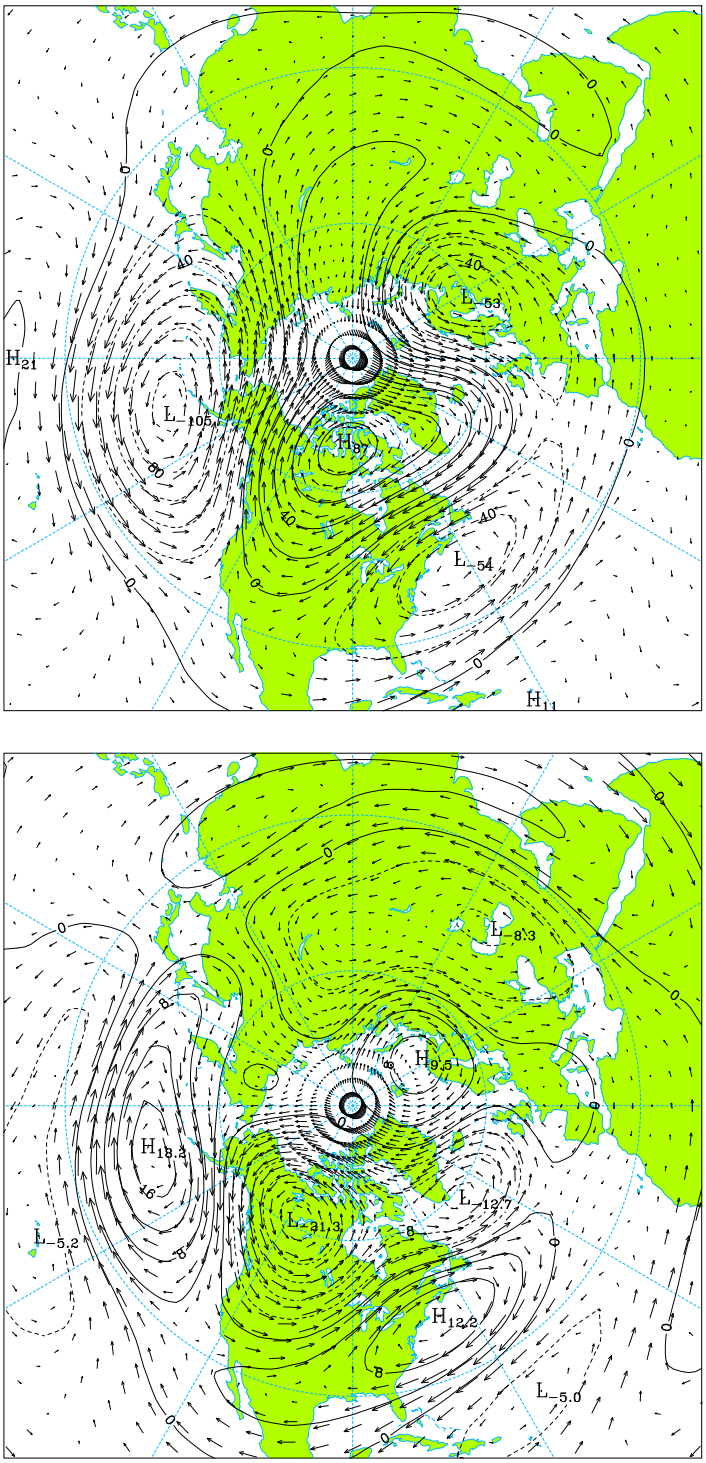

Figure 4.38: Polar stereographic projections of the barotropic *(top)* and 5$^{\text{th}}$ baroclinic *(bottom)* components of the combined EOF2.

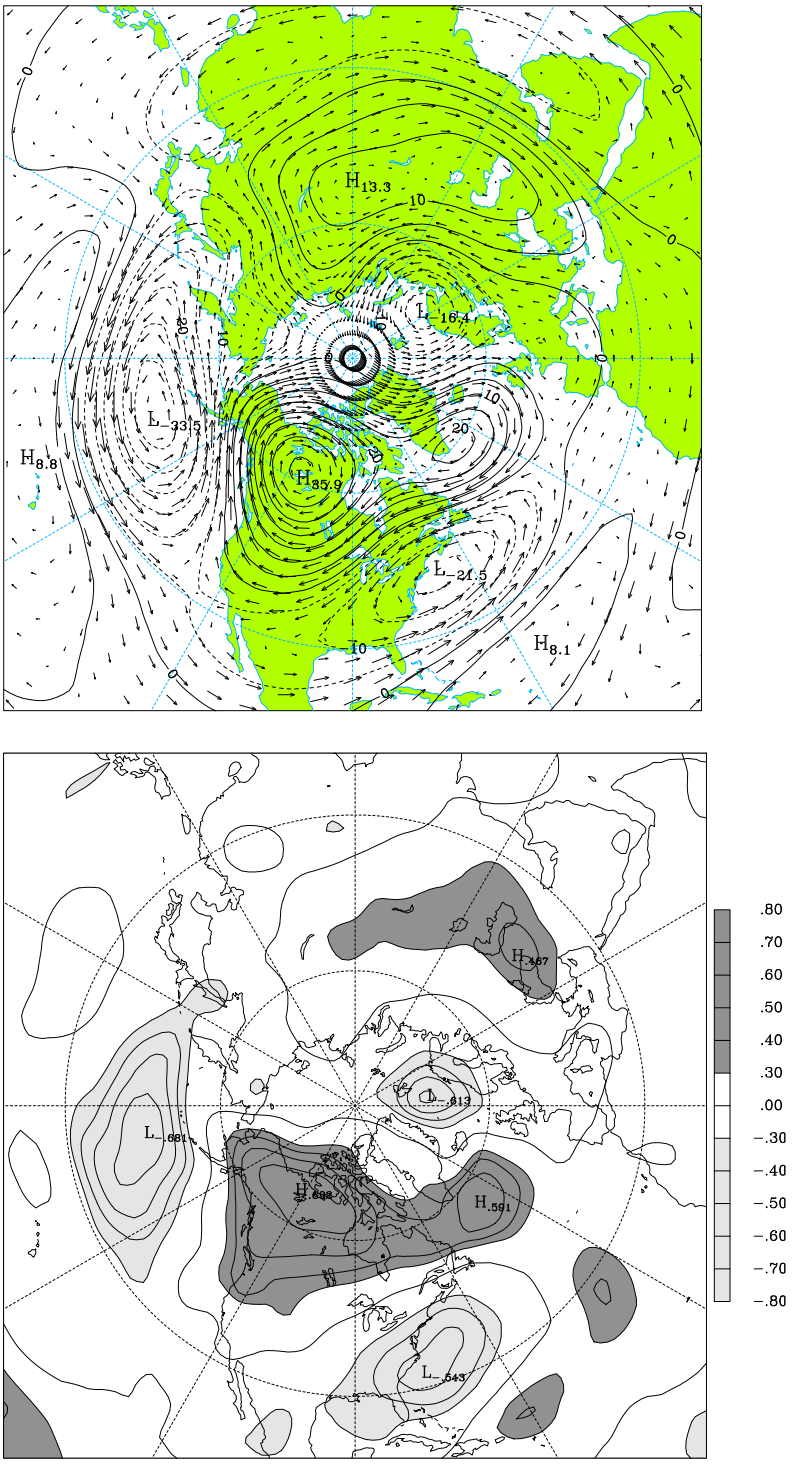

Figure 4.39: Thermal wind and thickness anomalies associated with the EOF2 for the layer 850-300 hPa *(top,* $v_{max.} = 3.2\,\mathrm{m\,s^{-1}}$*)*, and correlation map between the combined PC2 and the 850 hPa temperature anomalies *(bottom)*.

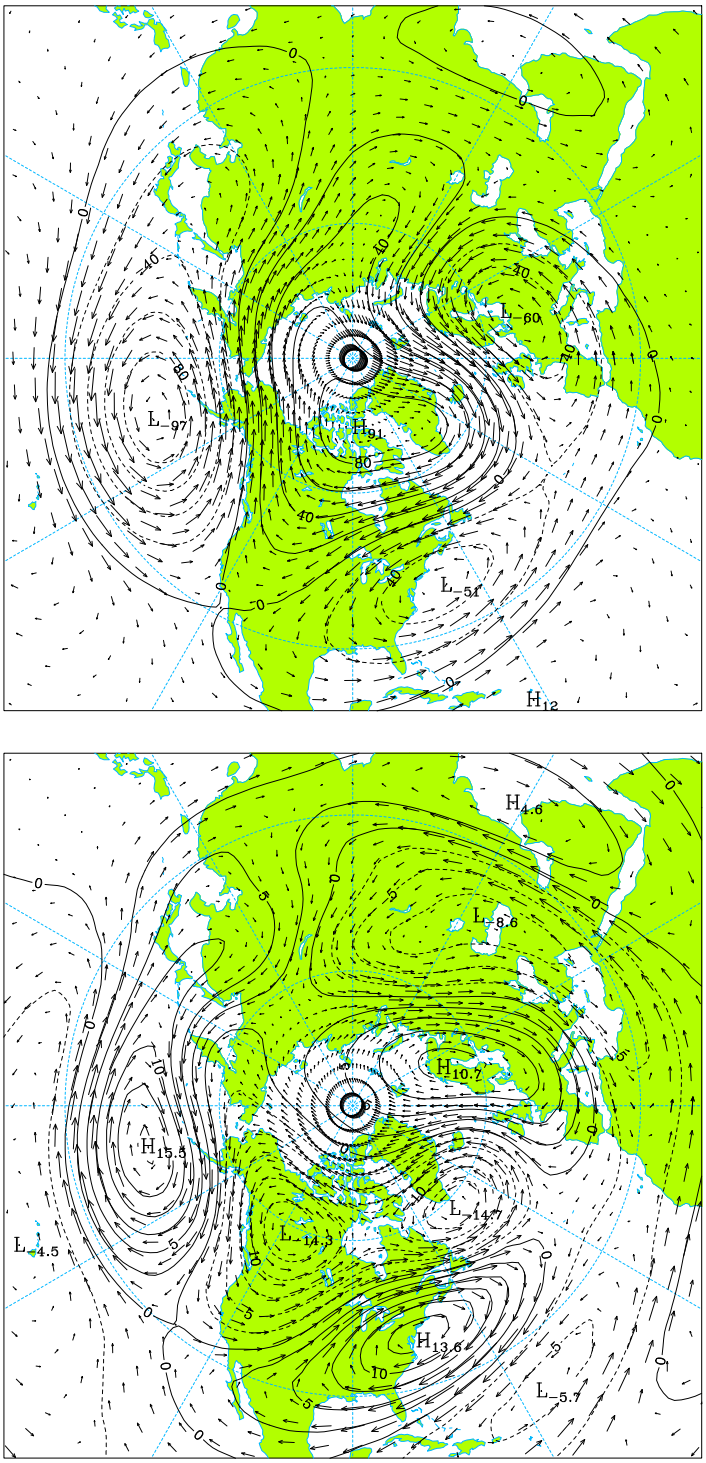

Figure 4.40: Polar stereographic projections of the barotropic *(top,* $v_{max.} = 7.5\,\mathrm{m\,s^{-1}}$*)* and 5$^{\mathrm{th}}$ baroclinic *(bottom,* $v_{max.} = 1.8\,\mathrm{m\,s^{-1}}$*)* components of the combined EOF1, based in the whole period 1973-96.

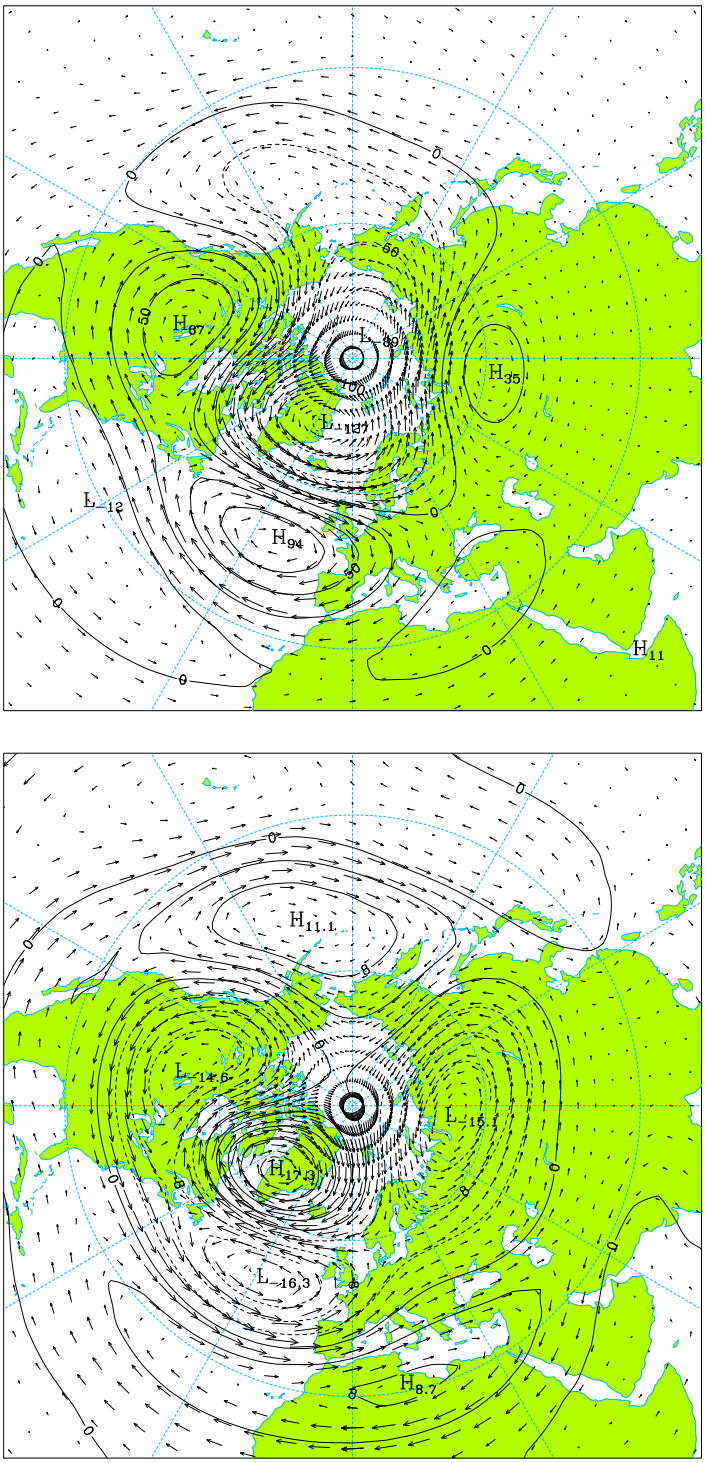

Figure 4.41: As in figure 4.40 but referring to the combined EOF2 *(top,* $v_{max.} = 9.8\,\mathrm{m\,s^{-1}}$*; bottom,* $v_{max.} = 1.8\,\mathrm{m\,s^{-1}}$*)*.

4.6 Second baroclinic component

The vertical structure function of the second baroclinic component of the NCEP atmosphere has relatively small values in the troposphere ($|G_2(p)| \leq 0.28$, if $p \geq 130$ hPa). In the stratosphere $G_2(p)$ has much higher values, with a maximum in the lower stratosphere, $G_2(20) = 3.1$ (*cf.* fig. 4.1). As a consequence of this vertical structure, the projection of the lower stratospheric circulation is the dominant contribution for the second baroclinic component. Hence the variability of the the second baroclinic component should reproduce, at least on the first patterns, the variability of the lower stratospheric circulation.

Perlwitz and Graf [1995] and Graf *et al.* [1997] found two natural modes of coupling between the stratospheric and the tropospheric circulation. One mode, with baroclinic characteristics, describes in the stratosphere the strength of the winter circumpolar vortex, while in the troposphere it has a structure similar to the NAO pattern. The other mode, with an equivalent barotropic vertical structure, is characterized in the stratosphere by a zonal wavenumber 1 disturbance of the polar vortex, and in the troposphere by a PNA-like pattern.

According to Graf *et al.* [1998] and Graf and Perlwitz [1998], the coupling between the polar vortex and the NAO may play an important role in the greenhouse forcing of the winter circulation over the North Atlantic and surrounding countries. These authors suggest that the observed trends of the geopotential, temperature and precipitation fields on the Northern Hemisphere winter may result from the more frequent occurrence of the positive phase of the natural coupled mode polar vortex-NAO. The positive phase of this mode corresponds in the stratosphere to a deepening the polar night vortex with strong westerlies. In the troposphere the positive phase corresponds to an enhancement of the westerlies over the North Atlantic and consequently to most advective temperature anomalies with cooling over the Northwest Atlantic and warming over mid-latitude Eurasia.

According to a mechanism suggested by the same authors, the initial strengthening of the polar vortex may result from an early strong heating (and elevation of the geopotential) of the tropical troposphere due to increased tropical and subtropical evaporation caused by greenhouse gases. This effect, mainly in the low latitudes, also raises the isobaric surfaces of the lower stratosphere leading to a strengthening of the meridional geopotential gradient in the middle and high latitudes and consequently to

a strengthening of the polar vortex. Stronger then normal westerlies in the polar vortex prevents planetary wave energy from propagating vertically into the stratosphere (*Charney-Drazin theorem* [Andrews *et al.*, 1987, sec.4.5]), leading to further cooling of the inner region of the vortex and more strong westerlies. In the troposphere the interference with the reflected planetary waves leads to a shift in phase and amplitude of the planetary waves which finally produces a NAO-like pattern. This positive feedback process makes the strong polar vortex and enhanced NAO phase more stable, and thus, more probable than the opposite phase, leading to the observed trends in the geopotential, temperature and precipitation fields [Graf and Perlwitz, 1998].

The process may still be amplified at the end of the winter and early spring through the reduction of the ozone concentration in the lower stratosphere [Graf *et al.*, 1998]. The strengthening of polar vortex may also result from the warming of the tropical stratosphere due to absorption of terrestrial radiation by the stratospheric aerosols resulting from volcanic eruptions, as that of El Chichón in Mexico in 1982, and Mount Pinatubo in Philippines in 1991 [Graf *et al.*, 1996].

It should be noted that the referred authors admit, alternately, the possibility that the observed trends may be due to long-period natural variability of the polar vortex-NAO mode.

The above mentioned studies raised the interest in the analysis of the principal variability modes of the second baroclinic component as well as its connection with the variability of the barotropic component of the NCEP atmosphere.

Figure 4.42 shows the horizontal spectrum of the total transient energy associated with the second baroclinic component. It can be observed that the variability of this component is clearly dominated by zonal and wavenumber 1 anomalies ($s = 0, 1$). The meridional spectrum of the zonal modes (s=0) presents an energy maximum at the Kelvin mode ($l = 0$) and another peak at the fifth zonal Rossby mode ($l = 5$). These two maxima are separated by the second and third zonal Rossby modes that have small energy. The Kelvin mode and the first zonal Rossby mode are symmetric modes and are associated with the variability of the equatorial stratosphere. The second maximum which appears at the fifth zonal Rossby mode is associated with the variability of the stratosphere in the middle and high latitudes.

The geographical distribution of total transient energy associated with the 2^{th} baroclinic component (fig. 4.43) shows little variability in the tropical stratosphere,

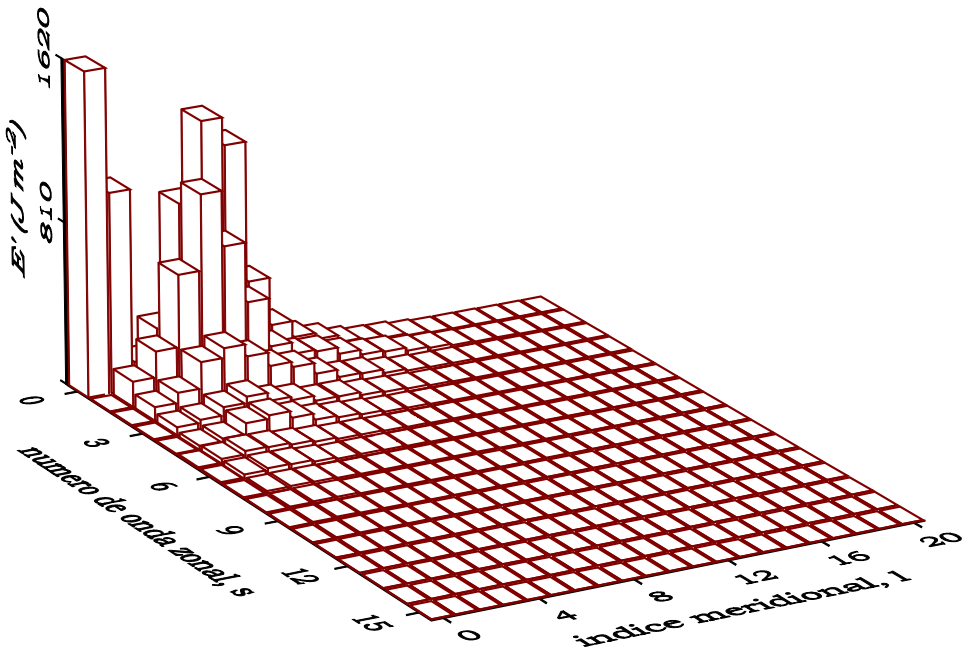

Figure 4.42: Total transient energy associated with Rossby and Kelvin ($s \leq 2,\ l = 0$) modes of the 2$^{\text{th}}$ baroclinic component of the NCEP atmosphere.

with values smaller than 10 kJ m^{-2}. The transient energy has a predominant zonal symmetric distribution with a strong meridional gradient in the Northern Hemisphere, reaching values above 100 kJ m^{-2} in the polar regions.

The patterns associated with the first three EOFs of the second baroclinic component are presented in figures 4.44-4.46. Because we are dealing with global pattern whose main structures appear in the high latitudes of the Northern Hemisphere, each pattern is represented in an equidistant cylindrical projection and in a stereographic polar projection. The first three PCs together explain 53.7% of the total transient energy associated with the second baroclinic component. The PC1, PC2 and PC3 explain, respectively, 27.9% 13.5% and 11.3% of the total transient energy. It should be noted that in the CPCA we retained only the Rossby modes with zonal wavenumbers $s \leq 4$ and meridional indices $l \leq 10$, and Kelvin modes with $s \leq 2$ (*cf.* fig. 4.42).

The extratropical patterns of the geopotential fields associated with the EOFs 1 and 3 (figs. 4.44 and 4.46, top) are very similar, respectively, to the first and second EOFs of the 50 hPa geopotential height, obtained by Perlwitz and Graf [1995] based in observations for the period 1957-1993. In turn, EOF2 presents a pattern of the extratropical geopotential field (fig. 4.45, top) very similar to one of the third EOF of

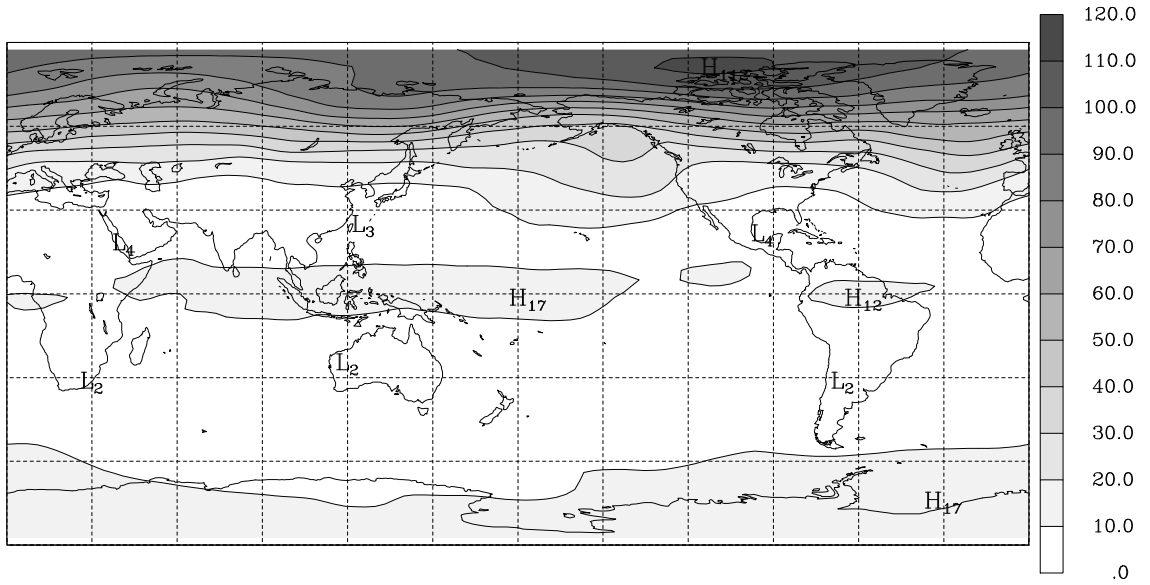

Figure 4.43: Total transient energy ($\mathrm{kJ\,m^{-2}}$) associated with the second baroclinic component of the NCEP atmosphere.

Perlwitz and Graf, except for a zonal phase shift of $\sim 30^{o}$.

In the middle and high latitudes of the Northern Hemisphere, the EOF1 describes the strength of the circumpolar night vortex. EOFs 2 and 3 represent distortions of the polar vortex by zonal wavenumber $s = 1$ anomalies, but in the case of EOF3 we note the superposition of a zonal wavenumber $s = 2$. These references to the spectral composition of the EOFs may be confirmed by the observation of the figure 4.47 that shows the contribution of each Rossby or Kelvin mode for the total transient energy associated with each EOF.

In the case of EOF2, the high values of the energy associated with the zonal Kelvin mode and the first zonal Rossby mode (fig. 4.47) are related to the zonal current in the equatorial stratosphere (fig. 4.45). This zonal current has a meridional symmetry about the equator and must be related to the Quasi-Biennial Oscillation (QBO) in the equatorial stratosphere. In fact, being 51% of the energy of the EOF2 due to the zonal Kelvin mode and to the first zonal Rossby mode, the sign of PC2 must be in agreement with the phase of the QBO. However, it should be noted that the projection of the stratospheric circulation onto the second baroclinic component represents a weighted mean with the highest weights in the 20-30 hPa layer (*cf.* fig. 4.1). Hence it is possible that as a result of the vertical integration, the contributions due to the westerly winds in a layer cancel the contributions due to the easterly winds in another layer. Even so,

the visual comparison of the time series of PC2 with a time series of the vertical profile of the QBO [van Loon and Labitzke, 1993, fig. 2] shows a good signal correlation, i.e., when the westerlies in the lower stratosphere are predominant the PC2 is positive, and is negative when the easterlies are predominant.

There are studies that associate the variability of the extratropical stratosphere with the phase of the equatorial QBO in a given level or layer, for example, in the 40-50 hPa layer [e.g., van Loon and Labitzke, 1993]. However, because of the vertical integration in the normal mode scheme, the result here obtained for the EOF2 is not directly comparable with the results of those studies.

To compare the results here obtained with the ones obtained by van Loon and Labitzke [1993], we calculated the correlation coefficients between both the PC1 and the PC2 of the second baroclinic component and the time series of the zonal mean equatorial wind at each stratospheric level of the NCEP reanalysis. The values of the correlation coefficients are given in table 4.1 and are also represented in figure 4.48. This figure also shows the stratospheric part of the vertical structure function $G_2(p)$, and the correlation curve of the PC1 with the zonal mean wind at the latitude 65° N.

The correlation between the PC2 and the zonal mean wind over the equator [fig. 4.48, curve $r\,(\mathrm{PC2}, u(0^{\mathrm{o}}))$] presents a maximum of 0.72 at the 30 hPa level. The highest sensitivity of the PC2 to the phase of the QBO around the 30 hPa level must be related with two factors which reinforce each other: (1) the vertical structure function $G_2(p)$ has higher weight in the 20-30 hPa layer, where the (2) the QBO has the largest amplitude (*cf.* Holton [1992, sec. 12.6]).

The PC1 has high correlation values with the averaged zonal wind at latitude 65° N

Table 4.1: Values of the correlation coefficient between the PCs 1 and 2 of the second baroclinic component and the time series of the zonal mean equatorial wind at each stratospheric level of the NCEP reanalysis. The values greater than the level of statistical significance of 99% are marked with '$*$'. The remaining values are smaller than the level of statistical significance of 90%.

	$\overline{u}(p)$, p in hPa					
	$\overline{u}(10)$	$\overline{u}(20)$	$\overline{u}(30)$	$\overline{u}(50)$	$\overline{u}(70)$	$\overline{u}(100)$
PC1	-0.10	0.17	0.39*	0.44*	0.40*	0.19
PC2	0.17	0.55*	0.72*	0.49*	0.33*	0.17

[fig. 4.48, curve $r\,(\mathrm{PC1}, u(65^{o}\,\mathrm{N}))$], presenting a slightly pronounced maximum of 0.91 at the 30 hPa level. Thus, PC1 describes the strength of the polar vortex in the whole 10-100 hPa layer. On the other hand the correlation curve of PC1 with the zonal mean equatorial wind, $r\,(\mathrm{PC1}, u(0^{o}))$, presents values higher than the statistical significance level of 99% for the isobaric surfaces of 30, 50 and 70 hPa, with a maximum value of 0.44 at the 50 hPa level. This significant correlations between the PC1 (polar vortex) and the QBO indices in the lower stratosphere are in accordance with the results obtained by van Loon and Labitzke [1993, fig. 3a]. The results of these authors suggest that the polar vortex tends to be stronger during the westerly phase than during the easterly phase of the wind in the lower (40-50 hPa) equatorial stratosphere.

The EOF2 (fig. 4.45) represents the covariability pattern between the 'vertical weighted means' of the equatorial QBO and the extratropical stratospheric circulation. This consideration raises the question to know whether the extratropical signal of the QBO in the wavenumber $s = 1$ reflects an effect only observable in the higher levels of the NCEP stratosphere, or whether, in the contrary, the signal is also observable in the lower levels. To answer this question the winter monthly means of the geopotential field at each level of the NCEP stratosphere were separated in two groups, according to the phase of the zonal wind at the 30 hPa level of the equatorial stratosphere. Thus, for each stratospheric level we calculated two composites, one associated with westerly winds and another associated with easterly winds at the 30 hPa level of the equatorial stratosphere. In the construction of the composites we considered only the months whose difference between the monthly mean and climatological mean values of the zonal wind was greater than half standard deviation. With this restriction it was guaranteed that the westerly and easterly winds corresponded to positive and negative anomalies, respectively.

The previous procedure was repeated, grouping the monthly means of the geopotential field according to the phase of the zonal mean wind at the 50 hPa level of the equatorial stratosphere.

The map on the top of figure 4.49 represents the difference between the composites of the 30 hPa geopotential height fields of the extratropical stratosphere, based in the phase of the zonal wind at the 30 hPa level of the equatorial stratosphere (westerly phase - easterly phase). Each composite was calculated over 28 monthly means. The bottom panel in the figure shows the same difference, but the composites were based on the phase of the wind at the 50 hPa level of the equatorial stratosphere. In this

case, the composite associated with the westerlies was based on 29 monthly means, and the one associated with the easterlies was based on 21 monthly means. Its important to mention that the maps of figure 4.49 reproduce the main characteristics of the differences of the composites of the geopotential height fields at the 10, 20, 30 and 50 hPa levels of the NCEP stratosphere (not shown).

The difference between the composites of the geopotential fields associated with the westerlies and with the easterlies at the 50 hPa level (fig. 4.49, *bottom panel*) is in accordance with the results of Holton and Tan [1982] and van Loon and Labitzke [1993]. These authors found that the polar vortex tends to be deeper and the heights in the middle latitudes to be higher in the west phase, and the polar night westerly jet stream therefore tends to be stronger in the west than in the east phases of the QBO in the lower stratosphere. However the difference between the geopotential composites based in the phase of the winds at the 30 hPa level (a level where the QBO has large amplitude), shows a distortion of the polar vortex by anomalies dominated by the wavenumber $s = 1$ (fig. 4.49, top) as indicated by the EOF2.

Figures 4.50-4.52 present the patterns of zonal anomalies of the differences between the composites of the geopotential fields at the 10, 20, 30, 50 and 70 hPa levels. The composites were selected according to the phases of the wind at the 30 hPa level of the equatorial stratosphere. As it can be observed in these figures, the QBO phases at the 30 hPa level of the equatorial stratosphere appear associated, in all the levels of the lower extratropical stratosphere, with distortions of the polar vortex by anomalies dominated by the zonal wavenumber $s = 1$. However, at the 50 and 70 hPa level the superposition of anomalies with zonal wavenumber $s = 2$ seem to be equally important.

Finally it should be noted that Holton and Tan [1982] also referred the existence of a QBO signal in the amplitude of the stationary wave $s = 1$ in the early winter (November-December), with the largest amplitudes occurring during the easterly phase of the equatorial QBO at the 50 hPa level.

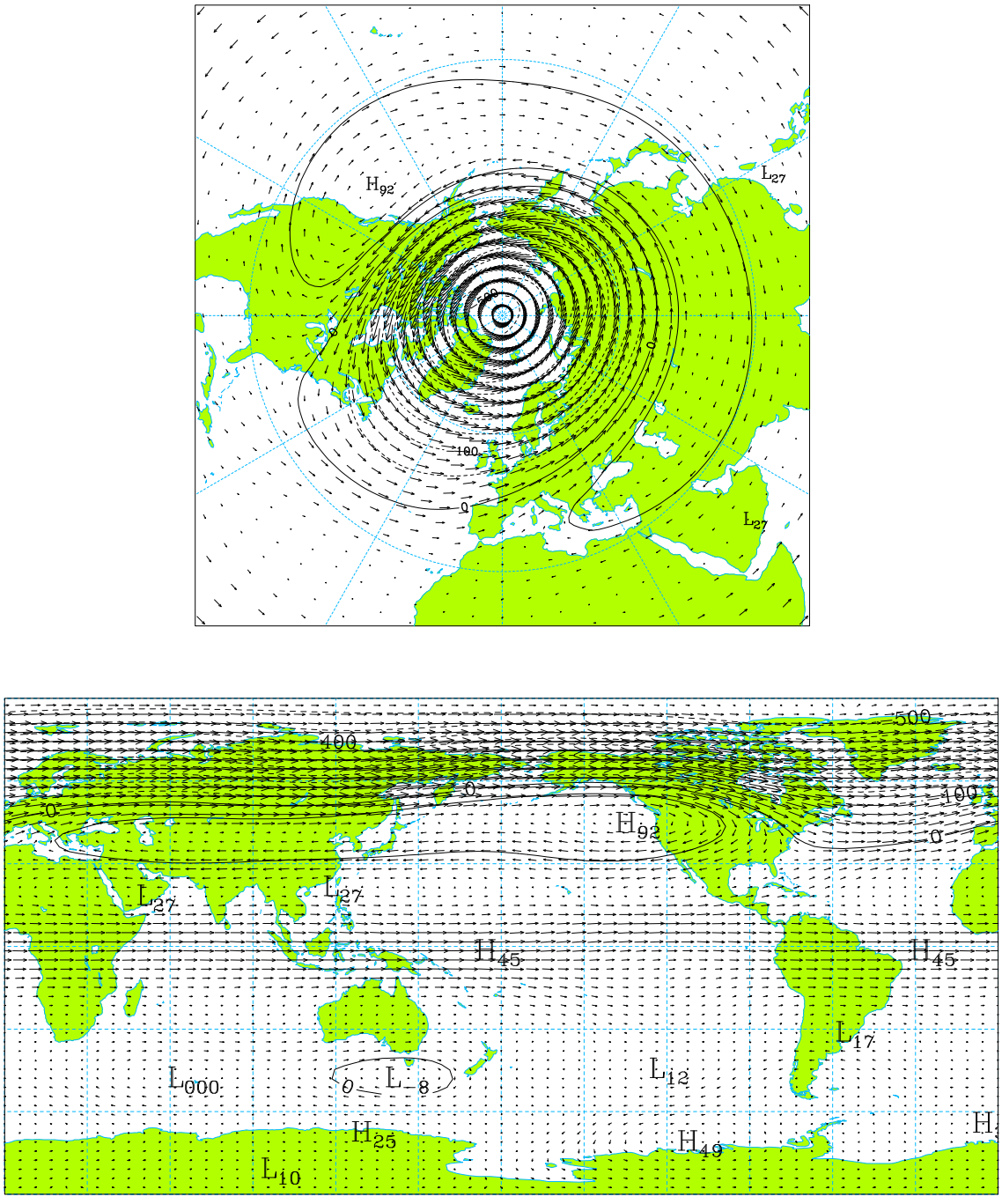

Figure 4.44: Polar stereographic *(top)* and cylindrical equidistant *(bottom)* projections of the pattern associated with the first EOF of the 2$^{\text{th}}$ baroclinic component of the NCEP atmosphere ($v_{max.} = 16.4\,\mathrm{m\,s^{-1}}$).

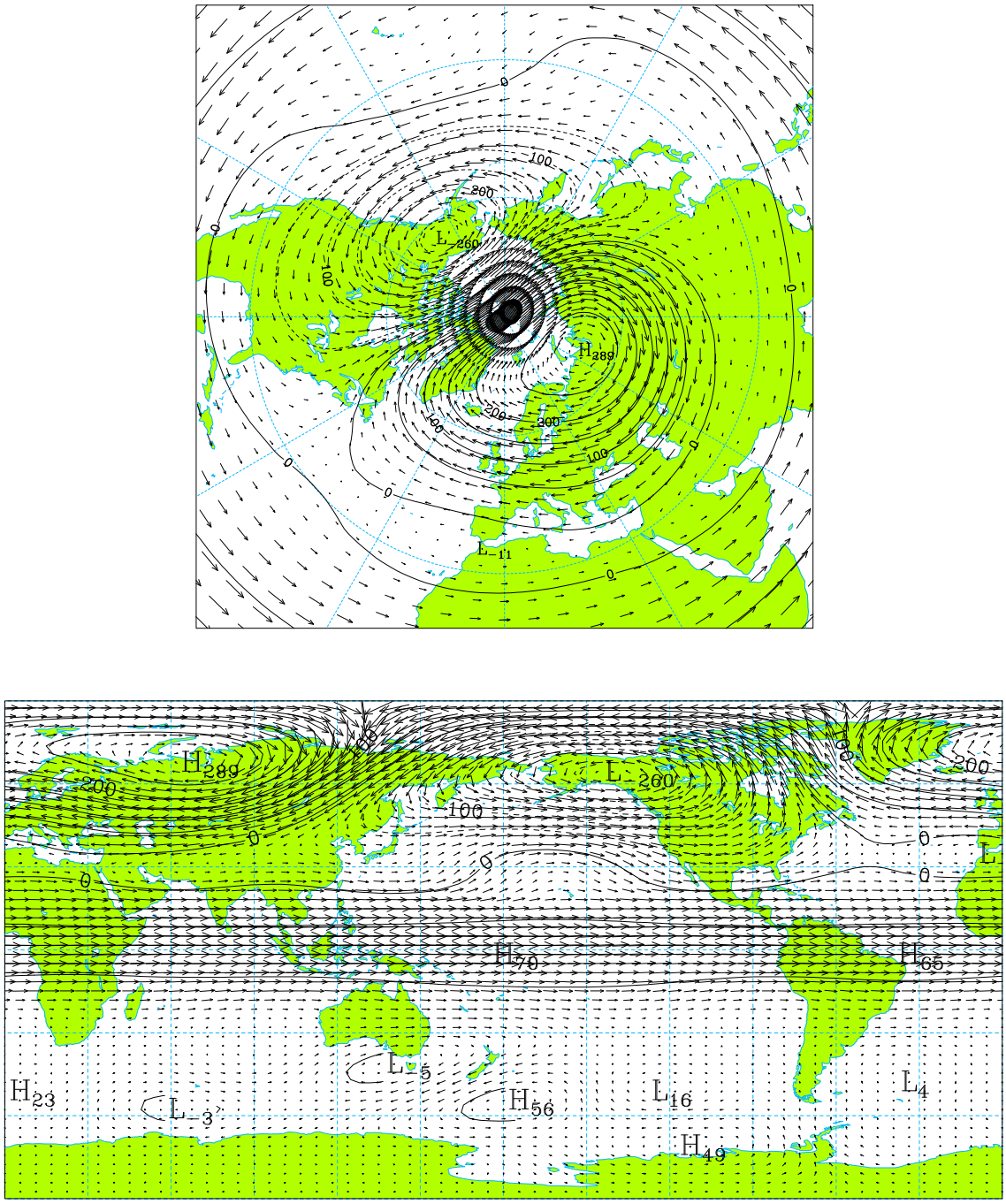

Figure 4.45: As in figure 4.44 but respecting to the EOF2 ($v_{max.} = 15.2\,\mathrm{m\,s^{-1}}$).

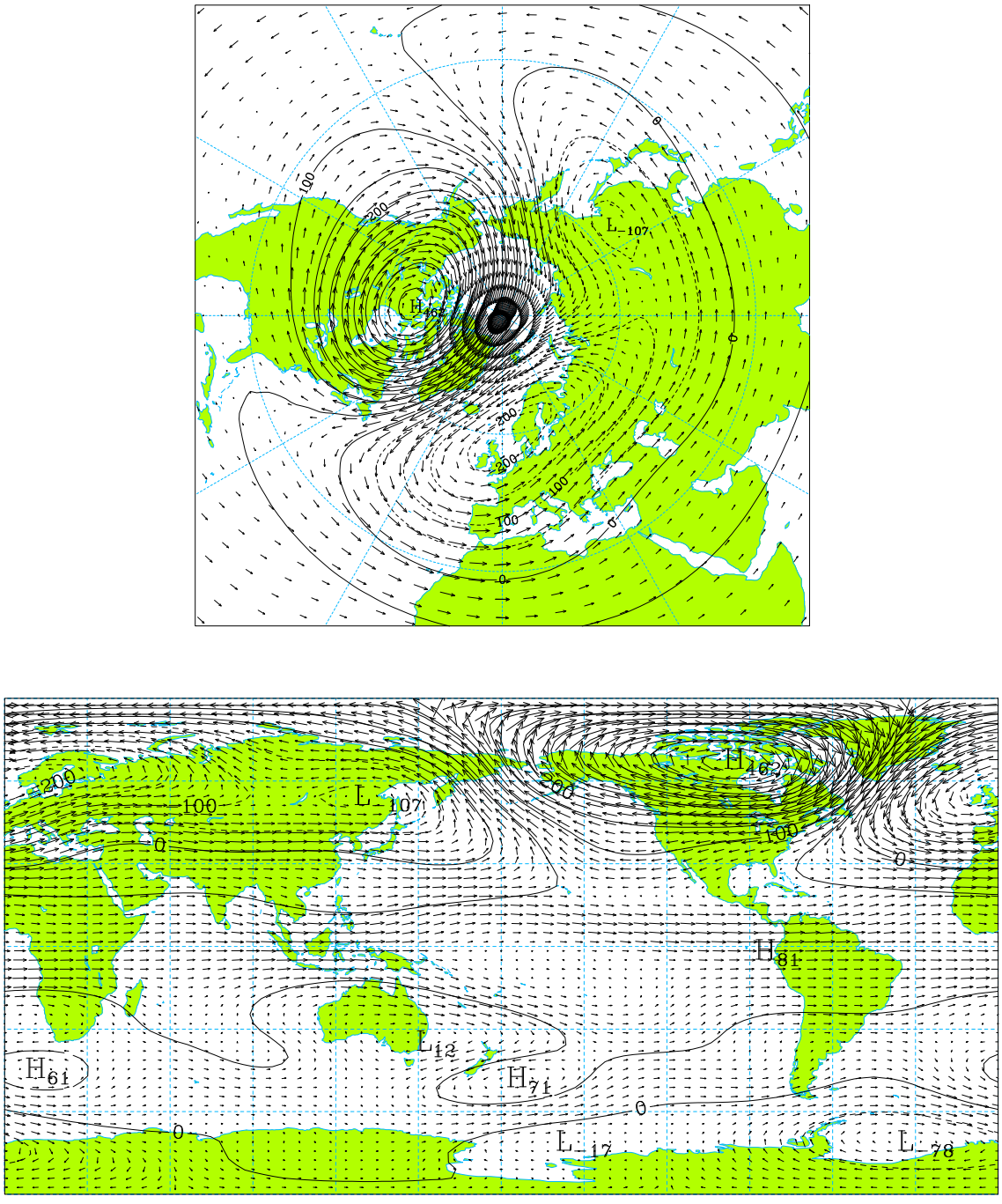

Figure 4.46: As in figure 4.44 but respecting to the EOF3 ($v_{max.} = 18.1\,\mathrm{m\,s^{-1}}$).

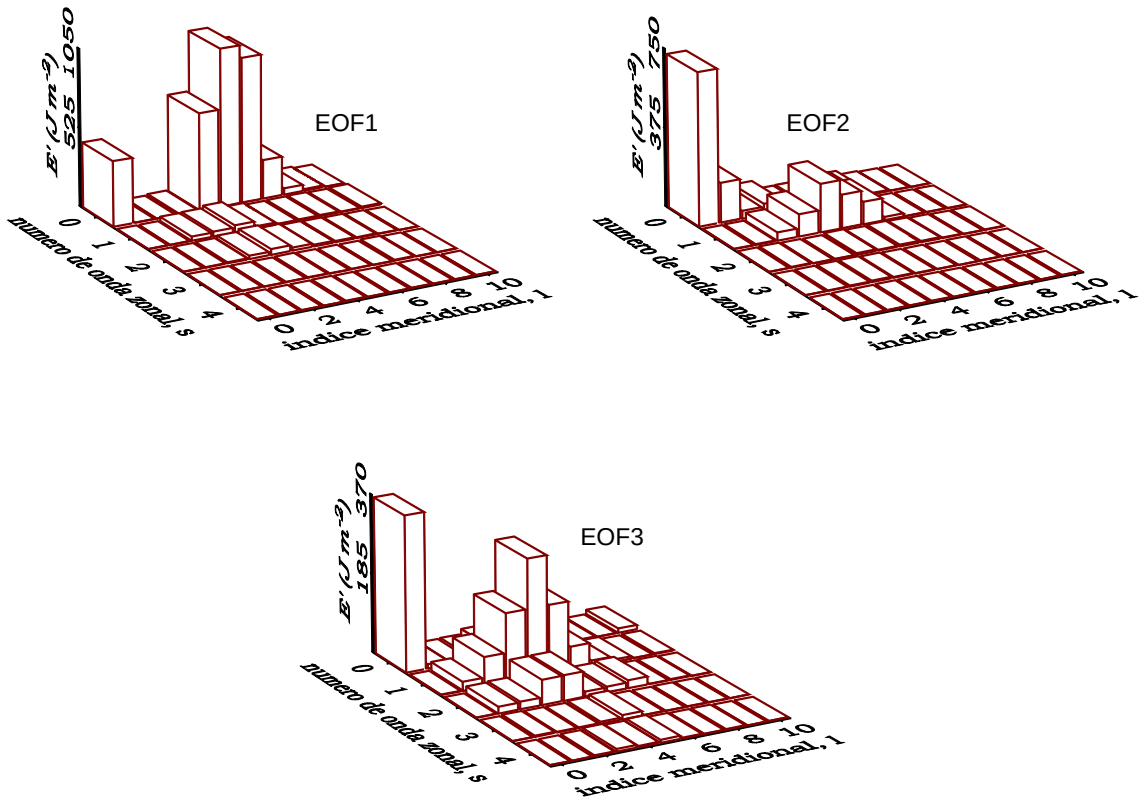

Figure 4.47: Horizontal spectra of the total transient energy associated with the first three EOFs of the second baroclinic component of the NCEP atmosphere.

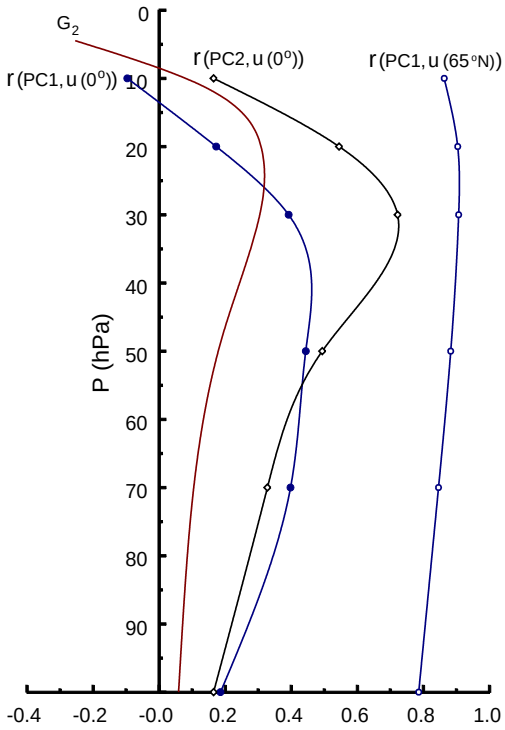

Figure 4.48: Correlation coefficients between the PCs 1 and 2 of the 2$^{\text{th}}$ baroclinic component and the time series of the zonal mean equatorial wind at each stratospheric level of the NCEP reanalysis, $r\,(\text{PC1}, u(0^{\text{o}}))$ and $r\,(\text{PC2}, u(0^{\text{o}}))$, respectively; and between the PC1 and the time series of the zonal mean wind at latitude 65$^{\text{o}}$ N, $r\,(\text{PC1}, u(65^{\text{o}}\,\text{N}))$. It is also represented the stratospheric part of the vertical structure function G_2, divided by 10.

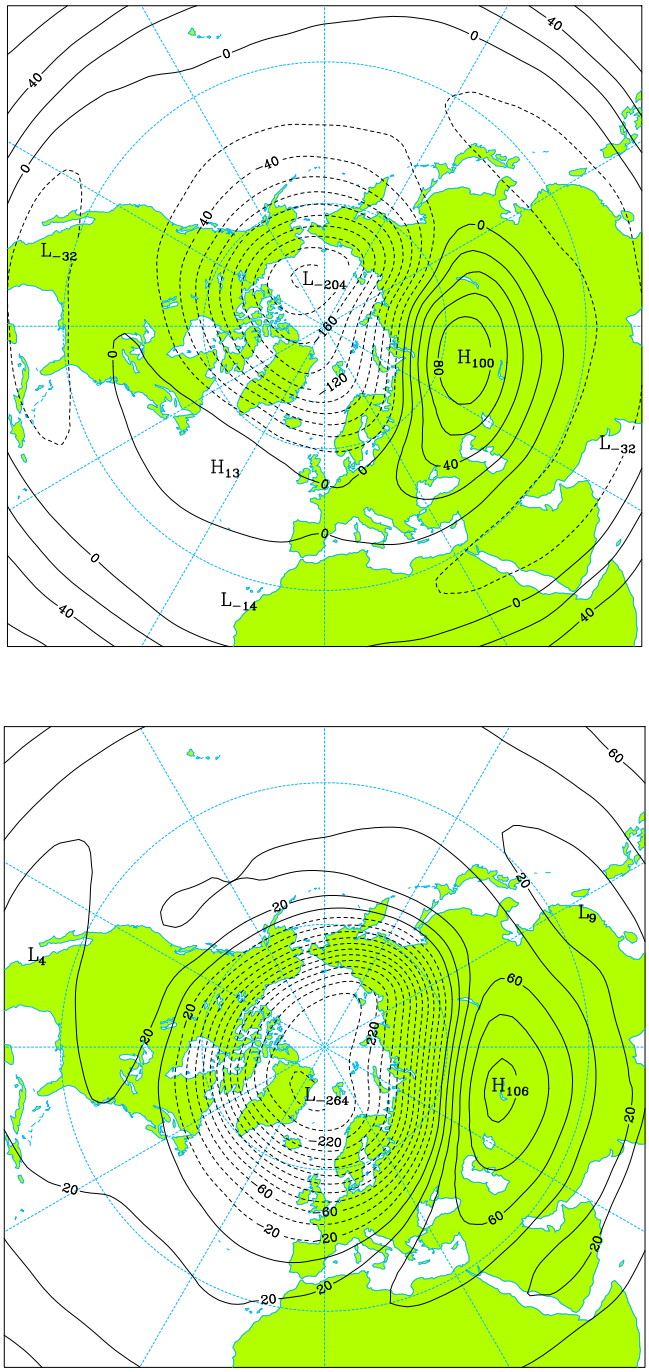

Figure 4.49: *(Top)* Difference between the composites of the 30 hPa geopotential height fields of the extratropical stratosphere, based in the phase of the zonal wind at the 30 hPa level of the equatorial stratosphere (westerly phase - easterly phase). *(Bottom)* The same difference but the composites were based on the phase of the wind at the 50 hPa level of the equatorial stratosphere.

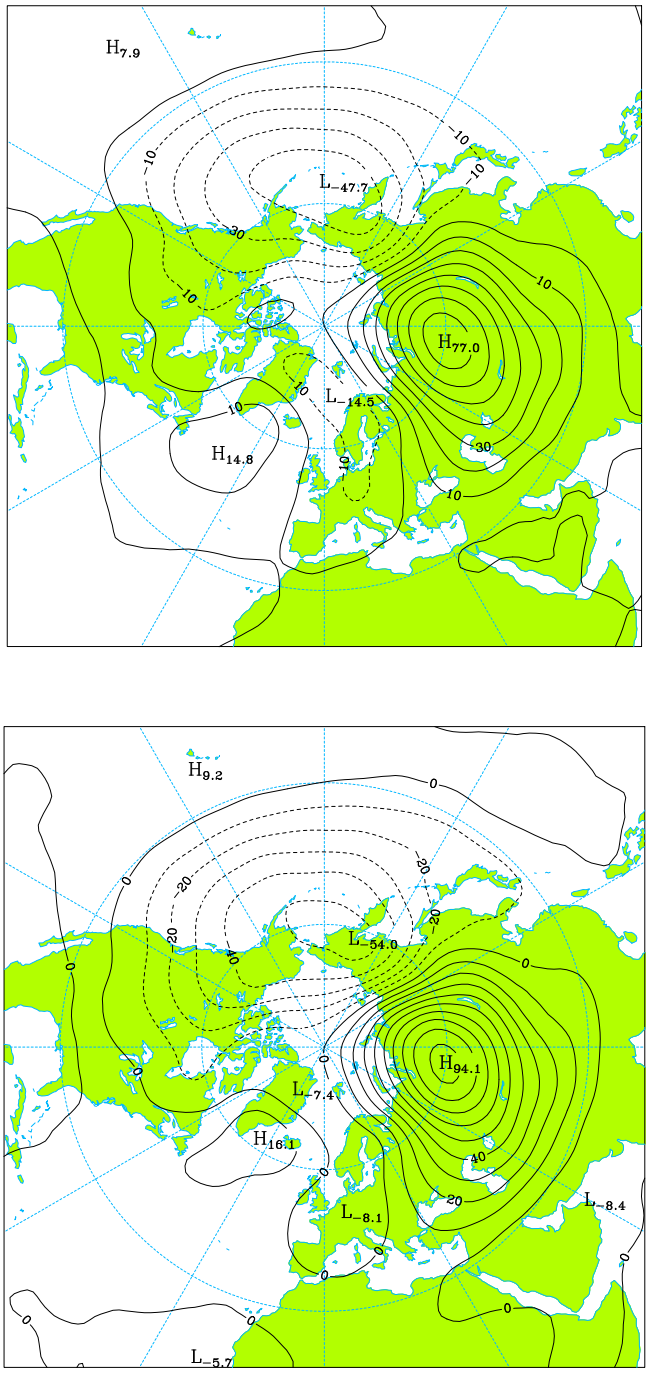

Figure 4.50: Patterns of zonal anomalies of the differences between the composites of the geopotential fields based in the phases of the equatorial QBO at 30 hPa (westerly phase - easterly phase). *In the top* it is represented the anomaly pattern for the 70 hPa geopotential height fields, *in the bottom* it is represented the same field at the 50 hPa level.

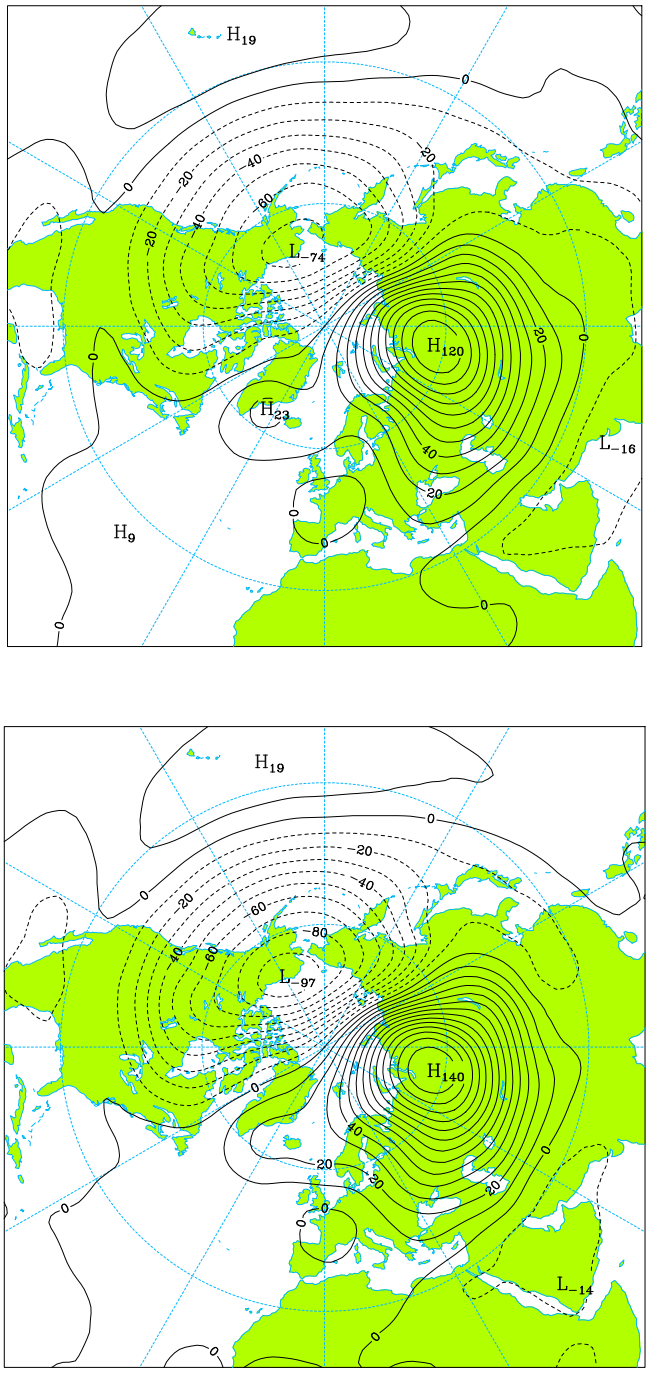

Figure 4.51: As in figure 4.50 but referring to the 30 hPa geopotential height field *(top)* and the 20 hPa geopotential height field *(bottom)*.

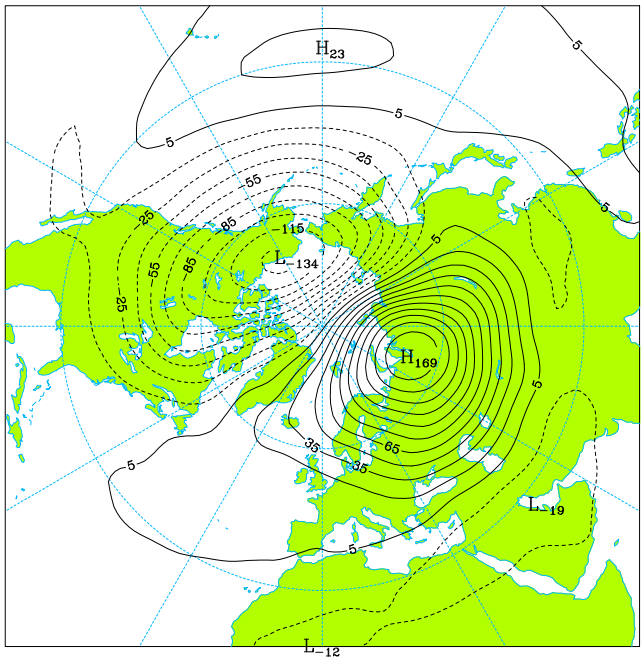

Figure 4.52: As in figure 4.50 but referring to the 10 hPa geopotential height field.

4.7 Connection between tropospheric and stratospheric circulations

A method for the study of the connections between the variability of the second baroclinic component (stratospheric circulation) and the variability of the barotropic component (tropospheric circulation) would be the calculation of the combined CPCA on the two components. However, as the CPCA maximizes the variance (energy) and the individual PCs of the barotropic component have much higher energy than the individual PCs of the second baroclinic component, it would be expected that the patterns associated with the barotropic component, in the case of the combined CPCA, result similar to the patterns obtained when performing the CPCA only on the barotropic component. On the other hand, the CPCA on the barotropic component, for the 1973-1996 period, did not give separated signals for the NAO and PNA teleconnection patterns. This results suggest that the combined CPCA on the barotropic and second baroclinic components should not be an adequate method to study the connection between the variability of the tropospheric and stratospheric circulations, for the time series in question.

The method used in this work is based in the results obtained by Perlwitz and Graf

[1995] and Graf and Perlwitz [1998]. The polar vortex represents a well-documented physical structure and constitutes, in the works of those authors, the stratospheric component of a 3-dimensional mode of the atmospheric variability. The tropospheric component of that 3-dimensional mode has a pattern similar to that of the NAO. Hence, in this work, we assumed that the second baroclinic component of that variability mode is represented by the EOF1 (fig. 4.44), and we calculated the respective barotropic component by means of a multiple linear regression between the PC1 of the second baroclinic component and the PCs of the barotropic component.

Table 4.2 presents the single correlation values between PC1 of the second baroclinic component and each one of the first 10 PCs of the barotropic component, which explain together 67.5% of the variability of the barotropic component.

Because the PCs of the barotropic component are orthogonal among themselves, the variance of the PC1 of the second baroclinic component, explained by the multiple linear regression, is given by the sum of the variances explained individually by each PC of the barotropic component. Thus only the first two PCs of the barotropic component were retained in the multiple linear regression, obtaining a multiple correlation coefficient equal to 0.61. It should be noted that if the PC5 was included the multiple correlation coefficient would rise to 0.67, but the regression pattern would be still very similar to that obtained with only the first two PCs.

Figure 4.53 shows the regression pattern, i.e., the pattern associated the the linear combination

$$\frac{1}{\sqrt{a_1^2 + a_2^2}} \left(a_1 \cdot \mathrm{EOF1} + a_2 \cdot \mathrm{EOF2}\right) \tag{4.9}$$

of the first two EOFs of the barotropic component. The coefficients a_1 and a_2 are the regression parameters associated with the PC1 and PC2, respectively. This regression pattern explains 12.7% of the variability of the barotropic component in the period of

Table 4.2: Correlation values between PC1 of the second baroclinic component and the first 10 PCs of the barotropic component. The values above the statistical significance level of 95% are marked with '$*$'.

	Barotropic component ($m = 0$)									
	PC1	PC2	PC3	PC4	PC5	PC6	PC7	PC8	PC9	PC10
PC1 ($m = 2$)	0.41*	0.46*	0.05	0.08	0.27*	-0.07	0.11	0.03	0.11	0.14

1973-1996.

As in the works of Perlwitz and Graf [1995] and Graf and Perlwitz [1998], the variability pattern of the barotropic component (tropospheric circulation), associated with the strength fluctuations of the winter stratospheric polar vortex (PC1, m=2), is similar to the pattern of the NAO (*cf.* figs. 4.14, 4.19 and 4.53).

In section 4.3.1 by visual inspection of the patterns associated with the first two EOFs of the barotropic component, as well as of the correlation maps between the respective PCs and the 850 hPa temperature anomaly fields, it was suggested that similar patterns to that of the NAO and the PNA could be obtained through linear combinations (rotations) of those two EOFs. As it was also referred, expressions 4.4 and 4.5 were therefore not based in a objective criterion.

The NAO-like pattern (fig. 4.53) appears now associated with the linear combination 4.9, based in an objective criterion.

The pattern associated with the linear combination orthogonal to (4.9) is now given by

$$\frac{1}{\sqrt{a_1^2 + a_2^2}} \left(a_2 \cdot \mathrm{EOF1} - a_1 \cdot \mathrm{EOF2}\right), \tag{4.10}$$

This pattern is presented in figure 4.54 and shows a PNA-like structure. It should be noted that, while in the linear combinations 4.4 and 4.5 the coefficients of EOFs 1 and 2 were equal, in the linear combinations 4.9 and 4.10 the normalized values of the regression parameters $\left(\sqrt{a_1^2 + a_2^2} = 1\right)$ are $a_1 = 0.6$ and $a_2 = 0.8$.

The PNA pattern, given by the expression 4.10, explains 14.1% of the variability of the barotropic circulation of the NCEP atmosphere. The correlation coefficient between the time series of the projections of the barotropic circulation onto this PNA-like pattern and the PC3 of the second baroclinic component is equal to 0.50, a value above the statistical significance level of 99%. A significant correlation was expected, since the pattern associated with the PC3 of the second baroclinic component (fig. 4.46) is similar to the stratospheric pattern associated with the second pair of canonical variables obtained in the study of Perlwitz and Graf [1995, fig. 7]. The respective tropospheric canonical pattern is similar to the PNA teleconnection pattern. Perlwitz and Graf [1995] calculated also the correlation coefficients between the second pair of canonical variables and a time series of the averaged SST anomalies in the oriental region of the Tropical Pacific (an El Niño index), and obtained values above the statistical significance level of 95%.

Table 4.3: Correlations between the linear combinations (LC) 4.9 and 4.10, the PCs 1 and 3 of the second braroclinic component (m=2), and the Niño3.4 and NAO indices. Values above the confidence level of 95% are marked with '$*$', and the values above the confidence level of 99% are marked with '$**$'.

	LC (4.9)	LC (4.10)	Niño3.4	NAO
LC (4.9)			0.00	0.73^{**}
LC (4.10)	-0.18		0.54^{**}	-0.21
PC1 (m=2)	0.62^{**}	-0.11	-0.11	0.27^{*}
PC3 (m=2)	0.11	0.50^{**}	0.53^{**}	0.07

To summarize the results obtained in this work, relative to the connection between the stratospheric and tropospheric circulations, table 4.3 presents the values of the correlations between the linear combinations (LC) 4.9 and 4.10, the PCs 1 and 3 of the second braroclinic component (m=2), the Niño3.4 index and a NAO index. The NAO index was calculated by the Climatic Research Unit of East Anglia University as the normalized pressure difference between a station on the Azores (Ponta Delgada) and one on Iceland (Reykjavik).

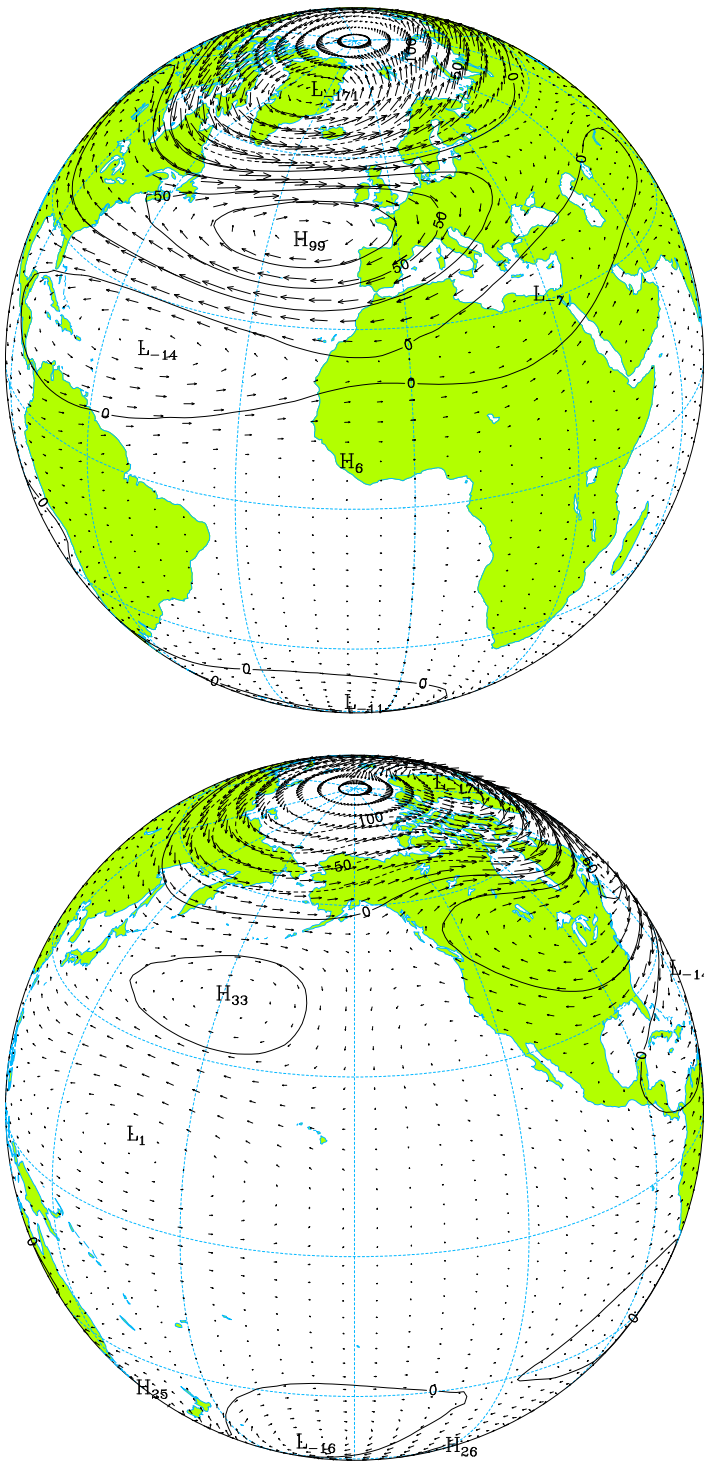

Figure 4.53: Regression pattern associated with the linear combination (4.9) of the first two EOFs of the barotropic component of the NCEP atmosphere ($v_{max.} = 11.6\,\mathrm{m\,s^{-1}}$).

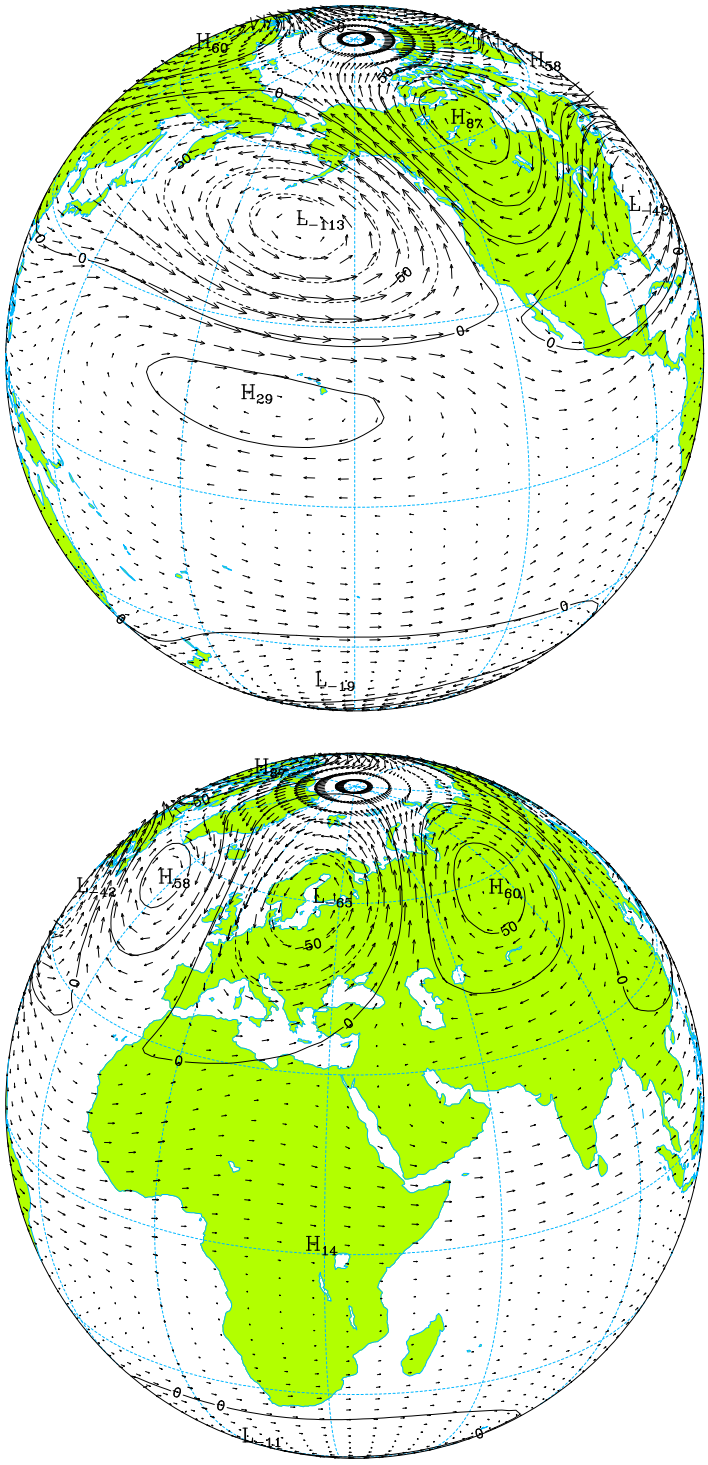

Figure 4.54: Pattern associated with the linear combination (4.10) orthogonal to the one represented in figure 4.53 ($v_{max.} = 9.0\,\mathrm{m\,s^{-1}}$).

Chapter 5

Concluding Summary

The free and forced variabilities of the winter (DJF) global atmospheric circulation simulated by the VII.1 version of Melbourne University AGCM were analyzed in the present work. The analysis was based in an ensemble of 10 independent integrations of the atmospheric circulation, all forced by the observed SST and sea ice cover fields, for the 1979-88 period. The simulated variability was compared to the observed variability, based on the NCEP reanalysis for the period 1973-96. In the case of the reanalysed atmosphere, besides the variability modes corresponding to the ones analyzed in the simulations, it was also possible to study the variability of the lower stratospheric circulation and its connection to the variability of the tropospheric circulation.

The variability of the atmospheric circulation was estimated by the joint variabilities of the geopotential and horizontal wind fields. These fields were previously expanded in the normal mode bases of the reference atmospheres of the model and of the reanalysis, respectively, in the case of the simulations and of the observations. The variability was then calculated in the transformed space of the projections, and has been quantified by the global mean total transient energy per unit of horizontal area. The total transient energy was defined as the total (kinetic+available potential) energy associated with the anomalies of the monthly means. The expansion in the normal mode basis allowed also to decompose the variability of the global circulation into barotropic and baroclinic components as well as into the components associated with the gravity-inertial and planetary (Rossby) waves.

The model simulates fairly well the variability pattern of the barotropic component over all the Pacific and North America, the maximum values of the simulated total transient energy being about 80% of the corresponding observed values. However,

over the North Atlantic the simulated variability presents a dipolar structure as in the observations, but the simulated dipole is shifted eastward about 20° with respect to the observed dipole. The maximum value of the simulated total transient energy is only 37% of the maximum value of observed total transient energy over that region. This difference between the simulated and observed variabilities over the North Atlantic may be the result of an insufficient resolution of the model to represent the synoptic activity over that region.

The variability field of the simulated vector $(u, v, \phi)^T_{m=0}$ represents the total transient energy associated with the simulated barotropic circulation. This field may be decomposed into the variability fields of the horizontal wind (kinetic transient energy) and of the geopotential (available potential transient energy). Comparing these fields with the respective fields of the observed barotropic circulation, we concluded that the model simulates more adequately the kinetic transient energy. However it should be noted at this respect that the geopotential field intervenes in the motion dynamics only through its gradient and the gradient operator has characteristics of a high-pass filter. Due to these facts it should be expected that inaccuracies in the longest waves do not reflect, in a considerable way, in the gradient of geopotential field. Thus, the analysis of the variability of the vector $(u, v, \phi)^T$, even when the simulated ϕ component presents some discordances with the respective observed component, will certainly be more adequate to a dynamical study of atmospheric circulation variability than a more 'traditional' analysis, restricted to a study of the geopotential field in a given level.

The forced variability of the simulated barotropic circulation presents a striking contrast between the Hemisphere west of 60° W which includes all the Pacific Ocean and North America, and the complementary Hemisphere (*cf.* figs. 3.16-3.18). The signal to noise ratio, E'_{SST}/E'_{INT}, presents values above 70% over the central region of the Pacific, indicating that a large fraction of the variability of the intertropical circulation is associated with the underlying SST anomalies. Concerning to the extratropical circulation one observes regions over North Pacific and North America where the signal to noise ratio reaches values between 10% and 20%, which are small but are much larger than the values obtained over the North Atlantic and the European region, where the signal to noise ratio is below 5%.

A complex principal component analysis (CPCA) revealed the PNA teleconnection pattern as the major mode of the internal variability of the barotropic component of the simulated global circulation (fig. 3.23). In the same analysis the teleconnection pattern

of the NAO appeared as the fourth internal variability mode of the global barotropic circulation (fig. 3.25). The reason for the NAO appearing only as the fourth internal variability mode must be related to the fact that the model underestimates relatively more the extratropical barotropic variability over the North Atlantic region.

The results of a combined CPCA on the barotropic and fourth baroclinic components of the simulated atmosphere suggest an equivalent barotropic vertical structure for the PNA, while the NAO presents baroclinic characteristics (*cf.* figs. 3.28-3.31).

The first variability pattern of the forced barotropic circulation, simulated by the model, explains approximately half of the forced barotropic variability (fig. 3.32). This pattern, which is obtained through the CPCA on the forced barotropic component, is very similar to the schematic illustrations of the global pattern of middle and upper tropospheric anomalies, during the mature stage of an ENSO event in the NH winter (DJF), as were been proposed by Horel and Wallace [1981] and Karoly [1989]. It is a pattern that presents a structure similar to the PNA over the Northern Hemisphere, and an approximately symmetric structure with respect to the equator over the Southern Hemisphere, but with smaller amplitude and westward shifted. The association of this variability mode with the SST anomalies in the Tropical Pacific is confirmed by the correlation map between the PC1 of the forced barotropic circulation and the time series of SST anomalies, in each grid point the forcing field (fig. 3.36, on top). In fact, that map shows a pattern of high correlation very similar to the pattern of SST anomalies during the mature stage of an ENSO event in the NH winter (DJF).

The CPCA performed on the forced fourth baroclinic component (forced component of the circulation projected onto the vertical structure function $G_4(p)$) revealed a circulation pattern associated with the anomalies of the Walker circulation (figs. 3.34 and 3.35, top panels). This pattern explains 42% of the forced variability of the fourth baroclinic component of the simulated circulation. The correlation map between the respective PC and the time series of SST anomalies, at each grid point of the forcing field, confirms the relation of that pattern with the SST variability in the tropical Pacific associated with the ENSO cycle.

The study of the observed variability of the barotropic component of the atmospheric circulation, represented by the NCEP reanalysis, revealed also two global variability modes associated with the teleconnection patterns of the NAO and the PNA. These circulation patterns were obtained, like the respective simulated patterns, through a CPCA on the barotropic component of the reanalysis for the period

of December 1976 to February 1988 (figs. 4.19 and 4.20). However in the case of the reanalyzed atmosphere the teleconnection pattern of the NAO appeared as the major variability mode explaining 15.8% of the variability of the barotropic circulation, and the pattern associated with the PNA appeared as the second variability mode and explaining 12.9% of the variability.

Considering the whole period from January 1973 to December 1996 the teleconnection patterns of the NAO and the PNA only appeared as two distinct variability modes of the global barotropic circulation, when the first two EOFs of the barotropic component were linearly combined (figs. 4.14 and 4.15, and figs. 4.53 and 4.54). The need to rotate the first two EOFs of the barotropic component to obtain separate patterns for the NAO and PNA may be interpreted as a consequence of the statistical fluctuations of sampling and/or a consequence of circulation fluctuations on timescales greater than the interannual scale. The last hypothesis is consistent with the circulation regime shift during the period of December 1976 to February 1988 over the North Pacific (*cf.* fig. 4.18).

The results of the combined CPCA on the barotropic and fifth baroclinic components of the NCEP atmosphere confirm the results obtained with the simulations, suggesting that the NAO possesses baroclinic characteristics (figs. 4.32-4.35). With respect to the vertical structure of the PNA the results do not appear conclusive, in the sense that the covariance pattern associated with the barotropic component of the NCEP atmosphere does not represent correctly the teleconnection pattern of the PNA. In fact, in the mentioned pattern the centres of the anticyclonic circulation over North America and the depression off the Atlantic Coast of the United States appear shifted northeastward relatively to the respective centres of the PNA (figs. 4.36-4.39).

The calculation of the canonical correlation between the barotropic component of the NCEP atmosphere and the index Niño3.4 (fig. 4.21) revealed a canonical circulation pattern very similar to the first forced pattern of the simulated barotropic circulation. However the variability centers in the simulated pattern appear shifted westward about 15 to 30º relatively to the respective centers of the observed canonical pattern.

The first variability pattern of the fourth baroclinic component of the NCEP atmosphere (fig. 4.25) is very similar to the first variability pattern of the fourth baroclinic component of the forced circulation simulated by the MU AGCM (fig. 3.34, top). The fact that the observed pattern, like the simulated pattern, represents tropical circula-

tion anomalies associated with the ENSO cycle was confirmed again by the correlation pattern between the respective PC and the SST anomalies (fig. 4.26, *bottom panel*).

The observed variability of the lower stratospheric circulation was also analyzed by means of a CPCA on the second baroclinic component of the NCEP atmosphere. The analysis was concentrated in the first three EOFS, which represent together 53.7% of the variability of the second baroclinic component (figs. 4.44-4.46). The PC1 represents the strength of the northern winter circumpolar vortex, while the second variability pattern represents an association between the equatorial QBO and a distortion of the polar vortex by anomalies dominated by the zonal wavenumber $s = 1$. The third mode represents also a distortion of the polar vortex dominated by the zonal wavenumber $s = 1$, but in this case the superposition of the zonal wavenumber $s = 2$ is also important.

The connection between the stratospheric and tropospheric circulations was investigated through the calculation of the single correlations between the respective PCs as well as by means of a multiple linear regression between the PC1 of the second baroclinic component and the PCs of the barotropic component. The results of this study show that the strength of the stratospheric night polar vortex is associated with the amplitude of the NAO in the troposphere. The third variability mode of the stratospheric circulation is associated with a PNA-like pattern in the troposphere. These results confirm the ones obtained by other authors [e.g., Graf *et al.*, 1998; Graf and Perlwitz, 1998] and may reflect important mechanisms in the radiative forcing of the circulation due to greenhouse gases.

In view of the obtained results, one can concluded that the expansion of the atmospheric circulation in a normal modes basis constitute a method, not only adequate, but mostly useful for the study of the global circulation variability. In fact, besides the fundamental dynamic characteristics retained in the base vectors and the associated capacity of performing a dynamically consistent filtering of both wind and mass fields, the usefulness of the method results mainly from the fact that the computed statistics are based on the very primitive variables of global circulation, therefore not simply relying on information provided by a 'proxy' variable of circulation, such as the 500 hPa geopotential field. A well illustrating example of the usefulness of the method is given by the procedure that lead to the forced pattern of the simulated barotropic circulation, based in a global analysis of the barotropic Rossby modes. Another example is given by the analysis of the second baroclinic component of the

NCEP atmosphere that revealed an association between the equatorial QBO and a distortion of the stratospheric night polar vortex dominated by the zonal wavenumber $s = 1$, while a more 'traditional' analysis associated the phases of the QBO in lower (40-50 hPa) equatorial stratosphere with the strength of the stratospheric night polar vortex.

Bibliography

Anderson, J. F. and W. F. Stern, 1996. *Evaluating the potential predictive utility of ensemble forecasts.* J. Climate, **9**, 260-269.

Andrews, D. G., J. R. Holton and C. B. Leovy, 1987. *Middle Atmosphere Dynamics.* Academic Press, 489 pp.

Barnett, T. P., K. Arpe, L. Bengtsson, M. Ji and A. Kumar, 1997. *Potential predictability and AMIP implications of midlatitude climate variability in two general circulation models.* J. Climate, **10**, 2321-2329.

Bengtsson, L. O., 1992. *Climate system modeling propects, 705-724.* Climate System Modeling, K. E. Trenberth (ed.), Cambridge University Press, 788 pp.

Blackmon, M. L., Y.-H. Lee and J. M. Wallace, 1984. *Horizontal structure of 500 mb height fluctuations with long, intermediate and short time scales.* J. Atmos. Sci., **41**, 961-979.

Boer, G. J., et al., 1991. An intercomparison of the climates simulated by 14 atmospheric general circulation models. Rep. WMO/TD 425, World Meteorol. Soc., Geneva, Switzerland.

Boer, G. J., et al., 1992. An intercomparison of the climates simulated by 14 atmospheric general circulation models. J. Geophys. Res., **97**, 12771-12786.

Bretherton, C. S., C. Smith and J. M. Wallace, (1992). *An intercomparison of methods for finding coupled patterns in climate data.* J. Climate, **5**, 541-560.

Carson, D. J., 1998. *Seasonal forecasting.* Q. J. R. Meteorol. Soc., **124**, 1-26.

Castanheira, J. M., C. C. DaCamara and A. Rocha, 1999. *Numerical solutions of the vertical structure equation and associated energetics.* Tellus, **51A**, 337-348.

Chen, W. Y., 1989. *Estimate of dynamical predictability from NCM DERF experiments.* Mon. Wea. Rev., **117**, 1227-1236.

Chen, W. Y. and H. M. Van den Dool, 1997. *Atmospheric predictability of seasonal, annual, and decadal climate means and the role of the ENSO cycle: A model study.* J. Climate, **10**, 1236-1254.

Cheng, X., G. Nitsche and J. M. Wallace, 1995. *Robustness of low-frequency circulation patterns derived from EOF and Rotated EOF analyses.* J. Climate, **8**, 1709-1713.

Cohn, S. E. and D. P. Dee, 1989. *An analysis of the vertical structure equation for arbitrary thermal profiles.* Q. J. R. Meteorol. Soc., **115**, 143-171.

Davies, J. R., D. P. Rowell and C. K. Folland, 1997. *North Atlantic and european seasonal predictability using an ensemble of multidecadal atmospheric GCM simulations.*. Int. J. Climatol., **17**, 1263-1284.

Deardorff, J. W., 1977. *A parameterization of ground-surface moisture content for use in atmospheric prediction models.* J. Appl. Meteor., **16**, 1182-1185.

Dütsch, H. U., 1978. *Vertical ozone distribution on a global scale.* Pageoph., **116**, 511-529.

Eckart, C., 1960. *Hydrodynamics of Oceans and Atmospferes.* Pergamon Press, Oxford, 290pp.

Fraedrich, K., 1994. *An ENSO impact on Europe? A review.* Tellus, **46A**, 541-552.

Gates, W. L. and A. B. Nelson, 1975. *A new (revised) tabulation of the Scripps topography on a 1^0 global grid. Part I : Terrain heights.* The Rand Corporation, R-1276-1-ARPA, 132pp.

Graf H.-F., I. Kirchner and I. Schult, 1996. *Modelling Mt. Pinatubo climate effects, 219-231.* in: The Mount Pinatubo eruption: Effects on the atmosphere and climate, edited by G. Fiocco, D. Fuà and G. Visconti. NATO ASI series I, Vol. 42, Springer-Verlag.

Graf H.-F., J. Perlwitz and I. Kirchner, 1997. *Coupled modes of tropospheric and stratospheric circulation in nature and in models.* in: Stratospheric Processes and

Their Role in Climate (SPARC), Proceedings of the First SPARC General Assembly, Melbourne, Australia, Dec. 1996, WCRP-99, WMO/TD-No. 814, May 1997,129-132.

Graf H.-F., I. Kirchner and J. Perlwitz, 1998. *Changing lower stratospheric circulation: The role of ozone and greenhouse gases.* J. Geophys. Res, **103**, D10, 11251-11261.

Graf H.-F. and J. Perlwitz, 1998. *Secular variability of the North Atlantic Oscillation.* Proceedings of the 2nd European Conference on Applied Climatology, 19-23 October 1998, Vienna, Austria.

Graham, N. E., T. P. Barnett, R. Wilde, M. Ponater and S. Schubert, 1994. *On the roles of tropical and midlatitude SSTs in forcing interannual to interdecadal variability in the winter Northern Hemisphere circulation.* J. Climate, **7**, 1416-1441.

Hansen, J. W., A. W. Hodges and J. W. Jones, 1998. *ENSO influences on agriculture in the southeastern United States.* J. Climate, **11**, 404-411.

Hansen, J. W., J. W. Jones, C. F. Kiker and A. W. Hodges, 1999. *El Niño-Southern Oscillation impacts on winter vegetable production in Florida.* J. Climate, **12**, 92-102.

Harzallah, A. and R. Sadourny, 1995. *Internal versus SST-forced atmospheric variability as simulated by an atmospheric general circulation model.* J. Climate, **8**, 474-495.

Holton, J. R., 1992. *An Introduction to Dynamic Meteorology.* Academic Press, 511 pp.

Holton, J. R. and H.-C. Tan, 1982. *The quasi-biennial oscillation in the Northern Hemisphere lower stratosphere.* J. Meteor. Soc. Japan, **60**, 140-148.

Horel, J. D. and J. M. Wallace, 1981. *Planetary-scale atmospheric phenomena associated with de Southern Oscillation.* Mon. Wea. Rev., **109**, 813-829.

Hough, S. S., 1898. *On the application of harmonic analysis to the dynamical theory of the tides – Part II. On the general integration of Laplace's tidal equations.* Phil. Trans. Roy. Soc. London, **A191**, 139-185.

Ji, M., A. Leetmaa and V. E. Kousky, 1996. *Coupled model predictions of ENSO during the 1980s and the 1990s at the National Centers for Environmental Prediction.* J. Climate, **9**, 3105-3120.

Karoly, D. J., 1989. *Southern Hemisphere circulation features associated with El Niño-Southern Oscillation events.* J. Climate, **2**, 1239-1252.

Kasahara, A. and K. Puri, 1981. *Spectral representation of three-dimensional global data by expansion in normal mode functions.* Mon. Wea. Rev., **109**, 37-51.

Kawamura, R., M. Sugi and N. Sato, 1995. *Interdecadal and interannual variability in the northern extratropical circulation simulated with the JMA global model. Part I: Wintertime leading mode.* J. Climate, **8**, 3006-3019.

Kumar, A. , M. Ji, A Leetmaa and P. Sardeshmukh, 1996. *Assessing a GCM's suitability for making seasonal predictions.* J. Climate, **9**, 115-129.

Kushnir, Y. and J. M. Wallace, 1989. *Low-frequency variability in the Northern Hemisphere winter: geographical distribution, structure and time-scale dependence.* J. Atmos. Sci., **46**, 3122-3142.

Kutzbach, J. E., 1992. *Modeling large climatic changes of the past, 669-688.* Climate System Modeling, K. E. Trenberth (ed.) Cambridge University Press, 788 pp.

Lau, N.-C., 1988. *Variability of the observed midlatitude storm tracks in relation to low-frequency changes in the circulation pattern.* J. Atmos. Sci., **45**, 2718-2743.

Lau, N.-C. and M. J. Nath, 1996. *The role of the "atmospheric bridge" in linking tropical Pacific ENSO events to extratropical SST anomalies.* J. Climate, **9**, 2036-2057.

Leith, C. E., 1973. *The standard error of time-average estimates of climate means.* J. Appl. Meteor., **12**, 1066-1069.

Leith, C. E., 1978. *Predictability of climate.* Nature, **276**, 352-355.

Li, Z.-X., 1999. *Ensemble atmospheric GCM simulation of climate interannual variability from 1979 to 1994.* J. Climate, **12**, 986-1001.

Longuet-Higgins, M. S., 1968. *The eigenfunctions of Laplace's tidal equations over a sphere.* Phil. Trans. Roy. Soc. London, **A262**, 511-607.

Lorenz, E. N., 1970. *Climate change as a mathematical problem.* J. Appl. Meteor., **9**, N. 3, 325-329.

Lorenz, E. N., 1982. *Atmospheric predictability experiments with a large numerical model.* Tellus, **34**, 505-513.

Lorenz, E. N., 1990. *Can chaos and intransitivity lead to interannual variability?* Tellus, **42A**, 378-389.

Madden, R. A., 1976. *Estimates of the natural variability of time-averaged sea-level pressure.* Mon. Wea. Rev., **104**, 942–952.

Manabe, S. and R. F. Strickler, 1964. *Thermal equilibrium of the atmosphere with a convective adjustment.* J. Atmos. Sci., **21**, 361-385.

Manabe, S. and R. T. Wetherald, 1967. *Thermal equilibrium of the atmosphere with a given distribution of relative humidity.* J. Atmos. Sci., **24**, 241-259.

McAvaney, B. J., W. Bourke and K. Puri, 1978. *A global spectral model for simulation of the general circulation.* J. Atmos. Sci., **35**, 1557-1583.

Milliken, G. A. and D. E. Johnson, 1984. Analysis of messy data: Vol. I. Designed experiments. New York: Van Nostrand Reinhold, Co.

Nakamura, H., M. Tanaka and J. M. Wallace, 1987. *Horizontal structure and energetics of Northern Hemisphere winter teleconnection patterns.* J. Atmos. Sci., **44**, 3377-3391.

Palmer, T. N. and D. L. T. Anderson, 1994. *The propects for seasonal forecasting–A review paper.* Q. J. R. Meteorol. Soc., **120**, 755-793.

Peixoto, J. P. and Habraham H. Oort, 1992. *Physics of Climate.* American Institute of Physics, 520 pp.

Perlwitz, J. and Hans-F. Graf, 1995. *The statistical connection between tropospheric and stratospheric circulation of the Northern Hemisphere in winter.* J. Climate, **8**, 2281-2295.

Philander, S. G., 1990. *El Niño, La Niña, and the Southern Oscillation.* Academic Press, 293 pp.

Phillips, J., B. Rajagopalan, M. Cane and C. Rosenzweig, 1999. *The role of ENSO in determining climate and maize yield variability in the U.S. cornbelt.* Int. J. Climatol., **19**, 877-888.

Pitcher, E. J., M. L. Blackmon, G. T. Bates and S. Muñoz, 1988. *The effect of North Pacific sea surface temperature anomalies on the January climate of a general circulation model.* J. Atmos. Sci., **45**, 173-188.

Renshaw, A. C., D. P. Rowell and C. K. Folland, 1998. *Wintertime low-frequency weather variability in the North Pacific-American sector 1949-93.* J. Climate, **11**, 1073-1093.

Richman, M. B., 1986. *Rotation of principal components.* J. Climatol., **6**, 293-335.

Rodwell, M. J., D. P. Rowell and C. K. Folland, 1999. *Oceanic forcing of the wintertime North Atlantic Oscillation and European climate.* Nature, **398**, 320-323.

Ropelewski, C. F. and M. S. Halpert, 1989. *Precipitation patterns associated with the high index phase of the Southern Oscillation.* J. Climate, **2**, 268-284.

Rowell, D. P., C. K. Folland, K. Maskell and M. N. Ward, 1995. *Variability of summer rainfall over tropical north Africa (1906-92): Observations and modelling.* Q. J. R. Meteorol. Soc., **121**, 669-704.

Rowell, D. P., 1998. *Assessing potential seasonal predictability with an ensemble of multidecadal GCM simulations.* J. Climate, **11**, 109-120.

Saravanan, R., 1998. *Atmospheric low-frequency variability and its relationship to midlatitude SST variability: Studies using the NCAR Climate System Model.* J. Climate, **11**, 1386-1404.

Scheffé, H., 1959. *The analysis of variance.* John Wiley and Sons, 477 pp.

Schneider, S. H., 1992. *Introduction to climate modeling, 3-26.* Climate System Modeling, K. E. Trenberth (ed.) Cambridge University Press, 788 pp.

Schubert, S. D., 1986. *The structure, energetics and evolution of the dominant frequency-dependent three-dimensional atmospheric modes.* J. Atmos. Sci., **43**, 1210-1237.

Smith, T. M. and R. E. Livezey, 1999. *GCM systematic error correction and specification of the seasonal mean Pacific-North America region atmosphere from global SSTs.* J. Climate, **12**, 273-288.

Simmonds, I., 1985. *Analysis of the 'spinup' of a general circulation model.* J. Geophys. Res., **90**, 5637-5660.

Simmonds, I., G. Trigg and R. Law, 1988. *The climatology of the Melbourne University general circulation model.* Publication No. 31, Department of Meteorology, University of Melbourne, 67 pp.

Simmonds, I. and A. H. Lynch, 1992. *The influence of pre-existing soil moisture content on Australian winter climate.* Int. J. Climatol., **12**, 33-54.

Sneddon, Ian N., 1974. *The use of integral transforms.* TMH edition, McGraw-Hill, 539 pp.

Stern, W. and K. Miyakoda, 1995. *Feasibility of seasonal forecasts inferred from multiple GCM simulations.* J. Climate, **8**, 1071-1085.

Shukla, J., 1998. *Predictability in the midst of chaos: a scientific basis for climate forecasting.* Science, **282**, 728-731.

Swarztrauber, P. N. and A. Kasahara, 1985. *The vector harmonic analysis of Laplace's tidal equations.* SIAM J. Sci. Stat. Comput., **6**, 464-491.

Tanaka, H. L., 1994. *Normal mode energetics of the general circulation during the FGGE winter.* Sci. Rept., Inst. Geosci., Univ. Tsukuba, Sect. A, **15**, 1-19.

Trenberth, K. E., 1985. *Potential predictability of geopotential heights over the Southern Hemisphere.* Mon. Wea. Rev., **113**, 54-64.

van Loon, H. and K. Labitzke, 1993. *Interannual variations in the stratosphere of the Northern Hemisphere: A description of some probable influences.* Interactions Between Global Climate Subsystems, The Legacy of Hann. Geophysical Monograph 75, IUGG Vol. 15.

Wallace, J. M., 1996. *Observed climate variability: Spatial structure, 31-81.* Decadal Climate Variability, edited by D. Anderson and J. Willebrand. NATO ASI Series I, Vol. 44, Springer, 493 pp.

Wallace, J. M. and D. S. Gutzler, 1981. *Teleconnections in the geopotential height field during the Northern Hemisphere winter.* Mon. Wea. Rev., **109**, 784-812.

Walland, D. J. and I. Simmonds, 1996. *Sub-grid-scale topography and the simulation of Northern Hemisphere snow cover.* Int. J. Climatol., **16**, 961-982.

Warren, S. G., C. J. Hahn, J. London, R. M. Chervin and R. L. Jenne, 1988a. *Global distribution of total cloud cover and cloud type amounts over land.* US Dept. of Energy/Office for Energy Research/National Center for Atmospheric Research, Washington, DC, DOE/ER/60085-H1 NCAR/TN-273+STR.

Warren, S. G., C. G. Hahn, J. London, R. M. Chervin and R. L. Jenne, 1988b. *Global distribution of total cloud cover and cloud type amounts over the ocean.* US Dept. of Energy/Office for Energy Research/National Center for Atmospheric Research, Washington, DC, DOE/ER-0406 NCAR/TN-317+STR.

Webster, P. J. and H.-R. Ghang, 1988. *Equatorial energy accumulation and emanation regions: impacts of a zonally varying basic state.* J. Atmos. Sci., **45**, 803-829.